MAPS, RISK AND VISUALIZATION-SUPPORTED REPORTS FOR MULTIMODAL MEDICAL IMAGE DATA

DISSERTATION

zur Erlangung des akademischen Grades

DOKTORINGENIEUR (Dr.-Ing.)

angenommen durch die Fakultät für Informatik der Otto-von-Guericke-Universität Magdeburg

von Nico Merten, M. Sc.
geboren am 31. März 1988 in Adenau

Gutachter

Prof. Dr. Bernhard Preim
Prof. Dr. Thomas M. Deserno
Prof. Dr. Heinrich Müller

Magdeburg, den 4. Dezember 2019

Submitted: 4. December 2019
Defended: 19. May 2020
Final Print: 19. June 2020

ZUSAMMENFASSUNG

Die Auswertung multimodaler medizinischer Bilddaten, das heißt von Daten, die mit verschiedenen bildgebenden Geräten, wie zum Beispiel Computer- oder Positronen-Emissions-Tomographen, aufgenommen werden, bieten unterschiedliche *Perspektiven* auf Gewebe. Einerseits sind diese für verschiedene Aufgaben vorteilhaft, wenn nicht sogar notwendig, um zum Beispiel metabolische Auffälligkeiten genau auf ihren morphologischen Ursprung beziehen zu können. Andererseits bringt diese erhöhte Anzahl von Bildquellen einen hohen mentalen Aufwand mit sich, da sie *simultan* zu bewerten und miteinander abzugleichen sind. Um Ärzte bei verschiedenen Aufgaben zu unterstützen, existieren in der klinischen Praxis bereits grundlegende Visualisierungs-, Bildanalyse- und Interaktionsmethoden.

In dieser Arbeit werden neue Visualisierungstechniken für (multimodale) medizinische Bilddaten vorgestellt. Diese zielen primär darauf ab, die oben genannten Methoden zu verbessern und Ärzte und/oder klinische Experten kognitiv zu unterstützen. Die Anatomieausbildung, interventionelle Radiologie und die Dokumentation von Befunden, Diagnosen und Behandlungsentscheidungen sind Disziplinen, die von solchen Methoden profitieren. In Bezug auf den Titel dieser Arbeit werden beispielsweise kartenbasierte Präsentationen, sogenannte *Floor Maps*, eingesetzt, um Medizinstudenten am Anfang ihres Studiums räumlich komplexe anatomische Anordnungen näher zu bringen. Darüber hinaus werden Techniken vorgestellt, die kognitive Unterstützung bei der Diagnose, der Interventionsplanung und -durchführung in der interventionellen Radiologie bieten. Beispielsweise verorten diese Techniken metabolisch verdächtige Läsionen *auf einen Blick* mit ihrem anatomischen Kontext oder unterstützen Ärtze klinisch praktikable Instrumentenpfade in solche Läsionen zu finden und zu bewerten. Am Ende wird eine Verarbeitungspipeline beschrieben, um klinische Berichte von thorakalen Lymphknotenmetastasen von Patienten mit primären Lungenkarzinomen zu erstellen.

Die meisten der in dieser Arbeit vorgestellten Techniken wurden von klinischen Experten, das heißt unter anderem von Anatomielehrern, Neuroradiologen und Nuklearmedizinern, evaluiert. Diese Auswertungen erfolgten über interaktive Fragebögen und/oder *think-aloud*-Gesprächen. Insgesamt bestätigten die Experten die individuellen Potentiale und Möglichkeiten der vorgestellten Methoden, so zum Beispiel die Potentiale

- gebäudeähnliche Präsentationen und Interaktionsmöglichkeiten zu verwenden, um die zweidimensionale Exploration von medizinischen Bildern zu verbessern,
- einer visualisierungsgestützten Risikobewertung, um das Finden und Bewerten von nadelbasierten Eingriffen in der Wirbelsäule zu unterstützen,
- von Visualisierungen, die Transparenzen, Silhouetten- und Kantenhervorhebungen kombinieren, um metabolische *Hotspots* in der Lunge darzustellen und
- der Verwendung von Patienten-unabhängigen und kartenbasierten Darstellungen, um die Erzeugung von klinischen Berichten und die interdisziplinäre Kommunikation, zum Beispiel in *Tumor Boards*, zu vereinfachen.

ABSTRACT

The assessment of multimodal medical image data, i. e. of images that are acquired via different imaging devices, such as Computed or Positron Emission Tomography scanners, offer different *perspectives* on tissue. On the one hand, for certain clinical tasks, such multiple perspectives are beneficial if not even necessary, for example, to accurately relate metabolic peaks to their morphological origin. On the other hand, however, with an increased number of image sources, the mental effort to assess all image sources *simultaneously* increases. In clinical practice, basic visualization, image analysis and interaction facilities already exist to support physicians.

Within this thesis, new approaches and visualization techniques for (multimodal) medical image data are presented that aim to enhance the aforementioned (established) facilities and to support physicians and/or clinical experts cognitively. Anatomy education, interventional radiology, and the documentation of findings, diagnoses and treatment decisions are disciplines and/or tasks that can benefit from such support. With respect to this thesis' title, for example, map-based presentations, so-called floor maps, are employed to provide building-like overviews of spatially complex anatomical arrangements to human medicine students to support their initial understanding about such anatomical regions. Furthermore, techniques that provide cognitive support during diagnoses, intervention planning and execution in interventional radiology are presented. These techniques, for example, relate metabolically suspicious lesions to their anatomical context *at a glance* or support physicians to find and assess clinically feasible instrument pathways into such lesions. Finally, a processing pipeline is described to create clinical reports with respect to thoracic and/or mediastinal lymph not metastases in patients with primary lung cancer.

Most of the techniques presented in this thesis were evaluated by clinical experts, e. g. by anatomy teachers, neuroradiologists or nuclear medicine physicians. These evaluations were carried out via interactive questionnaires and think-aloud interviews. Overall, the experts acknowledged the potentialities of the presented methods, i. e. the potential

- to employ building-like presentations and interaction facilities to enhance the two-dimensional exploration (slicing) of medical images,
- to improve the pathway finding process for needle-based interventions in the spine via visualization-supported risk assessment,
- to employ combinations of transparencies, silhouettes and boundary enhancements to convey metabolic hotspots in the lung and
- to use patient-unspecific map-based presentations to simplify the processes of clinical reporting and interdisciplinary communication, e. g. in tumor boards.

CONTENTS

ACRONYMS

AC	Attenuation Correction
AABB	Axis-Aligned Bounding Box
BE	Boundary Enhancement
BEP	Bull's Eye Plot
BIM	Building Information Modelling
BMD	Bone Mineral Density
CT	Computed Tomography
CTA	Computed Tomography Angiography
CFD	Computational Fluid Dynamics
CSV	Comma-Separated Values
DICOM	Digital Imaging and Communications in Medicine
DGN	Deutsche Gesellschaft für Nuklearmedizin e.V.
DNA	Deoxyribonucleic Acid
DOF	Depth of Field
DSA	Digital Subtraction Angiography
DXA	Dual-Energy X-ray Absorptiometry
DVR	Direct Volume Rendering
eV	Electronvolt
FBO	Framebuffer Object
F+C	Focus and Context
FDG	Fludeoxyglucose
fMRI	Functional Magnetic Resonance Imaging
FOI	Feature of Interest
FOV	Field of View
FPS	Frames per Second
GLCM	Gray Level Co-Occurrence Matrix
GLUT	Glucose Transporter
GUI	Graphical User Interface
GPU	Graphics Processing Unit
HU	Hounsfield Unit
IVR	Indirect Volume Rendering
kVp	Kilovoltage Peak
LN	Lymph Node
LNS	Lymph Node Station
LOD	Level of Detail
LOR	Line of Response
LUT	Lookup Table
MIP	Maximum Intensity Projection
MPR	Multiplanar Reformation
MR	Magnetic Resonance
MRA	Magnetic Resonance Angiography
MRI	Magnetic Resonance Imaging
NLST	National Lung Screening Trial
NMR	Nuclear Magnetic Resonance
NSCLC	Non Small Cell Lung Cancer
OABB	Object-Aligned Bounding Box
OECD	Organisation for Economic Co-operation and Development
OIT	Order-Independent Transparency
OR	Operation Room
PACS	Picture Archiving and Communication System
PCA	Principal Component Analysis
PDF	Portable Document Format
PERCIST	Positron Emission Tomography Response Criteria in Solid Tumors
PET	Positron Emission Tomography
PNG	Portable Network Graphics
POI	Point of Interest
RECIST	Response Evaluation Criteria in Solid Tumors
RF	Radio Frequency
RFA	Radio Frequency Ablation
ROI	Region of Interest
SCLC	Small Cell Lung Cancer

SIRT	Selective Internal Radiation Therapy
SNR	Signal-to-Noise Ratio
SOI	Structure or Slice of Interest
SPECT	Single Photon Emission Computed Tomography
STIR	Short Tau Inversion Recovery
SUV	Standard Uptake Value
TE	Echo Time
TF	Transfer Function
TOF	Time-of-Flight
TR	Repetition Time
US	Ultrasound
VSWM	Visuo-Spatial Working Memory
VOI	Volume of Interest
WM	Working Memory
WMC	Working Memory Capacity

1 INTRODUCTION

MULTIMODALITY per se is challenging and takes effort to be obtained. It is easier to briefly reflect on something from only one perspective, which is a valid and natural starting point, e. g. to start learning something new. However, this results in one-sided knowledge. As soon as more perspectives receive attention and are reflected on in more detail, deeper understanding can be obtained.

This also applies to multimodality in a medical image context. For some applications, a single perspective can be sufficient, e. g. examining radiographs for broken arms. Other medical fields, e. g. oncology and interventional radiology, benefit or even require a combination of multimodal images. For example, combinations of Computed Tomography (CT) and Positron Emission Tomography (PET) images allow physicians to conclude about the morphology and physiology of anatomy. Both perspectives are important, because not everything that appears to be suspicious, behaves suspiciously, but if something behaves suspiciously, its position, size and shape must be ascertained with high fidelity to choose the right treatment. Many scans have a 3D (x, y, z) data layout, i. e. they are stacks of 2D (x, y) images or slices, but they are typically assessed in a slice-based manner. *Slicing* through image stacks enables physicians to *read* in-plane spatial relationships of different kinds of anatomy, but it also requires them to mentally fuse adjacent slices to assess relationships along the third anatomical axis. On the one hand, they are well-trained to do so. On the other hand, assessing even one medical scan in such a manner requires high mental effort, but in scenarios with multimodal image data they also have to merge multiple image sources into one mental representation. To support such and comparable tasks, there exist basic presentation and interaction facilities in clinical practice, e. g. color-coded superimpositions or synchronized slicing. Naturally, there exists a research interest in more sophisticated techniques. However, w. r. t. presentation and visualization techniques, visual clutter must be balanced, since large amounts of information are available that can be presented, while certain pieces of information have to be preserved or enhanced to support certain tasks.

1.1 THESIS CONTRIBUTIONS

In this thesis, visualization techniques and approaches for multimodal medical images are presented that offer exploration and assessment support for anatomy education, interventional radiology, and the documentation of findings, diagnoses and treatment decisions. Thus, the (overarching) main goal is to enhance established (visualization and/or presentation) facilities in clinical practice, not to replace them.

Traditional anatomy education is a combination of lectures, cadaver dissection classes, and self-studying with text books, so-called atlases [383]. Typically, physicians and professional illustrators collaborate to create anatomy illustrations that show certain anatomical structures and their surroundings, e. g. in a dedicated learning unit, with a higher and a lower degree of detail, respectively. In other words, the degree of abstraction can vary. In the early 1990s, an increased interest in digital solutions arose, and since then various digital atlases and web-based applications were developed [196]. There exist solutions that use multi-viewer approaches with real medical images on one side and Indirect Volume Rendering (IVR) of anatomy models on the other side to support exploration and to depict spatial relationships in 3D. With respect to such multi-viewer setups, here, a novel visualization method is presented that displays gross anatomy via floor maps, which are usually employed to provide spatial overviews of multi-story buildings. There already exist methods that utilize maps for medical image data, e. g. to visualize safety margins for needle insertions or post-interventional evaluations of ablation zones [187, 403]. However, no methods exist to transform medical images into multi-story-like layouts.

Interventional radiology is comprised of various stages, e. g. diagnosis and intervention planning. The assessment of multimodal medical images is a crucial part in most of them. To enhance the aforementioned basic presentation and interaction support, multimodal visualization techniques for PET, CT, and Magnetic Resonance (MR) images are presented. Although interventional radiology comprises various types of intervention [412], here, visualization techniques are described for Selective Internal Radiation Therapies (SIRTs) in the lung and Radio Frequency Ablations (RFAs) in the spine. For SIRTs, an illustrative approach is presented that combines Order-Independent Transparencies (OITs) and Boundary Enhancements (BEs) for CT and PET images in 3D. In contrast, for RFAs, a two-step risk assessment method is presented that intends to offer cognitive support during intervention planning (Step 1) and physical support for robot-assisted bone drilling during intervention execution (Step 2) (cf. *Division of Work*). For Step 1, methods were developed to visualize safety margins between intervention instruments and risk structures in 2D and 3D. Here, CT and MR images were used.

During any stage of hospitalization, findings, diagnoses, treatment decisions, and treatment responses are documented in reports. Such reports usually consist of text and tables with partially standardized phrasing and relevant measurements only, e. g. to describe cancerous infiltration of tissue or the size of lung nodules. On the one hand, this results in documents that represent patients w. r. t. their disease and treatment objectively, but on the other hand, this does not reflect the visual nature of image-heavy medical fields [394]. Therefore, a pipeline is presented to create visualization-supported reports. This pipeline is described in the context of thoracic lymph node metastases in patients with primary lung cancer based on PET and CT images. The visualizations are done in 2D and 3D, but the chapter will be focused on a 2D map-based approach. Furthermore, to tackle the issue of ambiguous color information for color-coded superimpositions on screen or paper, a method is presented that creates color palettes for Region of Interest (ROI) annotations complementary to color codings used for superimpositions.

1.2 THESIS STRUCTURE

This thesis is comprised of the following chapters:

- Chapter 2. In this chapter, a background on CT, PET, MR, and multimodal imaging is provided. While these modalities are described, similarities and differences in the imaging processes and resulting images are highlighted. Furthermore, clinical benefits and necessities for combinations of PET and CT, and CT and MR images are presented, and how they are *read* in a clinical workflow.
- Chapter 3. This is also a background chapter and complements the previous one by providing an overview of visualization techniques for multimodal medical image data. Here, a broad overview of related work is provided, while differentiating combinations of morphology and physiology, e. g. PET and CT, combinations of morphology and morphology, e. g. CT and MRI, and others.
- Chapter 4. The 4th chapter presents a novel approach that transforms pre-labeled medical image data of gross anatomy into 3D floor maps. Furthermore, the chapter presents backgrounds on abstraction, cognition, and color coding of maps and medical image data. Given that image data is made available via segmented and/or labeled structures, the presented method is independent from the utilized modalities.
- Chapter 5. This chapter presents a two-step method to assist physicians prior and during RFAs of spine metastases. Step 1 aims to offer cognitive support during intervention planning via 2D and 3D visualizations, and Step 2 intends to offer physical support during robot-assisted bone drilling of vertebrae in the future. The chapter is complemented by backgrounds on the spine and RFAs in general, a requirement analysis for software that intends to assist RFAs, and an evaluation of two neuroradiologists. The presented method uses CT and MR image data.
- Chapter 6. In this chapter, an illustrative visualization method is presented that aims to assist physicians during diagnoses and intervention planning of SIRTs in the lung. Additionally, an approach is presented to enhance pulmonary arteries in low-dose CT images, namely the LANCELOT method. The chapter is also comprised of backgrounds on the lung and SIRTs, a requirement analysis, and evaluations of all methods. The presented methods use low-dose CT and PET image data.
- Chapter 7. The 7th chapter presents a processing pipeline to create visualization-supported clinical reports. The method is presented in the context of primary lung cancer w. r. t. thoracic lymph node metastases. Various abstraction and color-coding concepts are presented to convey thoracic lymph node diseases. The chapter is complemented by an evaluation of two nuclear medicine physicians and a brief presentation of how visualizations can be used for patient education prior to interventions. The presented methods were applied to CT and PET image data.
- Chapter 8. In the final chapter, the thesis is concluded by summarizing and discussing contributions, limitations and open ideas for further research.

2 BACKGROUND ON MULTIMODAL MEDICAL IMAGING

This is the first background chapter in which an overview of mono- and multimodal imaging is given. In simplified terms, an imaging modality utilizes a physical phenomenon to acquire images of gross human anatomy or physiological processes. There exist various imaging modalities, but this thesis will be focused on Computed Tomography (CT), Positron Emission Tomography (PET), and Magnetic Resonance Imaging (MRI). In the next section, their basic acquisition principles will be explained, while similarities and differences between them and the resulting images are highlighted. Subsequently, multimodal imaging w. r. t. certain combinations is explained. For example, which design choices have to be considered when merging PET and CT hardware into one scanner and how X-rays can be used for PET Attenuation Correction (AC). Section 2.3 describes how multimodal medical images are *read* in clinical practice. With respect to the following contents of this thesis, this chapter is concluded by a short summarization.

2.1 MEDICAL IMAGING MODALITIES

It is astonishing that we have access to imaging devices that use physical phenomena, e. g. electromagnetic radiation, radioactive decay, or magnetism, to depict the insides of our bodies. Depending on which phenomenon is used, the resulting images either depict morphology or physiology. This statement, however, is not true for the phenomena themselves, because magnetism, for example, can be used to depict morphology (MRI) and functionality (fMRI).

2.1.1 COMPUTED TOMOGRAPHY (CT)

CT scanners use X- or Röntgen rays to acquire images. X-rays are electromagnetic radiation and were discovered by Röntgen in 1895 [408]. Approximately one century earlier, Herschel and Ritter discovered infrared and ultraviolet light in 1800 and 1801, respectively [189, 407]. However, it was Hertz who proved and described the existence of electromagnetic waves in 1887 [190]. Just like Röntgen, Hertz and his student Lenard experimented with cathodes and cathode rays, and although it appears that they discovered X-rays in 1892, it was Röntgen who first published his article about these *unknown rays* in 1896.[1] However, it took another 76 years until Hounsfield and Ambrose acquired the first CT scans by utilizing X-rays in patients with brain tumors [12, 200]. The brain was and still is used for early imaging studies in humans since, in contrast to the thorax and abdomen for example, it is fixed in the skull and does not move.

[1] https://en.wikipedia.org/wiki/Heinrich_Hertz, last accessed July 13, 2019

CT images are acquired via transmissive X-radiation. In other words, radiation source and detectors are placed outside of the patient (see Fig. 2.1). Depending on the radiodensity of transversed tissue, X-rays are attenuated differently. For example, bone tissue is more radiodense than skin, and thus, passing out X-rays are weaker when they traversed a lot of bone tissue. For each anatomical region, i. e. virtual cross-section or slab of patient tissue, this is repeated multiple times along the patient's vertical axis, which results in multiple radiodensity profiles per cross-section. When all regions are scanned, the Fourier slice theorem, which builds on the Radon transformation, is used to combine said profiles to create tomographic, cross-sectional image stacks that depict patient tissue [370, 387]. In contrast, spiral or helical CT scanners move patients continuously through the rotating radiation source, which results in shorter acquisition but longer reconstruction times [183]. For an in-depth description of CT, see the book of Jiang Hsieh [202].

CT belongs to the imaging modalities that are used to depict morphology in high detail (see Fig. 2.2). For example, w. r. t. the subsequent image reconstruction, so-called ultra-high-resolution CT scanners can acquire images with an image matrix size of 2048×2048 pixels, an in-plane pixel resolution of $0.156\,mm^2$, and a slice thickness of $0.25\,mm$ [182]. Clinical applications for such high resolution images are, for example, the assessment of cranial arteries or lung parenchyma [182, 352]. However, such devices are currently used for clinical studies only. CT scans from *everyday* scanners typically have image matrix sizes of 512×512 pixels, an in-plane pixel resolution of $1\,mm^2$ to $0.3\,mm^2$, and

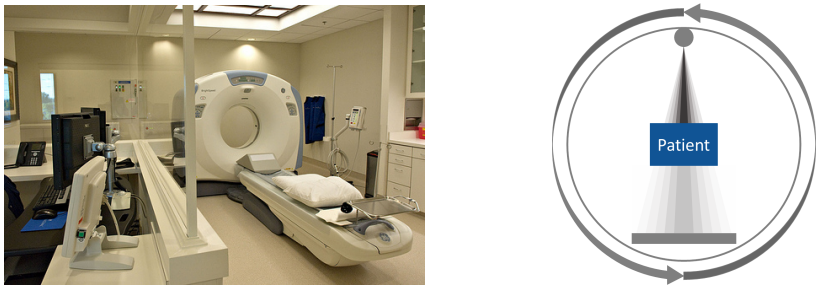

(a) **(b)**

Figure 2.1: Subfigure **(a)** depicts a *GE BrightSpeed CT Imaging Suite* (GE Healthcare, Chicago, Illinois, United States) with the control room on the left and the scanner on the right. Both areas are divided by radiodense walls and lead glass to decrease the radiation exposure of scanner operators. Subfigure **(b)** illustrates the simplified concept of how CT scanners utilize transmissive X-radiation to acquire images along a patient's vertical axis. X-rays are emitted from the rotating radiation source (•), which are attenuated by the patient's anatomy, and are then captured by the detector. Here, a uniform attenuation of all rays is assumed, whereas in reality each ray can be attenuated differently w. r. t. the radiodensity of the traversed tissue. Typically, one tomographic image is acquired per rotation, but modern scanners can record up to 256 images per rotation along the vertical axis [132].

a slice thickness of 3 *mm* to 1 *mm*. Regarding acquisition time, CT scans can be acquired in a few seconds, i. e. during breath-holding of approximately 5 *s* to 15 *s* [155, 483]. In addition to spiraling X-ray sources, the use of multiple X-ray detectors further improved acquisition times by scanning multiple tissue cross-sections simultaneously. Depending on the clinical application, image contrast of blood vessels and gastrointestinal organs w. r. t. surrounding tissue can be enhanced by intravenously and orally administered contrast media, respectively. However, this is not feasible in all patients due to iodine and/or barium allergies [4]. In Germany, in 2017 roughly 2900 CT scanners were installed.[2]

2.1.2 INTERMISSION – ELECTROMAGNETIC RADIATION AND MATTER

This section intends to be a transition between CT and PET from an electromagnetic radiation perspective, because, although both modalities are different *from afar*, they are similar on an atomic scale. These similarities and differences affect the image quality and radiation exposure for patients, which are also explained here.

There exist various types of electromagnetic radiation. These types are distinguishable w. r. t. their frequency, wavelength, and energy. Regarding their energy, electromagnetic radiation can also be divided into ionizing and non-ionizing radiation. For example, infrared, micro-, or radio waves cannot ionize other atoms or molecules. In contrast, X-rays can do so, which means that they are powerful enough to *kick out* electrons from molecular bounds. These free electrons become ionized and have a high reactivity with other molecules, which can cause mutations [396].

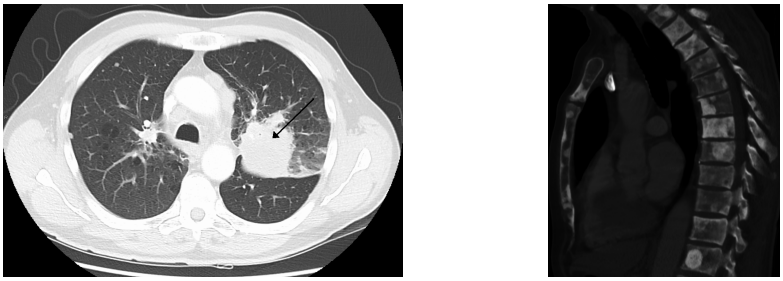

(a) **(b)**

Figure 2.2: Two CT images of cancerous tissue in the lung and spine. Subfigure **(a)** depicts an axial cross-section of a large primary lung carcinoma on the right side (cf. Ch. 6). In contrast, Subfigure **(b)** shows multiple bone metastases in the spine and sternum from prostate cancer (cf. Ch. 5). Both images depict morphological abnormalities with high contrast to surrounding tissue.

[2] https://data.oecd.org/healtheqt/computed-tomography-ct-scanners.htm#indicator-chart, last accessed August 2, 2019; https://www.statistik-bw.de/VGRdL/tbls/tab.jsp?rev=RV2014&tbl=tab20&lang=de-DE, last accessed August 7, 2019

The three main interactions between electromagnetic radiation and matter are the Compton effect, photoelectric effect, and pair production, which are depicted in Figure 2.3. However, the ratio of these interactions heavily depends on photon energy and molecular composition of tissue [38]. For X-ray-based image acquisitions, pair productions cannot happen, since this type of interaction requires higher Electronvolt (eV) energy levels, i. e. $\gtrsim 1\ MeV$, while X-ray images are typically acquired at energy levels around $130\ keV$ and less. The X-ray energy level is donated by the scanner's Kilovoltage Peak (kVp), which represents the X-ray tube's current and thus the maximum energy level of outgoing X-rays. Rather than having the same energy level, the outgoing photons lie on a spectrum, e. g. from $40\ keV$ to $130\ keV$ with a mean energy level of about $80\ keV$ for a kVp of 130 [510].

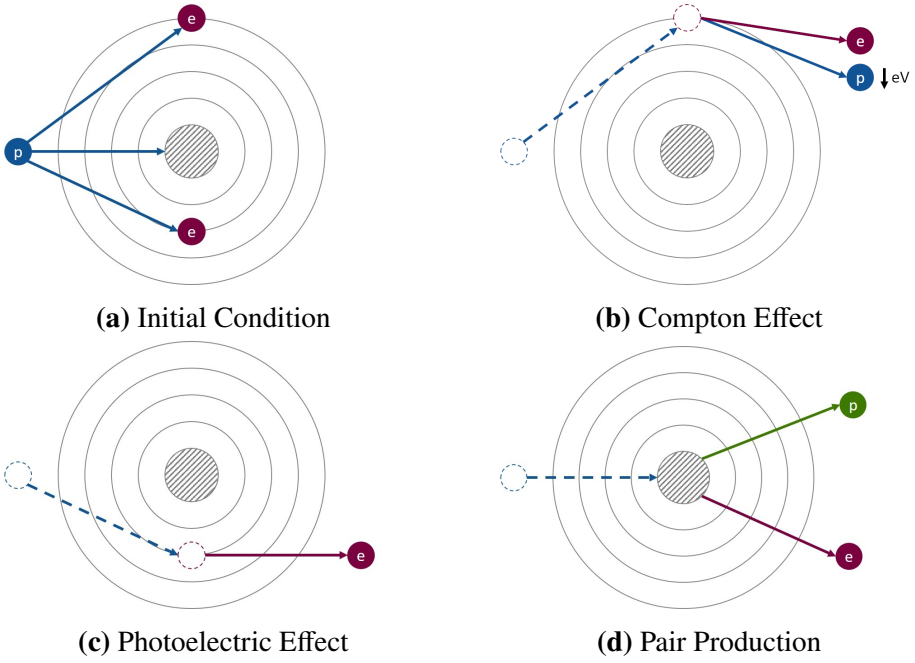

(a) Initial Condition **(b)** Compton Effect

(c) Photoelectric Effect **(d)** Pair Production

Figure 2.3: The three main interactions between electromagnetic radiation and matter. Subfigure **(a)** shows the initial condition in which a photon gets close to an atom. When the photon gets near an electron, the electron is *kicked out* of its atomic bound and is ionized. If an outer shell electron is hit **(b)**, the photon is scattered and looses energy ($\downarrow\ eV$), but can still interact with other atoms. This is called the Compton effect. This particular depiction is also called *coherent* or *forward scatter*, since the photon's trajectories prior and after collision are similar [38]. In contrast, for *incoherent* or *backward scatter*, old and new trajectory would oppose each other. If an inner shell electron is hit **(c)**, the photon is annihilated. This is called the photoelectric effect and for photon energies $\lesssim 100\ keV$ the contribution of this effect becomes negligible [219]. For the last effect, a photon has to get close to an atomic nucleus **(d)**. Subsequently, its energy can get converted into an electron-positron pair. However, this can only occur at energy levels $\gtrsim 1\ MeV$, i. e. not during X-ray-based but during PET image acquisitions.

The images were inspired by [38, Fig. 2].

Overall, Compton interactions are the predominantly occurring events between X-ray and PET radiotracer photons and tissue [91]. They occur when photons get close to outer shell electrons of atoms. As a result, the electron is liberated from its atomic bound, while the photon is weakened and scattered. Ionized electrons can damage other molecules and depending on the photon's initial energy, multiple Compton events can occur [218, 396]. This increases a patient's radiation exposure and decreases the image quality, since photons are often scattered away from their original trajectories. Thus, they are less likely to hit radiographic films, CT detectors, or gamma cameras during radiography, CT, and PET image acquisitions, respectively. Alternatively, scattered photons can hit the detector, but not at their intended positions, which decreases image contrast and increases image noise.

In contrast, when a photon gets close to an inner shell electron, photoelectric effects can occur [118]. Here, the affected electron also gets ionized, but the photon gets completely absorbed or annihilated. This also increases the patient's radiation dose, but less than before, since this event can only occur once per photon. Moreover, the image quality is not decreased, since annihilated photons do not contribute to the resulting images.

DISCUSSION ON KVP. Choosing the right kVp for X-ray-based image acquisitions is crucial for good image quality. Lower energy levels result in better soft tissue contrast. This is because soft tissue, in contrast to bones for example, is primarily comprised of elements that have a low electron count, such as carbon or oxygen, which decreases the probability of photoelectric effects to occur [73, 118, 242, 510]. However, this also results in an increased radiation dose. In contrast, higher energy levels decrease X-ray absorption, since photons are more likely to just pass through patient tissue, but with increasing energies Compton scattering becomes more prominent, which decreases the image contrast. This becomes more complex in big patients, since they are composed of more soft tissue. Thus, to achieve similar image contrast, higher energy levels have to be used for large patients. In other words, choosing a *good* kVp is a balancing act between radiation absorption and image quality. Furthermore, the kVp also influences the CT-based attenuation correction of PET images, which will be explained in Section 2.2.1 [242].

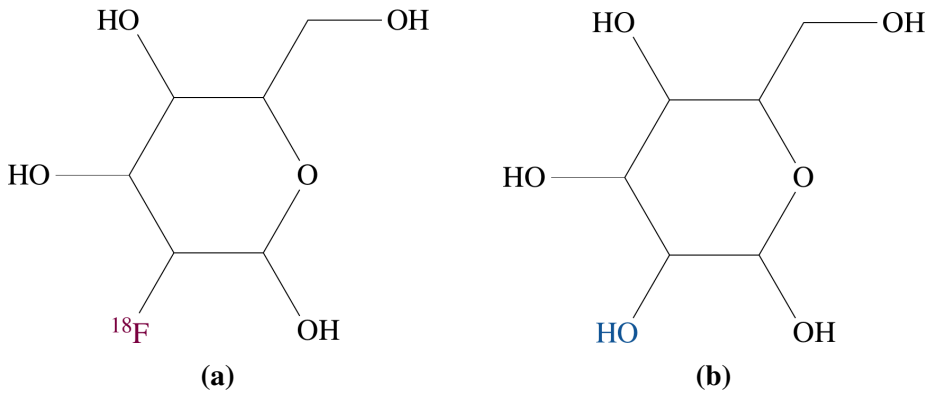

Figure 2.4: ^{18}F-FDG **(a)** is often described as a glucose **(b)** analog. Both molecules are virtually identical, since the only difference is the radioactive fluorine isotope ^{18}F that is substituted for a hydroxyl group.

For pair productions to occur, two conditions have to be met [57]. First, photons require high energy levels, i. e. $\geq 1.022\,MeV$, and secondly, they have to get close to nuclei of atoms [393]. The strong electromagnetic field of a nucleus absorbs the photon and converts its energy into an electron and positron. A positron is an electron's anti-particle. The energy is divided evenly, so both the electron and positron have energies of $511\,keV$, and excess energy is converted into kinetic energy. In contrast, when electrons and positrons get close, they annihilate each other and produce two photons with energies of $511\,keV$ each. This is called electron-positron annihilation, which is the reverse process of pair production.

These processes are important for PET imaging. In Figure 2.4, the molecular structure of ^{18}F-Fludeoxyglucose (FDG) is depicted, which is the most commonly used PET radiotracer in cancer imaging. The radionuclide ^{18}F undergoes radioactive β^+ decay and converts its nucleus' protons into positrons. This applies to many PET radiotracers, hence the name positron emission tomography. These positrons can then trigger annihilation events, which result in two photons, which in turn are captured by the PET detectors. However, these photons can also trigger Compton scattering events. Regarding the patient's exposure to radiation, pair productions contribute less than the Compton and photoelectric effects, but the *damage* is very organ-specific, i. e. the lung and thyroid are very prone to X-rays, while the bladder is subjected to much radioactive decay [362].

2.1.3 POSITRON EMISSION TOMOGRAPHY (PET)

Before tomographic PET images could be acquired, planar scintigraphy images were taken with so-called *recorders* that had gamma ray-sensible paper or films inside them [15]. Among others, Anger built such devices in the 1950s that later became gamma cameras, whose basic principle is still used in PET and SPECT scanners today [16]. Kuhl et al. [259, 260] acquired the first scintigraphy images using ^{131}I and ^{198}Au radiotracers to depict thyroid and liver tumors. The first tomographic PET scans were acquired in 1975 by Ter-Pogossian et al. in dogs [472]. One of the first commercial designs that pushed clinical research programs with PET was the Emission Computerized Axial Tomograph (ECAT) [219]. This was in 1999. However, the first commercially available scanners that used block detectors (see below) were already presented around 1988 [219]. In 2018, Cherry et al. presented the first full-body PET scanner with a vertical FOV of $200\,cm$ [80].

In Figure 2.5, an open PET scanner is depicted. Inside the scanner, multiple block detector rings are installed that approximately cover $16\,cm$ to $25\,cm$ along and 360° around the patient [219]. This makes it possible to just move patients through the detector rings without rotating them, which decreases the noise exposure of patients considerably. Depending on the scanned body region, the patient's tallness, and detector ring count, bed and patient are moved in 5 to 7 discrete, partially overlapping steps [219]. Jones and Townsend report [219] that there were advances in the 1990s to build cheaper scanners that discarded approximately 60 % of the detectors [482]. This made it necessary to rotate the PET detectors to acquire tomographic images, which increased acquisition times and thus

[3] Interestingly, the first hybrid PET/CT scanners were available in 2001. Only three years later, Townsend predicted that combined scanners would replace PET-only devices [483]. In the same year, PET-only scanners could no longer be bought from larger vendors [219].

decreased patient throughput. Therefore, the research interest for cheaper PET scanners dropped. The first design of hybrid PET/CT scanners was proposed in 1991, which would enable patients to remain stationary between both scans, which in turn would decrease the overall acquisition time and result in coregistered images.[3] For more details on the history of PET scanners, see the article of Jones and Townsend [219].

PET BLOCK DETECTORS. PET detectors are multi-layered hardware pieces and they are called *block detectors* due to their block-like appearance [219]. In the first layer, i. e. nearest to the scanner gantry, multiple *scintillators* are ordered in a matrix. Scintillators are materials that translate ionizing radiation/ excitement into light impulses. Generally, these light impulses are too weak to be detected by the cameras in the last layer. Thus, in between, photomultipliers are used to enhance these impulses. The ratio between scintillators, photomultipliers, and cameras is not 1:1:1 and a block detector is typically comprised of an 8×8 or larger scintillator matrix, four photomultipliers, and one camera [219].

In contrast to CT scanners that use transmissive radiation, PET block detectors capture and/or count emitted photons (see Fig. 2.5). These photons are emitted by the radioactive ligand of intravenously administered radiotracer, e. g. ^{18}F. After administration, the tracer is spread through the body via the cardiovascular system and its *biological component*, e. g. FDG, connects to suitable receptors, which takes time. Typically, patients have to wait 30 *min* to 60 *min* between administration and image acquisition [298].

^{18}F-FDG. In simplified terms, ^{18}F-FDG works in the following way: FDG connects to so-called Glucose Transporters (GLUTs) that are present on cell membranes to transport glucose inside cells to fuel them with energy. Cancerous tissue prefers glucose over oxygen

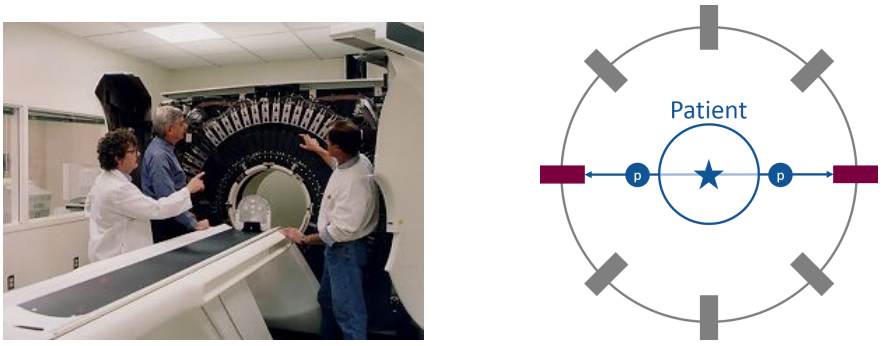

(a) **(b)**

Figure 2.5: Subfigure **(a)** depicts a *GE Advance PET Scanner*. Here, the front cover was removed and the PET block detector ring is revealed that captures photon hits. This is schematically shown in Subfigure **(b)**, where an annihilation event (★) emits two photons, which hit a pair of detectors. If two photons hit opposing detectors in a very short time frame, typically $\lesssim 10\,ns$, these hits are called coincidences or coincidental photons hits, which contribute to the final images.

Image **(a)** was uploaded by "Was a bee" on Wikimedia Commons and was released into the Public Domain. Image **(b)** was inspired by [483, Fig. 2].

to fuel its abnormal growth, and to extend its blood vessel network via angiogenesis. Thus, when compared to surrounding tissue that typically relies on oxygen for energy, cancerous tissue has more GLUTs [495]. Consequently, more radiotracer is accumulated in cancer tissue, which in turn results in increased coincidence counts from such body regions. In other words, PET images depict where radiotracer is utilized, and thus, PET is called a physiology-depicting imaging modality. Moreover, FDG has to compete with other glucose-like substances for GLUTs, and thus, patients should fast for around $4\,h$. This time frame can be extended to $6\,h$ in patients with diabetes [313].

This also explains why PET scans have higher acquisition times than CT scans. For CT, X-ray photons quickly traverse patient tissue and are captured by the detectors. In contrast, radiotracers must be given time to accumulate photon hits. PET image acquisitions can range from $10\,min$ to $60\,min$, but can take up to several hours [497]. Similar to CT, pregnant women should not undergo PET image acquisitions. Furthermore, mothers should also interrupt breastfeeding when getting a PET scan [497].

PET VS. SPECT RADIOTRACERS. Generally, PET radiotracers have a biological and a radioactive component. In contrast, Single Photon Emission Computed Tomography (SPECT) radiotracers are typically unbound radioactive isotopes, such as ^{123}I or ^{99m}Tc, which do not have a biological component. They are often taken up *directly* by the patient's body, e. g. by hormones. In comparison, SPECT tracers have a longer half life than PET tracers (^{18}F: $1.83\,h$, ^{99m}Tc: $6.01\,h$, ^{123}I: $13.13\,h$) [310]. Therefore, PET tracers have to be synthesized on-site, which requires hospitals to buy and maintain synthesis devices, e. g. cyclotrons or other *synthesis boxes*, which are large, often radio-shielded, and costly machines [302, 423]. Another difference is that SPECT radiotracers emit photons at lower energy levels (^{18}F: $511\,keV$, ^{99m}Tc: $140\,keV$, ^{123}I: $159\,keV$) [302], i. e. they do not trigger pair production events, and thus, only one photon camera is necessary. However, modern SPECT scanners can have two gamma cameras, which improves image quality.

There exist various PET radiotracers and which one is chosen depends on the clinical application. As mentioned before, ^{18}F-FDG is chosen for tumor imaging due to increased glucose receptors. In contrast, ^{18}F-Sodium-Fluoride (^{18}FNa) is used for bone scintigraphy (see Fig. 2.7), since bone tissue accumulates flourine around bone abnormalities, e. g. fractures or metastatic lesions [49]. Another example is the amino acid tracer ^{18}F-Fluoroethyltyrosine (^{18}F-FET) that, in contrast to FDG, does not accumulate in inflammatory cells, e. g. arteriosclerosis, and has a lower uptake in brain cells, which results in higher sensitivity when imaging brain tumors [113]. For more details on PET radiotracers, how they are synthesized, and how our bodies utilize them, see the book of Saha [423].

PHOTON SCATTERING. *Coincidental photon hits* happen when two opposing detectors capture incoming photons in a short time frame (cf. Fig. 2.5). However, it is not guaranteed that these photons originate from the same positron-electron annihilation event. This is shown in Figure 2.6. A perfect PET scan would only be comprised of real coincidences. However, even with precautions, such as scatter correction and single rate counting, up to 40 % to 50 % of the total coincidence count can result from scattered and random coincidences, respectively [483]. Scatter correction can be done by applying

energy thresholds for incoming photons, since they loose energy in case of scatter events with tissue ($< 511\ keV$; cf. Fig. 2.3) [41]. Single counts occur when only one photon hits a detector. This can happen, for example, if emitted photons originate outside the scanner's current Field of View (FOV), since the radiotracer is distributed throughout the patient's body, while photon capturing is done during discrete bed positions.

PET IMAGE QUALITY. Counting single photon hits and coincidences outside the actual coincidence time window allows for an estimation of how many random coincidences occurred [483]. Early PET scanners were built with collimator-like shields, namely septa, which were made of lead or tungsten and were mounted between adjacent detector rings.

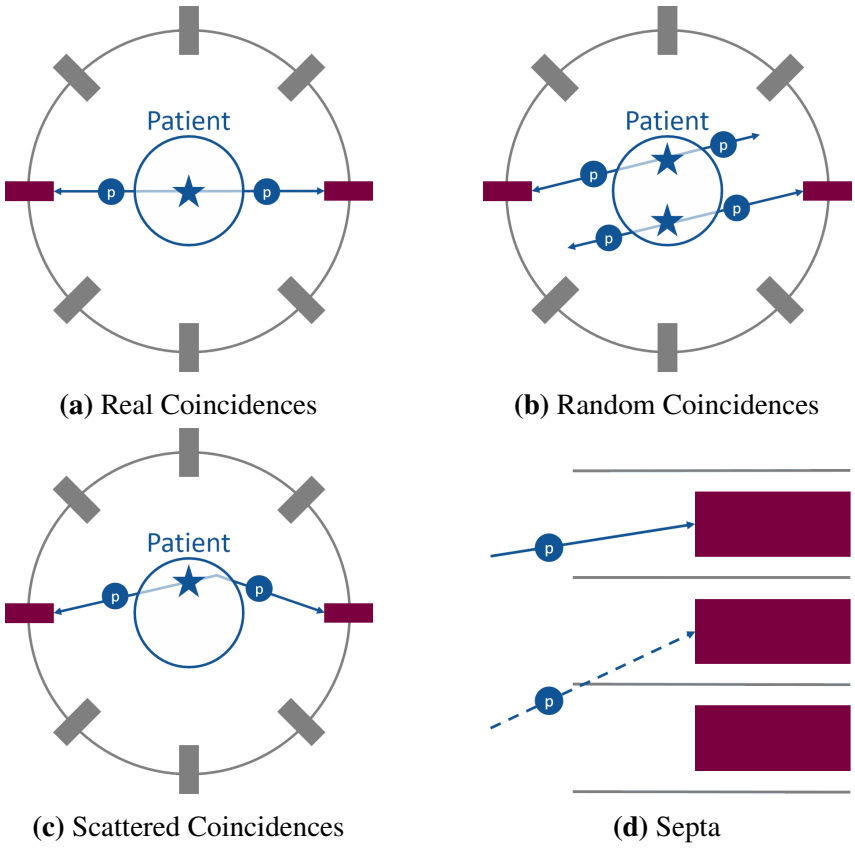

(a) Real Coincidences **(b)** Random Coincidences

(c) Scattered Coincidences **(d)** Septa

Figure 2.6: Although PET detectors record coincidental photon hits, it is not guaranteed that they originate from the same annihilation event (★). There exist real **(a)**, random **(b)**, and scattered **(c)** coincidences. For real coincidences, emitted photons are captured w. r. t. their true Line of Response (LOR) (↔). Random coincidences occur when two photons from separate annihilation events hit some detectors in a shorter time frame than they hit their true detector pairs. Scattered coincidences occur when a photon gets scattered from its LOR and triggers a different pair of detectors (cf. Fig. 2.3). Moreover, these two events can coincide. In early PET scanners, one way to overcome this was to install lead or tungsten septa between detector rings that would block photons coming in from large angles **(d)**.

Images **(a–c)** were inspired by [483, Fig. 2], while Image **(d)** was inspired by [483, Fig. 6].

This limited each ring's FOV, which in turn limited random and scattered coincidences, but real coincidence counts were also decreased for photons with unfavorable LORs. One advantage was that PET scanners could be operated in *2D mode*, i. e. image reconstruction could be done plane-wise, but the scanner's sensitivity, i. e. the true positive coincidence count, was also decreased significantly [483]. To increase the sensitivity, vendors later installed retractable septa, which enables PET scanners to be operated in *3D mode*, which resulted in scatter and random events occurring about three times more often.

Improved detector materials enabled shorter coincidence time windows, and thus, improved image quality (see Fig. 2.7). For captured coincidence events, the respective annihilation events can be placed virtually anywhere on their LORs, i. e. the virtual line between the triggered detectors. This uncertainty can be limited by decreasing the coincidence time window, since this limits the risk of unwanted trigger events during real coincidences. In other words, decreasing the coincidence time window narrows the spatial location of the corresponding annihilation event, i. e. at which voxel coordinates in the resulting image stack the coincident count has to be incremented. Modern scanners can push this Time-of-Flight (TOF) time frame down to 400 ps, but there already exist theoretical approaches to further decrease this window to 10 ps, which would result in a spatial uncertainty of around 1.5 mm along LORs [278, 483].

Another aspect is the detector size. Current scans have an image matrix resolution of around 200×200 pixels, a pixel resolution of 4 mm^2, and a slice thickness of 3 mm [343]. Similarly, theoretical groundwork describes how pixel resolution could be improved to 0.5 mm^2 [461]. For small animal PET scans, i. e. at a much smaller FOV, pixel resolution can be improved to 0.2 mm^2 at a slice thickness of 0.58 mm [466]. Given that such and other advances would be used for PET scanners for humans, PET and CT images would be on par w. r. t. their ability to depict a high degree of detail. For a more detailed discussion on these and other factors, see the article of Moses [343].

To further improve the PET image quality, AC is used to distinguish real from unwanted coincidence events. Coincidences along LORs with a high risk of scattering, i. e. LORs that go through a lot and/or very dense tissue, are *rewarded* by linear upscaling. Originally, in PET-only scanners, this was done with radioactive germanium rods or caesium point sources. However, hybrid PET/CT scanners are replacing PET-only devices that use low-dose CT scans for AC, and thus, AC is explained in Section 2.2.1. In Germany, in 2019 191 PET-only scanners were installed of which 132 are hybrid PET/CT scanners.[4]

2.1.4 MAGNETIC RESONANCE IMAGING (MRI)

In contrast to electromagnetic radiation, the physical phenomenon of magnetism was found and used much earlier. The first scientific description of magnets and their properties, such as having poles that repel and attract each other, was done by Petrus Peregrinus in 1289. Peregrinus also described how compasses work, which enabled medieval Europe to navigate around the globe [14, 345]. In regard of medicine, magnetic materials were first

[4] https://www.nuklearmedizin.de/patienten/standorte/standort_search.php?navId=68, last accessed July 17, 2019

used to stop bleeding, to treat burns, or to *pull* out foreign objects out of wounds, such as arrow heads [14]. Around the same time when Röntgen researched X-rays, Zeeman demonstrated how atoms behave differently when under the influence of strong magnetic fields [525]. This lead to the theory that atoms possess their own magnetic fields, which were first measured by Rabi et al. around 40 years later [386]. This phenomenon was named Nuclear Magnetic Resonance (NMR) and was later independently proven by Bloch (in

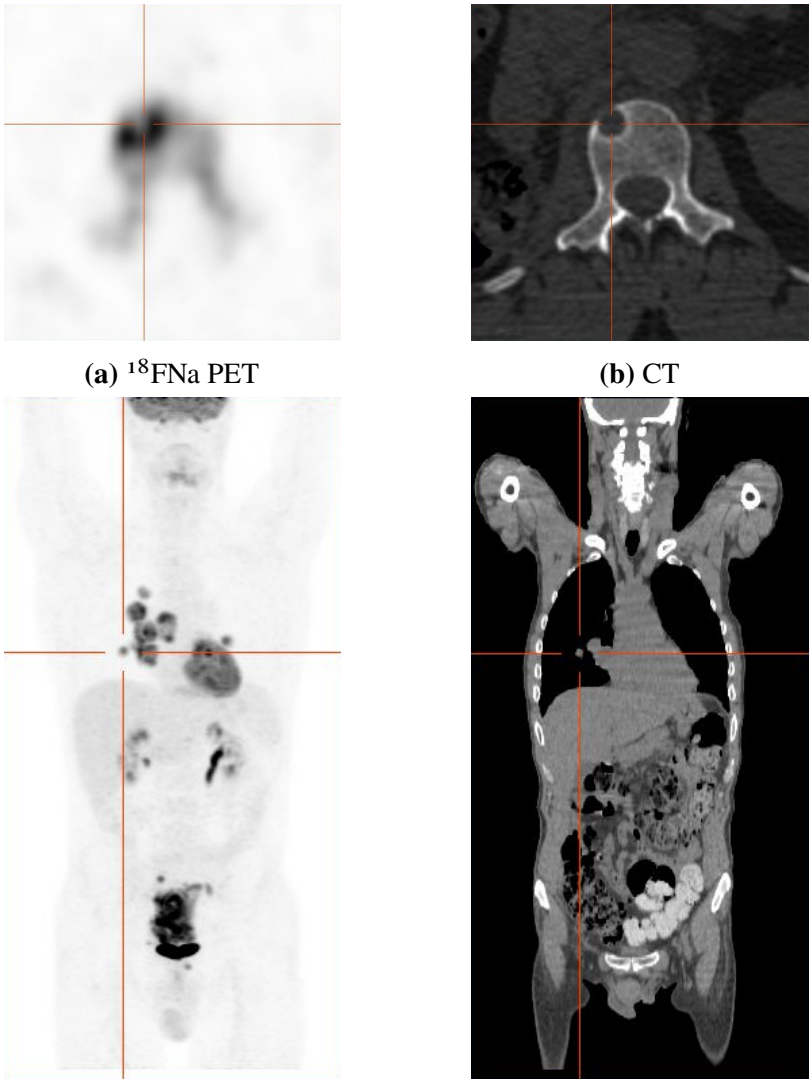

(a) ^{18}FNa PET **(b)** CT

(c) ^{18}F-FDG PET **(d)** CT

Figure 2.7: Subfigures **(a–b)** depict a vertebral metastasis from kidney cancer and Subfigures **(c–d)** depict various hotspots, e. g., in the right lung. The crosses are centered around findings. PET scans provide a rough spatial overview, but the image quality is not sufficient enough to make decisions about morphological details.

water) and Purcell (in paraffin) [58, 385]. However, Lauterbur, Mansfield, and Damadian are the spiritual fathers of modern MR imaging for

- acquiring the first MR image of a water-filled phantom [271],
- finding NMR diffractions in solids using magnetic field gradients [311],
- and measuring T_1 and T_2 proton relaxations in healthy and cancer tissue [100].

From this point on, the history of MR imaging becomes convoluted, since "*within a year of the appearance of that image [[271], 1973], four methods of NMR imaging had been demonstrated by four geographically disparate groups*" [345]. For a detailed presentation of the history of magnetism and its early uses in medicine, see the work of Mourino [345].

The following explanations on how MR imaging works were taken and compiled from the works of Roth, Westbrook and Köhler [247, 417, 513]. Figure 2.8 depicts a modern MRI scanner and an overview of MR imaging physics. In simplified terms, MR scanners apply and disable strong magnetic (gradient) fields and Radio Frequency (RF) impulses to patients, while proton responses in hydrogen are measured. Hydrogen is targeted because human tissue, e. g. fat and water, is primarily composed of hydrogen, and due to its "*large magnetic moment*", since only one proton is present in hydrogen and thus responses well to external magnetism [513]. In contrast to CT and PET, no ionizing radiation is used during MR imaging. However, strong magnetism is, for example, not feasible in patients with cardiac pacemakers, metallic implants, or tattoos with iron-based ink [10, 239, 247].

PROTON SPIN AND ALIGNMENT. Rather than keeping still, protons naturally *spin* around individual *spin axes*. For MR imaging, the MR scanner applies a strong external magnetic field called B_0. This results in the protons' spin axes being aligned parallel or antiparallel to B_0's field direction $\vec{B}_0$. The numbers of parallel- and antiparallel-aligned axes are roughly the same, however, since a "*parallel alignment is energetically more favorable*", little more protons get aligned in a parallel manner [247]. This state is called *equilibrium*. In a perfect equilibrium, the *net magnetization* $\vec{M}$, which is the sum of all protons' moments, would be zero. The small majority of parallel-aligned proton spin axes is enough for $\vec{M}$ being parallel to $\vec{B}_0$, which is sufficient for MR imaging [247].

LARMOR FREQUENCY. Using stronger B_0 field strengths results in two effects. First, although $\vec{M} \parallel \vec{B}_0$, protons still precess around their aligned spin axes. The precession speed/ frequency varies for different atoms, e. g. hydrogen protons precess faster than oxygen protons, and they precess faster in stronger magnetic field. This frequency is also called the *Larmor frequency* and in a $1\,T$-strong magnetic field, the Larmor frequency for hydrogen protons is $\approx 42.58\,MHz$ [267, 286]. MRI scanners in clinical workflows achieve $1.5\,T$ to $3\,T$, but research devices can achieve field strengths of $15.2\,T$ and more for small animal imaging [168].[5] Secondly, the majority of parallel-aligned spin axes increases [417]. This results in more protons being available during resonance signal capturing, which in turn improves the image quality (explained below).

[5]The *Bruker BioSpec* (Bruker Corporation, Billerica, Massachusetts, United States) small animal MRI scanners can achieve up to $21\,T$; https://www.bruker.com/products/mr/preclinical-mri/biospec/overview.html, last accessed August 27, 2019

PROTON RELAXATION AND RESONANCE. While the spin axes are aligned, the scanner sends out RF impulses that *excite* protons. These impulses have two major properties. First, they are sent out perpendicular to $\vec{B}_0$ and secondly, their frequency is equal to the Larmor frequency of hydrogen protons. As a result, "*about half of the protons spin axes flip by* 180°", which results in $\vec{M}$ shifting until $\vec{M} \perp \vec{B}_0$ [247]. This is important for T_1-weighted MR imaging. Furthermore, individual proton precessing is synchronized. This effect is

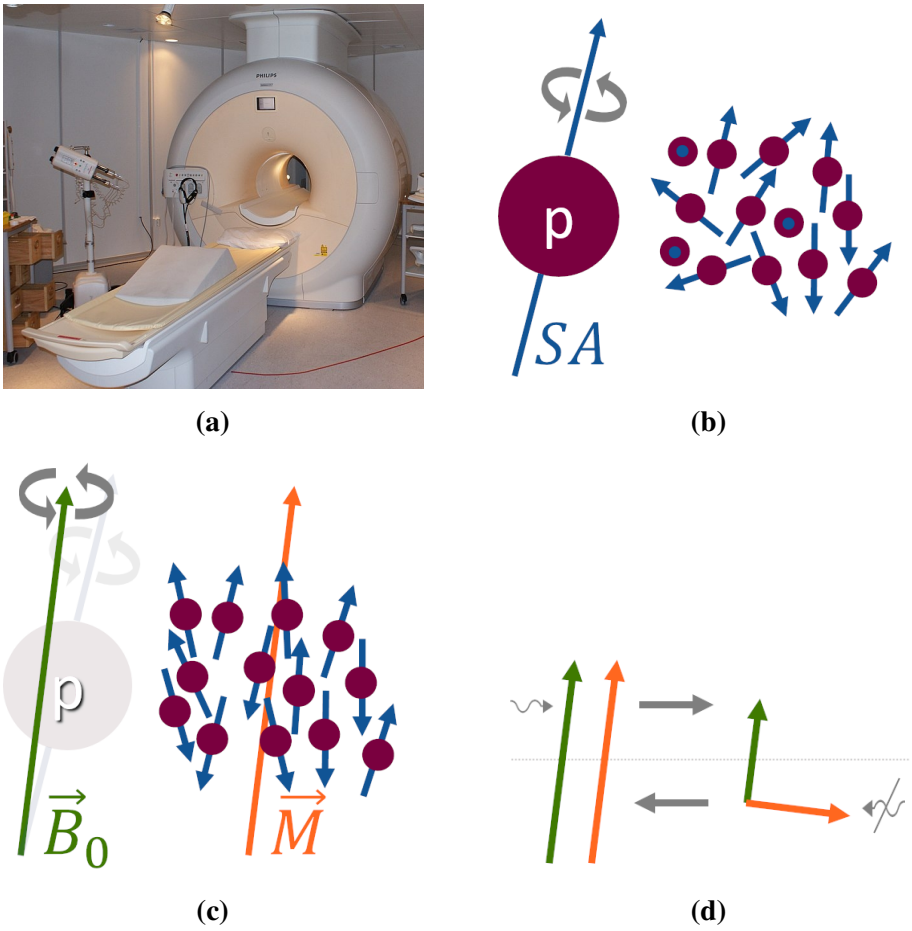

Figure 2.8: Subfigure **(a)** depicts a *Philips Diamond Select Achieva 1.5 T* (Philips Medical Systems, Hamburg, Germany) MRI scanner. Subfigures **(b–d)** show the simplified physics behind MR imaging. Rather than keeping still, protons rotate around individual spin axes **(b)**. If an external magnetic field B_0 is applied, the protons' spin axes *precess* around B_0's field direction $\vec{B}_0$ **(left c)**. Since more protons align parallel than antiparallel to $\vec{B}_0$, their overall net magnetization $\vec{M}$ becomes $\vec{M} \parallel \vec{B}_0$ **(right c)**. When radio frequency impulses ($\rightsquigarrow$) with the precession frequency of the targeted element, i. e. hydrogen, are introduced, the protons get *excited* and $\vec{M}$ shifts so that $\vec{M} \perp \vec{B}_0$ **(top d)**. When impulses are removed, the protons *relax* and $\vec{M} \parallel \vec{B}_0$ is restored **(bot d)**.

called *phase coherence*, which is important for T_2-weighted MR imaging. When the RF impulses stop, the protons *relax*. This results in the previously exited protons releasing energy that they absorbed during the RF impulse. This effect is called *resonance*, which is captured and spatially encoded into images. Therefore, this imaging technique is called magnetic resonance imaging.

T_2 – SPIN-SPIN RELAXATION. Two types of resonance effects occur during proton relaxation and both effects "*are independent from another and happen simultaneously*" [247]. However, T_1-related relaxation takes longer than T_2-related relaxation. First, the synchronized proton precession de-phases again (*spin-spin relaxation*) within a constant time window T_2. T_2 denotes "*when the transversal magnetization [is] reduced by about* 63 %" [247], or, in other words, when protons precess individually again. How fast protons do this, depends on their molecular connection, i. e. if they are connected to carbon (fat) or oxygen (water), and on the proximity to other spin-spin relaxations [513]. For example, fats are large and inert molecules that can absorb relaxation energy *better* and provide more space for hydrogen protons. Therefore, hydrogen protons in fat restore their original precession faster. In other words, when the T_2 relaxation signal is captured, less resonance energy from these fat-bound protons can be recorded and, therefore, fat typically appears dark in T_2-weighted MR images. In contrast, water molecules are smaller and they have a higher molecular motion, and thus, they take longer for precession de-phasing. Therefore, more spin-spin relaxation energy remains in water-bound protons during T_2 signal capturing, and thus, water appears brighter in T_2-weighted MR images.

In contradiction to these explanations, when looking at Figure 2.9b, fat (back skin) appears just as bright as water. This is due to very short Echo Times (TEs) that were used during image acquisition. TEs are the time frames in milliseconds between excitation and relaxation capturing [513]. Therefore, if short TEs are chosen, there are no large differences in spin-spin relaxations between fat- or water-bound hydrogen protons, and thus, their grayvalue contrast is small. To ensure good fat-water contrast in T_2-weighted imaging, typically TEs around $70\,ms$ and longer are chosen. Many tumor types have high water and ("*slow-flowing*") blood concentrations, and thus, T_2-weighted imaging is typically well-suited to depict them (see Fig. 2.9b) [513].

T_1 – SPIN-LATTICE RELAXATION. The second relaxation effect is called *spin-lattice relaxation*. When RF impulses are removed, the former net magnetization, i. e. prior to the RF excitement, re-established. This point is reached "*when about* 63 % *of the longitudinal magnetization are restored*" [247], which happens in a constant time window T_1. In other words, the overall net magnetization $\vec{M}$ shifts back from $\vec{M} \perp \vec{B}_0$ to $\vec{M} \parallel \vec{B}_0$. This *degree of restoration* is measured during T_1 signal capturing. Similar to before, fat-bound hydrogen protons undergo this process faster than water-bound hydrogen protons, and thus, $\vec{M}$ and $\vec{B}_0$ will be more parallel in fat-based than water-based tissue during T_1 recording. Therefore, fat typically appears bright in T_1-weighted MR images, while water appears dark [513].

ECHO AND REPETITION TIMES. With each new RF impulse, spin-lattice relaxations are reset. The frequency of RF impulses is denoted by Repetition Times (TRs) in milliseconds. To ensure high fat-water contrast in T_1-weighted images, TEs are shorter than in T_2.

This is done to maximize $\vec{M}$ differences in fat- and water-based tissue. Thus, T_1-weighted images can be acquired faster, since shorter TEs result in shorter TRs [417]. In numbers [513]:

- $TR(T_1) \approx 300\,ms$ to $600\,ms$ and $TE(T_1) \approx 10\,ms$ to $30\,ms$
- $TR(T_2) > 2000\,ms+$ and $TE(T_2) > 70\,ms+$

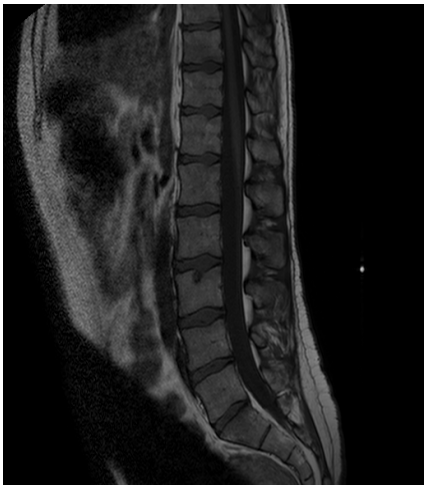

(a) T_1-weighted

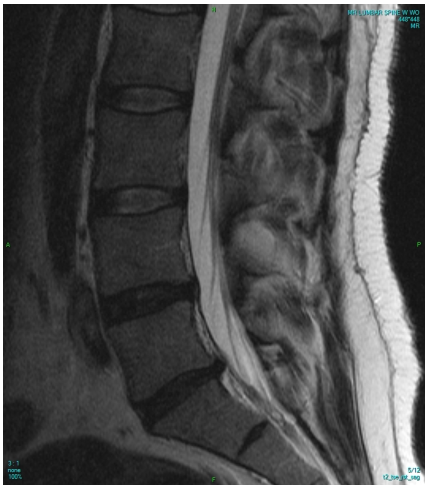

(b) T_2-weighted

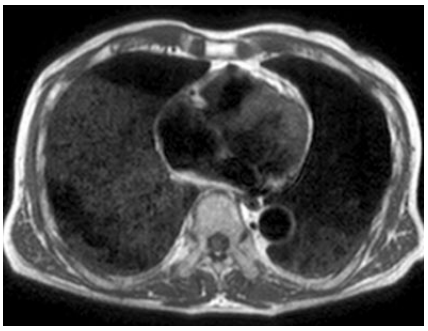

(c) T_1-weighted

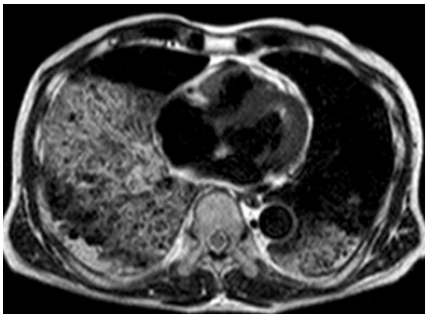

(d) T_2-weighted

Figure 2.9: Subfigures **(a–b)** on top show two T_1-weighted MR images of two individual patients. The *cerebrospinal fluid* (*liquor*) in the spinal canal is primarily water-based, and thus, it appears dark in T_1 and bright in T_2 MR images [457]. The bottom Subfigures **(c–d)** depict a 73-year-old patient with *mucinous bronchioalveolar carcinoma* on both sides [98]. Due to high water and "*slow-flowing*" blood contents, the cancer tissue appears brighter than surrounding lung tissue [513].

Overall, acquisition times from 5 *min* to 15 *min* can be achieved, which sorts MR between CT and PET imaging w. r. t. acquisition times [174]. Similar to PET, this results in breathing motion artifacts that can be resolved via synchronization of breathing and resonance capturing, for example [27, 417]. Generally, this results in longer acquisition times.

MAGNETIC GRADIENTS. B_0 is spatially uniform, which results in identical field strengths at each location within the scanner. To make spatial regions within B_0 distinguishable, i. e. "*to selectively exite a region – or slice – of tissue at a time*" [417], three orthogonal gradients, namely G_x, G_y, and G_z are applied to distort B_0 [247, 417]. Gradients are magnetic coil systems in the scanner hardware that can be switched on and off. Furthermore, all gradients are perpendicular to each other and have increasing field strengths along their main axes. In other words, by distorting B_0, body regions become distinguishable from each other due to different field strengths.

The first gradient is called the *slice-selecting gradient* that makes Larmor frequencies unique along its axis with higher precessions for higher field strengths. This gradient is applied during RF impulses [513]. Prior to gradient application, RF impulses would excite all protons. However, now, only a small portion of hydrogen protons within a slice can get excited by RF impulses.[6] Typically, this gradient is chosen w. r. t. the clinical application, i. e. G_x makes proton precession unique along the sagittal image plane (side-to-side; e. g. spine imaging), G_y along the coronal image plane (front-to-back; e. g. heart imaging), and G_z along the axial image plane (head-to-toe; e. g. brain imaging) [513].

This comes with the downside that "*a range of frequencies must be transmitted to produce resonance across the whole slice (and therefore to excite the whole slice)*" [513]. This range of frequencies is called *transmit bandwidth* and with increasing bandwidth, more frequencies are used for a single impulse, which results in increasing *slice thickness*. Decreasing transmit bandwidth improves spatial resolution, since less protons can resonate subsequently. However, for the same reason, the Signal-to-Noise Ratio (SNR) will worsen proportionally in the resulting images [513]. Moreover, given that anatomy coverage stays unchanged, acquisition time increases. Additionally, small frequency gaps must be left between impulses to prevent *cross excitation* artifacts, which are a result of overlapping transmit bandwidths and thus, overlapping relaxation signals [513]. When gap sizes are increased, the risk of these artifacts is reduced, but less anatomy is scanned. Using multiple RF bandwidths is also the reason that MR image stacks have anisotropic voxel sizes along gradient direction, e. g. $\approx 0.5 \times 0.5 \times 4\,mm$ for spine imaging (G_x).

Additionally to the slice-selection gradient, *phase-shifting* and *frequency-encoding gradients* are applied [513]. The phase-shifting gradient is applied just after RF removal. Due to varying field strengths, the selected slice is divided into rows or columns and protons therein precess faster or slower. The second gradient is active for about $4\,ms$, which is enough time to enforce varying phase shifts in adjacent rows or columns after gradient removal [513]. The third and last gradient is applied to alter precession speed during signal capturing. Consequently, w. r. t. different types of tissue, there now exist *voxels* of patient tissue in which protons have unique precession phases and speeds. Subsequently, these

[6] Or slab of tissue, if you will.

combinations are translated into darker or brighter image intensities [247]. There exist various MR imaging sequences, e. g. to suppress fat- or blood-bound proton resonances, which basically are scheduling protocols for RF impulses and gradient field changes [44].

The assumption that identical tissue voxels at different positions response identically to gradient fields does not apply, because the magnetic fields and resonance capturing processes are imperfect. For example, magnet field inhomogeneities result in virtually unpredictable image intensity artifacts such as bias fields, which are depicted as smooth intensity gradients. This makes it very challenging to define reusable windowing or Direct Volume Rendering (DVR) Transfer Function (TF), but there exist bias field correction algorithms to tackle such artifacts [227, 297].

MR IMAGES AND APPLICATIONS. Similar to acquisition times, currently used MRI scanners typically acquire images with a spatial resolution and stack size that lie between those of CT and PET. For example, $3\,T$ scanners can achieve image matrix sizes of 256×244 pixels and more with a voxel resolution of $0.86 \times 0.74 \times 2.2\,mm$ [191, 513]. However, along the third main axis (slice-selection gradient), they often have considerably less voxels, e. g. 20 or less slices for spine imaging. Seven Tesla MRI scanners can push these limits even further with TOF sequences that can depict very fine brain blood vessels in high detail (4 tissue slabs with $1296 \times 972 \times 96$ voxels per slab and $150\,\mu m^3$ per voxel) [317]. However, such scans require up to $2\,h$ and longer to be acquired, which in turn makes patient fixation and/or motion artifact correction necessary, since, at this scale, even very small patient movement will result in major image artifacts [317].

CT and MRI scanners can depict morphology in great detail, but while X-ray attenuation characterizes the radiodensity of tissue, capturing proton resonances enables much better depiction of soft tissue contrast. Additionally, in contrast to CT and PET, MRI scanners also allow for functional image acquisition of so-called fMRI scans [70]. Here, brighter image regions represent brain areas with increased blood oxygen concentration, or, in other words, brain areas that are more active than others, since patients perform little tasks during image acquisition. With respect to the large variety of imaging sequences, MRI scanners can be employed for a wide range of clinical applications, such as brain tumor [35], bone cancer [146], stroke, multiple sclerosis, dyslexia, schizophrenia [277], and lung disease/ function imaging [27]. Similar to CT, contrast media can be administered to achieve high image contrast between blood vessels and/or gastrointestinal organs and background anatomy. However, gadolinium- (for T_1), iron-oxide (for T_2), barium-, or iodine-based contrast agents might not be feasible in all patients due to allergies and can come with side effects such as nausea and pain [317, 513].

Overall, MRI scanners are more expensive than CT scanners and, presumably, also more expensive than PET scanners. However, they require an additional cyclotron to synthesize radiotracers. MRI scanners have a high electricity consumption, because high currents are necessary to repeatedly apply and remove RF impulses and gradient fields [247, 417]. This also results in loud noises and high temperatures during imaging, which can be addressed by MR-compatible earphones and cooling, respectively [369, 417]. Additionally, MRI scanner magnets are very costly, since "*a small increase in magnet radius results in*

a large increase in magnet cost", which also explains why MRI scanner gantries are typically more narrow than CT scanner gantries [523]. For more details on MR imaging, see the works of Bernstein, Köhler, Roth, Westbrook and their respective colleagues [44, 247, 417, 513]. In Germany, in 2017 roughly 2900 MRI scanners were installed.[7]

2.2 MULTIMODAL MEDICAL IMAGING

Combining two imaging units into one machine has various advantages. For example, overall acquisition time is reduced, since two scans can be acquired in one session, which in turn increases patient throughput [219]. Additionally, not having to transition patients between scanning makes subsequent image registration easier. Moreover, since only one patient bed is necessary, combined imaging suites are potentially cheaper but in cases of maintenance, two scanners are blocked.

The multimodal medical image data that were used for this thesis were either acquired via hybrid PET/CT or monomodality scanners. Thus, the combination of PET and CT will be explained in more detail. Hybrid PET/MR imaging will also be explained more thorough, since currently there is a high research interest in these devices due to the overall high versatility of MR imaging. However, since no such image data was used for this thesis, the focus will be on highlighting similarities and differences w. r. t. hybrid PET/CT imaging. For the sake of completeness, other hybrid imaging devices, such as SPECT/CT scanners, will be explained briefly.

2.2.1 PET AND CT

Combining PET and CT images enables physicians to relate suspicious morphological and physiological findings with high fidelity. The first built hybrid imaging prototype was a SPECT/CT scanner that was presented by Lang and Hasegawa in 1991 [266]. In the same year, Nutt and Townsend proposed a first design for a hybrid PET/CT scanner, but it appears that the very first design was already developed in Japan 1984 [219]. The first commercially available hybrid PET/CT scanners were installed in 2001 and since then "*essentially all PET scanners are physically combined with an anatomical [CT or MR] imaging device*" [48, 219]. Although there were concerns about these new machines, e. g. regarding costs and reliability, the possibility to strongly tie morphology and physiology together outweighed them, but it also appears that commercial interests had a strong impact, too [481]. In Figure 2.10, a modern hybrid PET/CT scanner is depicted. In this design, a motorized patient bed is moved through the scanner gantry, but there exist other approaches, such as moving the scanner on rails while the patient bed remains stationary [481]. With respect to anatomy coverage and patient size, PET/CT scanners can achieve acquisition times of about 10 *min* to 15 *min* [481].

PET-ONLY AC. Originally, for PET-only AC, radioactive germanium rods or caesium point sources were installed in front of the PET detectors that rotated around the gantry. Thus, similar to CT but at higher energy levels, two transmission scans were acquired

[7] https://data.oecd.org/healthcare/magnetic-resonance-imaging-mri-units.htm#indicator-chart, last accessed August 2, 2019

prior to the real PET scan to generate attenuation profiles. However, in addition to the aforementioned benefits, in PET/CT scanners X-rays can be used for PET image AC, which reduces acquisition times considerably [219]. Here, attenuation means "*the removal of annihilation events from a LOR, either by Compton scattering or photoelectric absorption*" [483]. In other words, the underlying problem is that scattered photons are not only removed from their true LORs, but they can potentially contribute to false LORs [483] (cf. Fig. 2.6).

PET-based AC works as follows: For each LOR, an attenuation factor AF

$$AF(LOR_i) = \frac{I_0(LOR_i)}{I(LOR_i)} \tag{2.1}$$

is defined by the uncompromised photon count I_0 from the 1st transmission scan without a patient, and the compromised photon count I from the 2nd transmission scan with a patient [483]. During image reconstruction of the 3rd (emission) scan, low photon counts along heavily attenuated LORs ($I_0 \gg I$) are upscaled under the assumption that they had to traverse more and/or scatter-heavy patient tissue. In other words, if for certain LORs only few coincidences from emitted photons are captured, i. e. they are assumed to be unscattered and come in at their expected energy level of $511\ keV$, while the transmission scans declared these LORs scatter-heavy, coincidence counts along these LORs (w. r. t. the spatial uncertainty related to the annihilation events) are *rewarded* via upscaling.

X-RAY-BASED AC. With X-rays, the attenuation correction is similar, but takes less time. However, the different energy levels of X-ray (mean of $70\ keV$ to $80\ keV$) and radiotracer photons ($511\ keV$) make it necessary that the CT-based attenuation profiles are upscaled [481, 510]. Typically, this is done by acquiring a low-dose CT scan prior to PET imaging to obtain attenuation factors. Additionally, a 2nd very low-dose *scout* scan is acquired to define the anatomy coverage for the scan. In simplified terms, first, the CT images are resampled to match the PET images' lower resolution and, subsequently, a bilinear scaling function is applied to the Hounsfield Units (HUs) (see Fig. 2.11).

(a) **(b)**

Figure 2.10: Subfigure **(a)** depicts a *Siemens Biograph PET/CT System* (Siemens Healthcare, Erlangen, Germany), whereas Subfigure **(b)** shows a schematic setup of hybrid PET/CT scanners. The CT unit can acquire images for diagnostic and attenuation correction purposes.

For X-ray-based AC, there are two major assumptions. First, it is assumed that softer tissue is a mixture of air and water and secondly, harder tissue is a mixture of water and bone. Thus, a function with three key points at air, water, and cortical bone tissue is defined with linear interpolation between two adjacent key points, since, secondly, it is assumed that there is only little variation of tissue between these key points. However, typically, instead of water ($HU \approx 0$), blood ($HU \approx 60 - 100$) is chosen to be the second key point, since blood can be regarded as an air-water mix, while having a higher radiodensity [510]. The function depends on the used kVp level, since lower X-ray energies allow for better depictions of soft tissue contrast, but result in increased radiation absorption, and thus, harder tissues such as bones have higher HUs [73, 510]. The reason is that harder types of tissue are comprised of more calcium and phosphorus, which have higher electron counts than other elements that are found in softer tissue, e. g. carbon or oxygen, and a high electron count results in more photoelectric effects (cf. Fig. 2.3) [118, 242, 460]. This feature is exploited in bone density imaging, namely in Dual-Energy X-ray Absorptiometries (DXAs), to assess the mineral composition of bones (cf. Ch. 5). In practice, the attenuation coefficients of air, water, and cortical bone tissue at $511\ keV$ are used as key values. However, they must be chosen w. r. t. the scanner's kVp. Body-foreign materials, such as implants or administered contrast media, can make this straightforward approach challenging, since such materials cannot be expressed as a combination of air,

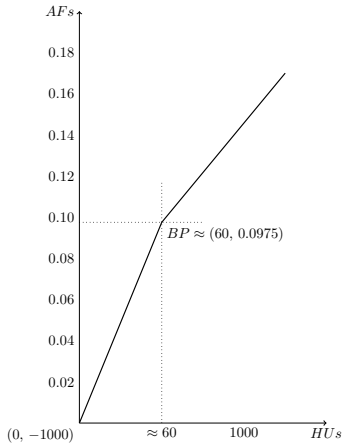

(a)

See [435, Figs. 1(2, 4), p.243].

Figure 2.11: Subfigure **(a)** depicts a simplified bilinear AC function to upscale X-ray to PET radiotracer energy levels. Typically, three key points at air ($-1000\,HU$), water or blood ($0 - 100\,HU$), and bone tissue ($\leq 2000\,HU$) are defined. The second key point is also called the *Breaking Point* (BP). Attenuation factors between key points are interpolated linearly. The y-axis shows the photon attenuation coefficients of air, water, and cortical bone tissue at $511\ keV$ [510]. The images in **(b)** show PET images before (top) and after (bottom) CT-based attenuation correction [435].

Image **(a)** was inspired by [481, Fig. 8].

water/ blood, and bone tissue [510]. For more details on CT-based attenuation correction for PET images, see the articles from Carney and Watson et al. [73, 510].

The subsequent image registration of PET and CT images is easier for scans from hybrid PET/CT scanners, since patients remain fixated during both image acquisitions. However, the different acquisition times, i. e. seconds for CT versus minutes for PET, can result in spatial mismatches up to $4.5\,cm$ for findings in the lung or liver [81]. Especially small lesions are affected by that, but exact determinations of size, shape, and position heavily influence diagnoses and therapy decisions [282]. This problem can be addressed by shorter coincidence time windows and various breathing protocols for patients to synchronize anatomy motion and signal capturing. Offering various breathing protocols is especially important in patients with lung diseases, since their abilities of breath-holding or shallow breathing can be severely compromised. An exemplary PET/CT protocol from patient fasting to image reconstruction is described by Townsend [481].

2.2.2 PET AND MRI

Around the same time when PET and CT hardware were combined, the same was done with PET and MRI scanners [83]. Depending on the clinical application, MRI can be regarded as superior to CT, since no ionizing radiation is used, due to the improved soft tissue contrast and the wide range of imaging sequences [34, 99]. One early design by Shao et al. [440] utilized long ($\approx 4\,m$) optical fiber cables between the PET scintillators and photomultipliers. This was done to prevent having magnetic materials between the MRI magnets, since they encompassed the PET detector ring. However, due to the long fiber cables, the incoming light impulses were weak and temporarily shifted, which decreased PET image quality [523]. One milestone was presented by Schlemmer et al. [430], who

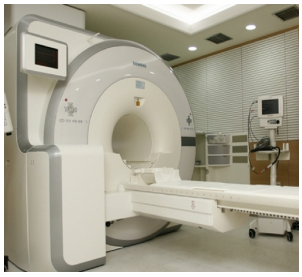

(a)

(b)

Figure 2.12: Subfigure **(a)** depicts a *Siemens Biograph 3T mMRI* scanner [368]. This machine uses a single-gantry design with combined PET and MRI hardware. In contrast, Subfigure **(b)** shows a *Philips Ingenuity TF Whole Body PET/MR* system with a multi-gantry design (also called *tandem*) [523].

conducted a feasibility study for brain imaging with an *inserted* $3\,T$ MR/PET scanner. For a more detailed historic overview, see the article of Muzic and Zaidi et al. [350, 523].

Modern scanners use a single- or multi-gantry system, where PET and MRI hardware are either combined into one or separated into multiple units (see Fig. 2.12). The main challenge in hybrid PET/MRI scanners are the reciprocal influences between both hardware units. On the one hand, PET photomultipliers are sensitive to magnetic fields and on the other hand, PET hardware can cause magnetic interferences in B_0 [34, 440]. Given that the gantries of the scanners have the same diameter, a multi-gantry system can be cheaper, since smaller MRI magnets are required. In contrast, *true* hybrid scanners require less space, enable overall faster image acquisition, and easier image registration of patient morphology and physiology [34, 523]. However, technically, they are more challenging to build. In Figure 2.13, the three major designs for hybrid PET/MRI scanners are depicted, namely the split, inserted, and integrated designs. The last design represents the hardware setup that is used by the most modern hybrid scanners.

MR-BASED AC. MRI-based attenuation correction of PET images is more complex than its CT-based equivalent. The main reason is that attenuation of electromagnetic radiation

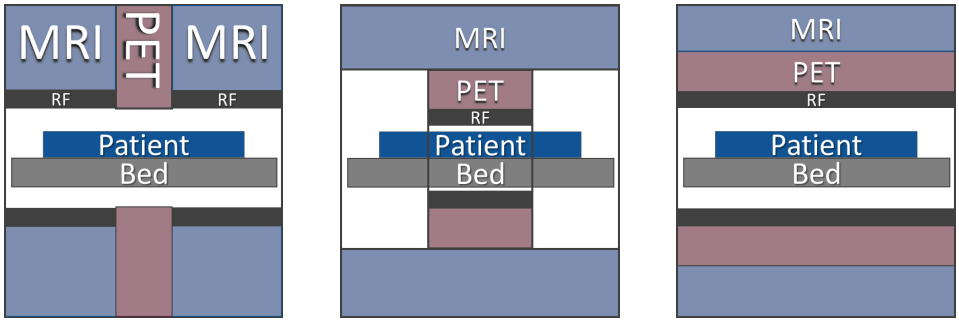

(a) Split Design **(b)** Inserted Design **(c)** Integrated Design

Figure 2.13: The three main designs for combined PET/MRI scanners. In early designs, similar to Shao et al. [440], the MR hardware was split into two parts and the PET detector ring was installed between them. To reduce interferences, PET and MRI hardware were shielded away from each other **(a)**. Later designs used *PET inserts* that were inserted in the MRI scanners' gantry **(b)**. The major drawback was that the gantry diameter was heavily narrowed, e. g. from $200\,mm$ to around $120\,mm$, which in turn heavily limits application possibilities [523]. However, this design was attractive, since MRI hardware had not to be altered, i. e. no larger magnets were needed, which limited costs. Moreover, the PET images had a high spatial resolution, e. g. with a voxel size of $1.25\,mm^3$, which made this setup formidable for brain imaging [430]. The last design represents an approach for *true* hybrid PET/MRI scanners **(c)**. Here, PET hardware is fully encompassed by MRI hardware. Since PET and MRI hardware interfere with each other, thin copper screens can be used in between [523].

The images were inspired by [523, Figs. 3, 5, 6 and 9] and [430, Fig. 1].

is used for PET and CT, which *only* has to be upscaled (cf. Fig. 2.11). For PET and MRI, this relationship is not present. There exist various methods, such as template-, atlas- and segmentation-based approaches [504]. For example, the general approach of segmentation-based methods is a multi-class classification of MR images, e. g. into air and adipose, soft and bone tissue, which is done separately for whole-body and brain imaging [34, 43]. After image registration, class-specific attenuation coefficients from the MR are applied to the PET images. On the one hand, T_1-weighted images, which are recorded anyway for diagnostic purposes, can directly be used for this. This results in patient- and scan-specific attenuation coefficients. On the other hand, in T_1-weighted brain imaging, bone and air pixel can have similar intensity values, which requires more refined classification approaches. For example, a priori knowledge related to the shape, position and/or symmetry of the head and brain can be introduced to improve the classification [504]. Furthermore, they only use a small number of classes, e. g. 3 to 4, and thus, only few and discrete attenuation coefficients are used. In contrast, template- or atlas-based methods can use continuous ranges of attenuation coefficients and thus, AC becomes tissue-specific. However, template/ atlas-to-patient mapping can take long and the results can be heavily compromised by morphological abnormalities, such as tumors or deformations, e. g. due to breathing motion. A visual comparison between CT- and MRI-based AC of PET images can be found in Figures 2.15c and 2.15f. For a more in-depth discussion on MRI-based attenuation correction methods of PET images, see the article of Wagenknecht et al. [504].

Typical PET/CT and PET/MR imaging protocols are similar [34]. On the one hand, lightweight protocols can be conducted in less than 20 *min* [111], however, "*a typical whole body study including organ-targeted sequences can easily take 60-min or more*" [34]. This is due to the longer scanning times of MR images. PET/MRI acquisition protocols are somewhat simpler, since PET and MR images can be acquired simultaneously during discrete bed positions [34]. Furthermore, breathing protocols and patient fixation help to limit breathing motion artifacts, since both images are acquired during the same respiratory movement [523]. However, since fixation for MR imaging takes more time than for CT imaging, radiation exposure to clinical staff can be increased [34, 523].

Overall, "*PET/MRI is expected to supersede PET/CT in imaging cancers which are anatomically better defined by MRI compared to CT, due to its superior soft-tissue contrast*" [34]. Clinical areas include oncology, cardiology, neurology, and psychiatry [34, 117, 523]. Furthermore, in contrast to CT, MR imaging can depict physiology, too, which makes it possible to combine multiple physiological image sources. However, from an economical point of view, hybrid PET/MRI scanners are more expensive to buy and maintain than their PET/CT counterparts [117]. Furthermore, CT still exceeds MRI w. r. t. bone density imaging (cf. Ch. 5). Another downside is that the number of patients is limited. For example, pregnant or breastfeeding patients could still undergo MR, but not PET imaging, whereas patients with metallic implants could still undergo PET, but not MR imaging [34]. In Germany, currently, around 10 hybrid PET/MRI scanners are installed.[8]

[8] https://www.mta-dialog.de/artikel/dfg-foerdert-kombiniertes-petmrt-geraet.html, last accessed August 5, 2019

2.2.3 OTHER COMBINATIONS

In this section, other multimodal imaging combinations are briefly discussed.

SPECT AND CT. After Anger invented the Gamma Camera in 1958 and further research was done, Kuhl and Edwards presented the *Mark III Scanner* in 1970 [16, 261]. This scanner was used in a patient with brain cancer. Similar to PET, a radiotracer is required to acquire SPECT images, e. g. ^{99m}Tc. In contrast to PET, for SPECT imaging, emitted photons are captured *directly* by slowly rotating gamma cameras close to the patient.

The first hybrid SPECT/CT scanners were described by Hasegawa et al. in the late 1990s, while the first commercially available system, the so-called *GE Discovery VG Hawkeye*, was introduced in 1999 [179]. Today, SPECT/CT is typically used for tumor, bone, brain, and lung function imaging [123]. Similar to PET/CT, SPECT images undergo a CT-based attenuation correction. With respect to lung function imaging, a combination of ventilation (e. g. ^{133}Xn) and perfusion (e. g. ^{99m}Tc) scans is performed in around $13\,min$. Here, physicians search for physiological and/or functional discrepancies, i. e. if certain lung segments are solely ventilated (*shunt*), e. g. due to blood or water in the alveoli, or solely perfused (*dead space*), e. g. due to embolism via blood clots or cancer tissue [123, 251, 512]. Subsequently, CT makes it possible to find the morphological reason that resulted in physiological change. With respect to bone cancer imaging, SPECT radiotracers are accumulated in regions with a high osteoblast and low osteoclast concentration.[9] Here, CT is used to conclude about the primary cancer's origin and to find lesions for which SPECT-only assessments have a considerably lower specificity [146] (cf. Ch. 5).

SPECT AND MRI. Naturally, the idea to combine SPECT and MR image arose. However, "*the development of hybrid SPECT/MRI systems is still in its infancy*" [64]. Similar to hybrid PET/MR imaging, interactions between SPECT and MR hardware must be understood, e. g. shifting of photon hits due to the strong magnetic field [71, 167]. Early designs and approaches, e. g. by Cai, Hamamura, and Meier et al. [71, 167, 318], used *inserted designs* (cf. Fig. 2.13b), for which tube-like SPECT detectors are inserted into the gantries of MRI scanners. However, this makes the *combined* gantry very narrow ($\varnothing \approx 2\,cm$ to $12\,cm$), and thus, currently, only feasible for small animals. Here, MRI is also used for attenuation correction of SPECT images. Given that gantry sizes will increase, the first human brain imaging prototypes could be presented in the next few years.

CT AND MRI. The major advantage of combined CT and MR images is that they depict hard and soft tissue at great detail, while registration errors are decreased due to combined scanner hardware. There exist various approaches to combine both scanning units, but the most adapted one appears to be a *subsequent design* (cf. Fig. 2.10), in which MRI hardware is build in front of the CT scanning unit [506, 518]. To limit CT-MRI hardware interferences, the field strength of B_0 is rather low, e. g. about $0.2\,T$ to $0.5\,T$.

TRI-MODAL IMAGING. There exist approaches to combine PET, SPECT and CT hardware in one device, which was recently tested in small animals [142, 425]. Further-

[9] Osteoblasts synthesize bone tissue, osteoclasts break down bone tissue (cf. Ch. 5).

more, w. r. t. multi-physiology imaging, radiotracers are researched that can emit low- ($\lesssim$ 100 keV) and high-energy photons ($\gtrsim$ 300 keV) simultaneously, e. g. xenon (^{123}Xe), that might be interesting for such machines [392].

2.3 READING OF MULTIMODAL MEDICAL IMAGES

The potential and necessity to examine multiple scans of different modalities was understood very early. However, this also requires physicians to *read* more image data, i. e. images of Modality 1, Modality 2, and combinations. For combinations of physiology and morphology, an early approach was to use registration markers to superimpose X-ray *roentgenograms* and *photoscans* from scintigraphy recorders on lightboxes [261, 260]. This general principle is still used today for digital examinations of PET and CT image stacks, which is depicted in Figure 2.14. In contrast, software toolboxes use color coding for superimposed images, which is not possible for X-ray film. Here, the CT images are still rendered in grayscale, while PET images are color-coded using, for example, red-to-white or blue-to-white color scales.[10]

Before the modalities are assessed in unison, they are typically examined independently [256]. For CT images, due to HUs, software toolboxes have a set of default windowing functions, e. g. for various anatomical regions and findings [490]. For lung cancer imaging, CT is the predominantly used modality, due to its higher spatial resolution to depict morphological changes. However, not all suspicious findings in CT relate to cancerous

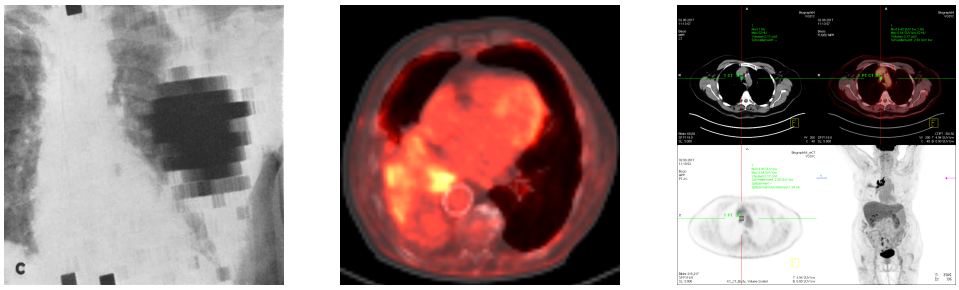

(a) **(b)** **(c)**

Figure 2.14: Subfigure **(a)** shows a superimposed roentgenogram and photoscan. The squares are registration markers that were used to accurately align anatomy and radiotracer hotspots. This principle is still used today for digital PET/CT examinations **(b)**. Related to hanging protocols that present multiple images in a consistent manner, software toolboxes for PET/CT images typically present scans in four viewers, i. e. CT-only, PET/CT via color-coded superimposition, PET-only in axial mode, and PET-only via frontal Maximum Intensity Projection (MIP) **(c)**.

Image **(a)** reprinted by permission of The Radiological Society of North America (RSNA ®; Kuhl D. E., Chamberlain R. H., Hale J. Gorson R. O., Radiology, 1956, 66, 730–739, RSNA) [260, Fig. 8C]. Image **(c)** is a screenshot from the *Siemens Syngo VG51C* toolbox. The original medical images in **(b-c)** were provided and used with permission by Philipp Genseke.

[10] This appears to be vendor-dependent, i. e. Siemens toolboxes primarily use red-to-white color scales, whereas GE toolboxes rather use blue-to-white color scales.

tissue growth, such as calcified nodules and thus, ^{18}F-FDG PET scans can be subsequently assessed for metabolic peaks. For PET-only presentations, a standard windowing function typically assigns a light to mid-gray *color* to the liver, since it is assumed that the average FDG uptake of the liver is roughly the same for all patients [364]. Generally, a narrow windowing "*is primed for sensitivity whereas a wider windows enables superior characterisation*", which is beneficial to delineate soft tissue and multiple PET hotspots [195]. Related to hanging protocols, PET/CT images are usually presented in four viewers with synchronized exploration facilities, such as slicing and windowing. Moreover, digital hanging protocols can also include other presets, e. g. initially presented slices and image legends w. r. t. patient, study, or acquisition details. If necessary, they can be further tailored to fit the needs of physicians and clinical applications [381].

A combination of morphology and physiology is not only beneficial to make treatment decisions, but to evaluate treatment responses, too. Treatment responses are primarily assessed by morphological change via the Response Evaluation Criteria in Solid Tumors (RECIST), but cancer morphology can remain stable for various weeks after treatment [119, 456]. Thus, quantified metabolic responses, which can manifest earlier, can be examined with the Positron Emission Tomography Response Criteria in Solid Tumors (PERCIST) [364, 456]. However, as of today, a combined criteria catalog does not exist. With respect to hanging protocols, treatment responses are typically assessed by presenting two morphology-depicting image stacks next to each other to evaluate morphological changes, while physiological changes are compared via Standard Uptake Values (SUVs). Both is done on a per-finding basis.

Merging or fusing CT and MR images offers the possibility to depict soft and hard tissue at great detail together in one image. However, in clinical practice, this is not done. The main reason is that CT or MR images, in contrast to PET or SPECT images, are comprised of more high intensity values. In other words, color-coded superimposition is unfeasible, since there would be too many highlighted regions of interest, e. g. bones for color-coded CT or fat for color-coded MR images, while important features, such as cancer tissue, will not be highlighted. Moreover, while easier for CT images due to HUs, transfer and windowing functions for MR images are very challenging to define, which in turn makes (combined) 3D rendering challenging.

Therefore, more research was done towards 2D image fusion and presentation techniques. Generally, one structure of interest, e. g. the skull in CT, is cut out and replaces the same structure in the other modality [112, 212]. This can also be regarded as a multimodal focus-context approach, since the focus object *skull from CT* is depicted in an MRI context. However, this has to be done with great care and heavily depends on the clinical context, since image fusion not only adds, but also removes visual information, which can be crucial for diagnoses and therapy decisions. For example, in patients with spine metastases, the evaluation of both image sources is necessary to conclude about the primary cancer's origin and to evaluate bone density prior to treatment (see Ch. 5). Therefore, CT and MR images are assessed subsequently in a single viewer or next to each other in multiple viewers and/or on multiple displays.

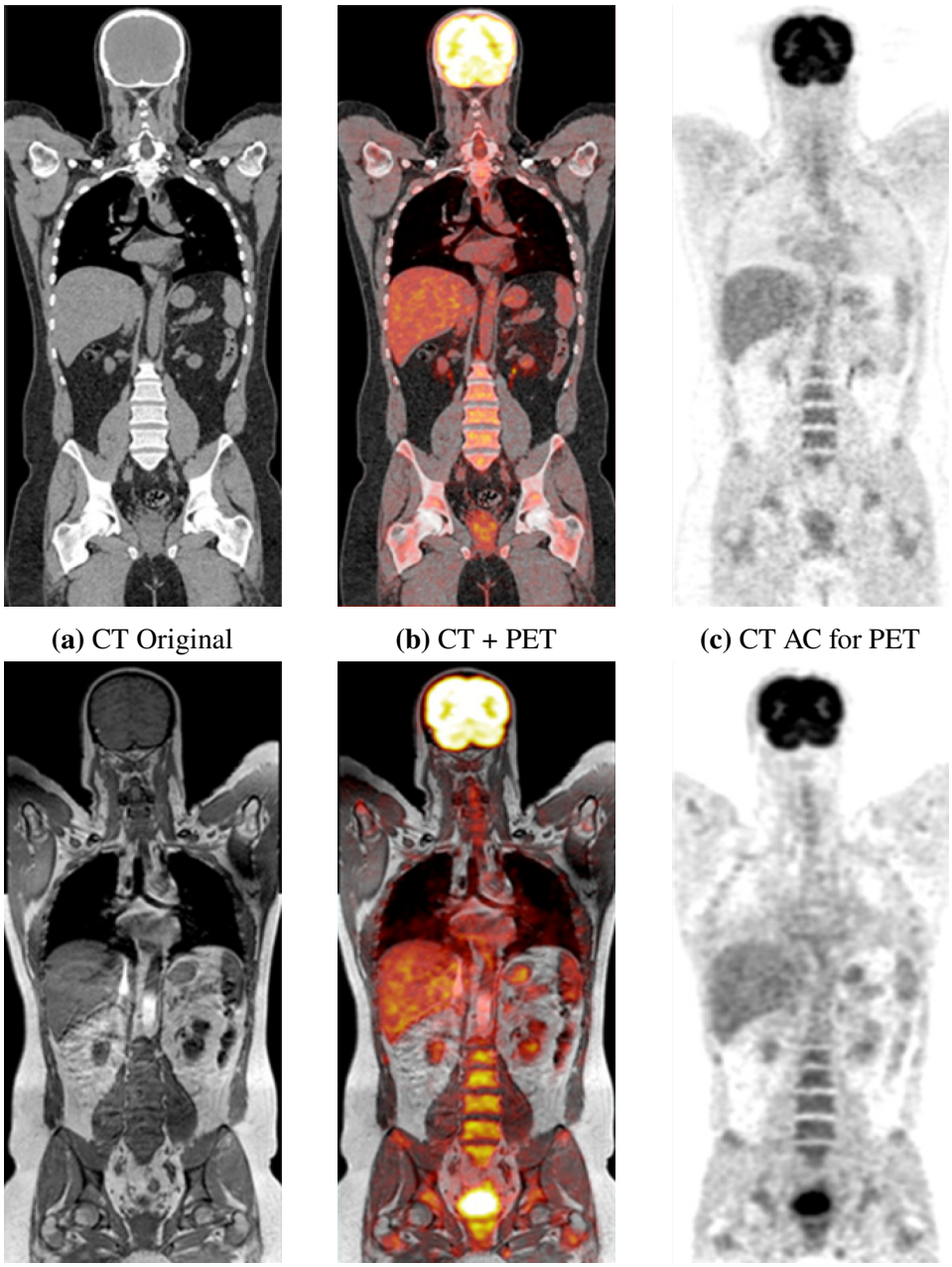

(a) CT Original **(b)** CT + PET **(c)** CT AC for PET

(d) MRI Original **(e)** MRI + PET **(f)** MRI AC for PET

Figure 2.15: The same patient subsequently imaged with hybrid PET/CT and PET/MRI scanners [523]. ^{18}F-FDG was used for the PET images. The PET/CT scans were acquired before the PET/MR images and thus, Subfigure **(c)** does not depict a radiotracer accumulation in the bladder. The authors do not specify which MRI sequence was used for Subfigure **(d)**, but it should be a T_1-weighted image due to high-intensity fat tissue (cf. Sec. 2.1.4).

All images were taken from [523, Fig. 14] and were reprinted by permission of John Wiley and Sons (Source: Zaidi H. and del Guerra A., An Outlook on Future Design of Hybrid PET/MRI Systems, Medical Physics).

2.4 SUMMARY

In this chapter, benefits and limitations of multimodal medical imaging were discussed. From a clinical perspective, hybrid devices reduce acquisition times, which in turn increases patient throughput. Additionally, refined acquisition protocols, e. g. synchronized patient breathing and scanning, reduce the risk of mismatches between morphology and physiology, which in turn improves the reliability of multimodal visualizations. Since patients do not have to be moved between multiple scanners, both image stacks are present in the same coordinate system, and thus, subsequent processing, e. g. image registration and visualization, is easier and typically leads to more exact results. Only basic visualization techniques are used in clinical practice, but there exist various approaches to combine multiple medical image sources in one presentation, and thus, more sophisticated methods will be presented in the next chapter.

For the floor map method presented in Chapter 4 pre-labeled CT images were used. However, in general, the method is independent from modalities. The combination of CT and MR images is important for spine RFAs (cf. Ch. 5). Here, during the diagnosis and intervention planning stages, the morphology of bone metastases is assessed to conclude about their origin and about feasible instrument trajectories to treat them. For the methods presented in Chapter 6 and 7, PET and CT images are combined into illustrative visualizations and visualization-supported reports in the context of lung cancer staging w. r. t. Lymph Node Station (LNS) metastases and treatment via SIRTs.

3 BACKGROUND ON VISUALIZATION TECHNIQUES FOR MULTIMODAL MEDICAL IMAGES

This is the second background chapter and complements the first one by providing an overview about visualization techniques for multimodal medical images. This will be done w. r. t. modality combinations, clinical application, and type of visualization technique. Disregarding these aspects, the basic approach for such visualization techniques is to take *key features* from one modality and embed them in another one, e. g. PET hotspots in CT. With an increasing number of image sources, visualization techniques become more complex, since more information is available per pixel and/or voxel. Therefore, facilities have to be provided to reveal key features, e. g. by cutting away information *in front* [500]. To achieve precise results and accurate localization of said features in their new context, image registration is often necessary to align multiple image sources with each other [274, 275]. However, this topic is out of the scope of this thesis, and thus, will only be reflected on briefly (Sec. 3.2).

In the next section, general goals and requirements of multimodal visualization techniques are discussed [274] (Sec. 3.1). Subsequently, selected categories of such techniques are presented in more detail, i. e. slider-based blending (Sec. 3.3), surface-based techniques (Sec. 3.4), slice-based overlay and replacement (Sec. 3.5), smart visibility (Sec. 3.6) and visibility-driven techniques (Sec. 3.7), techniques to combine more than two image sources (Sec. 3.8), and techniques for 4D (x, y, z, t) image sources (Sec. 3.9). Finally, this chapter is concluded with a brief summarization and outlook.

Categorizing multimodal visualization techniques is challenging, since most authors combine various approaches and methods. In other words, although used in a certain section, some works could also be described in different and/or multiple sections. For the most part, the categorization of Lawonn et al. [274] is taken as a starting point, however, certain categories, e. g. *Visibility-Driven X-of-Interest* techniques, will be explained in more detail, while combinations of techniques will be highlighted.

Note that rather being developed with (multimodal) medical images in mind, most of the subsequently presented principles, e. g. ghosted or cut-away views, originate from industrial and/or product design, e. g. to convey insights into complex machinery.[1] Furthermore, regarding the following subfigure captions, some state the specifically depicted combination of modalities. If no further details are provided, the depicted modality or combination of modalities could not be ascertained.

[1] See the homepage from Kevin Hulsey: www.khulsey.com/, last accessed September 6, 2019

3.1 GENERAL GOALS AND REQUIREMENTS

Here, general goals and requirements of visualization techniques for multimodal medical image data are presented.

REVEALING KEY FEATURES. Similar to balancing soft tissue contrast and image noise for X-ray-based images, visualizations have to balance visual complexity (cf. Sec. 4.2) and preservation and/or enhancement of key features. The definition of key features heavily depends on the application [147, 274]. For example, such features can be metabolically active lesions, heavily altered bone tissue or just certain structures. In clinical practice, image data is assessed *directly*, i. e. in (multiple) 2D viewers, and thus, the risk that the presentation itself conceals crucial information is rather low. In contrast, this cannot be guaranteed for 3D visualizations, since, for example, PET hotspots can be excluded due to unfavorable slab definitions or be occluded by surrounding tissue. Therefore, key features should be made clearly visible, for example by attention-catching colorizations and/or by tying the visualization technique to the 3D scene camera, e. g. by omitting anatomy between camera and features to make them visible from all viewpoints automatically [275]. However, certain colors could already be used for different purposes, e. g. PET color coding, which can limit the set of available colors (cf. Fig. 2.14 and Sec. 7.6).

SPATIAL RELIABILITY. Consequently, when key features are embedded, the spatial reliability between them and their new context should be high. With respect to PET/CT, Lawonn et al. [275] state that "*it [the technique] should relate the metabolic activity to nearby anatomical structures for accurate localization*". However, some rendering techniques, e. g. DVR or IVR, are more suitable to do so than others, e. g. MIPs.

LIMIT PREPROCESSING. Prior to the visualization, key features have to be defined, e. g. via segmentation. Typically, this is not done in clinical practice, but a major exception is the treatment planning for radiation therapies, for which manual and/or (semi-)automatic segmentations are obtained [429]. Generally, preprocessing should be kept at a minimum.

TECHNIQUE VERSATILITY. Inspired by cooperations with clinical partners, visualization techniques are very often inspired by a certain application scenario, i. e. with respect to certain organs, types of treatment, and image data available. However, techniques should follow a more general approach, e. g. independent from the targeted organ, while offering application-specific solutions when possible.

LINKING TO ORIGINAL IMAGES. Visualizations (purposefully) introduce a certain degree of abstraction. However, in some clinical contexts, a few millimeters can alter diagnoses and therapy decisions [201, 282]. Thus, visualizations and the original images should be presented in unison and, if possible, with synchronized user interaction facilities, e. g. to highlight suspicious findings in 2D (3D) when users select them in 3D (2D).

OTHERS. There exist further requirements, e. g. for planning radiation therapies or neurosurgical interventions. These will be discussed in their respective sections.

3.2 IMAGE REGISTRATION

In the previous chapter, it was discussed that image stacks can vary significantly w. r. t. their image matrix and/or voxel dimensions. Using hybrid imaging devices can improve these aspects, e. g. by reconstructing both image sources into the same coordinate system, which makes superimpositions more accurate. However, within each voxel, a considerable amount of tissue information is compiled, which especially renders structure boundaries *uncertain*. Thus, for example, it can be challenging to decide if certain voxels belong to tumor or healthy tissue. Additionally, image registration is typically accompanied by image intensity interpolations, since volume grids are transformed, e. g. via rotation or scaling, which in turn results in *smoothed* intensities. In combination, registration results involve some degree of uncertainty which is a problem for, e. g., taking measurements. It can be argued that some inaccuracies in visualizations are negligible, since the original and unaltered images have to be used to make diagnoses and treatment decisions. Nevertheless, for most visualization techniques, registration is often necessary to *accurately* align images.

3.2.1 APPLICATION SCENARIOS

There exist various application scenarios for image registration [381]. One example are (multimodal) overlay and/or fusion techniques that merge multiple image sources into one presentation (cf. Sec. 3.5). Thus, to preserve spatial relationships and to not occlude key features by accident, images have to be aligned. Moreover, for some types of intervention it is necessary to accurately align pre- and intra-operatively acquired images, e. g. for interventions in the spine, since pre-operative scans are typically acquired with patients lying on their backs, whereas they lie face down during the actual interventions (cf. Ch. 5). This is important, for example, to enhance the intra-operative scans by annotations and/or segmentation results from the planning phase (cf. Sec. 3.9 and Fig. 3.5a).

3.2.2 IMAGE REGISTRATION APPROACHES

Here, rigid, affine, segmentation-based and image property-based image registration approaches will be described briefly. For more details, see the works of Haskins, Maintz and Viergever et al. [181, 309, 499]. The image data used in this thesis was either pre-registered or the employed registration procedure will be explained in the respective sections.

RIGID TRANSFORMATIONS. Rigid techniques employ transformation matrices that apply translations and/or rotations to images [181, 309, 499]. Such registration techniques can be employed via

- *extrinsic*, i. e. outside of the patient, or
- *intrinsic*, i. e. on the inside of the patient,

features [309, 499]. Extrinsic registration is done by employing screw markers or fixation, whereas intrinsic rigid image registration, for example, can be done via anatomical landmarks. On the one hand, extrinsic approaches result in highly accurate registration results. Moreover, fixation setups can provide further assistance during intervention, e. g. instrument guidance. This limits their applicability to more stationary anatomy, such as the

brain. Since drilling is necessary, such approaches are also invasive. On the other hand, intrinsic approaches employ user-defined or automatically obtained image landmarks. Such landmarks are sets of points that, for example, are based on geometric information, such as curvature features of image-prominent structures, e. g. bones in CT. With respect to research, "*extrinsic approaches are hardly found any more*", whereas "*in surgical and radiotherapeutical procedures extrinsic matching remains in use*" [499].

AFFINE TRANSFORMATIONS. In addition to rigid transformations, affine transformations also allow for, e. g., image scaling and shearing. Although such transformations preserve some features, e. g. parallel lines stay parallel, image scaling has to be employed carefully, since scaled tumor tissue can easily alter diagnoses and treatment decisions.

SEGMENTATION-BASED REGISTRATION. For such techniques, the same structure has to be segmented in all image sources. Such techniques can be employed in a rigid manner, i. e. one scan is transformed w. r. t. both segmentation masks but "*this does not imply that the registration transformation is also rigid*" [309]. Due to the vast amount of segmentation methods being available, such techniques can be further enhanced. However, the registration results heavily depend on the segmentation masks' quality. Alternatively, segmentations can also be deformed, which is done iteratively until a *good fit* of all masks is reached. On the one hand, such methods enable image registrations of deformed organs, but on the other hand, a major drawback can be that the "*deformable model matches the anatomy perfectly, except in the one interesting image area where a large tumour growth has appeared*" [309]. This can be addressed by locally adapting deformation constraints, e. g. by virtually making tumor tissue more *rigid*, and thus, more robust against deformations. Such methods only utilize small image portions for image alignment and, overall, it appears that the research interest for such techniques decreased, since more powerful hardware made it possible to utilize the full images and derived properties [499].

IMAGE PROPERTY-BASED REGISTRATION. Property-based methods extract certain features from image intensities. For example, by computing the centers of gravity and principal axes (0th- and 1st-order moments), images can be aligned quickly but not very accurately [309]. In contrast, *entropy-based* methods aim to maximize *mutual information* between images, for example [309, 381]. If image intensities are used directly, methods are rather suited for monomodal image registration, since modality-specific intensities do not represent the same type of information, e. g. radiodensity (CT) vs. proton relaxation (MRI) vs. photon coincidences (PET). Thus, for multimodal registration, image intensities are sometimes rescaled into the same value ranges (cf. Secs. 3.5 and 3.7).

For *entropy-based* methods, combined 2D histograms of two images are created by aligning their image intensities along the x- and y-axes. Histogram values denote the absolute – or relative $p(i, j)$ – occurrence of *overlapping* intensities [374].[2] Subsequently, such methods find minimal transformations for which the joint *Shannon Entropy*

$$-\sum_{i,j} p(i,j) \log p(i,j) \tag{3.1}$$

[2]This is similar to Gray Level Co-Occurrence Matrices (GLCMs).

is minimized [374]. The joint entropy increases with image *misalignment*, since $\log p(i, j)$ values decrease exponentially with decreasing $p(i, j)$ values. In other words, transformations that *maximize* $p(i, j)$ for some intensity combinations and *minimize* it for the rest, result in *good* registration results, since their mutual information is maximized.

3.3 SLIDER-BASED BLENDING

In Figure 3.1, the slider-based approach from Rosset et al. is depicted [414]. Here, DV-rendered CT images and MIP-rendered PET images are combined, but the general approach can be applied to 2D presentations, too. Using a slider, which is indicated at the bottom, users adjust the modality-specific contribution of the PET/CT image sources in the final presentation, i. e. from 0 % to 100 %. In other words, after the corresponding transfer and windowing functions are applied, a global alpha value denotes how visible each modality is. The authors also discuss how this approach can be used for multi-MRI presentations, e. g. T_1 and Short Tau Inversion Recovery (STIR).[3] However, similar to PET or SPECT images, their exemplaric STIR-MR images only have a few (water) *hotspots*, which leads to similar results, although two morphology-depicting image stacks were used. Their approach focuses on diagnostics without any apparent restrictions regarding the scanned anatomy, but other clinical applications, such as therapy planning, should be feasible, too.

3.3.1 INTERMISSION – COMBINING VOLUME RENDERING AND MIPS

In contrast, Cheirsilp et al. [75] utilize an approach that combines IV-rendered surface meshes and color-coded MIP-rendered PET images (see Fig. 3.2). Besides this, the authors present an algorithm suite to segment and separate several structures in the thorax, e. g. the trachea and bronchi, the aorta, lung parenchyma, the ribs, the spine, and the sternum. Thus, their method is focused on diagnostics, e. g. bronchoscopies, and therapy planning applications, e. g. radiation therapies.

They did not employ a slider-based technique, however, their results also appear visually *layered*, since the MIP-rendered PET images are presented *on top* of the lung. This is a general shortcoming of MIPs, i. e. depth cues do not exist. On the one hand, MIPs can be generated straightforwardly, typically do not require user input, and when depicted *on*

See [414, Fig. 1].

Figure 3.1: A slider-based blending between CT and PET. Similar to 2D PET/CT presentations, the CT data is presented in grayscale, while the PET images are color-coded using a *hot* color scale. This approach is used in the *OsiriX MD* software (Pixmeo SARL, Bernex, Switzerland). Although this image series depicts 3D presentations, the underlying technique is applicable in 2D, too.

[3] STIR sequences suppress fat by introducing an additional "*preparation pulse*" prior to the RF impulse that aligns $\vec{M}$ and $\vec{B}_0$ perpendicularly (cf. Fig. 2.8). Thus, during relaxation, fat cannot release energy during signal capturing, and thus, will appear black on the resulting images. Explanation taken from https://www.mr-tip.com/serv1.php?type=db1&dbs=T1%20T2%20STIR, last accessed September 2, 2019

top, there is no risk that hotspots become occluded by morphology. Thus, they are always well visible. On the other hand, without user interaction, e. g. repeated 3D rotations, and high mental effort, morphology and physiology are challenging to relate accurately. Furthermore, surface abnormalities can become occluded by physiology.

This was also discussed by Ropinski et al. [409], who presented a Graphics Processing Unit (GPU) ray casting method for PET/CT images in mice with atherosclerotic plaques. Similarly, the authors also did not employ a slider-based approach, but they state that "*just blending the result of the DVR CT rendering and the MIP PET rendering would affect the spatial comprehension [...]. To get a correct occlusion relation, during the MIP generation we only consider those PET samples which lie in front of the lumen wall*" [409]. A more detailed comparison of DVRs and MIPs can be found in the article of Fishman et al. [131].

3.3.2 INTERMISSION – TRI-MODAL SLIDER-BASED BLENDING

Inspired by slider-based blending for two modalities, we developed a prototype with a tri-modality blending GUI widget for PET, CT, and MR images (see Fig. 3.3). This prototype – and any other piece of software presented and discussed in this thesis – was developed in MeVisLab 2.8.2 (MeVis Medical Solutions AG, Bremen, Germany) [406]. Similar to the method of Rosset et al. [414], the final contribution of each modality is defined by an individual alpha value. These weights are computed via barycentric coordinates in an equilateral triangle. When compared to the previously presented methods, two advantages are that all image sources are registered with each other and no MIP rendering is employed. Thus, each modality can be assessed in the context of the others. However, MRI volume

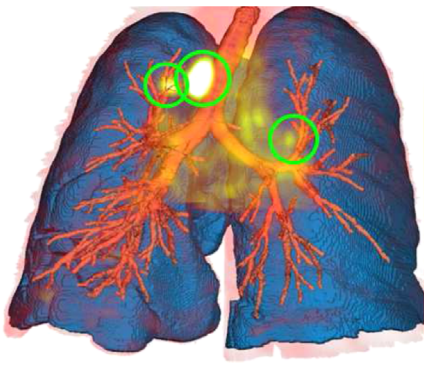

Figure 3.2: IV-rendered surfaces of the lung and trachea, and MIP-rendered PET images by Cheirsilp et al. [75]. The results appear *layered*, since the MIP is rendered *on top* of the surface meshes. Thus, they do not become occluded, but it is challenging to relate them to their morphological origin. The green circles encompass PET hotspots. Here, also a (*hot*) color scale was used (cf. Fig. 3.1).

rendering is challenging and since three image sources are used, now there are two modalities that can occlude suspicious findings in the third one.

3.4 SURFACE-BASED TECHNIQUES

The general approach of surface-based techniques is that a context organ is extracted from a morphology-depicting modality, e. g. CT or MRI, while surface regions are color-coded w. r. t. physiological or functional information, e. g. from PET or fMR images. In Figure 3.4, four different examples from Abellán, Jainek, Nguyen and Stokking et al. are depicted [1, 211, 360, 462]. For these methods, brain surface models were extracted from MR images. CT images could also be used for this, however, MR images provide superior soft tissue contrast, and thus, they depict brain lobes, sulci (inward ridges), and gyri (outward ridges) in great detail, which in turn enables a detailed separation into different brain areas.

Stokking et al. [462] describe a method that generates gradient-based surface renderings (see Fig. 3.4a). Subsequently, the gradient is projected inwards, which implicitly begins an inward ray casting. Since the ray depth can be adjusted, brain parts to be sampled can be selected. Furthermore, users can choose what value will be used for the colorization, e. g. if the first hit or an aggregated value, such as the maximum, is used. Finally, these values are color-coded and since the brain surface itself is rendered via *grayscale* Phong shading, the resulting color patches draw the user's attention towards key features. Although the technique was not evaluated regarding its clinical applicability, it could be argued that it is feasible for diagnostic and treatment evaluation purposes, since images of patients with Tourette syndrome and epilepsy were used.

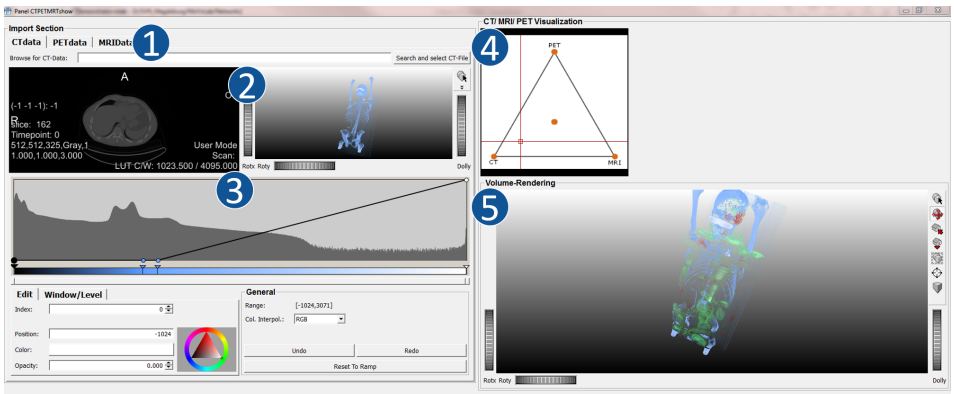

Figure 3.3: A tri-modality blending prototype for PET, CT, and MR images. The enumerated Graphical User Interface (GUI) regions denote various functionalities, i. e. the import of image data **(1)**, an overview of the original and DV-rendered images **(2)**, a 1D transfer function that translates image intensities into colors and opacities **(3)**, the tri-modality blending widget **(4)**, and the resulting tri-modality DVR **(5)**. The widget is an equilateral triangle and the blending weights are computed via barycentric coordinates. Here, **CT** accounts for the majority of the final presentation with minor contributions from the **PET** and **MR** images.

Figure 3.4b shows a technique presented by Nguyen et al. [360] that depicts DV-rendered (f)MR images of the brain with functional hotspots. One of the main contributions of their system is that it can process real-time fMRI data. In other words, their system enables MRI scanner operators to assess brain function in 3D visualizations while they instruct patients to do certain little tasks, e. g. finger opposition tasks [462].[4] Interestingly, they interpret functional information as emissions, and thus, it appears like the fMRI hotspots "*shine through*" [360]. However, similar to MIPs and projection-based augmented reality, this omits depth-related information about the functional signal, e. g. where it originates from [185]. Thus, the authors also employ cutting planes to reveal them (not depicted). With respect to performance, the fMRI signal was updated each 0.21 *s* to 3.02 *s*, while frame rates of roughly 13 Frames per Second (FPS) were achieved during user interactions. Given that the article was published in 2010, more modern GPUs could achieve *real* real-time assessments of brain morphology and functionality, which could be beneficial for

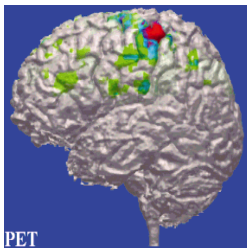

See [360, Fig. 4].

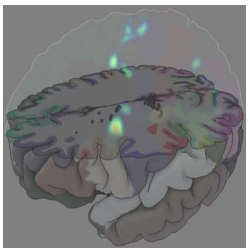

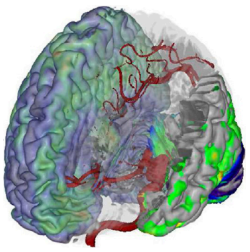

(a) MRI + PET **(b)** MRI + fMRI **(c)** MRI + fMRI **(d)** MR(I/A) + PET

Figure 3.4: Subfigure **(a)** depicts an early method by Stokking et al. [462] to fuse PET and MR images via DVR. Here, within a user-defined distance, the surface normal (gradient) is projected inwards to denote the surface's color coding w. r. t. quantified PET information. Nguyen et al. [360] combine on-the-fly fMRI and MR images **(b)**. Interestingly, they interpret functional information as emissions, which results in the impression that fMRI hotspots lighting up. Similarly, Jainkek et al. [211] depict functional hotspots as light-like sources on the brain surface **(c)**. Furthermore, they color-code various brain areas, which gives their results an atlas-like appeal. Abellán et al. [1] present a DVR-only rendering system to combine PET and MR(A) images **(d)**. They also employ surface transparencies to enable users to look into the brain, e. g. to assess blood vessel network abnormalities.

[4] "*The stimulation was evoked by a simple finger opposition task [...]. The task entailed repeatedly and sequentially touching the thumb once with each one of the digits.*" [462]

various neuroscientific applications. For further information on fMRI and its (clinical) applications, see the book of Filippi [128].

Jainek et al. [211] present an illustrative approach (see Fig. 3.4c). The authors enrich the final presentation by additionally color-coding different brain areas, which they acquired with the FreeSurfer software suite.[5] This gives their results an atlas-like appeal. To avoid ambiguous surface colorizations, i. e. between morphology and functionality, a cutting plane can be used to erase brain morphology. The authors combine ambient occlusion, image-space-enhanced silhouettes and boundaries, and varying transparencies, which in combination result in a very stylistic presentation.

With respect to combinations of transparent and opaque surfaces, Abellán et al. present comparable results, however, they "*apply DVR to all the modalities*" [1] (see Fig. 3.4d). Additionally, their technique can include angiographic information, e. g. from contrast media-enriched MRI scans, which can reveal aneurysms or other blood vessel abnormalities. This technique could be used for visualization-supported studies in diagnostic, treatment planning, or treatment evaluation settings, since the spatial relationship between the brain and its blood vessel network is preserved, while occlusion artifacts are addressed via transparencies [69, 151]. However, multiple (color-coded) semi-transparent layers in front of objects can hinder their assessability, since they artificially darken objects. Thus, delineations between key features and adjacent structures can become more challenging.

REMARKS ON TRANSPARENCIES. Since deep-seated hotspots can still be occluded, Nguyen et al. [360] employ transfer function-based *filtering*, i. e. brain morphology opacities are heavily reduced, until only functional information remains. However, in contrast to the methods of Abellán and Jainek et al. [1, 211], the outmost brain surface is not preserved, i. e. by a transparent layer. On the one hand, this enables a clearer presentation of functional hotspots and the brain's inner morphology, since no additional layer is rendered between the scene camera and brain cross-section. Furthermore, this makes rendering easier, since no transparent objects have to be considered. On the other hand, this makes it challenging to spatially relate morphology and functionality and, depending on the amount of omitted morphology, it becomes virtually impossible to convey which brain regions are active. For more details on the perception of transparencies, see the work of Singh et al. [447].

3.5 OVERLAY AND FUSION TECHNIQUES

Essentially, overlay and fusion techniques take certain key features – or whole slices – from one image stack (source) and display them *on* and *in* a different one (target), respectively. With respect to the target images, this can be done more or less *invasively*, e. g. (color-coded) source slices can be superimposed with decreased opacity, which lets the target images still contribute to the final presentation (cf. Figs. 2.14 and 2.15). Other methods, however, fully replace target image regions, e. g. vertebrae can be segmented in CT and are then embedded in MR images, which makes it possible to assess soft and hard tissue abnormalities simultaneously (see Fig. 3.6). Therefore, in the following, the keywords *overlay* and *fusion* will be used for techniques that either preserve visual information

[5] http://surfer.nmr.mgh.harvard.edu/, last accessed September 4, 2019

from target images or replace parts of them. However, these keywords are often used interchangeably and can be regarded as special cases of each other.

3.5.1 OVERLAY TECHNIQUES

Schulz et al. [434] present a method that combines pre-operational Computed Tomography Angiography (CTA), and intra-operational fluoroscopic and Digital Subtraction Angiography (DSA) images (see Fig. 3.5a). Bony structures, such as the spine, and contrast-enhanced blood vessels, such as the aorta (not depicted), are used as landmarks during aortic repairs. Moreover, pre-operational user-defined surgical landmarks, such as instrument *landing zones*, are used for superimposition (red circles). Rather than being truly multimodal, this approach is multidimensional, since CT scans are 3D and fluoroscopic images are planar. However, since blood flow features from CTA and DSA images, which are considered functional features, can also be included, the method can still be considered multimodal.

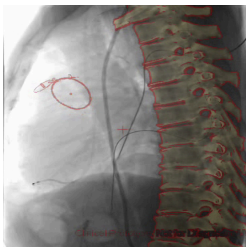

(a) CT on Fluor.

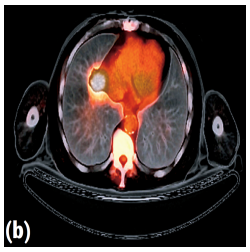

(b) PET on CT

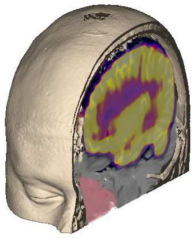

(c) PET on MRI

See [134, Fig. 6(e)].

(d) Model on US

Figure 3.5: Here, four overlay techniques are presented. The order of modalities in the captions denotes which one is the *source* and which one is the *target* modality. For example, in Subfigure **(a)**, the results of Schulz et al. [434] are depicted who use color-coded and boundary-enhanced vertebrae from CT images (source) to enhance 2D fluoroscopic images (target). This is done to provide assistance during interventions, e. g. aortic repairs, via anatomical and user-defined landmarks, which were defined during intervention planning. Similar to color-coded 2D superimpositions in clinical use, Kim et al. [235] introduced a dual-Lookup Tables (LUTs) method to depict PET/CT images in 2D and 3D **(b)**. Similarly, Abellán et al. [1] also employ transfer function fusion and in combination with 3D cutting planes this "*create[s] the sensation of painting one volume on top of the other*" [1] **(c)**. In the last example, the method of Ford et al. [134] is presented that superimposes a heart model with planar Ultrasound (US) images **(d)**. This model consists of pre-labeled anatomical landmarks that are registered with the US images, and thus, the resulting visualization is quasi-patient-specific.

Kim et al. [235] introduced a dual-LUTs method to superimpose CT with PET images in 2D and 3D (DVR-only; see Fig. 3.5b). Related to *Bernstein Polynomials* that are used to determine *pulling weights* of control points in Bézier curves, their method assigns fusion weights to both modalities and ensures that *opacity peaks* do not appear in the same (normalized) image intensity intervals. In other words, at any point in the dual-LUT, the fusion weight sum does not exceed 1. Consequently, in extreme cases, one modality can fully replace the other one, which implicitly makes this method an image fusion method, too. However, if both fusion weights are set to 0.5, *classical* results are achieved (cf. Figs. 2.7, 2.14, and 2.15).

Similarly, Abellán et al. [1] also employ LUT fusion and combine it with cutting planes in their DVR-only pipeline (see Fig. 3.5c). Here, color-coded PET images are "*painted*" on MRI cross-sections [1]. Although users can change the contribution of the MR images (target), brain matter is rendered in grayscale to emphasize metabolic information.

For the last example, the method of Ford et al. [134] was chosen (see Fig. 3.5d). Here, the authors combine a textured heart model with US images. However, it is challenging to conclude which *modality* is the source or target modality. On the one hand, visually, the US images are embedded in the 3D heart model. On the other hand, certain anatomical landmark labels in the heart are registered with their US image counterparts, which results in the heart model being deformed w. r. t. captured heart beats from US images. This enables physicians and patients to perceive US images in their spatial context. Moreover, and although only slightly discussed by the authors, w. r. t. physician training and doctor-patient communication, such approaches could deepen the understanding of relationships between (heart) morphology and functionality. Arguably, this is especially beneficial for US images, since it requires a lot of training to *read* them. With respect to doctor-patient communication, this can potentially make patients overcome their fear of clinical procedures and raise their awareness about their current situation [18, 159].

3.5.2 IMAGE FUSION TECHNIQUES

In contrast, image fusion techniques can be regarded as being more invasive, since target image regions are fully replaced. Consequently, the target modality does not contribute to the final presentation. Miles et al. [333] present a graph-cut approach to fuse CT and MR spine images in 2D (see Figs. 3.6a to 3.6c). In simplified terms, their method finds edges around cortical bone tissue in CT and MR images. Furthermore, the method ensures that fused images have similar intensities around fused regions to not make CT information too dominant, since bone tissue (source) is embedded in an MR context (target). This is done by setting negative CT image intensities to zero, which omits most of the soft tissue information. However, image contrast depends on the scanner's used kVp setting, which affects the results (cf. Sec. 2.1.2). Subsequently, the CT and MR image intensity histograms are aligned with each other. Consequently, the final images can depict soft and hard tissue abnormalities at the same time.

In contrast, Gaemperli and Hosokawa et al. [140, 199] present methods that fuse functional (SPECT, source) and morphological (CTA, target) information in 3D. For lung function testing and perfusion damage treatment (here: *balooning*), Hosokawa et al. [199]

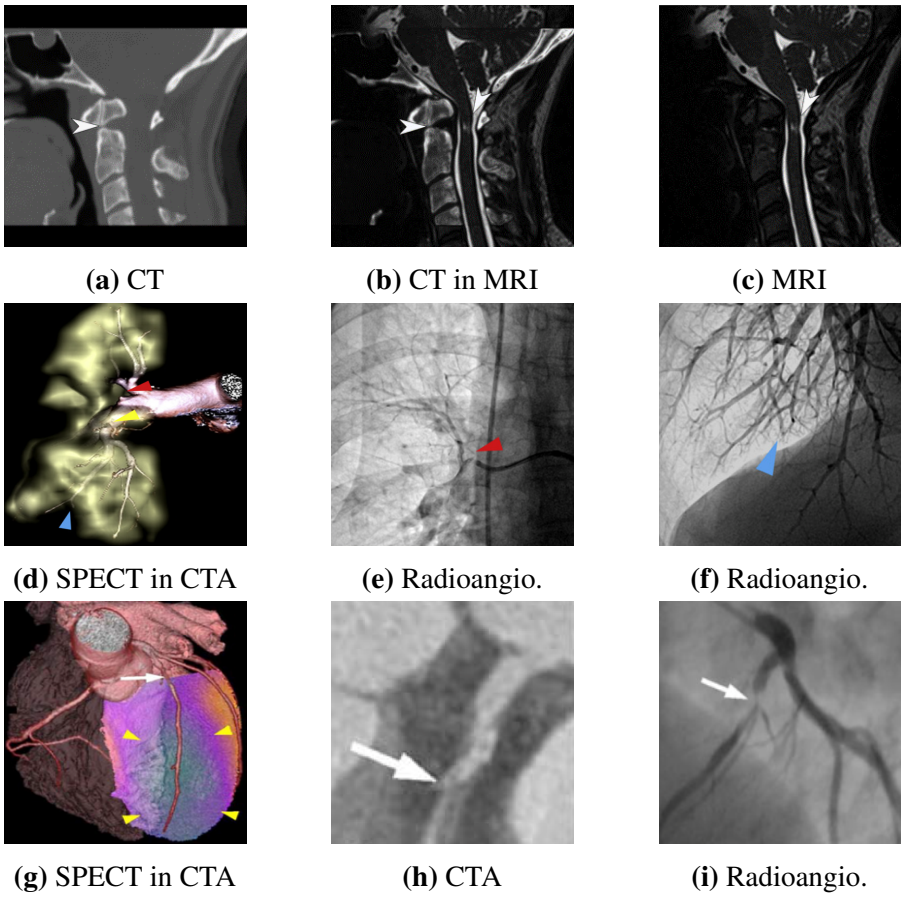

(a) CT **(b)** CT in MRI **(c)** MRI

(d) SPECT in CTA **(e)** Radioangio. **(f)** Radioangio.

(g) SPECT in CTA **(h)** CTA **(i)** Radioangio.

Figure 3.6: In the graph-cut-based method of Miles et al. [333], CT and MR images are fused in 2D that enable a simultaneous assessment of soft and hard tissue abnormalities **(a–c)**. Here, abnormally shaped vertebrae (↑) appear to have caused spinal cord damage (↑). Hosokawa et al. [199] use a DVR approach to combine CTA and SPECT images in the context of lung function tests and perfusion damage treatment **(d–f)**. The morphological origins (↑↑↑) of the hindered perfusion are highlighted in the Subfigures **(e–f)**. Gaemperli et al. [140] present a 3D CTA/SPECT fusion technique that depicts functional information in its spatial context via DVR **(g–i)**. Here, a myocardial stenosis (↑) results in a decreased perfusion of the heart muscle (↑). Similarly, the morphological origin is highlighted in the Subfigures **(h–i)** (↑). These examples underline the importance that 3D visualizations should be accompanied by the original 2D image data.

present apparently DV-rendered images in which lung parenchyma is replaced by perfusion information (radiotracer: ^{99m}Tc; see Figs. 3.6d to 3.6f). Note that the authors of this work are clinicians, and thus, technical details about the employed techniques are missing. However, this also shows that 3D visualizations are used to present clinical case reports.

Gaemperli et al. [140] also present a 3D SPECT/CTA fusion technique for assessments of myocardial ischaemias (see Figs. 3.6g to 3.6i). Here, one CTA and two SPECT perfusion scans, one before and one after a treadmill stress test, are acquired. Regarding the final presentation, volume rendered SPECT perfusion images replace heart morphology, which reveals perfusion damage in its spatial context. Such reductions can be caused by stenoses or plaque in the myocardial arteries. The authors combine this approach with color-coded Bull's Eye Plots (BEPs), sometimes also called *Polar Maps* or *Solar Polar Maps* due to their radial layout and color coding [248, 509]. BEPs are a map-based (unfolding) method that depicts the heart muscle's perfusion via projection on a horizontal plane [351, 381]. Map-based methods will be explained in more detail in the next chapter.

3.6 SMART VISIBILITY TECHNIQUES

According to Viola and Gröller, smart visibility techniques are "*expressive visualization techniques that smartly uncover the most important information in order to maximize the visual information of the underlying data*", which "*is achieved through dynamic change in visual representations, through deformations, or through changing the spatial position of the data*" [500]. Smart visibility techniques display *all* the available information at once, but provide interaction facilities to reveal "*underlying data*", i. e. to resolve occlusion problems and enable users to look through surfaces to assess key features. Such key features can be provided by another modality, image source, or type of information. Some of the major smart visibility techniques will be presented in the following sections, namely cut-away, ghosted, and Focus and Context (F+C) visualization techniques.

3.6.1 CUT-AWAY VIEWS

As the name suggests, cut-away techniques cut away surfaces to reveal underlying key features. Burns et al. [68] present a dual-angle cut-away DVR approach that cuts away surface information w. r. t. the scene camera's position and an object of interest (see Fig. 3.7a). Here, the object of interest is a US image that gets partially occluded by the spine to enhance its spatial relationship to other structures. The outer (*context*) dataset is a standard CT scan. Using two depth-offset cutting angles, namely θ_1 and θ_2, a "*transition region*" d in between them can be used to partially blend in structures from the outside dataset. Typically, cut-away techniques, such as the one presented by Viola et al. [502], do not allow for such a region (see Fig. 3.7b). On the one hand, if no such regions are allowed, the object of interest is not occluded, and thus, clearly visible, but the visual transition is very *abrupt*, which in turn makes it easier to distinguish the focus object from its surroundings. On the other hand, if techniques allow for such regions, objects of interest can become partially occluded, which can be used as a depth cue. Thus, objects can be related more easily to their spatial context, i. e. to anatomical (risk) structures that are in front of rendered slices. This can be useful for needle-based interventions.

Kirmizibayrak et al. [244] describe a multi-cut-away approach that can be executed repeatedly to subsequently strip modality *layers* (see Fig. 3.7c). In other words, initially, users see a DV-rendered surface, e. g. the face from MR images. Subsequently, they can use a *Magic Lens* to reveal the next layer, e. g. blood vessels in MRI, and punch away the outer layer in the lens' region [51]. This can be repeated until they reach the last layer, e. g. a skull from CT images. Consequently, during preprocessing, all data sets have to be registered with each other to ensure accurate spatial relationships between all images.

Lawonn et al. [272] present a visualization method that simultaneously visualizes blood flow and vessel wall thickness (see Fig. 3.7d). There exist various blood flow visualization techniques that are out of the scope of this thesis. For more details on such techniques, see the survey of Oeltze-Jafra et al. [365]. However, arguably, they can be considered multimodal techniques, since the blood vessels can be acquired via US-based or contrast

See [68, Fig. 7].

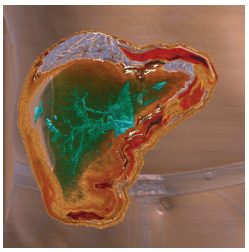

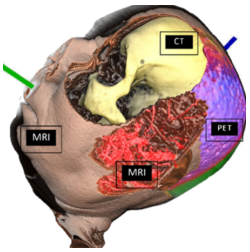

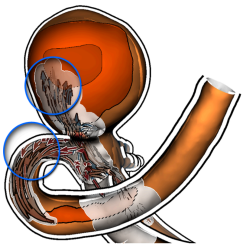

(a) US in CT **(b)** Monomodal **(c)** Various **(d)** CFD in CTA

Figure 3.7: Here, four cut-away smart visibility techniques are depicted. Burns et al. [68] present a dual-angle cut-away technique that omits every visual contribution of the *context* dataset between the scene camera and a user-defined object of interest **(a)**. However, employing two depth-offset cutting angles enables users to define a "*transition region*" to superimpose key features again. Although they are occluded, this enhances spatial relationships between them and their surroundings. In more conventional approaches, i. e. when only one cutting angle is employed, the results look similar, but the transitions between context and objects of interest are generally more *abrupt*. This can make it easier to distinguish both image sources **(b)**. Kirmizibayrak et al. [244] employ a multi-cut-away technique that subsequently cuts away modality layers via magic lenses that also convey previews prior to cutting [51] **(c)**. However, such techniques require image registration to ensure accurate alignment of all image sources. The last example is taken from Lawonn et al. [272], who simultaneously visualize blood flow (Computational Fluid Dynamics (CFD) simulation) and blood vessel morphology (CTA) **(d)**. With respect to these different types of information, such techniques can also be considered multimodal also. In the original image, the highlighted regions were depicted in greater detail, i. e. emphasizing how blood is color-coded differently w. r. t. its vessel wall proximity.

media enhanced image acquisitions (morphology), while the blood flow is measured via 4D PC-MR images or simulated via CFD [150, 247] (functionality). With respect to the scene camera, the vessel surface is automatically cut away when blood flows behind the vessel wall. Thus, blood flow information is revealed and can be assessed occlusion-free.

There also exist *peel-away* techniques that reveal inner structures by peeling away outer surfaces [53].[6] The key difference between peel-away and cut-away techniques is that the latter fully removes cut-away information, while the first somehow preserves it, e. g. via an attached slab of skin. However, such techniques are out of the scope of this thesis.

3.6.2 GHOSTED VIEWS

In contrast to cut-away techniques, ghosted views employ transparencies to enable an occlusion-free assessment of key features beneath surfaces (see Fig. 3.8). In other words,

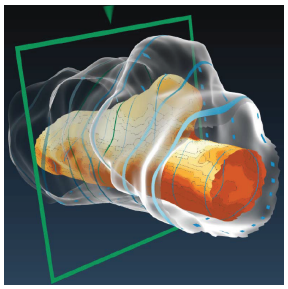

(a) US

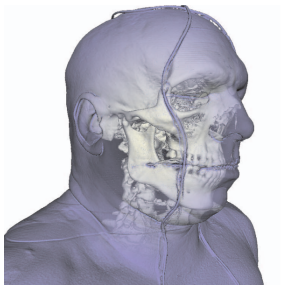

(b) CT

See [419, Fig. 4(d bottom)].

(c) CTA

Figure 3.8: Ghosted views present *context* objects with decreased visibility to reveal underlying features. Typically, this is achieved by decreasing the opaqueness of outer surfaces. Similar to the blood flow visualization technique by Lawonn et al. [272] from Figure 3.7d, Glaßer et al. [150] presented a technique to visualize multiple blood vessel walls **(a)**. The outer vessel wall is ghosted by applying Fresnel shading to the surface opacity, i. e. surface geometry that more parallel than perpendicularly aligned w. r. t. the viewing direction is rendered more opaque. This results in (white) surface highlights, which also represent surface unevenness. Using the *ClearView* system by Krüger et al. [255], users can combine various surface features, such as the orientation and curvature, to decrease opaqueness **(b)**. Although it is not apparent in the depicted example, the mouse cursor is a magic lens that lets users reveal underlying structures interactively (cf. Fig. 3.7c). The last subfigure depicts the *obscurance*-driven rendering method by Ruiz et al. [419] **(c)**. In simplified terms, uncluttered and smooth regions, i. e. non-obscure regions, have their visibility decreased. The depicted examples do not use multimodal image sources, but it is easy to imagine how the general principles can be used for multimodal images, e. g. to softly decrease surface visibility to reveal PET hotspots or poorly ventilated and/or perfused lung parenchyma close to the lung surface.

[6] Depending on the amount of peeling, the results look like an opened flower's calyx (dt. *Blumenkelch*.)

outer surfaces can still contribute to the final presentation, but are rendered translucent, similar to how we imagine ghosts to look like.

Glaßer et al. [150] describe a visualization technique that depicts multiple blood vessel walls (see Fig. 3.8a). The inner vessel wall is color-coded and depicted fully opaque, e. g. to encode hemodynamic parameters, such as the wall shear stress, whereas the outer vessel wall is depicted using Fresnel shading (see Fig. 3.8a). In simplified terms, w. r. t. the scene camera's position, surface areas with a high curvature are presented more opaque (white highlights), while areas with a more perpendicular orientation are rendered more transparent. Since the 3D visualization is linked to a 2D viewer that presents the original US images, the green frame and arrow highlight the respective *slice* in the 3D visualization.

Krüger et al. [255] describe their *ClearView* system that employs various smart visibility techniques (see Fig. 3.8b). Their method lowers the transparency of surfaces by combining position, normal, curvature, and/or distance information. For example, the *position information* relates to the screen-space mouse cursor position and surface areas around the projected mouse cursor position get rendered more transparent. This can be hinted at more *vaguely*, e. g. via non-boundary transparency fading, or more explicitly, e. g. via a magic lens metaphor. Regions with high curvatures, e. g. around the contrast media tubes adjacent to the eye, are rendered more opaque to preserve image regions with large morphological changes [459]. Furthermore, more perpendicularly aligned regions, e. g. around the jaws and cheeks, are rendered more translucent. In contradiction to this section's topic, Krüger et al. [255] specifically declare their technique being an F+C technique. However, in comparison, their results look very similar, i. e. with the skin being ghosted.

For the last example, the *obscurance*-based volume rendering technique introduced by Ruiz et al. [419] was chosen (see Fig. 3.8c). Following the definition of Zhukov et al., the term "*obscurance measures the part of the hemisphere obscured by the neighbor patches. E.g., near a corner of a room the obscurance of patches is higher than on the plane open parts*" [527]. In other words, more cluttered voxel regions are considered more *obscure*, and thus, are *naturally* darker. Furthermore, the authors utilize *voxel saliency*, i. e. voxel regions with a high variability of obscurance have a large saliency. Therefore, rather "*smooth or uniform region[s]*" [419], such as the skin, have small saliency values, and thus, they are depicted more bright and translucent, which reveals inlying structures with higher saliency (morphological) variability. Saliency can be used as a parameter to automatically create *interesting* viewpoints, i. e. perspectives that depict a high degree of morphological change, which could point users to interesting (suspicious) regions [498].

Although the authors do not specifically declare their technique to be a ghosting technique, skin tissue is clearly depicted *ghosted*, while, overall, their results have a very illustrative style and appear pencil-shaded. One key feature of obscurance-driven techniques is that they solely rely on geometry, i. e. obscurance and saliency values can be computed prior to the actual rendering and they do not rely on illumination. However, they only represent an approximation of realistic self-shadowing. In contrast, illumination-based techniques for volume rendering can create more realistically appearing results,

but they typically also result in higher computational costs. For more details on such approaches, see the works of Jönsson and Sunden et al. [221, 464].

3.6.3 FOCUS-AND-CONTEXT VISUALIZATIONS

Here, various F+C visualization techniques will be discussed.

SMART VISIBILITY VS. F+C TECHNIQUES. As mentioned before, clearly distinguishing F+C from smart visibility techniques is challenging. Lawonn et al. "*assume that at least the focus object is segmented*" [274], but there exist techniques that do not require segmentation prior to visualization [68, 244, 272]. Similarly to overlay and fusion techniques, the terms F+C and smart visibility can also be used interchangeably and both types of techniques can be understood as special cases of each other. In other words, here, the categorization of related work is more appearance- and presentation-driven, whereas Lawonn et al. [274] use a more processing pipeline-centered approach by declaring *segmentation* as the key difference for categorization. However, the authors suggest this being the key difference, since the resulting surface models make it easier "*to illustrate the focus object so that it is perceivable*" while "*simultaneously illustrating the surrounding context structures without distracting from the focus*" [274].

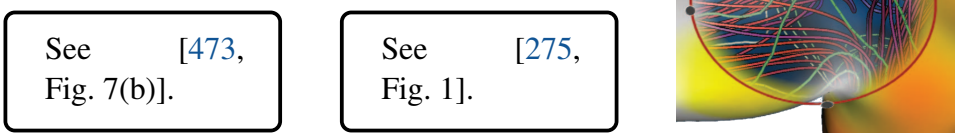

(a) CT and MRI **(b)** PET in CT **(c)**

Figure 3.9: The basic idea of F+C visualization techniques is to reveal focus objects (key features) and present them in a way that the user's attention is drawn to them, while context objects are only used as a visual framework. Tietjen et al. [473] presented a technique that highlights focus objects by depicting them in a more attention-drawing way **(a)**. Moreover, they broke with the traditional binary categorization, i. e. structures are either a focus or a context object, and introduced a category in between, namely *Near Focus Objects*. Here, this category is represented by grayscale-shaded bony structures, whereas context objects are solely depicted by boundary lines. Focus objects are color-coded, and thus, naturally draw the user's attention. Lawonn et al. [275] introduced a rendering technique for PET/CT images that places a magic lens between scene camera and focus object **(b)**. Thus, context geometry, such as the patient's skin, is automatically *cut away* during exploration. In contrast, Gasteiger et al. [143] attach a magic lens to the user's mouse cursor. This only reveals key features in user-defined areas **(c)**.

With respect to surface-based techniques, F+C techniques can be differentiated further, since surface-based techniques typically depict key features *on* surfaces, while F+C typically depict key features *under* surfaces. However, the previously presented methods of Abellán et al. [1] can also be considered F+C and/or smart visibility techniques, since the brain provides an anatomical context, while key features (blood vessels or PET images) are highlighted via color-coding (cf. Figs. 3.4d and 3.5c).

Tietjen et al. [473] present various illustrative rendering techniques to combine prelabeled organ surface models (see Fig. 3.9a). By employing different rendering styles, users can be guided to application-specific and/or user-defined key features. Here, user-guidance is achieved by rendering the focus objects (liver with tumor and primary blood vessels) using colors and illumination, while context objects (other organs and bones) are presented via (filled) line rendering. The authors break with the typical binary categorization into either context or focus objects and introduce a third category of structures in between, namely *Near Focus Objects*, which are "*important objects for the understanding of the functional interrelation or spatial location*" [473]. In other words, they are presented more prominently than context objects, but less prominently than focus objects, e. g. via grayscale shading. CT and MR images were used, but the general idea of applying different presentation styles could be applied to combinations of morphology and physiology/ functionality, too. In some way, by combining volume rendering (CT) and MIPs (PET), it can be argued that some authors already did so [75, 136] (cf. Figs. 3.1 and 3.2).

Lawonn et al. [275] introduced an F+C technique that uses CT images to provide an anatomical context for PET hotspots (see Fig. 3.9b). While the skin is presented with a combination of feature lines and toon shading, users can interact with a TF to *filter* the PET images. Basically, the PET image intensities are thresholded, i. e. until only hotspots remain, and are then presented via DVR [136, 275]. To reveal metabolic peaks, a magic lens is placed between the scene camera and *filtered* PET image values, and thus, all information in between is cut away. This is done by decreasing the respective opacities in the CT's TFs, e. g. of the patient's skin and/or scanner table. Thus, suspicious peaks become visible from all possible view points and by depicting PET information in red, the user's attention is drawn to them naturally [380]. Although the authors do not explicitly declare the skeleton as such, it is somewhat used as a near focus object to enhance spatial relationships between morphology and physiology.

LINKING SCENE CAMERA AND VISUALIZATION TECHNIQUE. On the one hand, linking scene camera and magic lens results in a strong user guidance and, potentially, in a positive user experience, since the user's attention is always drawn to potential findings that might have gone unnoticed otherwise [141, 275, 327]. On the other hand, a 3D visualization should only be used for exploration support, while the original image data is displayed *nearby* to allow for the actual assessment.

FIXED THRESHOLDING FOR PET IMAGE SEGMENTATION. Applying fixed (global) thresholds to PET image intensities typically results in one or more clearly delineated hotspots. However, *poorly* defined thresholds can result in challenging-to-assess presentations, e. g. lesion boundaries are overestimated, i. e. lesions in PET become larger than

their CT or MRI counterparts [136]. However, fixed thresholding can be done straightforwardly, which in turn benefits usability. For a more in-depth discussion of PET image segmentation methods, see the review article from Foster et al. [136].

For the last example, the *FlowLens* technique of Gasteiger et al. [143] was chosen (see Fig. 3.9c). Closely related to typical lens tools, this approach enables users to reveal blood flow to search for suspicious flow behavior on demand, i. e. with the mouse cursor. From a workflow perspective, various parameters can be displayed on the vessel surface, e. g. the wall shear stress, and if users find suspicious surface regions, they can use the lens tool to assess the underlying blood flow, which can be the source of suspicious surface regions.

SEPARATING SCENE CAMERA AND VISUALIZATION TECHNIQUE. On the one hand, linking lens and mouse cursor guarantees that the user's attention is focused on the opened surface area and underlying functional information. However, overall, assessments rely on the user's incentive to *read* the whole blood vessel. On the other hand, key features can only be revealed by the user, i. e. although suspicious findings *can* be revealed, even more suspicious findings may remain occult and although this puts a high burden on users, they can explore everything freely, since they can shift their focus to other areas. In other words, users can *look away*, since their attention is not constantly drawn to the same structures and/or features. To overcome this, Gasteiger et al. [143] also include a cut-away (*front face culling*) option, which cuts away surfaces that are oriented towards the scene camera to reveal all blood flow. Since back-facing geometry is preserved, the general shape is preserved as well, since the blood vessel can occlude itself.

3.7 VISIBILITY-DRIVEN X-OF-INTEREST TECHNIQUES

There exist various visibility-driven visualization techniques for (multimodal) medical images. Here, *X* denotes *what* is interesting. For example, a 3D position or a structure that is located there can be interesting. Slices (single or MIP-aggregated) can also be interesting to users or combinations and *cross-sections* of them, i. e. ROIs and/or Volumes of Interest (VOIs). This category is primarily inspired by the works of Correa and Jung et al. [93, 222], who introduced *Visibility Histograms*. Such and conventional histograms are similar in the regard that bins along the x-axis represent certain *objects*, i. e. (groups of) intensity values and key features, respectively. However, whereas conventional histograms plot absolute and/or relative counts of said image intensities along the y-axis, visibility histograms depict the *visibility* of the corresponding key features, such as ROI VOI-labeled PET hotspots. For example, this is done by compositing opacity values of the *source* modality, e. g. PET, w. r. t. opacity values of the target modality, e. g. CT, along DVR rays (cf. Figs 3.11 and 3.12). Thus, *high bins* represent high visibilities of their corresponding features, since they are not or only slightly occluded by other information. In IVR settings, a different measurement can be the ratio between all potentially visible surface patches (front faces) and non-occluded patches [498]. However, this favors large objects without respect to their actual interestingness.

Note that the variability of the herein discussed methods is high, i. e. some of them could have been explained in an earlier section. In the same sense, methods that were

presented earlier, especially in the sections about smart visibility and F+C techniques, could be explained here. For example, cut-away techniques often require users to define a structure or organ of interest, which is then revealed. In contrast to the survey of Lawonn et al. [274], the techniques in this section are explained in more detail.

3.7.1 POINTS AND STRUCTURES OF INTEREST

Here, points and structures of interest techniques for multimodal image data are described.

POI TECHNIQUES. Kim et al. [236] presented a POI technique to visualize PET/CT images in 2D and 3D (see Fig. 3.10a). In a multi-viewer setup, users can *select* PET hotspots in a combined MIP/DVR presentation by clicking on it. Subsequently, w. r. t. the PET image intensity, the corresponding 2D coordinate is determined and the transfer functions for both image sources are adapted. A Gaussian bell curve is used to define the

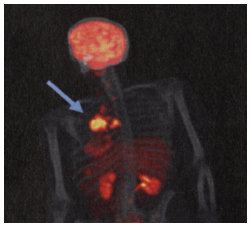

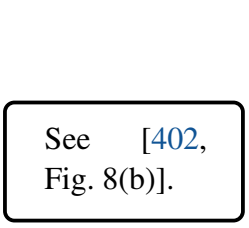

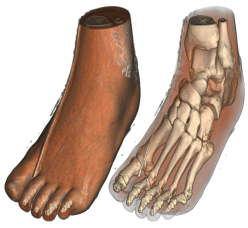

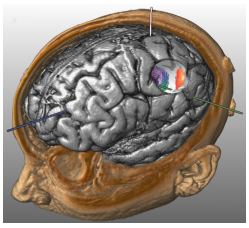

(a) PET in CT **(b)** Multi MRI **(c)** CT **(d)** Multi MRI

Figure 3.10: For Point of Interest (POI) and two ROI techniques, users trigger subsequent processing by *selecting* an interesting and/or suspicious *object*. In the first example by Kim et al. [236], users select a MIP-aggregated PET hotspot in a DVR and the visibility of PET and CT image intensities is altered to emphasize the *selected* PET hotspot **(a)**. For the approach of Rieder et al. [402], segmentation and ROI-based filtering is triggered when the user *selects* a brain lesion **(b)**. Subsequently, the tumor tissue mask is visualized in an open head DVR, while blood vessel morphology is preserved as spatial context. Correa et al. [93] introduced a Structure of Interest (SOI) technique that uses visibility histograms to correct user-defined TFs to increase visibility of *interesting* structures **(c)**. Here, *interestingness* is derived from user-defined opacities of certain HU ranges (cf. Fig. 3.12). In the last example Rieder et al. [401] present a multi-MRI visualization technique to support the treatment planning of brain tumors, e. g. via keyhole surgeries **(d)**. In contrast to Subfigure **(b)**, the blood vessels were substituted by reconstructed fiber bundles from Diffusion Tensor MR images. Furthermore, the planar cutting plane was substituted for a cylindrical cut-away tool. Thus, only a limited number of pathways can be assessed simultaneously. However, this can decrease mental load, and thus, improve user concentration.

[7] This is similar to *Smooth Brushing*.

opacities of the PET intensities with the bell curve's peak being placed at the selected image intensity. Thus, voxel opacity falls off smoothly w. r. t. the aforementioned position.[7] Similarly, a grayscale ramp curve TF is used for the CT images with the corresponding POI's CT intensity in the middle. Therefore, the full CT image intensity spectrum is rendered "*with emphasis on the anatomical structures within which the POI resides*" [236]. For another viewer, the aforementioned coordinate is used to create a quasi-slab rendering by automatically cropping a DVR in the *selected* PET hotspot.

However, the authors do not discuss how their technique works if *ambiguous* MIP-rendered PET intensities are selected, i. e. if the selected maximum can be found multiple times on the respective ray that has to be reconstructed to get the aforementioned coordinate. On the one hand, the color- and opacity-coding do not change, since they depend on the intensity. On the other hand, w. r. t. the selected hotspot's size, the potential coordinates can vary significantly, i. e. the corresponding lesion is sliced at very different positions. This can be addressed by *early ray termination*, i. e. the first coordinate with the selected PET intensity is used, and/or by instructing users to select the center of a hotspot. Although this does not prevent ambiguities, at least for rather spherical lesions, the probability that they are revealed around their midsection is increased.

In an early work of Rieder et al. [402], the authors presented a 3D visualization technique for various MR sequences to support the assessment of multiple instrument insertion paths during neurosurgical operation planning (see Fig. 3.10b). During preprocessing, a blood vessel, brain tissue, and tumor tissue masks are acquired. Thus, the authors combine a POI and ROI approach by letting users select a pixel or voxel that belongs to the targeted pathology. Since the tumor tissue segmentation mask can contain non-tumor tissue voxels, a spherical ROI is defined around the selection to exclude voxels outside a certain radius.[8] In Figure 3.10b, the color-coded *cloud* represents the ROI-filtered tumor tissue, which is embedded in the DV-rendered head and brain tissue. High visibility of the tumor is achieved by employing a cutting plane, while the blood vessels are preserved. This is done to maintain some spatial context and to convey which (big) blood vessels are in close proximity to the tumor, since they may not be harmed during operations.

POI VS. SOI. Structure of Interest (SOI) techniques can be regarded as an extension of POI techniques. For POI techniques, subsequent processing and visualization steps are centered around a selected point or coordinate. In contrast, for SOI techniques, a structure is selected or *created*, e. g. in a pre-labeled dataset and via segmentation, respectively. Thus, the aforementioned method of Rieder et al. [402] could also be categorized as a SOI technique, since visibility is maximized for a certain structure, i. e. a tumor.

SOI TECHNIQUES. Correa et al. [93] introduced visibility-driven TFs that use visibility histograms to conclude about how visible certain structures are (see Fig. 3.10c). Generally, manually adjusting TFs is a tedious process and although TFs can be re-used for various CT scans, this is typically not applicable in other modalities. Since the authors employ DVR for CT images, here, *structures* are defined as HU ranges that correspond with certain anatomical structures that have similar radiodensities, for example bones. Basically, their

[8] Since the radius is applied along all three main axes, this can also be called a VOI.

method derives user interest by interpreting manually defined TFs, i. e. HU ranges with high user-defined opacities are deemed interesting. In Figure 3.10c, a user defined that skin and flesh tissue is *somewhat* interesting (medium opacity), while bone tissue is very interesting (high opacity). However, bones are virtually completely occluded, which can be evaluated by accumulating the opacities of the "*domain values*" (here: HUs) along DVR rays [93]. After accumulation, histogram bins represent their corresponding HU's visibility. Subsequently, while preserving the general shape of the user-defined TF, the opacities of "*strong occluders*" are iteratively decreased until the visibility of interesting structures reaches a certain threshold [93] (cf. Fig. 3.12).

Theoretically, such an approach could be applied to multimodal images, too. However, first, the image intensity intervals of all image sources would have to be rescaled into the same range. Secondly, the visibility histogram might have to be extended to hold *semantical* knowledge about the image sources, because, for example, PET hotspots and bony tissue might get scaled into the same value range, although bones often have to be visually omitted to reveal metabolic hotspots.

Another SOI technique was presented by Rieder et al. [401], which can be regarded as an extension of their previously described work [402] (see Fig. 3.10d). Here, similar to the datasets that were made available for the *IEEE Visualization Contest 2010*, the authors fuse MR, fMR and Diffusion Tensor images.[9] In comparison, the results of both works are very similar with two key differences. First, instead of blood vessels, reconstructed nerve fiber bundles are used, which are key features during diagnosis and treatment planning, e. g. to decide on the general feasibility of a surgical treatment. Secondly, a cylindrical cut-away and/or magic lens tool is used to erase skull and brain tissue to reveal the targeted tumor. Thus, physicians can iteratively evaluate various entry points and pathways during treatment planning [187] (cf. Ch. 5). However, w. r. t. the cut-away cylinder's radius, only a limited number of potential pathways can be assessed at a time.

3.7.2 SLICES AND FEATURES OF INTEREST

Here, slices and features of interest techniques for multimodal image data are described.

SOI TECHNIQUES. Slice of Interest (SOI) techniques require users to define particularly interesting slices, e. g. where they suspect a small hotspot. Jung et al. [225] combine a PET SOI with opacity-aggregated CT slices (see Fig. 3.11a). Similar to Tietjen et al. [473] who introduced near focus objects, and thus, extended the *conventional* F+C binarization, Jung et al. introduced a method that superimposes PET images with CT images. The basic idea is to enhance physiological images via morphological landmarks, such as the skin's outline, bones or lung parenchyma, to improve orientation during assessments, However, the main challenge is not to occlude important image regions in the process. First, users define a particularly interesting slice and a certain number of CT images are aggregated and superimposed. Given that both image sources are registered with each other, this number is calculated by an iterative composition of CT images *in front of* the PET SOI until a visibility threshold is reached, e. g. until the visual contribution of both image

[9] http://sciviscontest.ieeevis.org/2010/, last accessed September 12, 2019

sources roughly equals 50 %. Visually, this results in the CT and PET images having the *correct order*. Assuming that users can manually define the CT image TF, the iteration process may terminate very early, i. e. when "*strong occluders*" were defined [93]. This would result in only little or no morphological enhancement.

Later, the authors added a distance-based weighting to the CT image aggregation, i. e. CT images that are further away from the user-defined SOI get their visual contribution decreased [223] (see Fig. 3.11b). Furthermore, they also discuss how multiple hotspots can be handled. If only one *hot* PET image area is present, the CT images can *just* be added until the visibility threshold is reached. However, if multiple "*peaks*" are present, more subtle "*peaks*" might become fully occluded [223].[10] The authors suggest that such regions could be merged if they are in close proximity. Alternatively, the SOI could be enhanced by adding multiple ROIs around the various hotspots and apply a ROI-dependent CT image superimposition. However, this could result in abrupt visual transitions.

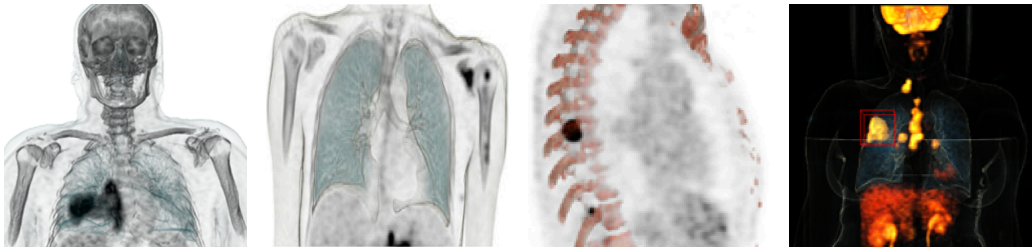

(a) CT in PET **(b)** CT in PET **(c)** CT in PET **(d)** CT in PET

Figure 3.11: Jung et al. [223, 225] utilized aggregated CT images to superimpose PET images via user interaction. Here, users select an interesting PET slice, and subsequently, various CT images *in front* of it are aggregated via opacity-based compositing. The slice's visibility is constantly re-evaluated and if a certain visibility threshold is undershot, the CT image aggregation is stopped. Later, the authors added depth-dependent image weighting, i. e. with an increasing distance between the Structure or Slice of Interest (SOI) and currently processed CT image the visual contribution of *this* CT image is decreased. In a more recent work, they generalized their approach by introducing Features of Interest (FOIs) **(c–d)**. Basically, users select a pixel, and thus, a ray is defined that is shot through a DVR. With respect to image intensities or other image/volume features, "*domain values*", e. g. HUs, are categorized based on their saliency [419, 527]. Here, a PET SOI was enhanced by superimposing it with a color-coded spine **(c)**. Additionally, the method can also be applied to PET/CT image sources *simultaneously* by applying the method to both image stacks separately with a subsequent visibility-driven ROI-based fusion to ensure PET hotspot visibility [222] (cf. Fig. 3.12) **(d)**.

[10] More prominent (darker) hotspots can *endure* more superimposition until occluded, which results in a clearer morphological context being introduced.

FOI TECHNIQUE. Recently, Jung et al. [226] generalized their previous work (see Figs. 3.11c and 3.11d). The concept of FOIs is rather abstract. They can be virtually anything, e. g. "*a tumour in a medical image volume or a tornado in a weather simulation volume*", which makes their method applicable to any domain [226]. They present their results w. r. t. mono- and multimodal medical image data, but also w. r. t. the well-known *Engine Block* volume dataset. The authors employ "*contextual salience information [...] where 'contextual saliency' is a biologically inspired attribute that aids the identification of features what the human visual system considers important*" [226] (cf. Ruiz et al. [419]). Basically, multiple layers with more or less detailed (granulated) saliency information are used.[11] The most simple multi-layer system would consist of two layers, where one layer represents foreground information (important), while the other one represents background information (not important). This very abstract approach makes their method very versatile w. r. t. its applicability to various domains, since these layers can be used to define various FOIs. With respect to the domain, for example, a FOI can be "*a tumour in a medical image volume or a tornado in a weather simulation volume*" [226].

FOI WORKFLOW. From a workflow perspective, users select a pixel, and thus, a ray is defined that is shot through a DVR. With respect to the image intensities along the ray, traversed voxels are classified into various saliency categories, i. e. they are assigned individual *saliency values*. In the most simple case, the "*domain values*" (image intensities) are used for classification, but more complex features, e. g. gradient magnitudes w. r. t. adjacent voxels, can also be utilized [93]. Subsequently, for each traversed voxel, the voxel neighborhood is evaluated w. r. t. its *homogeneity*, i. e. voxels within a homogeneous volume region are assigned different values than in heterogeneous regions. Afterwards, this saliency ray profile is repeatedly smoothed by assigning the same saliency value to adjacent voxels if they are similar, i. e. if their absolute difference falls below a certain threshold. This results in a saliency profile with a limited number of classes and since each class corresponds with, for example, certain "*domain values*", a DVR TF is defined with small "*tent-shaped*" peaks at a class [226] (cf. Fig. 3.12a). Henceforth, a class is called a feature, and thus, a FOI visualization technique. In other words, the technique categorizes voxel neighborhoods along a user-defined DVR ray w. r. t., for example, "*domain value*" homogeneity. For rendering, the *ColorBrewer* is used to create and apply a color scheme [178].[12] Although not specifically mentioned, it can be assumed that a *qualitative* (categorical) color scheme was chosen to visually emphasize multiple FOI categories.

FOIS FOR CT AND PET/CT. This technique can be applied to mono- and multimodal (medical) image data. In Figure 3.11c, the technique was applied to a CT image stack, which is then used to superimpose a PET image. Here, w. r. t. the user-defined ray, the spine (brown) was defined as a feature. In *true* multimodal applications, the method works similar. Basically, the method is applied to both image sources separately, and prior to the final DVR presentation sufficient PET hotspot visibility is achieved by applying a visibility-driven and ROI-based method to decrease CT image contribution [222] (see Fig.3.11d). The respective method will be explained in the next section. As depicted, various PET

[11] Visually similar to *Disparity Maps* for stereo vision image processing.
[12] http://colorbrewer2.org/, last accessed September 12, 2019

hotspots can be related to their morphological origins, while their (*hot*) color-coding enables a rough qualitative assessment due to varying PET image intensities.

The authors do not discuss differences when two *adjacent* rays are defined. On the one hand, adjacent rays should result in similar saliency profiles, since domain intensities along *both rays* should be similar. On the other hand, in extreme cases, e. g. when two rays are traversed just behind the spine with only one ray hitting bone tissue, the final presentations may differ substantially, since bones will most likely be defined as a feature (cf. Fig. 3.11d). However, the authors assume that users interact interest-driven, i. e. they will select pixels, and thus shoot rays, through the middle of interesting features (objects).

3.7.3 REGIONS AND VOLUMES OF INTEREST

Here, regions and volumes of interest techniques for multimodal image data are described.

ROI TECHNIQUE. Jung et al. [222] introduced a method to enhance visbility of PET hotspots in combined PET/CT DVR (see Figs. 3.12a and 3.12b).[13] In contrast to their later work, this method focuses on locally increasing hotspot visibility (cf. Fig.3.11). During ray traversal, the opacities in the CT and PET volumes are accumulated w. r. t. their intensities, which are rescaled into the same value range, e. g. $[0, 4095]$. Therefore, when the PET visibility histograms are evaluated, the PET image intensities in the selected ROI are compared to the opacities in the CT DVR TF. If "*strong occluders*" [93], typically bones, are present, their global visibility is iteratively decreased until the visual contribution of the selected PET hotspot reaches a certain percentage.

MULTI-ROI VISIBILITY. Using this method, potentially, multiple PET hotspots can be processed at once. However, with an increasing number of hotspots, it becomes more challenging to find an *optimal* solution to maximize the visibility of all hotspots, since the overall tissue variability of *occluders* eventually becomes too large. The most straightforward solution would be to just reduce all opacities in the CT TF but this would also decrease the morphological context for the PET images. In other words, the visibility of multiple hotspots can only be sufficiently improved simultaneously if the opacities of their *occluders* lie in the same range, e. g. skin and lung tissue versus skin, lung and bone tissue.

ROI OR VOI? The authors state that their method is ROI-based, i. e. a two-dimensional entity of interest. However, depictions in this and an earlier work suggest that really VOIs were used [224]. This would make sense, since the visibility of hotspots not only depends on the surrounding tissue but also on the scene camera's position. Thus, using only ROIs would severely limit the versatility of the presented method w. r. t. a free and interactive exploration. Presumably, the term ROI is chosen since a VOI looses its third dimension due to projection during the final presentation.

Zheng et al. [526] present a similar method using visibility histograms (see Fig. 3.12c). They also define ROIs (VOIs) around PET hotspots and evaluate their visibility w. r. t. occluding tissue information from CT. In contrast to the work of Jung et al. [222], their

[13] This was done using the *Voreen Volume Rendering Library*: `http://www.voreen.org/`, last accessed September 13, 2019

method is more versatile in regard of locally balancing the degree of morphological context. If more morphology is preserved, PET hotspot visibility might become compromised, but relating anatomy and function is simplified. In contrast, morphology can also be *punched out* in view direction, which omits spatial context but increases the hotspot's assessability.

3.8 BEYOND COMBINATIONS OF TWO IMAGE SOURCES

In this section, aspects to visualize more than two image sources are described.

DATA AVAILABILITY. Previously, various visualization techniques for mono- and multimodal medical images were presented. However, when multiple image sources were used, their number rarely exceeded two. One reason is that in clinical practice some anatomical

(a) PET in CT **(b)** PET in CT **(c)** PET in CT

Figure 3.12: ROI- and VOI-based methods address the challenge of increasing visibility of hotspots locally (cf. Fig. 3.11). In Subfigure **(a)**, the PET hotspot in the upper right lung is barely visible due to lung parenchyma. Here, also visibility histograms are used. During ray traversal, the opacities of the CT and PET images are accumulated w. r. t. their intensities. Subsequently, both image intensity histograms get rescaled into the same value range, and thus, opacities of "*strong occluders*" in CT can be specifically decreased [93]. The process is depicted in the Subfigures **(a)** and **(b)**: Since lung parenchyma occludes the selected PET ROI, the opacities of the corresponding HUs are lowered. Consequently, the visibility of the selected hotspot is increased. The green bars represent the visibility histogram, which is limited to one ROI here. Typically, there are more color-coded bars that represent various ROIs in the DVR above. Zheng et al. [526] also employ visibility histograms to increase PET hotspot visibility **(c)**. In contrast, their method is more versatile when balancing the degree of morphological context locally. For example, morphology can be fully *punched out* in view direction. This omits spatial context information, but increases the hotspot's assessability.

structures are not scanned with more than two modalities. For example, due to heavy breathing motion artifacts, MR imaging of the lung is challenging [27]. In contrast, PET/CT can be regarded as standard procedure to diagnose and *treat* lung cancer [119, 364, 282]. Thus, since no data exists, no tri-modal visualization techniques can exist. However, there exist image databases, e. g. the *Lung Image Database Consortium Image Collection* for nodules

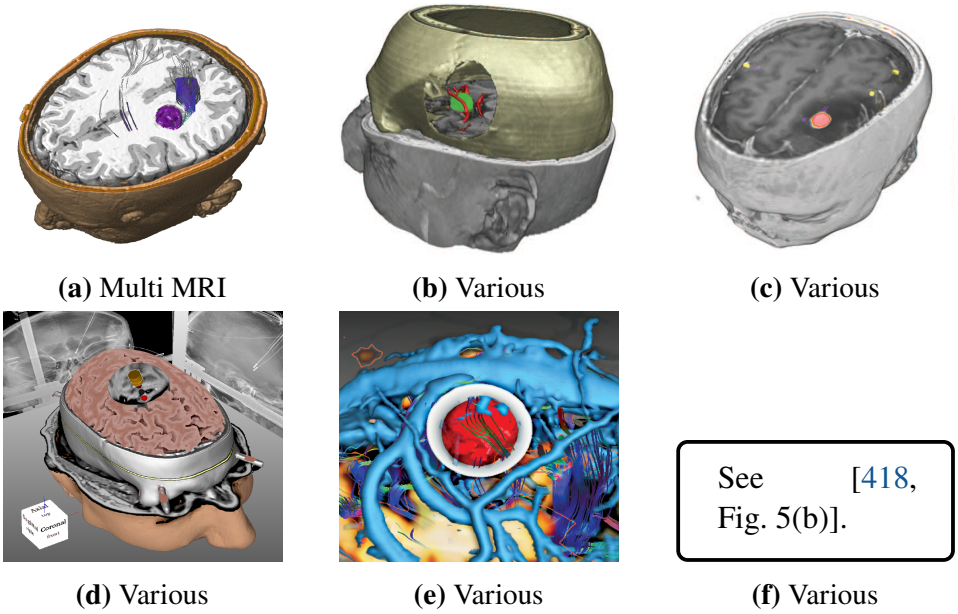

(a) Multi MRI **(b)** Various **(c)** Various

(d) Various **(e)** Various **(f)** Various

Figure 3.13: The multi-MRI visualization approach of Rieder et al. [401] was already explained above and the respective subfigure only presents their result from another perspective (cf. Fig. 3.10d) **(a)**. Beyer et al. [47] presented a volume bricking (chunking, streaming) method that only loads texture "*bricks*" currently required in the presentation **(b–c)**. They employ a multi-layer cut-away layout to subsequently strip morphology until key features, e. g. tumors, are revealed. Employing metabolic (red in **(c)**) and functional (yellow in **(c)**) hotspots enables physicians, if clinically feasible, to take *surgical detours*, e. g. to cut out and evaluate suspicious tissue via on-site histological testing. Bock et al. [59] also employed a layered cut-off approach, but additionally enhance spatial contexts via color- and depth-coded ribbons (yellow on skull) and intra-operative radiographies that enable physicians to evaluate instrument orientations during treatments **(d)**. For the IEEE Visualization contest in 2010, Diepenbrock and Röttger et al. [105, 418] presented their methods to assist neurosurgical keyhole interventions via multimodal CT, (f)MRI, and DTI rendering. While Diepenbrock et al. [105] *simulate* keyhole surgeries by offering users "*probe views*" **(e)**, Röttger et al. [418] present a more general approach with a spherical cut-away tool to omit morphology **(f)**.

in CT images, and thus, it can be hypothesized that, for certain organs, such databases will also exist for multimodal image sources in the future [19].[14] Another reason is that even if multimodal images can be acquired, e. g. for liver or brain cancer diagnostics, subsequent image registration is required, which typically is not trivial.

TRI-MODAL BRAIN IMAGING. In these regards, the brain and its adjacent structures can be treated more straightforwardly. The head (and neck) area consists of various types of tissue, which results in many imaging modalities being applicable. Moreover, since the brain is encompassed by solid bony tissue, there is virtually no organ movement, which benefits image registration and/or fusion [112, 212]. There exist some *free* multimodal brain datasets, e. g. the *CEREBRIX* dataset from the OsiriX Digital Imaging and Communications in Medicine (DICOM) Image Library or the datasets from the *IEEE Visualization Contest 2010* website.[15] Overall, tri-modal image acquisition (and above) is still done very selectively, while the clinical research agenda appears to be focused on whether PET/MRI or CT/MR imaging is more suitable for clinical application *X* [258, 449, 458].

MAIN CHALLENGES. Disregarding the specific application and given that a multitude of image data is available, the key challenge is to fuse multiple context (target) and multiple focus (source), potentially complementary (MRI and CT), image sources with each other. On the one hand, the amount of data might make a refined memory management necessary. Modern off-the-shelf hardware might address this problem during development, but time-oriented image sources or multi-patient studies might still be challenging to handle. However, it is not guaranteed that clinical hardware is on par. On the other hand, w. r. t. the final presentation, all information necessary to support data exploration and/or assessment should be presented without long loading and processing times, while the results themselves should not be visually cluttered.

Over the course of the previous sections, some tri-modal visualization techniques were already introduced, i. e. the multi cut-away approach of Kirmizibayrak et al. or the multi MRI visualization techniques of Rieder et al. [244, 402, 401]. Figure 3.13a depicts another image from the earliest work of Rieder et al. [401] (cf. Fig. 3.10d). Here, head information is cut away just beneath the tumor. Although no spatial context is provided towards the head's apex, the nerve fiber bundle subset that traverses through the tumor is preserved. Thus, physicians can examine which brain functions might be affected by an operation, which, for example, enables them to conclude about potential patient health implications.

VOLUME BRICKING. Arguably, one of the most iconic works when it comes to combining and visualizing multiple image sources is the work of Beyer et al. [47] (see Figs. 3.13b and 3.13c). The authors combine CT, MR, DSA, PET, and fMR images to support neurosurgical interventions, e. g. so called keyhole surgeries, for which only a small portion of the skull's surface is opened to insert instruments. From a technical point of view, the main contribution is a volume bricking (chunking, streaming) approach, i. e. instead of

[14] https://wiki.cancerimagingarchive.net/display/Public/LIDC-IDRI, last accessed September 13, 2019

[15] https://www.osirix-viewer.com/resources/dicom-image-library/, last accessed September 13, 2019

uploading all images on the GPU prior to rendering, only currently required DVR contents are put on the GPU. This was done, since, performance- and memory-wise, the GPUs in 2007 were much weaker than today, and thus, the technique could "*circumvent GPU memory constraints*" [47].[16] In other words, w. r. t. the amount of user interaction, e. g. volume peeling (clipping) the main computational effort is data streaming between CPU and GPU (memory). Furthermore, complete preprocessing, such as key feature segmentation, e. g. blood vessels and tumor tissue, or volume registration, can be achieved in about $10\,min$ to $20\,min$, which is reasonable given the clinical application and hardware contexts.

MULTI-LAYER CUT-AWAY LAYOUT. Similar results were presented by Bock et al. [59] (see Fig. 3.13d). High visibility of key features, e. g. blood vessels, tumor tissue, functional and physiological hotspots, is achieved by balancing spatial context. Beyer and Bock et al. [47, 59] utilize multi-layer cut-away layouts to present context objects, e. g., from bottom to top, by alternating between image sources, e. g. skin (MRI), skull (CT) and brain (MRI). Modality-individual cutting can be introduced, e. g. cutting MR images from the front and CT images from the top, to achieve high method versatility for various clinical scenarios, e. g. biopsies, neurosurgical interventions and operations, or deep brain stimulations [187].

The cutting process could be automated, e. g. by cutting the innermost modality just under the focus object and applying an equidistant layering below. However, this might be very operation-specific, e. g. if the operation instrument's entry angles have to be considered and certain pathways, for example *from above*, would be more feasible (cf. Ch. 5). Similarly, the work of Bock et al. [59] preserves the innermost modality to preserve brain morphology, while other authors describe how more refined cut-away tools (cylinders) can be utilized [401]. Furthermore, their method employs colored and depth-darkened ribbons as depth cues and intra-operatively acquired X-ray images that depict the inserted electrodes to convey a spatial overview [306].

THE IEEE VISUALIZATION CONTEST 2010. Here, two submissions for the IEEE visualization contest are presented in more detail, namely the methods of Diepenbrock and Röttger et al. [105, 418] (see Figs. 3.13e and 3.13f). The task was to combine CT and various MRI sequences, e. g. T_1, T_2, DTI or fMRI, to create visualization systems to assist multimodal brain diagnostics and the planning of neurosurgical operations. The key questions were "*What is the relation between the [brain] lesion, functional areas and white matter tracts?*" and "*How can the [brain] lesion be accessed most safely?*".

From a cut-away tool perspective, Diepenbrock et al. [105] utilize cylindrically shaped and Röttger et al. [418] utilize spherically shaped cut-away tools. On the one hand, this makes the method of Diepenbrock et al. [105] more *straightforward*, i. e. keyhole perspectives can be *simulated* via "*probe views*", whereas the approach of Röttger et al. is more general. The inspiration of "*probe views*" might have been taken from Beyer et al. [47], who described a "*flythrough navigation*" method that lets the scene camera fly through the cut-away morphology to the revealed key features. Furthermore, Diepenbrock et al. employ

[16] The authors presumably used a GPU with $512\,MiB$ memory, while most off-the-shelf cards only had half as much. However, even one dataset can be some hundreds of Megabyte large. https://www.overclockersclub.com/guides/roundup_graphics_2007/, last accessed September 14, 2019

Lift Charts for fMR images to highlight slices with functionality peaks [474] (cf. Ch. 4). On the other hand, Röttger et al. employ clustered DTI fiber bundles, which simplifies 3D assessments. In contrast, the results of Diepenbrock et al. are rather cluttered.

Both approaches have a very illustrative appeal to them. For more *realistic* volume rendering techniques that use more complex illumination models and multimodal (medical) images, see the works of Sunden et al. [464, 465].

MEMORY MANAGEMENT FOR IVR. IVR requires surfaces that are usually acquired via segmentation algorithms. Very often, the segmentation results are given in binary images, e. g. 0 encodes background and 1 encodes segmented objects. Subsequently, these masks are converted into surface meshes, e. g. via the *Marching Cubes* algorithm [299]. However, there also exist methods that result in a polygonal representation [108].

Here, it is assumed that segmentation results (masks) are represented as binary images. A straightforward approach is to encode multiple segmentation masks via bitmasks, i. e. each structure gets a certain bit flag and the resulting 0-and-1 chain encodes a voxel's tissue composition, e. g. only lung parenchyma (01), only blood vessel, e. g. aorta (10), or blood vessels in the lung (11). In the same way, OpenGL (Khronos Group, Oregon, United States) handles method option passes. Although this results in fast processing of segmentation masks, the maximum number is limited by the system's manageable bitmask size, e. g. between 32 and 64 options, which can hinder portability to older or smaller systems.

To address this aspect, Mühler et al. [347] introduced *Multicoded Segmentation Masks* (MCSM) that encode segmentation mask compositions via unique tokens. For example, lung parenchyma (1), blood vessels (2), and a combination (3) would be encoded differently. Consequently, if segmentation masks are added, only new tokens have to be added to the respective LUT. On the one hand, the upper definition limit of, for example, 2^{64} unique MCSM tokens might never be reached, whereas bitmasks are limited to, for example, 64 bit chain tokens. On the other hand, a LUT has to be provided to decode MCSM tokens into segmented structures.

3.9 MULTIMODAL VISUALIZATIONS FOR TEMPORAL MEDICAL IMAGES

In this last section, visualization techniques for temporal multimodal images will be presented. However, since no 4D image data was used for this thesis, this is done briefly.

One major application for 4D images is to measure organ movement to assist subsequent treatment, e. g. via radiation therapy [429]. With respect to modality-specific image acquisition times, spatial mismatches ranging from $2\,cm$ to $4.5\,cm$ can occur in the lung [81, 149, 169, 308]. Handels et al. [169] researched lung lesion motion in 4D CT data with a temporal resolution of 10 to 14 time steps per breathing cycle, i. e. between full inhalation and full exhalation (see Figs. 3.14a and 3.14b). For example, the authors present a color-coded *map* that depicts the spatial probability of a segmented tumor w. r. t. all time steps. This information can be used for radiation therapy planning, e. g. to adjust the orientation of radiation sources w. r. t. breathing motion. However, only CT images were used.

Schlachter at al. [428] presented a technique for 4D PET/CT images (see Fig. 3.14c). The combination with PET images enables a visualization how metabolic hotspots are displaced during breathing. Based on this, the authors include radiation dose information to support radiation therapy planning. With respect to the final presentation, the authors use a slider-based approach to enable users to scroll through multiple time steps. Furthermore, the images are presented in DVR and clipping planes are used to *open* surrounding morphology to assess lesion in detail. Their system is also able to depict structure-related safety margins, e. g. around the trachea and bronchi, to visualize which non-targeted (risk) structures might also become irradiated during treatment. In this context, employing safety margins is a key requirement. For more detailed explanations on "*Visual Computing in Radiation Therapy Planning*", see the survey from Schlachter et al. [429].

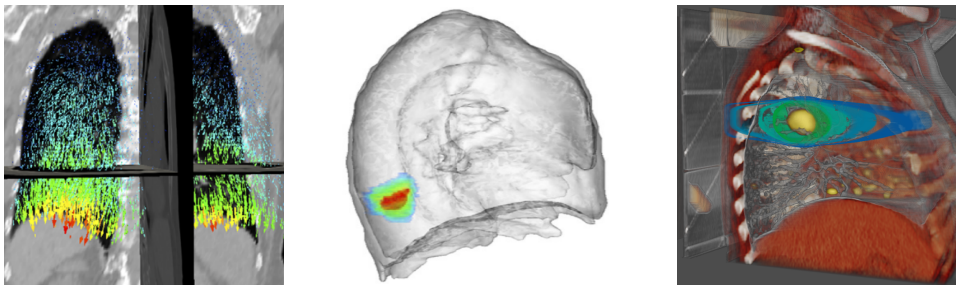

(a) 4D CT **(b)** 4D CT **(c)** 4D PET and CT

Figure 3.14: Employing visualization techniques for 4D image data enables physicians to assess lesion and/or tumor displacement. To assist radiation therapy planning, Handels et al. [169] present how lung lesions are displaced during breathing **(a–b)**. In the first subfigure, a "*3D motion field*" is depicted [169]. The color-coding represents the degree of displacement, i. e. red arrows indicate that lesions are displaced by $2\,cm$ and more. In Subfigure **(b)**, the probability of a lesion's position is color-coded w. r. t. manually segmented tumor tissue in 4D CT data. In contrast, *stronger* color-coding denotes an estimation where the lung tumor will "*appear*" most likely [169]. In a more recent work, Schlachter et al. [428] present a 4D PET/CT visualization technique **(c)**. With both image volumes being time-oriented, users can assess morphological and physiological displacements. Furthermore, the authors include radiation dose and radiation zone information to support radiation therapy planning [429]. Here, a clipping plane is used to cut away morphology between the scene camera and targeted lesion to enhance its visibility.

3.10 SUMMARY

In this chapter, various visualization techniques for multimodal medical images were presented. For techniques that do not employ multimodal image sources, possible extensions were presented. It was highlighted that a categorization of visualization techniques is challenging, since many techniques are combinations of others. Furthermore, basic image registration methods were described briefly.

In the next chapters, our methods and approaches will be presented. In Chapter 4, a floor map technique will be presented, which can be considered a ghosting and structure of interest technique, since OITs are employed, while certain features, e. g. a structure's shape, can be preserved [33]. Subsequently, on-mesh (surface-based) and in-volume approaches are combined that aim to support pathway definition during needle-based interventions (see Ch. 5; CT+MRI). This technique can be regarded as a combination of ghosting, cut-away, and F+C techniques, since, for example, volume-rendered bone tissue is cut away to *simulate* pathways for operation instruments [105, 401, 418]. In the 6th chapter, related to F+C and ghosting techniques, an illustrative visualization approach is presented that combines transparencies, boundary enhancements and silhouettes to support the perception of lung lesions (PET+CT). In the last chapter, a processing pipeline to create visualization-supported clinical reports is presented. Here, PET and CT images are used to create stylized lymph node maps for lung cancer staging [390].

4 MAP-BASED VISUALIZATIONS FOR GROSS ANATOMY

Maps are typically used for orientation and navigation tasks, however, they can also be works of art. When comparing individuals, their senses of direction can vastly differ. However, given the right presentation and interaction facilities, it can be argued that virtually anyone can use maps. One reason is that maps purposefully abstract (simplify) certain features, e. g., w. r. t. the map's scale (*zoom*), only the general shapes of streets are preserved, while smaller streets are completely omitted [501]. Another reason is that *we* mentally encode spatial environments in our *brains* [162] (cf. Sec. 4.3). In other words, *we* compile perceived and processed information about spatial relationships into so-called *mental* and/or *cognitive maps*.

In this chapter, a floor map technique will be presented that transforms segmented and/or labeled medical images into building-like presentations. Here, transparencies are combined with structure-of-interest options, e. g. to reveal and preserve shape features of interesting structures, respectively. Furthermore, interaction facilities are provided to engage users to simultaneously explore 3D floor maps and original 2D images. The technique was evaluated by three trained anatomy experts, i. e. physicians and anatomy teachers, to ponder about the feasibility of floor maps in a clinical context. The introduced degree of geometric abstraction is considerable, which, e. g., results in distorted spatial relationships between adjacent anatomical structures (rooms). Thus, applications in an educational context are currently more suitable than, e. g., diagnostics or radiation therapy planning. In this context, anatomy education is briefly discussed in Section 4.1.

In this chapter, map visualization techniques will be presented and discussed. This is done w. r. t. the concepts of generalization and abstraction (Sec. 4.2), map cognition (Sec. 4.3), color-coding of maps and medical images (Sec. 4.4), similar research questions of the map and medical image visualization research communities and the utilization of maps for medical image data (Sec. 4.5). Moreover, 3D indoor maps will also be discussed, since floor maps also have a 3D layout (Sec. 4.6). Subsequently, the proposed floor map technique will be presented, for example w. r. t. design choices and their implementation (Sec. 4.7). Finally, this chapter will be concluded with a short summarization (Sec. 4.8).

This chapter is based on:

[326] **Merten, N.**, Saalfeld, S., and Preim, B. "Floor Map Visualizations of Medical Volume Data." In: *Journal of WSCG* 27 (1) (2019), pp. 49–58

Maps were also utilized in some of our other works [321, 322, 320], but since they are more application-specific, they will be presented in their respective Chapters 5 and 7. However, the general remarks on maps within this chapter also apply to them.

4.1 ANATOMY EDUCATION

From a student's perspective, anatomy education is a combination of attending lectures and cadaver dissection classes, and studying with text books, so-called atlases [383]. In addition to explanatory texts, such atlases are very graphic, e. g. by showing more or less detailed illustrations that depict and highlight certain structures in their anatomical context, for example in dedicated learning units. Such illustrations are typically developed by collaborating physicians and illustrators. Typically, atlases are printed books (cf. [314, 424]), but since the early 1990s, an increased interest in digital solutions arose, e. g. via web-based applications [196] (cf. [460]). There exist multi-viewer applications that show medical photographs and/or radiological images side-by-side with, for example, IVRs of anatomical models to support the understanding of spatial relationships. On the one hand, this highlights the importance of coupling 3D presentations and *real* images. On the other hand, and in contrast to text books, digital atlases make it possible to employ refined exploration facilities that can support the learning process [451].

The proposed floor map method is rather suited for "*anatomical education and report generation, since, in the beginning, understanding spatial relationships between anatomical structures is more important than learning geometric details*" [326]. This, for example, is done by floor maps by highlighting areas with high anatomical variability. For more details, see the work of Preim and Saalfeld [383].

4.2 THE CONCEPTS OF GENERALIZATION AND ABSTRACTION

Many visualization techniques find their origins in cartography and semiology. Mapmakers began very early to think about combining spatial and other types of information, for example trading routes and/or political boundaries. Early maps were very graphic in the sense of icon-heavy and "*they ultimately express the many ways we attempt to understand the world*" [175, 176, 177]. Maps are their own graphical language that "*tell us much more than merely how to get from here to there*" [175]. Typically, maps are composed of N many *layers*. The basic layer, the so-called *base map*, offers the topographical context, e. g. via streets, rivers and mountains, while icons and other elements are layered *on top*, which makes them *theme maps*. Such theme maps can further enhance the provided context, but they can also be used as key features, for example, by depicting certain statistics POIs [252]. Two-dimensional PET/CT presentations are very similar in this aspect, since the CT images offer a morphological frame for physiological information (cf. Fig. 2.15).

PURPOSEFUL LIES. As Harley and Woodward discuss, maps are simple and also not simple. On the one hand, "*children can derive meaning from maps (and indeed draw them) from an early age*" while having "*an "extraordinary authority," even when they are in error*" [175]. On the other hand, "*however simple maps may appear at first sight, on analysis they are almost certainly less than straightforward*" while they "*are never completely translatable*" [175]. In this regard, Mark Monmonier wrote that "*[n]ot only is it easy to lie with maps, it's essential. To portray meaningful relationships for a complex, three-dimensional world on a flat sheet of paper or a video screen, a map must distort reality.*" [342]. However, such "*white lies*" or "*blunders*" (mistakes) can heavily influence

the cognition of observers [342]. Therefore, with respect to medical visualizations, certain processing steps should be applied with certain care, e. g. mesh smoothing prior to IVR, since they can distort *reality*, e. g. distances between anatomical structures.

MAP GENERALIZATION. Map depictions employ means of simplifications to convey spatial relationships [208]. This process is called *map generalization*. One well-known method is the Ramer-Douglas-Peucker [109, 389] algorithm to simplify polygonal chains, e. g. roads, rivers or state borders. This is done by reducing the number of control points along lines. An example is depicted in Figure 4.1, where the algorithm was used to simplify a pulmonary blood vessel tree. Other examples are the *merging* or *amalgamation* of lines and areas w. r. t. the map's scale, for example, if users interact (zoom) in a digital setup [252, 442]. Moreover, some elements can be fully omitted, such as smaller cities. On static maps, i. e. maps that do not *directly* allow for observer (user) interaction, such simplifications are absolute. However, dynamic maps can employ interactive and/or automatic generalization. For example, GPS devices can add or remove details, such as small streets, w. r. t. vehicle speed. For more details, see the work of Kraak, Monmonier, and Shea [252, 342, 442].

SIGNS, SYMBOLS AND GLYPHS. Maps are often accompanied by small stylized icons, namely symbols, which can depict certain POIs or other map elements. In contrast, in the medical visualization domain, such elements are rather called glyphs (cf. Sec. 4.5). It is challenging to design *good* symbols and/or glyphs, i. e. that are *directly* understood by a broad audience independent from their cultural origin, age, sex and other aspects. In the 1920s and 1930s, Otto Neurath and colleagues worked on a graphical "*international language*", namely the *International System Of Typographic Picture Education* (ISOTYPE) [359]. Originally, this system was aimed to educate workers by means of strong simplifications, e. g. by using only three *colors*, namely red, black and white. However, Neurath also incorporated his ideas into *Flow Map*-like presentations. Furthermore, he wrote that "*[t]he signs have to be clear in themselves, without help of words as far as possible*" [359]. Later, Gerd Arntz, who worked under Neurath, extended his work, for example, by employing a more naturalistic style and an overall larger color palette [17]. Especially their way of thinking to design symbols that can convey information at a glance still has meaning today [214]. In his book "*Semiology of Graphics*", which is the study of signs and sign design, Jacques Bertin discusses how to communicate information via "*marks*"

(a) **(b)**

Figure 4.1: A pulmonary blood vessel tree before **(a)** and after application of the Ramer-Douglas-Peucker algorithm [109, 389] **(b)**. Although the differences are subtle, the right vessel tree is *simpler* w. r. t. line straightness.

and "*visual variables*" [45]. In the sense of Neurath and Arntz, marks can be put together into symbols and combinations of symbols. In combination with visual variables, such as *colors* or *shapes*, symbols and/or signs can be utilized to convey information in, for example, diagrams and maps, but also in medical image visualizations [45].

ABSTRACTION OF POINT SETS AND OBJECTS. There exist various approaches that can be utilized to abstract geometry. Among others, these are:

- Axis-Aligned Bounding Boxes (AABBs) employ the image and/or volume space's main axes. Such cuboids result in strong geometrical distortions when the corresponding objects are not already somewhat axis-aligned.
- Object-Aligned Bounding Boxes (OABBs) typically result in more faithful approximations by utilizing the objects' center and main axes.
- Bounding Spheres can be used to generate good approximations of spherically distributed point sets or round objects. For elongated structures, such as extremity bones or blood vessels, however, they are rather not suitable (cf. [422, 522]).
- Convex Hulls create rubber band-like approximations which result in good fits in convex regions and worse fits in concave regions.
- Alpha Shapes are the more general case of convex hulls since they allow to exclude holes, e. g. in tori [116]. Similar to Voronoi diagrams, this is realized by analyzing point (vertex) sets in circles around control points. Interestingly, since α can be varied, multiple alpha shapes per point and/or point set can be created, which the authors call the "*Shape Spectrum*" [116].
- Visual Hulls also result in better fits than typical object hulls, however, they require multiple view points, i. e. 3D to 2D projections [270].[1] When only one viewpoint is employed, concave objects typically cannot be reconstructed and/or identified faithfully. However, by employing multiple viewpoints, concave details can be *carved out* by analyzing intersecting projection geometry, i. e. the visual hull. The basic idea is also used in tomographic image reconstruction (cf. Sec. 2.1.1).

These approaches can be utilized to create Level of Detail (LOD) representations of objects, e. g. by iteratively simplifying object geometry w. r. t., for example, the scene camera's zoom. On the one hand, this can be done to guide user attention to important image regions, e. g. by omitting geometric details and/or colors in non-interesting areas. This is also related to *our* visual perception and cognition, since *our* visual focus is very narrow, i. e. around $1°$, while *our* visual field is a product of eye cascades [377]. Some of the previously presented techniques, especially the lens-based ones, exploit this circumstance [51]. On the other hand, related to rendering performance, switching between two or more LOD presentations can be done to increase rendering speed under certain conditions, e. g. model rotations. Here, simplifications not only increase processing speed, since less geometry has to be transformed, but, overall, *our* eyes are rather distracted by moving geometry than being able to focus on local details, i. e. potential key features.

[1] This is similar to epipolar geometry in stereo vision.

MODEL, GENERATION AND IMAGE SPACE ABSTRACTION. With respect to these to aspects, Antonio Krüger describes a three-layer abstraction model [254]:

- Model space abstraction is applied to the 3D models, i. e. prior to rendering, e. g. by merging adjacent cubes into one larger cuboid. This is related to map amalgamations that merge and/or split areas w. r. t. the map's scale.
- Generation space abstractions are applied to the rendering pipeline, e. g. to alter the shading complexity or by replacing filled geometry by wire frames.
- Image space abstractions are applied to the final rendering, e. g. by applying filtering to omit or to emphasize details, e. g. boundaries and/or silhouettes (cf. Ch. 6).

GRAPHIC-TO-TEXT ABSTRACTION. As discussed above for maps but generally independent from the actual domain, visualizations are often *not simple*, and thus, require explanatory elements, such as legends or labels. However, user interaction can heavily alter the final presentation, which should also be reflected by said legends and/or labels. For example, if map elements are no longer visible w. r. t. the base map's scale, they do not have to be listed in the respective legend anymore. The same applies to printed and digital medical image visualizations, when certain structures are omitted due to rotations (poses) and/or zoom. In this regard, Preim and Michel [463, Ch. 12] describe an architecture for template-based interactive figure captions that adapt the textual degree w. r. t. certain features. Such features can be a map's scale or scene camera's position, but also more presentation-related aspects, such as colors or transparencies. Interestingly, visual emphasis is repeated in text by, for example, highlighting medical terms via boxes, which result in concise visual and textual presentations of what users see and/or should see. As very specialized application scenarios, Pitt and Michel [463, Chs. 11 and 20] discuss how to generate *textual* representations of images for blind people, for example tactile maps.

FOUR AXES OF ABSTRACTION. In a more recent work, Viola and Isenberg define abstraction as follows: "*An abstraction is a transformation which preserves one or more*

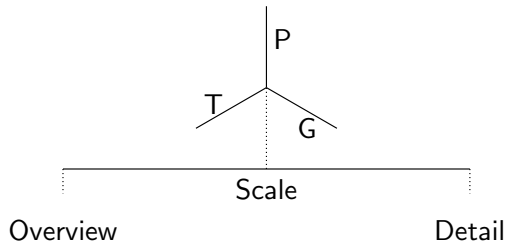

Figure 4.2: The three domains of abstraction described by Viola and Isenberg, namely **g**eometric, **p**hotometric, and **t**emporal abstraction [501]. The **scale** axis denotes how *deep-seated* the currently depicted information is. For example, visualizations of the whole human body or the globe would give **overviews**, while presentations of molecular processes or floor plans are more **detailed**.

Image was inspired by [501, Fig. 15].

key concepts and removes detail that can be attributed to natural variation, noise, or other aspects that one intentionally wants to disregard from consideration" [501]. In other words, abstraction condenses the overall amount of information, while "*key concepts*" (key features) remain purposefully preserved. The authors further state that "*importance changes [are] based on the research question, on the application domain, on the data size, on the user, on the specific situation, etc.*" [501]. As mentioned before, key features can be virtually anything, e. g. a certain anatomical structure, and w. r. t. the given application scenario, typically, they can be clearly named.

The authors propose four axes (categories) of abstraction (see Fig. 4.2):

- *Geometric abstraction* describes how shape details of objects are preserved or omitted, e. g. by approximating blood vessel geometry by cylinders [365, 522].
- *Photometric abstraction* describes the complexity of the employed illumination and shading. Techniques that apply high degrees of photometric abstraction employ very simple to no lightning propagation models, e. g. flat color shading.
- *Temporal abstraction* describes how many time-related details are preserved. For example, lung volume can be described at various time steps (low abstraction) or become simplified by, e. g., two key values that denote the minimum and maximum lung volume over one breathing circle (high abstraction).

The *scale* describes the *depth* of the currently visualized data w. r. t. its overall context. For example, a visualization of gross anatomy would be near the *overview* end of the scale axis, while visualization techniques of molecules would be near the *detail* end. Regarding maps, the same applies to presentations of the globe and indoor maps, for example.[2] For visualization techniques, there exist various positions on the scale axis for which the aforementioned abstraction characteristics can vary (cf. Sec. 4.5). For example and following Shneiderman's "*Visual Information Seeking Mantra*", the closer the scene camera gets to objects, the more geometric details are presented [163, 328, 443].

In comparison to the aforementioned three-layer abstraction model by Krüger [254], Viola and Isenberg also describe a model space (geometric axis) and generation space (photometric axis) [501]. With respect to image space abstractions, both the geometric and photometric axes are related, since certain features can be added and/or removed via post processing (cf. [438]). In contrast to the work of Preim and Michel [463, Ch. 12], textural abstractions are not addressed directly by the model of Viola and Isenberg. Although text-enriched maps are presented, for example of subway networks and their respective stations' names, implications of (interactive) legend and/or label alterations are not discussed [501]. However, temporal abstraction was not addressed by the previously discussed methods (cf. [379]). Employing the *scale*, i. e. the zoom level and/or nearness to certain objects (key features), was done by the model of Preim and Michel but not in the model of Krüger.

ABSTRACTION VS. REALISM. It is impossible to decide if realistic or abstracted depictions are *better*. On the one hand, realistic depictions, e. g. via "*life-like rendering*",

[2] Note that these are just exemplary extrema of the scale axis. For example, star maps of our galaxy and ionic crystal depictions of building material, e. g. of wood, are other potential extrema.

can benefit recognizability of, for example, anatomical structures during atlas and cadaver studies [485]. On the other hand, the amount of information provided can be overwhelming and hinder the learning process. Following the ideas of Schirra and Scholz [463, Ch. 22], "*abstraction and realism [...] are definitely not just opposite concepts, or form the end points of a more or less continuous linear scale*", since realistic depictions can be abstracted, e. g. spatial and/or depth abstraction in photographs, and vice versa, e. g. shape details of components in arrangement sketches. Furthermore, they state that the two key questions for (computational) visualizations are "*what aspects [...] have to be communicated, i.e., should be easily and clearly readable by the [...] end-user*" and "*how much of the naturalistic residue [...] has to be present in order to anchor sufficiently the [...] aspects to be originally communicated*" [463].

Interestingly, realism and/or abstraction have only little effect on memorability, while it is more important that final presentations are uncluttered [284]. However, to make (legal) decisions, e. g. for treatment decisions or during building processes, at least on demand, very detailed and realistic presentations and/or depictions, for example of original medical images or blue prints, should be made available [363] (cf. Fig. 4.17).

IMPLICATIONS FOR THIS THESIS. From image acquisition to presentation, patient anatomy is *abstracted* repeatedly. First, w. r. t. image quality and resolution, various amounts of tissue become compiled into image and/or volume elements. Then, images may become resampled and/or smoothed via attenuation correction, image registration and other preprocessing steps (cf. Sec. 2.2.1 and 3.2). Subsequently, and just as with maps, volumetric information is compiled into on-paper or on-screen representations, which can be further abstracted, for example w. r. t. geometric and photometric features [254, 463, 501]. Thus, the actually employed degrees of realism and/or abstraction are "*intent-based*" design choices to draw user attention to regions where it is needed [254]. This applies and medical image visualizations w. r. t., for example, user-defined key features (cf. Ch. 3). Some of the presented techniques depict their results as a combination of realistic and abstracted aspects, e. g. the shapes of objects are preserved while shading techniques with varying degrees of realism are used [473]. This also applies to the techniques presented in this thesis. However, overall, they rather tend to be more abstract and stylized.

4.3 THE COGNITION OF MAPS

To understand maps, it is important to understand how they are processed cognitively. Typically, maps have a purpose, i. e. to offer assistance during orientation and navigation. However, the degree of assistance can vary considerably. For example, maps can just provide a rough overview and leave the responsibilities of orientation and navigation to users. In contrast, dynamic maps, e. g. on mobile devices, can be adapted to users to offer step-by-step guidance. Consequently, dynamic maps are more convenient and can assist individuals, especially those with a rather *bad* sense of direction, to orientate themselves.

WORKING MEMORY. For orientation and navigation, a certain mental resource, namely Visuo-Spatial Working Memory (VSWM), is necessary to create so-called *mental maps*. Such *maps* can be regarded as mental representation of *our* surroundings (read below).

Zimmer et al. [529] state that the overarching mental resource, namely Working Memory (WM), is a "*cognitive component*" that "*temporarily maintains information that was either perceived but is no longer present in the environment, or that was internally generated, and it supplies a work space for transforming and manipulating elements of perception and thinking*". In other words, WM provides storage and processing facilities for already attained (spatial) knowledge and new impressions.

MENTAL MAPS. The term *mental map* was coined by Gould and White [154]. The basic concept was and is subject to many research disciplines, such as psychology, geography or neurology, and thus, the same principle is often named differently. The very first term "*cognitive map*" was introduced by Edward Tolman [478]. On the one hand, these terms are "*a convenient fiction*" [245], since they allow for a quasi-1-to-1 interpretation of real maps and *our* cognition of them. On the other hand, however, such *maps* "*are not just a set of spatial mental structures denoting relative position, they contain attributive values and meanings*" [245]. Therefore, in the context of this thesis, mental maps are regarded as a combination of spatial relationships between anatomical structures, overarching knowledge of anatomy and a given medical and/or clinical application scenario.

WORKING MEMORY CAPACITY. Roughly 60 years ago, Miller et al. [334, 335] coined the term WM, but it were Baddeley and Hitch [24] who proposed WM being a multicomponent resource, which still appears to be the most widespread theory. Zimmer et al. state that "*working memory is seen as a limited resource that constrains cognitive performances*" [529]. It still appears to be unclear how these components share and divide their Working Memory Capacity (WMC), i. e. how connected and/or separated the various processing and storage resources for visuo-spatial and phonological stimuli are [24]. Unsurprisingly, WMC depends on the complexity of visual stimuli. In *change detection tasks*, observers are presented an image with various items, e. g. letters or objects, and are then asked to name changes after the image is changed (cf. [379, 446]). For rather simple items, e. g. familiar letters, words or colors, observers can typically name around three to four changes, while for more complex objects, e. g. shaded polygons or foreign letters they can only name one or two changes correctly [11, 65, 469]. This number can be raised if objects undergo heavy change, e. g. a familiar letter is translated into a shaded polygon.

HARD-CODED BRAIN MAPS. However, spatial layouts are somewhat *hard-coded* into our brain. In 2014, the Norwegian couple May-Britt and Edvard Moser were awarded the *Nobel Prize in Physiology or Medicine* for their findings in rat brains [162]. Rats were *instructed* to chase little food pellets in small enclosures with a large "*cue card*", i. e. a fixed spatial landmark, being displayed to the rats at all times. Electrodes in the rats' entorhinal corti were used to measure brain activity. The key findings are that the rats, w. r. t. the cue card, remember their positional change and brain cells are triggered in a hexagonal grid when they come back to certain positions in their enclosures. In other words, they use a hexagonally shaped coordinate system for orientation. If the cue card is rotated around the enclosure, their brains' representation gets rotated accordingly. Although this was done in rats, it appears likely that humans also have such coordinate system brain cells. Said entorhinal cortex communicates with the hippocampus, which "*respond[s] to a*

wide variety of spatial inputs, including extrinsic landmarks" [162]. *We* know the resulting effect: *We* gradually build mental maps by subsequently connecting spatial fragments, e. g. streets and POIs. This was also discussed by Zimmer et al. [528, 529] who showed that our WM can execute navigation and orientation tasks via piecewise maps.

IMPLICATIONS FOR THIS THESIS. Exploiting this cognition-related potential was the main motivation for the floor map method presented in this chapter. The main critique of this statement would be that, in contrast to the aforementioned rats, users in front of screens are typically less involved in spatial-related tasks [162]. However, due to handheld devices, e. g., users are accustomed to the way maps depict and abstract information. In other words, medical and map visualization techniques purposefully abstract information, i. e. objects are depicted simpler than they really are. Thus, while less mental resources are necessary to interpret a presentation, more resources are available for certain tasks. This applies to a wide range of techniques and employing 3D map-based visualizations for volumetric image data might result in a favorable WM usage. However, 3D layouts typically result in occlusion artifacts, which in turn require user interactions. Although generally unfavorable, assuming that users are able to reconstruct spatial relationships from piecewise information, complex user interactions, such as rotations, should not introduce issues [529]. Therefore, and w. r. t. the proposed floor map technique, map-based visualizations are feasible for orientation and navigation tasks in medical image data.

FURTHER READING. Miller et al. [335] presented the underlying concept of working memory roughly 60 years ago. Thus, the aforementioned aspects only reflect on a very small portion of research. For example, Cowan [94] criticizes the WM model of Baddeley et al. [23, 24] w. r. t. its oversimplification in regard of a person's attention. In other words, WMC is managed differently during attentive phases. Since such discussions are out of the focus of this thesis, see the works of Chai and D'esposito et al. [74, 104].

4.4 COLOR-CODING

Colors are essential features for any visualization technique. Presumably, *color* is the first "*visual variable*" that comes into people's minds when they are asked to encode information [45]. This is also reflected by the memorability of images w. r. t. color, i. e. "*images with more hues are harder to remember*" [284]. Although this appears counterintuitive at first, i. e. very colorful presentations should be easier to remember [62], too many colors can result in visual clutter. To exploit this potential, color palettes (schemes, sets) have to be chosen with great care w. r. t. the data to be presented and the users [67]. Here, basic color-coding methods will be explained. Most of the color scales used in this thesis are inspired by the work of Cynthia Brewer et al. [67], who developed the aforementioned *ColorBrewer* online application. For more information on color perception, color harmony, color mapping, color models and their application, see the works of Itten, Fairchild, Faridul, Gramazio, Kremer, and Rhyne [122, 124, 156, 209, 253, 397].

DATA PERSPECTIVE. To create "*appropriate*" color schemes [67], the type(s) and amount of data has to be considered. In simplified terms, data can be

- *binary*, e. g. 0 or 1,
- *qualitative*, i. e. consisting of various clearly distinguishable categories (classes),
- *sequential*, i. e. a (continuous) series of values between two boundaries (extrema),
- *diverging*, i. e. sequential in opposite directions with a pivotal element in the middle

or combinations of them, i. e. so-called "*two-variable color schemes*" [67]. In this thesis, mostly, qualitative (categorical) color schemes are used that assign N-many well-distinguishable colors to anatomical structures or regions (cf. Chs. 6 and 7). With respect to risk visualizations, qualitative color schemes are employed to assist clinical decision-making (cf Ch. 5). For evaluations, most often 5-item Likert scales were used, which will be color-coded with a two-hue diverging color scale from red to blue, i. e.

For the proposed floor map method, more *natural* color schemes were chosen. On the one hand, the general idea of qualitative color scales is used, but on the other hand, more organ-specific colors are used which were taken from photographs. This was done to increase realism, i. e. to somewhat decrease the degree of *photometric abstraction* [381, 485, 502]. Since the floor map technique was developed with anatomy teaching in mind, more realistic colors decrease realism w. r. t. cadaverous tissue, since cadavers have rather limited and homogeneous colors, i. e. somewhere between yellow and brown. Real maps, e. g. on mobile devices, also balance color scale realism. For example, POIs and streets, such as gas stations, are color-coded more stylistically, e. g. yellow or white, while other elements, such as rivers or forests, are typically depicted more realistically, i. e. in various shades of blue and green. However, application-specific maps, such as forest maps, can easily exhaust the number of well-distinguishable colors, and thus, colors are often combined with other visual variables, such as texturing [45]. Therefore, the map's purpose should always be considered and color schemes should be chosen "*appropriately*" [67].

USER PERSPECTIVE. The perception of users, for example w. r. t. visual impairments, such as color perception deficiencies, may have to be considered [206]. However, respective correction methods were not employed in this thesis. Independent from such methods, it is also possible to create (user-specific) profiles with personalized color schemes that appeal to the taste of users. However, clinical disciplines that use photographic images, such as histopathology, ophthalmology or dermatology, require standardized color palettes [22, 37]. There also exist approaches to heavily abstract surgical images to help sensible individuals with affective reactions [46]. With respect to ergonomic use, pastel-like color palettes, i. e. more *soft* and *light* colors, are easier to look at, especially in dark environments, e. g. on monitors and/or in tumor boards.[3] In bright settings, however, lighter colors might loose their expressiveness and attention-drawing capabilities due to decreased contrast. In *emotional* settings, e. g. doctor-patient consultations, very vibrant colors and colors that entail cognitive connotations, such as "*red means bad*", should not be used to prevent misconceptions, which in turn might hinder understanding in patients.

[3] There is an increasing trend that software applications offer so-called *dark themes*.

4.5 MAP AND MEDICAL IMAGE VISUALIZATION TECHNIQUES

The map and medical image visualization communities have similar research questions. In this section, some approaches will be presented briefly. Furthermore and w. r. t. our floor map visualization technique, we were not the first authors to utilize map-like presentations for medical image data, and thus, such techniques will also be described briefly.

4.5.1 SIMILAR RESEARCH QUESTIONS

In this section, common research questions (and challenges) will be discussed.

NAVIGATION TASKS. We use maps for orientation ("*Where is X?*") and navigation tasks ("*How to get from Y to X?*"). Such tasks include touristic scenarios, e. g. in museums, but also emergency situations, e. g. to find escape routes in cases of fire. In medicine, navigation-related tasks, e. g., entail real and virtual endoscopy, e. g. in the colon and airways [75, 381]. Here, it is important to know where the virtual endoscope currently is and will be navigated to, e. g. by defining "*key frames*" that are processed iteratively via a "*fly-through*" [47, 381]. Disregarding the actual application, manual key frame definition can be tedious and automated methods can result in considerable time saving [60, 75, 152, 381, 471]. However, *pathways* in buildings and human tissue are very dissimilar, i. e. organic structures are rather round in a *chaotic* layout with sharp *turns* in all directions. In contrast, buildings are man-made structures with regular layouts and typically straight and cuboid-shaped paths, e. g. corridors, stairs or elevators. Such pathways and/or navigation paths can be key features, which can be very deep-seated in their context, which results in the necessity to employ revealing techniques (cf. Figs. 4.3 and 4.9).

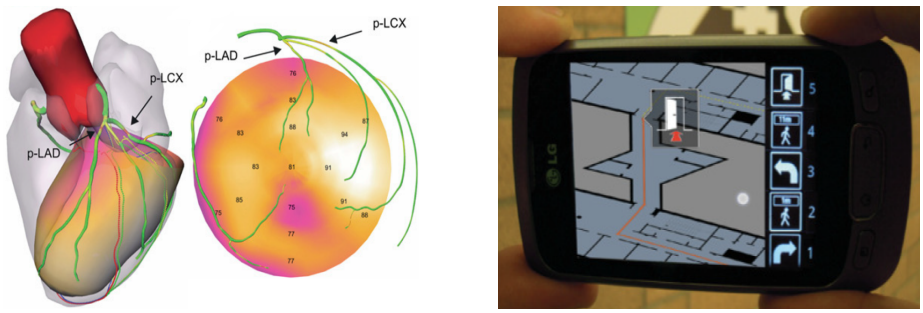

(a) **(b)**

Figure 4.3: Kirişli et al. [243] presented their *SMARTVis* system to relate morphological (CT) and functional (SPECT) information in 3D and BEP visualizations **(a)**. Poor perfusion can be treated via catheterization, for which the access path needs to be known [39]. For indoor navigation, Barberis et al. [31] presented a marker-based method **(b)**. Here, markers are placed inside buildings, which are used for orientation and navigation, e. g. to provide museum tours.

Similar to Gaemperli et al. [140] (cf. Fig 3.6), Kirişli et al. [243] presented a method that combines BEPs and 3D visualizations for SPECT/CT images to reveal pathologies in myocardial arteries (Coronary Heart Disease; see Fig. 4.3a). Typically, such pathologies are treated via drugs or surgery, but catheterizations and stent deployments are also treatment options [39, 61]. For the two latter treatments, it is necessary to guide instruments through blood vessels towards pathologies to reopen them. The authors do not present navigation techniques for such interventions, however, catheterizations and stent deployments can be regarded as navigation-related tasks.

Barberis et al. [31] presented their marker-based method for "*indoor navigation on mobile devices*" (see Fig. 4.3b). For this, various markers are distributed throughout the building, which are used for orientation and subsequent navigation. This approach can also be employed for more open areas, such as malls or plazas, but larger distances hinder marker visibility. When compared to other information sources designed for orientation and/or navigation, e. g. GPS that can be unavailable indoors, markers have the advantage, for example, that they can be reused for other purposes, e. g. "*localised advertisements*" [31]. However, markers need to be visible, i. e. their functionality heavily depends on lighting conditions, and during emergency situations their visibility may become heavily corrupted, e. g. by smoke in cases of fire.

FUNCTION IN SPATIAL CONTEXT. The importance of accurately relating context and focus objects was discussed in the previous chapter. One example was the PET/CT image visualization technique from Lawonn et al. [275] that cuts away surfaces to reveal physiological information (see Fig. 4.4a). In contrast, Chou et al. [82] describe their "*interactive Augmented Reality System*" in which various electronic devices, such as computers

See [275, Fig. 1].

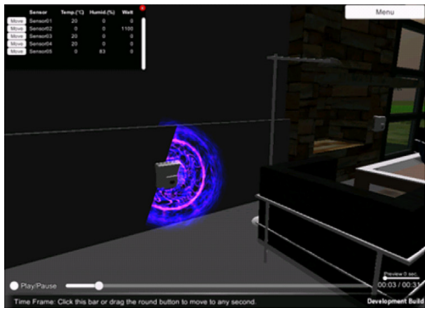

(a) **(b)**

Figure 4.4: In the approach of Lawonn et al. [275], physiological information is embedded in a morphological context using PET/CT images (cf. Fig. 3.9b) **(a)**. Similarly, Chou et al. [82] present an augmented reality system that can be used to reveal heavy electricity consumers **(b)**. Both methods employ attention-drawing approaches, such as vibrant colorizations, to guide users.

or fridges, are related to their energy consumption (see Fig. 4.4b). Both methods employ thresholding and attention-drawing depiction to highlight suspicious body regions and electricity consumers, respectively. Similar to Nguyen et al. [360], user guidance is implemented by emission-like *electrical spheres* (cf. Fig. 3.4b).

AUTOMATIC VIEWPOINT GENERATION. Interactive viewers, e. g. which allow for 3D rotations, can engage users to explore the depicted scene. However, in goal-driven scenarios, e. g. tumor assessment prior to surgical treatment, free interaction can result in time-consuming trial-and-error workflows. Thus, there exist methods that utilize certain metrics, such as surface features, to automatically create *good* default views [327, 498]. Subsequently, users can still explore the scene freely. With respect to maps, typical 2D maps do not suffer from occlusion problems. However, 3D maps, such as indoor maps, can depict walls to present room boundaries. Consequently, when poor perspectives are chosen, e. g. when the hemispherical viewing angle is small, walls become "*strong occluders*" [93].

Mühler et al. [346] present a method that combines various parameters to create *good* initial viewpoints in IVR settings (see Fig. 4.5a). For example, they consider the number of occluders between the scene camera and objects of interest, e. g. enlarged lymph nodes. Thus, to decrease the amount of visual change, e. g. when occluding surfaces are rendered more transparent or cut away completely, viewpoints with less occluders are preferred. Moreover, structures can also be assigned application-specific importance weights, i. e. viewpoints that would result in alterations of structures of high importance are avoided.

In contrast, Gai et al. [82] introduced an online application to render multi-story indoor maps (see Fig. 4.5b). One key feature of their method is that users can select floors for which *good* views are defined. For example, the authors consider the extents of the building and number of rooms to define *good* initial perspectives. On the one hand, the first principal direction of a floor is aligned perpendicular to the 3D viewer's horizontal axis, which can minimize the number of occluding walls in view direction. On the other hand, w. r. t. this direction, the camera is placed near the *half* with more rooms. In combination with the downward-pointing viewing direction, occlusion artifacts are further minimized.

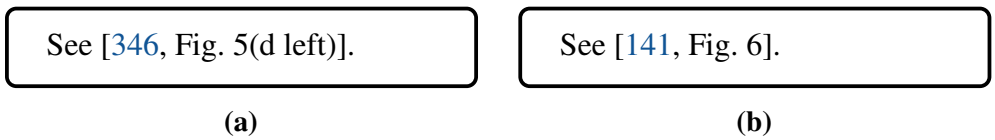

(a) **(b)**

Figure 4.5: There exist various techniques to automatically define *good* perspectives on scenes [358, 498]. Mühler et al. [346] present a method that creates *good* viewpoints on structures of interest, e. g. by preferring perspectives that have less objects *in front* **(a)**. In contrast, the method of Gai et al. [141] creates *good* views on floors, e. g. by rotating the building floor model in a way that more rooms are near the scene camera **(b)**. In combination with a steep viewing angle θ, this minimizes occlusion artifacts close to the scene camera.

LEVEL OF DETAIL TECHNIQUES. The key aspect of LOD techniques is that data abstraction is heavily tied to user interaction, e. g. zooming via mouse wheel scrolling. Zooming in 3D viewers changes the observer's distance to the scene objects. Similar to Depth of Field (DOF) techniques, the basic assumption is that with an increasing distance users cannot – or intentionally do not want to – focus on certain (key) features.[4] Consequently, when the scene camera is close to a certain (key) structure, more details can be added. The *transition*, however, can be smooth (continuous) or abrupt (discrete). For example, smooth transitions have multiple key frames with varying degrees of abstraction and for each step in between, these settings are somehow interpolated, e. g. by varying transparencies. Abrupt approaches also have such key frames, but there is no transition in between them, i. e. at some point the presentation just changes.

Meuschke et al. [328] present a smooth LOD approach to abstract line renderings of blood flow in (saccular) cerebral aneurysms (see Fig. 4.6a). They employ "*zoom levels*" that depend on the distance between the scene camera and the centers of blood flow clusters. Such clusters describe the general flow pattern, e. g. if streams of blood traverse the aneurysm's inner vessel wall *smoothly* or if vortices are formed somewhere. In any case, with decreasing distance, the (blood) flow is depicted less abstracted, i. e. by a single tube-like "*representative*" (high distance), by hull-like "*bounding geometry*" (intermediate

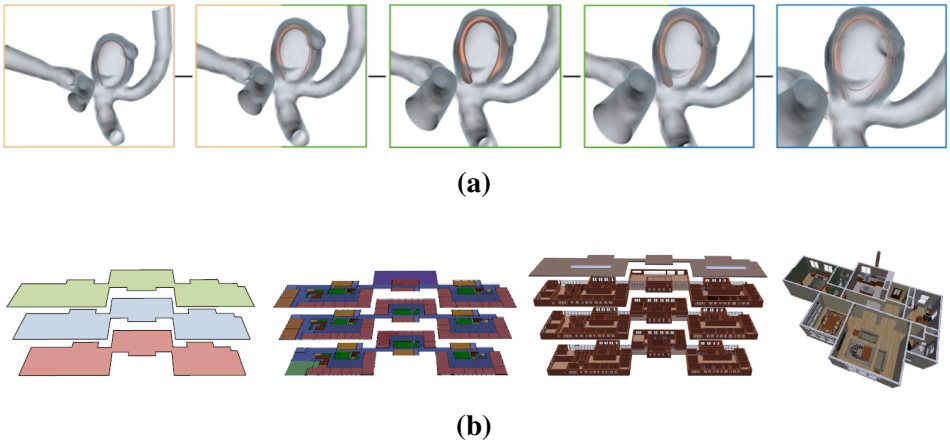

(a)

(b)

Figure 4.6: Level of Detail techniques can be used to interactively present certain (key) features at varying degrees of detail. Meuschke et al. [328] present a technique to smoothly transition between more or less detailed representations of blood flow patterns **(a)**. From left to right, more details of the blood flow are added. In contrast, Hagedorn et al. [163] propose a LOD approach for indoor navigation **(b)**. Here, from left to right, more building details are added. Presumably, there is no smooth transition in between these levels.

[4] Related to magic lenses, DOF-like presentations can also be faked, e. g. to artificially create a focus on certain image regions, such as persons in front of a heterogeneous background.

distance) or by various "*integral lines*" that are reconstructed from CFD-simulated flow (small distance) [328]. In between these distinct zoom levels, the transparencies of the corresponding representations are varied linearly to allow for a smooth visual transition between them (cf. Figs. 3.1 and 3.5b). Thus, blood flow patterns can be assessed at high detail, e. g. patient-specific, or more abstracted, e. g. in a cohort study setting [246].

Hagedorn et al. [163] propose a LOD technique that employs four distinct representations (key frames) for indoor "*routing*" scenarios (see Fig. 4.6b). Their basic assumption denotes that for navigation tasks not all spatial features have to be presented at all times. Here, at the lowest degree of detail, only the color-coded floors are presented. In contrast, when depicted at the highest degree of detail, "*interior and exterior details*" are presented, which can entail, for example, furniture or the building's facade. In between, more details are added, such as walls and doors. Presumably, the authors designed this approach to be used in an abrupt manner, i. e. there is no *blending* between these key frames.

GLYPH- AND SYMBOL-BASED TECHNIQUES. Glyphs or symbols are small "*symbolic or iconic*" elements that encode information [410]. Typically, they are used to superimpose their context (base map) with information from another source in a heavily abstracted manner. The main challenge is to design *good* symbols, since they are typically depicted in visual contrast to their context, which naturally draws the user's attention to them. One major advantage of them is that they can be used at varying levels of granularity, e. g. they can only be depicted at certain user-defined landmarks or at lattice points in an (ir-)regular grid. This allows the base maps (context) or any other theme map (quasi focus or near focus objects) to visually contribute more or less towards the final presentation. However, visual clutter, e. g. w. r. t. symbol count and/or their complexity, should be avoided.

Ropinski et al. [411] presented a F+C method to depict glyph-abstracted PET images (focus, source) on top of a volume-rendered heart (context, target; see Fig. 4.7a). As glyphs, the authors utilize supertori, i. e. a geometric shape between a regular torus and a square, with varying thickness. With these, anatomical regions with poor perfusion are highlighted via "*inverse parameterization*", i. e. areas with small domain values are depicted more prominently [410]. As intended, one's attention is naturally drawn to the emphasized heart regions that suffer from decreased blood perfusion [285]. Furthermore, the authors accompany their glyph visualizations by legends that allow for more in-depth

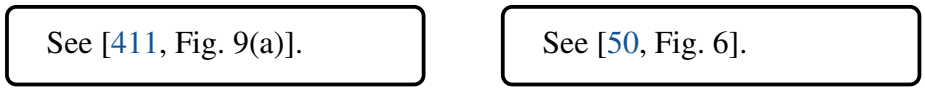

(a) **(b)**

Figure 4.7: Glyphs or symbols are small geometric elements that are typically used to encode key features in another context in a heavily abstracted manner. Ropinski et al. [411] encode PET images to highlight poorly perfused heart morphology via "*inverse parameterization*" [410] **(a)**. Biczók et al. [50] derive building "*popularity*" by depicting navigation behavior of campus visitors via pie chart-like circles **(b)**. Furthermore, both works employ legends to allow for in-depth glyph assessment.

assessments. In other words, while *the general idea* can be conveyed quickly, glyph *reading* requires time. For more details on glyph-based visualization techniques in medical image data, see the survey of Ropinski et al. [410].

Biczók et al. [50] present a "*traffic map*" that enhances maps by certain statistics (see Fig. 4.7b). As glyphs, the authors utilize pie chart-like circles that, e. g., encode user routing behavior. The single-hue color-coding (first theme map layer) encodes how *popular* the buildings are by counting geoposition requests from mobile devices. Although this introduces a bias w. r. t. the users' visitation times, the authors argue that this bias is negligible w. r. t. long acquisition times. The glyphs depict the ratio of how often users went to (white) or away from (black) a certain building. Arguably, this could be used to study customer behavior w. r. t. shop location and/or product placement.

OTHERS. Other similar research fields, for example, are related to the employment of magic lenses in F+C setups [143, 293] or on-the-fly management of labels [421, 524].

4.5.2 MAP-BASED MEDICAL VISUALIZATIONS

Here, three medical image visualization techniques are presented that utilize maps to encode information. On the one hand, this is done to clarify that we were not the first authors to utilize maps in a medical and/or clinical context. On the other hand, among others, the herein presented works of Hansen and Rieder et al. [172, 403] inspired us to also utilize maps for medical images and for our risk visualization techniques that will

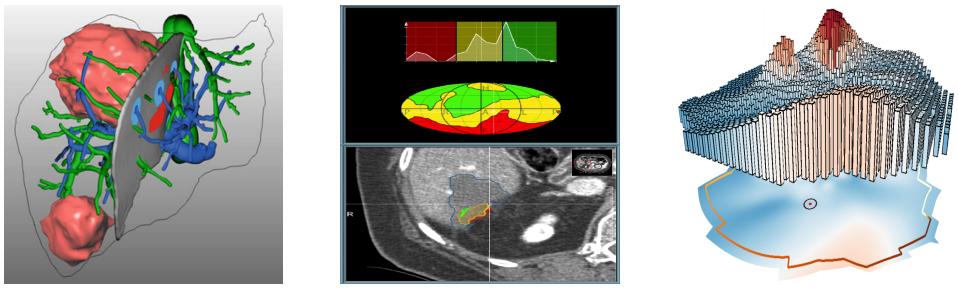

(a) **(b)** **(c)**

Figure 4.8: Map-based techniques are sometimes used for medical images. Hansen et al. [172] employ arbitrarily shaped 3D planes to colorize safety margins to chosen structures, e. g. blood vessels and tumor tissue **(a)**. Rieder et al. [403] utilize the *Mollweide Projection* to unfold ablation zones and potentially remaining tumor tissue **(b)**. Similarly, Meuschke et al. [329] flatten aneurysm surfaces and utilize 3D bar charts to visualize surface parameters, e. g. vessel wall movement **(c)**.

be presented in the next chapter. The term risk, as it will be discussed later, is often a combination of various aspects, for example safety margins to certain (risk) structures.

Hansen et al. [172] presented a so-called "*Risk Maps*" technique to visualize *risk* during liver tumor biopsies, ablations, and/or surgeries (see Fig. 4.8a). Here, maps are arbitrarily-shaped 3D planes, which are embedded in a context organ, e. g. the liver, and risks are color-coded safety margins between said maps and other structures, e. g. blood vessels and tumor tissue. The authors employ a categorical color scheme to make structures and structure-related safety margins well-distinguishable. Rieder et al. [403] take the term *map* literally and utilize the *Mollweide Projection* to unfold ablation zones and potentially residual tumor tissue after liver RFAs (see Fig. 4.8b). Typically, the Mollweide Projection is used to flatten the globe into 2D space and its key feature is that areas prior and after projection stay proportional. However, with increasing distance from the origin, the general shapes of structures become distorted. When combined with a categorical traffic light metaphor, such approaches allow for a *direct* interpretation of 3D information, which might require much slicing and mental effort otherwise. The original images, however, have still be to provided. As the final example, the technique of Meuschke et al. [329] was chosen (see Fig. 4.8c). Similarly, the authors flatten aneurysm surfaces to create map-like representations of certain features, e. g. vessel wall deformations. Moreover, such features can be visually repeated via 3D bar charts *on top*, and thus, they are additionally encoded via the visual variable *height* [45].

4.6 MULTI-STORY MAPS

Chen [76] states that 3D visualizations "*when compared with conventional ways of architectural communication which uses technical drawings*" are beneficial for the communication process between two parties with different levels of experience. This, for example, refers to doctor-patient and/or architect-client communication, but also to educational scenarios [159, 363]. However, there also exist various research challenges for such digital multi-story maps that have to be addressed to exploit their full potential. One challenge is to find and present *good* navigation routes in spatially complex environments, e. g. to find the nearest emergency exit. Exemplarily shown at the work of Boguslawski et al. [60], many authors focus on efficient indoor navigation, for example on mobile devices [31, 60, 78, 152] (see Fig. 4.9a). For navigation, not only spatial information has to be considered, i. e. to find the *cheapest* path, but also conditional exceptions, for example that certain corridors are closed during certain hours of the day or that elevators are prohibited in cases of emergency. Thus, Building Information Modelling (BIM) is typically used during construction planning to create digital representations of buildings, e. g. to describe elements of buildings and their relationships to each other [153]. Teo et al. [471] further enhance such indoor navigation methods by including information about the outside world, e. g. via city street maps. This is done to assist relief forces, such as firefighters and policemen, to find evacuation routes or strategic key locations for their large vehicles [77] (see Fig. 4.9b). Gai et al. [141] presented a web-based application that uses an ontological data structure interface to automatically create 3D indoor maps of multi-story buildings, such

as malls (see Fig. 4.9c). On demand, presentations can be further enhanced via detailed descriptions of facilities, such as the opening times and/or menus of restaurants.

RESOLVING OCCLUSION ARTIFACTS. Independent from the actual domain, 3D presentations often have to address occlusion problems. Similar to medical image visualizations, the opaqueness of outer surfaces, such as the facade, can be decreased (cf. Fig. 4.9). Jin et al. [217] discuss more interactive techniques for multi-story buildings. In their patent, the authors describe how visual emphasis can be created to highlight certain floors. For example, similar to fisheye lenses, selected floors can be distorted (*inflated*) to assign more rendering space to them. Another example is a drawer-like metaphor to *pull out* one floor to allow for an in-depth assessment of rooms therein.

4.7 FLOOR MAPS FOR MEDICAL IMAGES

Here, a visualization method is presented that can be used to transform medical images into indoor map-like presentations.

4.7.1 CONTRIBUTIONS

The key contributions are as follows:

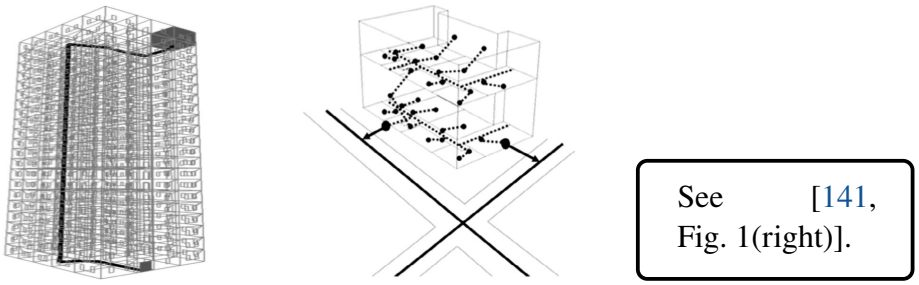

(a) **(b)** **(c)**

Figure 4.9: One research challenge for multi-story building maps is to find and present *good* navigation paths. Boguslawski et al. [60] presented a fully automated indoor-only routing algorithm, e. g. in cases of emergency **(a)**. Teo et al. [471] also included information about the outside world, for example, to find good routes and strategic points for relief forces and their large vehicles **(b)**. Gai et al. [141] presented a web application that offers a data structure interface to automatically create 3D indoor maps, for example of malls or other buildings **(c)**.

- A method that transforms pre-segmented and/or pre-labeled medical image stacks into building-like representations, namely floor maps (cf. Fig. 4.12). Although maps were already utilized by other authors, creating such presentations is a novelty.
- A GUI that offers support during interactive exploration of said floor maps and the original image data via 2D-3D and 3D-2D interaction facilities (cf. Fig. 4.17).
- An evaluation with three trained anatomy experts (cf. Sec. 4.7.7).

4.7.2 INTRODUCTION AND MOTIVATION

Over the last decades, much research was carried out to improve medical image scanners, for example w. r. t. spatial resolution (cf. Ch. 2). On the one hand, this improves the fidelity of the image data (*less uncertainty*), but on the other hand, this results in more visual information that has to be assessed. Volumetric medical image data is typically examined in a slice-based manner, e. g. via computer mouse scrolling. This enables observers to assess in-plane spatial relationships between anatomical structures in great detail, but it also requires them to mentally keep track of relationships along the third axis. Especially for medical students and physicians in training this can become mentally exhausting, because they are not yet accustomed to such tasks. Thus, there exists a strong research interest to support this task.

Three-dimensional maps are a well-known concept to provide spatial overviews in large buildings, such as malls, hospitals, or federal buildings (cf. Sec. 4.6). Many people are accustomed to such presentation, e. g. from handheld devices. Such maps support *our* visuo-spatial working memory that is used for orientation and navigation tasks (cf. Sec. 4.3). Typically, the degree of abstraction from 3D data into 2D representations is large, and thus, employing 3D maps for 3D medical image data is a straightforward design choice. Visualization techniques for maps and medical images purposefully simplify certain aspects, such as geometric details. Consequently, we hypothesize that floor maps are suitable to offer exploration support for medical image data.

From a feasibility point of view, the proposed method is focused on anatomy education, since, when one begins to study anatomy, roughly understanding spatial relationships between anatomical structures is more important than learning about geometric details. Report generation is another potential application scenario, which is particularly relevant for, e. g., radiation therapy and nuclear medicine (cf. Sec. 4.7.8 and Ch. 7). Other clinical disciplines and/or tasks, however, such as radiation therapy planning, will probably not benefit from the presented approach due to the relatively high geometric abstraction which distorts spatial relationships.

4.7.3 RELATED WORK

In this section, a brief overview about related methods is provided.

EXPLORATION SUPPORT. Tietjen et al. [474] presented a 2D exploration-supporting technique called *lift charts* (see Fig. 4.10a). During slice-based exploration, e. g. of axial slices, the spatial extent of labeled structures along the third anatomical axis is displayed in an additional 2D diagram. This is done by representing each structure as a bar and the bars' heights are their vertical extent w. r. t. the z_{min} and z_{max} coordinates of their respective AABBs. Thus, the result is a bar chart-like presentation with multiple vertical bars, which can be interpreted as *lifts*, which in turn allow users to visually cluster and distinguish vertical sections. With respect to color-coding, each structure is assigned a unique color.

Later, Balabanian et al. [28] utilized hierarchical lift charts for structures and their substructures. With respect to the currently observed hierarchy level, lift charts represent spatial relationships between structures and substructures on different scales. Diepenbrock et al. [105] extended lift charts to depict information from physiological and/or functional image sources (cf. Sec. 3.8). Instead of using morphology-depicting images, their lift charts utilize (*abstract*) fMR images. Thus, functional peaks perpendicular to the currently used slicing axis are highlighted.

ABSTRACTION OF LIFT CHARTS. Although lift charts are an easy-to-employ technique to improve the slice-based exploration of volumetric image data, their overall degree of abstraction is very high. Following the abstraction theory of Viola and Isenberg [501], lift charts introduce high degrees of geometric and photometric abstraction, since structures are represented by two values and one flat-shaded color only (cf. Fig. 4.2). In Figure 4.11,

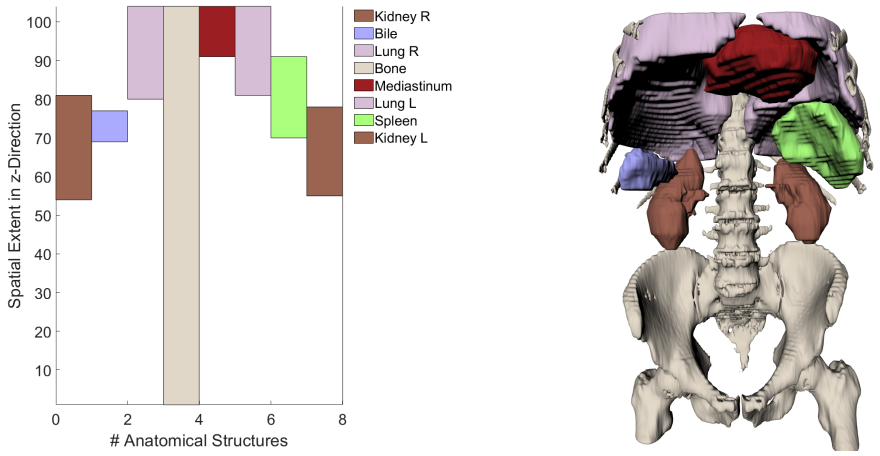

(a) **(b)**

Figure 4.10: Tietjen et al. [474] introduced *lift charts* to support slice-based explorations of medical images **(a)**. On the right, an IVR of the corresponding Data Set 1 is presented **(b)** (cf. Tab. 4.1).

Images originally published in Journal of WSCG [326, Fig. 2].

rough estimations of the individual degrees of abstraction for the lift charts of Tietjen et al. [474] and the proposed floor maps are depicted. Assuming *real-world anatomy* and *biochemical processes* as the endpoints of the scale axis, lift charts and floor maps are at very low points, since both techniques are typically intended to be applied to gross anatomy. Since no temporal data is used, both techniques do not introduce temporal abstraction.

ABSTRACTION THROUGH MORPHOLOGICAL CHANGE. Mindek et al. [338] introduced a "*representative slices*" technique to implicitly alter slicing speed during slice-based exploration. Representative slices are defined when structures undergo a certain degree of morphological change between adjacent slices, e. g. when blood vessel morphology changes due to an aneurysm. Thus, it is assumed that suspicious morphology is explored in more detail, since more slices are defined in such regions.

DISTINCTION OF OUR METHOD. Floor maps aim to offer support during slice-based exploration of medical image stacks (cf. Fig. 4.17). In contrast to lift charts, floor maps introduce less geometric abstraction, since more morphological details are preserved. Furthermore, less photometric abstraction is introduced, since structure colors were taken from organ photographs. They are combined with diffuse shading, which in turn emphasizes ridges between floors and rooms. Thus, the overall degree of abstraction is reduced and at the same time, image stacks are transformed into building-like representations. However, buildings are made up from floors and rooms, which typically results in occlusion problems. To address this, OITs are used to reveal inlying key structures.

4.7.4 CONCEPTUAL DESIGN OF FLOOR MAPS

Here, the conceptual design of how to translate anatomical structures into building-like representations is described.

ANATOMY PERSPECTIVE. The main challenge is to transform (scanned) human anatomy into floors and rooms. In general, larger anatomical structures, such as organs, have a spherical-like shape with soft edges. There are some exceptions, e. g. extremity bones or

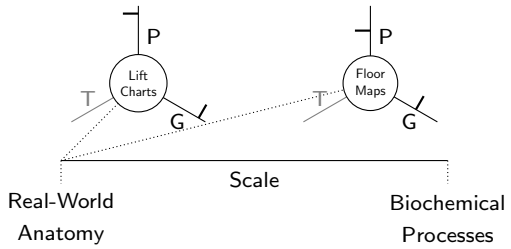

Figure 4.11: Abstraction rankings of lift charts and floor maps using the theory of Viola and Isenberg [501] (cf. Fig. 4.2). The axes show the **p**hotometric, **g**eometric, and **t**emporal abstraction categories. Ticks show the estimated degrees of abstraction in the respective category. Here, the T-category is not applicable.

Image originally published in Journal of WSCG [326, Fig. 3] and inspired by [501, Fig. 15].

intestines, which are also round but, overall, also very elongated. Smaller structures, such as blood vessels, are tubular with circular or ellipsoidal cross-sections.

BUILDING PERSPECTIVE. Buildings are man-made structures with great regularity. In many buildings, floor plans are vertically repeated and horizontally divided into floors of equal height. In smaller buildings, however, such as homes, room layouts of adjacent floors can be very different, whereas in larger buildings, room layouts can be very repetitive. Additionally, pathways, such as corridors or elevators, are typically straight cuboid-shaped tubes in horizontal or vertical direction.

FLOOR DEFINITION. In clinical practice, image stacks are typically assessed via axial slicing. Thus, floors are created along the z-axis and to make them well-distinguishable, small gaps are inserted between adjacent floors. Although this gap size can be adjusted, each division leads to geometric distortion. Therefore, the number of divisions must be minimal, which can be regarded as a key requirement. In other words, each slice of the used image stack is used exactly once during floor map creation.

ROOM DEFINITION. Anatomical structures can have complex spatial arrangements, e. g. the heart is encompassed by the lungs, but they are clearly separated. This characteristic is considered in the processing pipeline by creating rooms without overlaps (see Figs. 4.14 and 4.15). To enable users to visually cluster multiple rooms that represent similar anatomical structures, they are color-coded identically. For example, in Figure 4.12, the kidneys and lungs are both brown and pink, respectively.

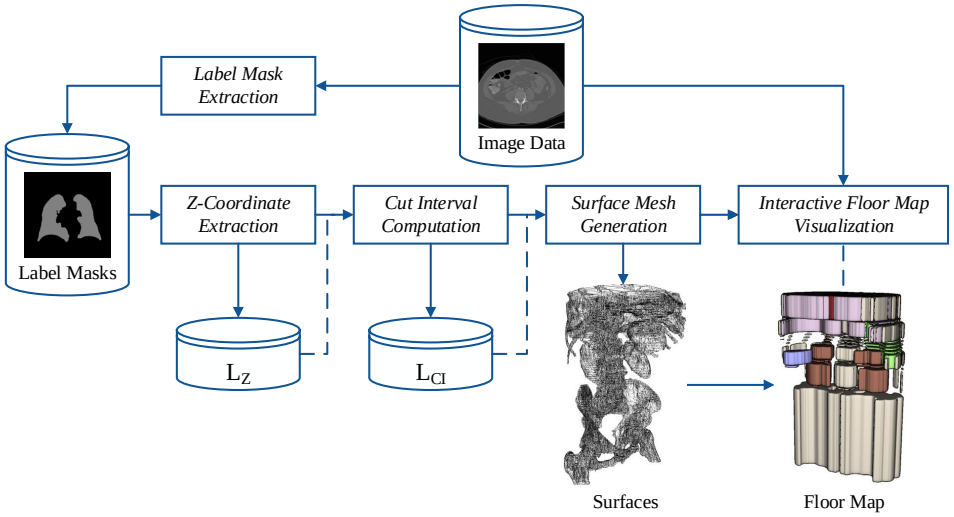

Figure 4.12: Pipeline to generate floor maps from medical images. L_Z is a compiled list of unique z_{min} and z_{max} coordinates of all segmentation masks' AABBs. L_{CI} is a list of cut intervals that are used to divide the segmentations into floors.

Image originally published in Journal of WSCG [326, Fig. 4]. Adapted for this thesis.

Table 4.1: Details on the data sets (DS) with their respective number of voxels, the labeled structure count (# S), and the anatomical site of the scan (cf. Fig. 4.18).

DS	DS size (voxels)	# S	Site of Scan
DS 1	$512 \times 512 \times 105$	8	lower thorax to pelvis
DS 2	$513 \times 513 \times 108$	22	head and neck area
DS 3	$512 \times 512 \times 99$	9	lower thorax and upper abdomen

Table originally published in Journal of WSCG [326, Tab. 1].

4.7.5 FLOOR MAP GENERATION

Here, the processing pipeline for the proposed floor map method will be presented.

IMAGE DATA AND IMPLEMENTATION. The method was developed using pre-labeled CT and MRI scans (see Tab. 4.1). The method is independent from the combination of modalities if the image sources are registered and if structures are made available via segmentation masks. The processing pipeline is depicted in Figure 4.12, which was implemented using *MeVisLab 2.8.2* [406]. During exploration, users are presented a GUI to simultaneously explore the original images and floor maps. Although it suffices to use segmentation masks, structure labels can be used for the final presentation.

LABEL MASK EXTRACTION. The pipeline requires segmentation or label images. Depending on the data set, structure segmentations were acquired using different segmentation algorithms. For example, the liver in DS3 was segmented with the *HepaVision2* software by Bourquain et al. [63] which employs a semi-automatic live wire approach. These algorithms produce binary masks that can be processed by our method directly. In contrast, the lymph node segmentation masks of DS2 were acquired using the model-based methods of Dornheim et al. [108]. These methods generate polygonal representations, which requires a subsequent transformation into binary masks. Typically, this is not ideal, since such conversions can affect the quality of the segmentation mask. This is not critical here, since floor maps were not developed with, e. g., treatment planning scenarios in mind.

Z-COORDINATE EXTRACTION. In the first step, the z_{min} and z_{max} coordinates of all structures' AABBs are extracted and compiled into a list called L_Z. Prior to compilation, certain structures can be marked *too small* if their spatial extent in z-direction ($z_{max} - z_{min}$) is below a user-defined threshold. Consequently, they are not divided into floors and their general shape is preserved. In other words, this *protects* small structures from geometric abstraction and/or distortion, which is typically greater for them than for larger structures. However, due to the aforementioned gaps that distort the original image stack in z-direction, such structures must be translated to their correct vertical position for the final visualization (cf. Fig. 4.16). Figure 4.13 shows lymph nodes that were marked being *too small* for divisions. This option can be used to define key features.

CUT INTERVAL COMPUTATION. The compiled z-coordinates are then used to calculate *cut intervals*, which are used to define floors. Similar to Mindek et al. [338], here, floors are defined when the composition of the segmentation masks between adjacent layers changes. On the one hand, this makes floors unique and on the other hand, this visually guides users to regions of high anatomical variability, since more floors are defined in regions where segmentation masks repeatedly begin and/or end. The list L_Z is then sorted in ascending order while double coordinates are removed, since the method only requires knowledge about layers in which the composition changes. For each remaining entry $e_k \in L_Z$ only one of the following statements (S1-S3) is correct:

$$\text{S1} \qquad e_k = z_{min_{S_i}}$$

$$\text{S2} \qquad e_k = z_{max_{S_i}}$$

$$\text{S3} \qquad e_k = z_{min_{S_i}} = z_{max_{S_j}}$$

This means that for each entry (slice) $e_k \in L_Z$ there exists at least one segmentation mask S_i that begins (S1), that ends (S2), or that at least one mask S_i begins while at least one other mask S_j ends (S3). Subsequently, all $e_k \in L_Z$ have to be flagged accordingly. Using an interval-like notation, for example for L_Z of DS1, the following line aims to provide a quick understanding of how cutting intervals are defined using the proposed method:

```
[...[ [...[ [...] ]...[ ][...][... ]
0  54 55  69 70  77 78  80 81  91  104
```

For each entry e_k, the color-coded token show which statement S1-S3 holds true: [is used for S1,] is used for S2, and][is used for S3. Note that rather benefiting the actual implementation, this notation solely aims to support reading.

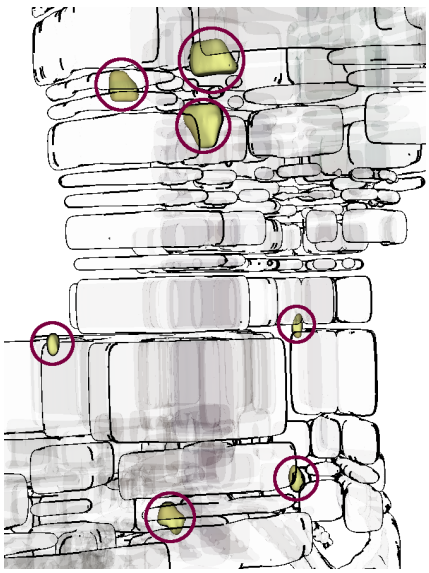

Figure 4.13: Lymph nodes that are defined as being *too small* are not transformed.

Image originally published in Journal of WSCG [326, Fig. 5].

The entries e_k are then processed in a pairwise manner using Algorithm 4.1. Depending on which statements S1-S3 hold true for e_k and e_{k+1}, an individual cutting interval is defined. Overall, there exist nine combinations, since e_k and e_{k+1} can either satisfy S1, S2 or S3. For example, when comparing 0 and 54, the segmentation mask composition

Algorithm 4.1: Cut interval generation to define floors.

```
Input: L_Z

for all e ∈ L_Z
if L_Z(e) == [
|   if L_Z(e+1) - L_Z(e) == 1
|   |   if L_Z(e+1) ==[ or L_Z(e+1) == ][
|   |   |   L_CI(e) = [L_Z(e), L_Z(e)]
|   |   elif L_Z(e+1) == ]
|   |   |   L_CI(e) = [L_Z(e), L_Z(e+1)]
|   |   endif
|   else
|   |   if L_Z(e+1) ==[ or L_Z(e+1) == ][
|   |   |   L_CI(e) = [L_Z(e), L_Z(e+1)-1]
|   |   elif L_Z(e+1) == ]
|   |   |   L_CI(e) = [L_Z(e), L_Z(e+1)]
|   |   endif
|   endif
endif

if L_Z(e) == ][
|   L_CI(e) = [L_Z(e), L_Z(e)]
|   e = e+1
|   if L_Z(e+1) - L_Z(e) == 1
|   |   continue
|   else
|   |   if L_Z(e+1) ==[ or L_Z(e+1) == ][
|   |   |   L_CI(e) = [L_Z(e)+1, L_Z(e+1)-1]
|   |   elif L_Z(e+1) == ]
|   |   |   L_CI(e) = [L_Z(e)+1, L_Z(e+1)]
|   |   endif
|   endif
endif

if L_Z(e) == ]
|   if L_Z(e+1) - L_Z(e) == 1
|   and L_Z(e) != L_CI(e-1)[1]
|   |   L_CI(e) = [L_Z(e), L_Z(e)]
|   |   continue
|   elif L_Z(e) - L_Z(e-1) == 1
|   and L_Z(e+1) - L_Z(e) > 1
|   |   L_CI(e) = [L_Z(e), L_Z(e)]
|   |   e = e+1
|   endif
|   if L_Z(e+1) ==[ or L_Z(e+1) == ][
|   |   L_CI(e) = [L_Z(e)+1, L_Z(e+1)-1]
|   elif L_Z(e+1) == ]
|   |   L_CI(e) = [L_Z(e)+1, L_Z(e+1)]
|   endif
endif
endfor

Output: L_CI
```

Algorithm originally published in Journal of WSCG [326, Alg. 1].

changes at slice 54. Thus, the first floor is defined from slice 0 to 53 and slice 54 is processed in the *next* step. For 70 and 77, slice 77 can be included in *this* processing step, and thus, must be skipped in the *next* one. The result is the cutting interval list L_{CI}:

$$\begin{aligned} L_{CI} = \{&[0, 53],\ [54, 54],\ [55, 68],\ [69, 69],\\ &[70, 77],\ [78, 78],\ [79, 79],\ [80, 80],\\ &[81, 81],\ [82, 90],\ [91, 91],\ [92, 104]\} \end{aligned}$$

Note that Algorithm 4.1 creates artifacts, such as cut intervals in the form $[X, Y]$ with $Y < X$. After artifacts have been removed, L_{CI} holds the minimum number of floor ranges. Thus, and w. r. t. the final presentation, visual distortion is minimized. To create the aforementioned gaps between floors, empty slices are inserted between the L_{CI} entries prior to mesh creation. We have found that one or two empty slices are sufficient, as larger gaps increase the need for manual navigation, e. g. via 3D rotations.

SURFACE MESH GENERATION. Subsequently, rooms have to be created. For each floor, this is achieved by segmentation mask projection and extrusion (see Fig. 4.14). First, each segmentation mask is projected along the z-axis, i. e. along the floor's vertical axis.

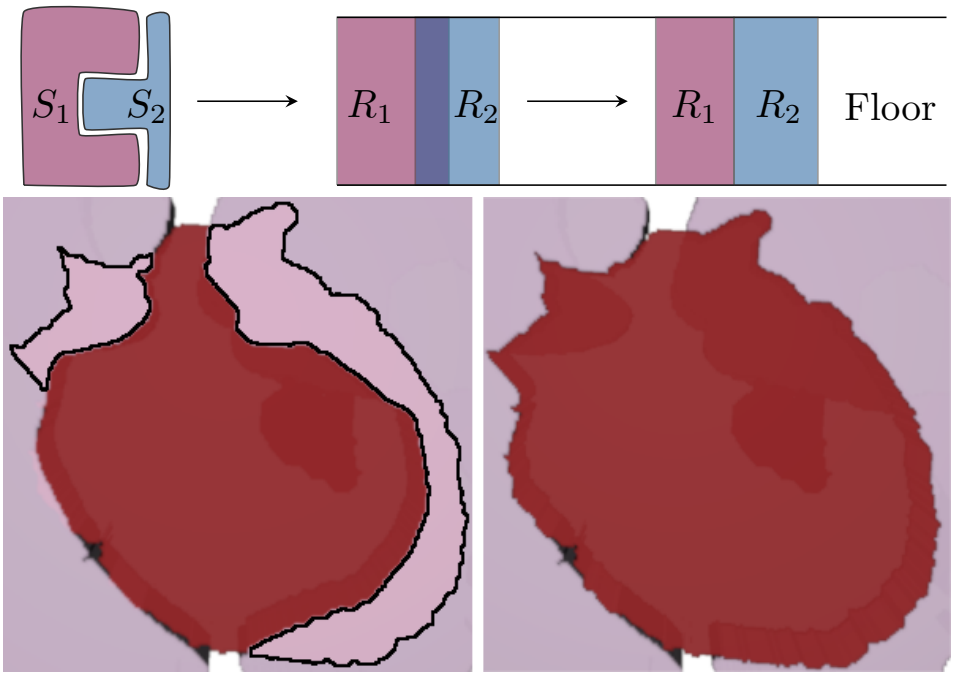

Figure 4.14: To create rooms, the maximum axial shape of each segmentation mask S_i is extruded vertically **(top)**. This can result in overlap artifacts between rooms R_i. This is addressed by assigning overlapping volumes to the smaller room. For example, the mediastinum (red) and the lungs (pink) overlap **(bottom)**. Since the mediastinum is smaller, the overlapping volumes are assigned to the mediastinum. For presentation purposes, the overlapping volumes' boundaries are enhanced.

Images originally published in Journal of WSCG [326, Fig. 6].

Secondly, the resulting shape is extruded along the floor's vertical axis again. This results in rooms that are defined by the maximum axial shape of their respective structures. Finally, meshes are created using the *Neighboring Cells Algorithm* by Bade et al. [25, 299].

This preserves some geometric features of the anatomical structures S_i, which, in combination with their vertical position, support recognizability. However, by using the maximum axial shape of structures, overlapping artifacts might be created, which do not appear in real-world anatomy (see Fig. 4.14). Although S_1 and S_2 do not overlap, the extrusion of their maximum axial shape results in an overlapping space between the corresponding rooms R_1 and R_2. This issue is addressed by performing pairwise overlapping tests between all rooms within a floor. If rooms overlap, the overlapping volume is assigned to the smaller room. This is done since smaller rooms are at a higher risk to be overlooked. In Figure 4.14, this applies to room R_2 and the red-colored mediastinum.

When overlaps are resolved like this, *kissing rooms* are created. Thus, four iterations of Laplacian smoothing via the *WEMSmooth* module in MeVisLab are applied with a smoothing factor of 1 ($\in [0, 1]$) for four iterations. On the one hand, this results in volume shrinkage, which further abstracts anatomical structures. On the other hand, however, since the rooms' sides are flat and stand perpendicular to each other, a few strong smoothing iterations result in the sharp edges being *filed down* evenly, which implicitly pushes adjacent rooms away from each other (see Fig. 4.15). After overlap removal, the mediastinum and

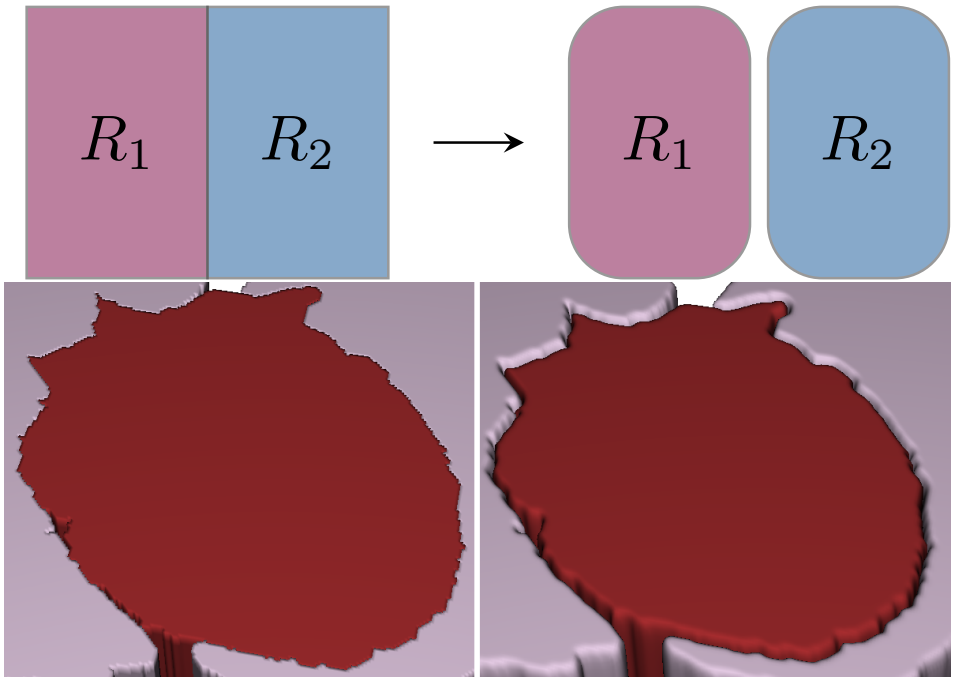

Figure 4.15: After overlap removal, *kissing rooms* are created **(top)**. Thus, Laplacian smoothing is applied. This results in *valleys* between rooms. In combination with diffuse shading, this makes adjacent rooms well distinguishable **(bottom)**.

Images originally published in Journal of WSCG [326, Fig. 7].

lungs can be clearly distinguished due to their color-coding and diffuse shading, which creates shadows around the just created valleys.

ADDING EXCEPTIONS TO TRANSFORMATIONS. Prior to mesh generation, users have two additional options to alter the transformation from segmentation masks into floors and rooms. This is another way to define key features (cf. Sec. 4.7.8). First, w. r. t. floor creation, structures can be *protected* from cuts. This is done by applying a morphological dilatation operator in z-direction to re-merge rooms along the aforementioned floor gaps. Alternatively, the resulting meshes could also be rescaled. If this is not done, structures can be too short w. r. t. their spatial context (see Fig. 4.16a). Secondly, w. r. t. room creation, the shape of structures can be preserved. In other words, instead of employing the maximum axial shape, the unaltered (natural) shapes of the anatomical structures are used. Additionally, both options can be combined, which is depicted in Figure 4.16. Here, the *musculi sternocleidomastoideus* (brown) were preserved.

Another feature can be used to preserve the structures' shapes in the lowest and upmost floors. This is shown in Figure 4.18b for DS2. Here, bone anatomy near the claviculae and the skull's apex are preserved to enable a visual *ease-in* and *ease-out*. In contrast, this option was not used for the pelvis and lumbar spine for DS1 in Figure 4.18a. On the one hand, not using this option preserves the floor (indoor) map concept, but on the other hand, the recognizability of structures can be hindered considerably.

INTERACTIVE FLOOR MAP VISUALIZATION. Figure 4.17 shows the GUI that allows for an interactive and simultaneous exploration of the original images and floor maps. On the left, users can slice through the original image source. In the floor map, an orange frame

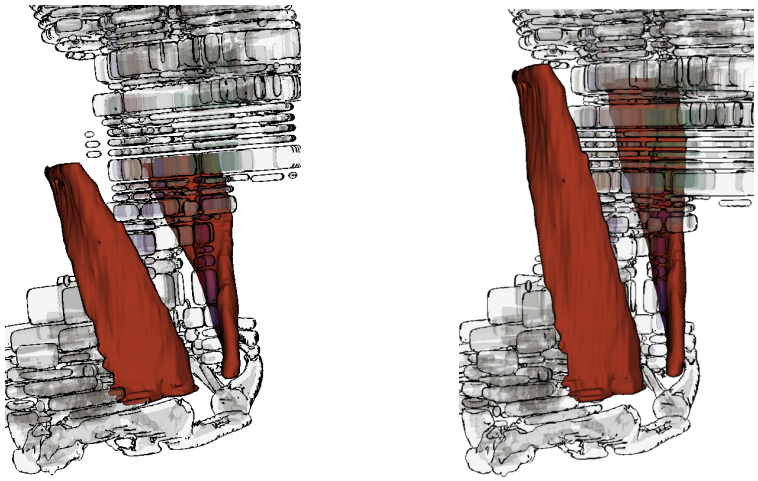

(a) Without Correction **(b)** With Correction

Figure 4.16: Due to the vertical floor gaps, structures have to be moved or re-merged prior to the final presentation (cf. Fig. 4.13). Furthermore, the shapes of structures can be preserved, which was done here for the *musculi sternocleidomastoideus*.

Image **(b)** originally published in Journal of WSCG [326, Fig. 8].

moves up and down accordingly, indicating the floor to which the currently displayed slice belongs (2D-3D). Note that this frame must be translated over floor gaps, since the original images do not contain empty slices. In addition, when users select rooms (structures), their boundaries are enhanced in both viewers (3D-2D). Thus, their boundaries are emphasized, i. e. via orange colorization, whereas in 2D, their predefined colors are used to create highlights. To address occlusion problems, structure-specific OITs can be adjusted [33].

4.7.6 RESULTS

The main contribution of this work is a processing pipeline that transforms pre-segmented and/or labeled image stacks into building-like representations (see Fig. 4.18). Algorithm 4.1 is the core of this method, which produces the smallest number of cut intervals to define floors. In Table 4.2, the computation times of all processing steps are shown. They were acquired using an i5-2500 processor with 3.3 GHz.

4.7.7 EVALUATION

In this section, we describe how the floor map technique was evaluated.

INTERVIEW SETUP. The proposed method was evaluated by three trained anatomy experts. They did not co-author the respective publication [326]. They were interviewed in an informal *think-aloud* setup using on-paper questionnaires. Two interviewees are physicians (I1 and I2), whereas the third one is a biologist (I3). Similar to Figure 4.17, they were able to use a software environment to explore all three data sets interactively while getting exploration support from lift charts and floor maps, respectively. They answered

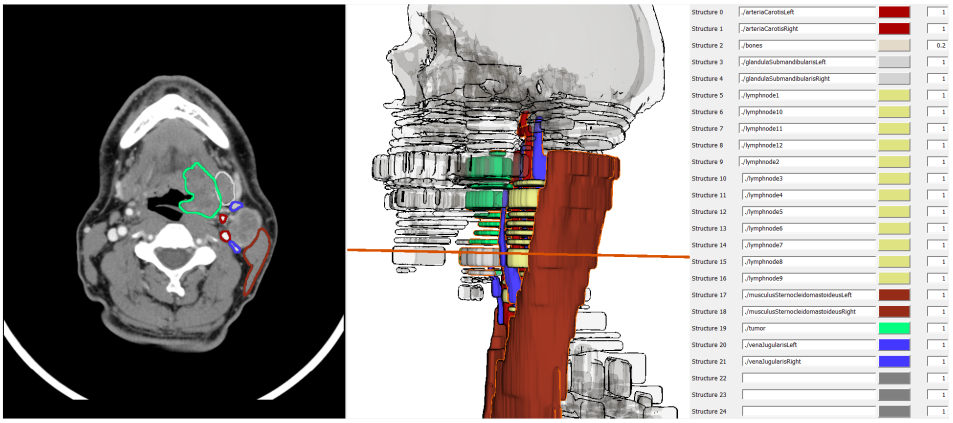

Figure 4.17: The GUI allows for a simultaneous exploration of the original images and the floor map visualization. Certain structures, such as a tumor (green), are highlighted in 2D and 3D. The orange-colored border (frame) in the 3D viewer corresponds with the currently displayed slice. On the right, the names, colors and opacities for all structures are shown. Users can interactively adjust these options.

Image originally published in Journal of WSCG [326, Fig. 9].

Table 4.2: Computation times for processing. For each data set, the number of structures (# S) and the number of resulting floors (# F) are denoted. No structure was marked *too small*, no shapes were preserved, and no structures were re-merged. The computational times are denoted in seconds and were averaged for five executions.

	Data Set (# S/ # F)		
	DS 1 (9/ 15)	DS 2 (22/ 28)	DS 3 (9/ 15)
Z-Coordinate Extraction	0.94	2.51	1.52
Cut Interval Computation	0.01	0.05	0.01
Vertex Mesh Generation			
Room Extrusion	12.66	32.94	10.93
Overlap Removal	21.68	47.64	14.34
Mesh Generation	29.65	64.01	30.92
Mesh Smoothing	2.43	3.08	4.41
Total Processing Time	67.37	150.23	62.13

Table originally published in Journal of WSCG [326, Tab. 2].

their questions using a five-item Likert scale (- -, -, ∘, +, ++). Their answers are summarized in Table 4.3. The questionnaires were divided into three parts, which are described below.

PART 1 – GENERAL QUESTIONS. First, the interviewees were asked about their clinical and technical experience (see. Tab. 4.3). They were asked the following questions:

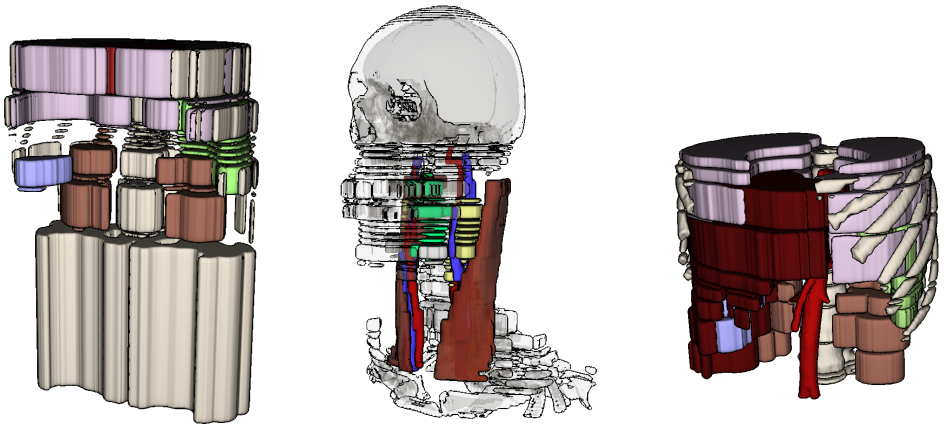

(a) Data Set 1 **(b)** Data Set 2 **(c)** Data Set 3

Figure 4.18: Three floor map visualizations depicting three different pre-labeled data sets (cf. Tab. 4.1). Various features can be employed to alter the final results. In Subfigure **(a)**, a standard floor map is depicted. Users can select various structures, such as muscles (brown) or blood vessels (red and blue), to re-merge them **(b)** (cf. Sec. 4.7.5). In the third example, the *natural* shape of the aorta is preserved **(c)**.

Images originally published in Journal of WSCG [326, Fig. 1].

Table 4.3: The results of the think-aloud evaluation of three trained anatomy experts. The numbers are denoted in years.

	Interviewees		
	I1	I2	I3
Part 1 – General Questions			
Gender	m	m	m
Age	26	27	43
Experience with Human Anatomy	2.5	3	12
Clinical Experience	4.5	0	0
Active Anatomy Teaching	0	3	12
Q1			
Q2			
Q3			
Q4			

	Lift Chart			Floor Map		
	I1	I2	I3	I1	I2	I3
Part 2 – Exploration Support						
Q5						
Q6						
Q7						
Q8						
Q9						
Q10						
Part 3 – Clinical Feasibility						
Diagnosis						
Therapy Planing						
Physician-Patient Consultation						
Interdisciplinary Communication						
Student Training						
Communication of Findings						

Legend: −− | − | ○ | + | ++

Table originally published in Journal of WSCG [326, Tab. 3].

Q1 How do you rate your anatomical knowledge?

Q2 How familiar are you with medical visualization techniques in general?

Q3 How familiar are you with exploration-assisting visualization techniques?

Q4 How do you rate your spatial thinking capabilities?

PART 2 – EXPLORATION SUPPORT. It was explained to the interviewees how to use the software environment. First, they were instructed to examine the data sets with lift charts. The currently displayed slice was highlighted in the lift charts, but structures could not be selected. Then, they examined the data sets with floor maps. After each exploration,

they were asked to answer the following questions w. r. t. each visualization technique (VT):

Q5 How easy is it for you to get a first overview of the data set using VT?

Q6 How easy is it for you to assess spatial relationships between structures using VT?

Q7 How much does VT support you to find anatomical abnormalities, e. g. tumors?

Q8 How easy is it for you to use VT for orientation?

Q9 How fast do you recognize segmented structures using VT?

Q10 Overall: How much do you like using VT?

PART 3 – CLINICAL FEASIBILITY. For the last part, they were asked to estimate both methods' feasibilities for certain clinical disciplines.

4.7.8 DISCUSSION AND FUTURE WORK

In this section, shortcomings and ideas to enhance floor maps will be discussed.

ENCOMPASSING STRUCTURES. It was demonstrated how the proposed method addresses overlapping artifacts (cf. Fig. 4.14). However, the used data sets did not have cases where one structure is embedded in another, e. g. tumors within organs. On the one hand, as long as suspicious structures are smaller than their context structure, overlapping volume will be assigned to it. However, this results in embedded structures being made larger than they actually are. On the other hand, if embedded structures are larger than their context structures, they will be removed. Therefore, an additional option should be included that detects and preserves embedded structures.

ELONGATED STRUCTURES. Elongated structures, such as blood vessels, are not distinguished from organs. Thus, they become severely deformed if they run somewhat horizontally through floors. On the one hand, their shape can be preserved, but on the other hand, this requires manual user input. This is no major drawback, since blood vessels are key features in many clinical scenarios, i. e. their natural shape will often be preserved. In contrast, they could be transformed differently, e. g. into vertically (elevators) or horizontally (hallways) cuboid-shaped corridors. Map generalization methods could also be applied, since, e. g., blood vessels are similar to lines on maps (Fig. 4.1).

COMPUTATIONAL PERFORMANCE. The *room extrusion*, *overlap removal* and *mesh generation* processing steps require the longest processing times (cf. Tab. 4.2). This could be addressed via parallel processing. However, in the case of overlap removal, a well-elaborated process and memory management would be necessary, since structures are processed pairwise (read below). Regarding mesh generation, the cell extent of the *Neighboring Cells Algorithm* can be increased, which in turn decreases mesh quality [25, 299].

NON-COMMUTATIVE OVERLAP REMOVAL. The results of overlap removal depend on the execution order. This does not apply if only two structures overlap each other. However, if more structures are involved, one of them can become very large by incorporating the

others. Currently, such cases are not addressed by the proposed method, however, they should be in the future, since some anatomical regions, such as the head and neck area, have a very high anatomical variability. More generally, to minimize geometrical distortion, overlapping artifacts could be addressed by more refined approaches, e. g. by methods that were developed to separate merged lung parenchyma [203].

EVALUATION – TOO MUCH GOING ON. Algorithm 4.1 minimizes the number of floor divisions, but the interviewees reported that "*there is too much going on*" (see Fig. 4.16). Cognitively, this can be explained by the work of Alvarez and Cavanagh [11]: *Our* WMC is limited w. r. t. the number of displayed objects and their complexity (cf. Sec. 4.2). With respect to lift charts, each structure is represented by one simple bar and although the rooms in floor maps also have a simple geometric appearance, the final presentation can be cluttered. This could be addressed by re-merging small structures in upper and/or lower direction. However, this would contradict the underlying idea of floor maps in which *clutterness* represents regions with a high anatomical variability. More generally, it would be interesting to know what users look at in floor maps, i. e. what they find salient, e. g. to gain insights how *distracting* floor divisions are [256, 421].

EVALUATION – READING REQUIRED. Floors are defined when the composition of segmentation masks changes [338]. The interviewees understood this design choice, however, they stated that it "*requires a lot of reading*". Typically, they orientate themselves using anatomical landmarks, such as vertebrae. With respect to lift charts, the interviewees said that a hierarchical division of lift charts would be beneficial, e. g. by dividing the spine into its cervical, thoracic and lumbar parts [28]. Thus, the proposed floor map method should be revised in this direction. However, using vertebrae as landmarks only works between the head and pelvis, and thus, landmarks have to be chosen w. r. t. the anatomical region.

EVALUATION – CLINICAL FEASIBILITY. Floor maps were evaluated w. r. t. their clinical feasibility. For diagnosis and therapy planning, distances between targeted and surrounding (risk) structures are important key features. When compared to lift charts, floor maps introduce less geometric abstraction, however, in-plane relationships can become distorted. Addressing this directly via floor maps is challenging, and thus, the original images are displayed in the GUI. For communication tasks, floor maps were rated as suitable as lift charts. With respect to patient consultations, the achieved results may be too confusing and/or overwhelming [159]. However, this has to be evaluated first. Furthermore, the claim that floors maps can support anatomy education cannot be fully supported currently. To do so, a more in-depth evaluation has to be conducted, e. g. by student interviews and/or via staged audits (exams) [151, 382].

COLORIZATION. Currently, colors are automatically assigned by a LUT that parses structure labels. On the one hand, the employed color palettes use a categorical color-coding to make rooms well distinguishable. The colors were manually derived from organ photographs, which makes them more realistic than conventional color schemes [67]. However, when comparing healthy and cadaverous tissue, the color palettes vary

significantly, i. e. cadaver tissue is homogeneously yellow-brownish. Thus, adding an additional color mode for this scenario might be an interesting feature. Furthermore, color vision deficiencies were not yet addressed [206, 253].

AUTOMATIC VIEWPOINT GENERATION. Above, automatic view generation techniques were discussed (cf. Sec. 4.5). Although floor maps would benefit from such a feature, e. g. via user-defined floors and/or rooms of interest, it was not added. However, the employed exploration-supporting interaction facilities, i. e. synchronized slicing (2D-3D) and structure selection (3D-2D), should not hinder the overall data set exploration and/or assessment, since *we* are able to construct concise mental representations from piecewise information [528]. Another idea for more refined interaction facilities, e. g. by pulling out individual floors, could be taken from Jin et al. [217].

KEY FEATURES IN CLUTTER. It was stated that *protecting* certain structures, e. g. if they are too small, makes them key features. For other visualization techniques, key features are typically presented in a way to naturally draw interest. Here, they are also presented in a unique way. However, numerous floors and rooms draw more attention than structures that are depicted in their normal way.

TRUE MULTIMODAL MEDICAL IMAGE DATA. Floor maps can be created from any combination of modalities if the image sources are registered. Inspired by the work of Nguyen et al. [360], physiological and/or functional hotspots could be included as *emissions*. From an interaction perspective, users could transform the presentation into a *lights out* mode, and thus, hotspots would highlight suspicious structures.

VARYING DEGREES OF ABSTRACTION. To define rooms, the maximum axial shapes of segmentation masks are utilized, which typically introduce a high degree of geometric abstraction [501]. With respect to the aforementioned possibilities to abstract point sets and objects, floor maps with varying degrees of abstraction could be created (cf. 4.2).

4.8 SUMMARY

In this chapter, a novel visualization approach was presented that transforms labeled medical image stacks into a three-dimensional map layout, namely floor maps. Although map-based approaches were already used by other authors in medical and/or clinical contexts, the novelty is that building-like representations can be created. Prior to that, w. r. t. visualization techniques for medical image data, visualization techniques for (digital indoor) maps, and *our* cognition of maps were discussed. Other aspects, such as similar research challenges for both domains, were also briefly presented. The proposed approach was evaluated by three trained anatomy experts. With respect to these results, the potential and limitations of floor maps were discussed.

In the Chapters 5 and 7 two other map-based visualization techniques will be presented, i. e. to visualize the safety margin-based risk of instrument pathways for needle-based interventions in the spine, and to present metastases-related diagnoses of lymph node stations in patients with primary lung cancer. Furthermore, w. r. t. color-coding of medical

images, two color-coding methods for PET images and therein defined ROIs will be presented in Chapter 7.

5 RISK VISUALIZATIONS FOR RFAS IN THE SPINE

RADIOFRQUENCY ablation (RFA) is an image-guided and minimally invasive type of intervention in radiology. Generally, during ablations, needle-like instruments are inserted into lesions, e. g. tumors and/or metastases, to trigger cell death by heavily cooling down or heating up surrounding tissue. There exist various types of thermal ablations, such as cryo-, microwave- and laser-based ablations, that destroy tissue via nitrogen, microwaves or concentrated light, respectively. The works presented in this chapter are focused on RFAs that employ alternating electrical currents to coagulate tissue [42, 503]. However, they are designed to be as generalizable as possible to also support other types of ablations. Typical target organs for RFAs are the lungs [103], the kidneys [220], the liver [337], the breast [361] or the prostate [441]. Moreover, in patients with bone lesions, RFAs can also be conducted for pain management purposes [144]. In patients with metastatic bone lesions, they can also be combined with other types of treatment, such as external radiotherapy, chemotherapy or surgeries [88]. However, in such patients, RFAs are primarily conducted in a palliative setting and curative prospects are often not realistic [129]. Generally, RFAs have the advantage that more surrounding healthy tissue can be preserved, but they are limited w. r. t. the targeted lesions' sizes.

In this chapter,

- a requirement analysis for computer- and robot-assisted RFAs and
- a two-step risk assessment method for pathway definition and creation

are presented. The requirement analysis – and partial implementation – are primarily used as an introduction for the two-step method, which this chapter is focused on. The proposed two-step method aims to assist physicians, e. g. neuroradiologists, during planning and execution of RFAs to treat spinal metastases (cf. *Division of Work* chapter). First, a background on the human spine w. r. t. its gross anatomy, bone biology and metastatic diseases is provided (Sec. 5.1). Subsequently, backgrounds on ablation techniques, such as cryo- and radiofrequency ablations, are provided (Sec. 5.2). In Section 5.3, an exemplary clinical RFA workflow is presented w. r. t., for example, visualization support during intervention planning and instrument guidance during intervention execution. Moreover, in this section, a brief background on robots in medicine will also be provided since our methods, in addition to manually conducted RFAs, aim to offer cognitive and physical assistance during robot-assisted drilling, too. Subsequently, we present our works in the Sections 5.4 and 5.5. This chapter is concluded by a short summary (Sec. 5.6).

This chapter is based on:

[325] **Merten, N.**, Saalfeld, S., Hanses, M., Becker, M., Adler, S., and Preim, B. "A Software Prototype for Treatment Planning and Intervention Support of Robot-Assisted Radiofrequency Ablations of Vertebral Metastases." In: *Proc. of German Society of Computer- and Robot-Assisted Surgery*. 2017, pp. 89–94

[319] **Merten, N.**, Adler, S., Georg, H., Hanses, M., Becker, M., Saalfeld, S., and Preim, B. "A Two-Step Risk Assessment Method for Radiofrequency Ablations of Spine Metastases." In: *Computers in Biology and Medicine* 108 (2019), pp. 174–181

[320] **Merten, N.**, Adler, S., Hanses, M., Saalfeld, S., Becker, M., and Preim, B. "Two-Step Trajectory Visualization for Robot-Assisted Spine Radiofrequency Ablations." In: *Proc. of Bildverarbeitung für die Medizin*. 2018, pp. 55–60

With respect to these publications, this chapter is organized in chronological order. First, a requirement analysis is presented (Sec. 5.4). Since not all of these requirements were fulfilled in the first prototype, we focused on how to find and define *good*, i. e. safe and clinically feasible, instrument pathways into vertebral metastases. Thus, we addressed the respective requirement by conceptualizing and evaluating a two-step method that is intended to offer cognitive and physical support during intervention planning and execution.

Note that many of the (technical) remarks in this chapter are a result of our collaboration with the Fraunhofer IFF and the University Clinic for Neuroradiology in Magdeburg. Thus, certain details can be very tailored to their setups and procedures, e. g. a certain choice of robot or combination of imaging modalities. However, similar setups and scenarios could also benefit from our findings and, where applicable, explanations will be formulated as general as possible. For example, this includes other needle-based interventions and/or tests, such as biopsies, and anatomical regions and/or organs, such as the lungs.

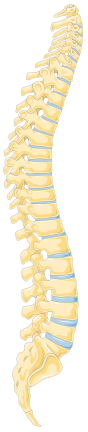

Figure 5.1: The human spine from the *atlas* (top), which serves as the skull's pedestal, to the *sacrum* (bottom), which is also the middle part of the pelvis.

5.1 BACKGROUND ON THE HUMAN SPINE

Here, brief overviews about the human spine's gross anatomy, its vertebrae, bone biology and consequences w. r. t. density changes due to bone conservation are provided. For more information, see [460, Ch. 5, p. 84].

5.1.1 GROSS ANATOMY – THE SPINE

Our spine is a multi-component and multi-part anatomical structure that stabilizes the upper body between the head and pelvis (see Fig. 5.1). Its primary component is bone tissue, in the form of multiple so-called *irregular* bones that are called vertebrae. In total, the spine is composed of 33 vertebrae and/or bones. Typically, the cervical (cf. Fig. 5.2a) and thoracic (cf. Fig. 5.2b) vertebrae are movable, whereas the lowest vertebrae of the lumbar part (cf. Fig. 5.2c) can sometimes be movable and sometimes be fixed [135]. Between vertebrae, there lie the so-called *intervertebral discs* which act as buffers against external forces which also allow for rotations and bending. Additionally, various ligaments, skeletal muscles and facet joints further stabilize the spinal column.

5.1.2 GROSS ANATOMY – VERTEBRAE

Bones are categorized into four groups [87], namely

- long bones, such as the claviculae and the femora,
- short bones, such as the patellae and the carpal bones,
- flat bones, such as the skull, the sternum and the ribs and
- irregular bones, such as the vertebrae and the sacrum.

Typically, vertebrae are *bulky* bones with a front, a middle, and a back part (see Fig. 5.3). Their front parts, i. e. their *bodies*, are connected via the intervertebral discs and have

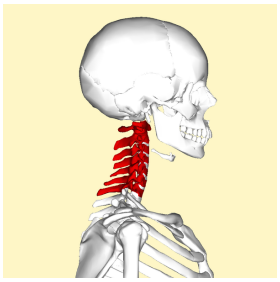

(a) Cervical Part

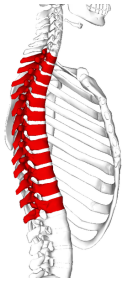

(b) Thoracic Part

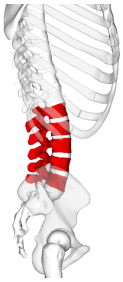

(c) Lumbar Part

Figure 5.2: The three main parts of the human spine. Typically, the cervical, thoracic and lumbar compartments consist of seven, twelve and five movable vertebrae, respectively. The sacrum and coccyx below the lumbar part are composed of five and four bones, respectively.

relatively large, flat and slightly concave surfaces. Independently from the spinal compartment, these parts are relatively homogeneous and only vary in size, i. e. they decrease in size in superior (cranial) direction. Their back parts, i. e. the back-pointing spinous processes and laminae, change their general directions. For example, the cervical dorsal processes (*thorns*) are long and proceed horizontally, whereas lumbar spinous processes are rather short and round. In contrast, some dorsal processes in thoracic vertebrae can also proceed downwards (cf. Fig. 5.3f). Generally, these processes increase the contact areas for ligaments and muscles, which increase the upper body stability and flexibility.

The middle parts of vertebrae consist of lateral processes, the so-called pedicles that encompass the spinal canal. The pedicles also connect the front and lateral parts of vertebrae, whereas the aforementioned laminae connect the middle and back parts. Generally, the spinal canal decreases in size in caudal (downwards) direction [300], since the spinal cord splits up repeatedly to connect organs and other structures to the brain via nerve fibers. The outgoing nerve fibers travel through the neuroforamina, which are the bridge-like cavities

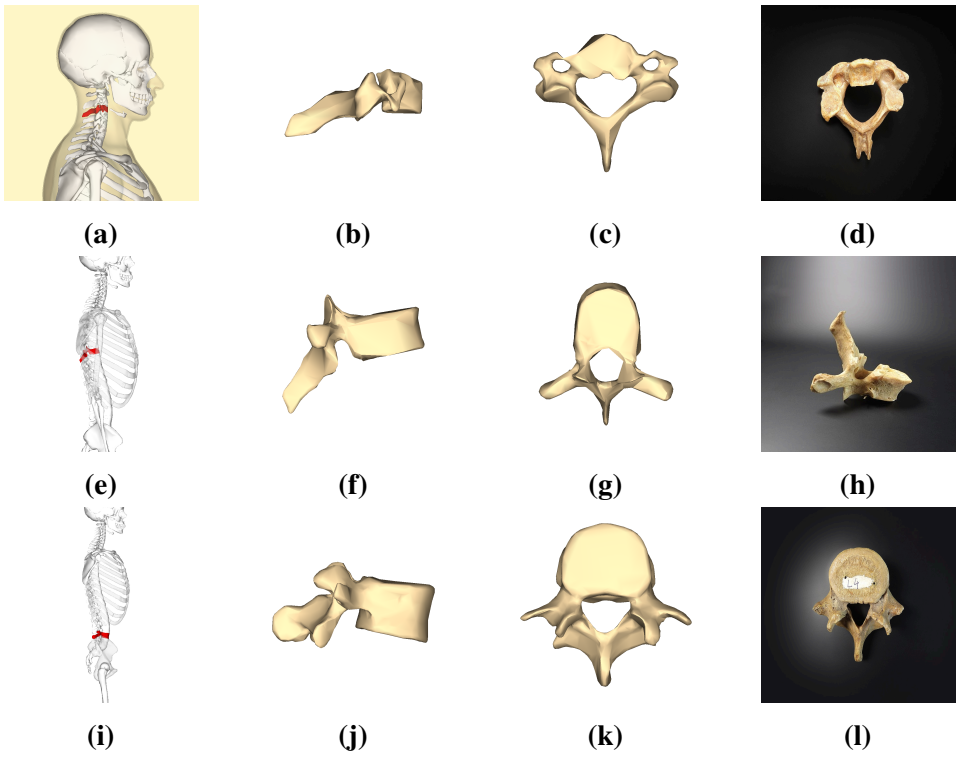

Figure 5.3: Various depictions of cervical **(b–d)**, thoracic **(f–h)** and lumbar **(j–l)** vertebrae. The Subfigures **(a,e,i)** are used to provide an anatomical context.

between pedicles of adjacent vertebrae (cf. Figs. 5.3b, 5.3f and 5.3j). The spinal cord in the canal is the major risk structure during RFAs w. r. t. pathway creation and ablation heat.

5.1.3 BONE BIOLOGY

Bones are a strong and very adaptive type of tissue [460]. Bone tissue is arranged in a so-called bone tissue matrix. There exist two types of matrices: The hull (mantle, outer shell) of bones, namely cortical or compact bone tissue, is very dense and hard. In contrast, less dense matrices, namely trabecular, cancellous and/or spongy bone tissue, provide inner-bone stability, but also reduce their overall net weight. Furthermore, this rather loose bone matrix offers more space for inlying blood vessels. Among other substances, bones are made up from water, collagen, calcium and phosphorus. Due to their higher electron counts, the latter two elements are the reason that more photons are absorbed during X-ray-based image acquisitions, i. e. that bone is more radiodense than other types of tissue, and thus, appears brighter [118, 242, 460] (cf. Ch. 2).

BONE TISSUE CELLS. There exist four major types of bone cells, namely *osteoblasts*, *osteoclasts*, *osteocytes* and *bone lining cells*. *Our* bone health is maintained by their communications and interactions with each other [133, 460]:

- *Osteoclasts* are responsible for bone resorption, i. e. they break down bone tissue.
- *Osteoblasts* are responsible for bone formation, e. g. they mineralize the bone tissue.
- *Osteocytes* and *bone lining cells* are derivatives from matured osteoblasts. For example, "*once embedded in the matrix, [osteoblasts] become osteocytes*" [460], which make up the majority of bone matrices.

In healthy bones, bone formation and resorption exist in an equilibrium-like state, but during aging "*minerilization increases [...] even though bone mass decreases*" [460]. However, imbalances can result in bone diseases or bone tissue disorders, for example

- *Osteolysis*, which describes the process of abnormal bone resorption or
- *Osteosclerosis*, which describes an excessive amount of bone tissue formation.

Consequently, bone density can be greatly reduced or increased, which can result in pain and/or loss in structural integrity [89].

IMBALANCES DUE TO CANCER TISSUE INFILTRATION. Primary bone cancer and/or metastases can harm bone cell communication, and thus, alter bone matrix density [349]. However, primary bone cancer is rarer than bone metastases from other sites [2, 3, 106] (see Tab. 5.1). Recent estimated numbers from the United States' Cancer Statistics show that in 2019 there were 3500 cases of primary bone cancer [445]. In contrast, the 5-year incidence rate of bone metastases in patients with primary breast cancer was reported to be roughly 6 % [188], for which roughly 270 000 new cases were reported [445]. Moreover, "*in patients with advanced metastatic disease[s]*" [437], the incidence of bone metastases can go up to 75 % [89, 90, 437]. With respect to the primary cancer's anatomical origin, the *disease pattern* can vary. For example, primary breast cancers primarily result in osteolytic disease patterns, whereas primary prostate cancers primarily

Table 5.1: Incidence rates of bone metastases w. r. t. certain primary cancers.

Primary	Estimated New Cases 2019 [445]	5-yr Incidence [%] [188]	Incidence During Advanced Metastatic Disease [%] [437]
Breast	271 270	6	65–75
Prostate	174 650	24.5	65–75
Lung	228 150	12.4	30–40
Melanoma	96 480	2.5	14–45
Renal	73 820	8.4	20–25

result in osteosclerotic patterns [349]. However and although osteolytic and osteosclerotic disorders are contrary to each other, actual disease patterns are often heterogeneous, i. e. the same bone can have soft and hard compartments (cf. Fig. 2.2b) [166, 349, 373].

5.1.4 INTERMISSION – BONE CONSERVATION AND VARIATIONS IN DENSITY

Step 2 of our two-step method aims to offer physical assistance during manual and robot-assisted bone drilling. Therefore, we conducted drilling experiments with dried and fat-freed vertebrae (cf. Fig. 5.20). Drying and fat-freeing are tasks in bone conservation which in humans are primarily done for education and research purposes. From a workflow perspective, bones are conserved via superficial cleaning, optional de-fattening, drying and sometimes bleaching for presentation purposes. There exist various de-fattening procedures, e. g. cooking in acetone or kerosene, however, it appears that de-fattening is mostly done as a preprocessing step for bleaching to make bones more durable and nice-looking [7, 238]. Bone drying is typically conducted in ovens at about 100 $°C$ for various hours [238]. Bone strength tests are often conducted via press-supported breaking tests, for example, to evaluate the effects of different conservation techniques on bone density. When fresh and frozen-fresh bones are compared, there are only minor differences, however, drying can result in major strength differences up to 50 % [238, 301]. Presumably, this is due to bone marrow and collagen denaturation, i. e. bones loose their elasticity and become more brittle [475].[1] In any case, since we used conserved bones, we expect that higher drilling forces would be required during intra-interventional in vivo bone drilling. With respect to the inter-operatively used cone-beam DynaCT images, this will be discussed below.

5.2 BACKGROUND ON ABLATION TECHNIQUES

Vogl et al. [503] define "*"tumor ablation" as the direct application of thermal or chemical therapies to a specific focal tumor (tumors) in order to achieve either eradication or*

[1] Something similar happens in fresh and seasoned wood w. r. t. their burning and smoking capabilities.

substantial tumor destruction". In contrast to surgeries, ablations are less invasive and typically leave more healthy tissue intact. For chemical ablations, aggressive substances, such as ethanol or acid, are injected into suspicious tissue via needles and/or catheters [6]. In the following, thermal ablation techniques will be explained in more detail.

5.2.1 CRYOABLATION – CELL DEATH THROUGH COOLING

In cases of cryoablations, which are somewhat similar to chemically-based ablations, liquid nitrogen, for example, is injected into tumor tissue to trigger cell death [450, 503]. Typically, this is achieved via catheters, over-catheter balloons or needles that are employed to administer said substances [6]. Subsequently, tissue is cooled down between $-20\,°C$ to $-75\,°C$, which results in irreversible cell damage during thawing [85, 233, 450]. However, with increasing distance to the cryogenic center, the cooling effect decreases "*and studies have shown that this temperature needs to persist to* $1\,cm$ *beyond the tumour periphery to ensure complete ablation*" [85]. For example, Bilchik et al. [52] reported that their cryogenic lesions had radii up to $3\,cm$. During interventions, the emerging *ice ball* can be evaluated via ultrasound. For larger lesions, multiple probes can be employed. However, this depends on the ablation zone shaping (read below). Moreover, while other thermal-based techniques *just* require power, cryoablations require an additional cryogenetic medium. Note that something similar was discussed before w. r. t., for example, PET and SPECT image acquisitions, since they also require additional radiotracers.

5.2.2 RADIOFREQUENCY ABLATIONS – CELL DEATH THROUGH FRICTION HEAT

For RFAs, electrodes that send out alternating currents are placed inside targeted lesions [6]. The energy level ranges from $375\,kHz$ to $500\,kHz$ and ion grids of surrounding tissue try to arrange their orientation w. r. t. the current's direction [6, 503]. However, since "*[t]issues are imperfect conductors of electricity*" [6], friction occurs that results in locally increasing temperatures [85]. With respect to heat, "*[a]t temperatures of around* $40\,°C$ *to* $45\,°C$*, irreversible cell damage occurs only after prolonged exposure (from* $30\,min$ *to* $60\,min$*)*" [85]. However, target temperatures range between $60\,°C$ to $100\,°C$ and "*[a]bove* $60\,°C$*, rapid protein denaturation occurs, which is immediately cytotoxic and leads to coagulative necrosis*" [85]. Typically, ablations can be implemented fairly quickly and typically do not take longer than $15\,min$ [281], whereas the whole intervention can last up to roughly $45\,min$ in the spine [144].

ABLATION ZONE SHAPING. There exist various types of RFA electrodes that can be employed to shape ablation zones [395]. Generally, RFA electrodes are straight needle-like instruments with an uninsulated tip, which applies the aforementioned alternating currents [6, 454]. The electricity is generated by a generator. In the following, the most common electrode types are discussed briefly and for more information see the works of Ahmed, Ellis and van Sonnenberg et al. [6, 120, 454].

- *Monopolar electrodes* only have one electricity pole, and thus, need grounding to enable the electricity to flow through patient tissue. Typically, this is achieved via so-called *grounding pads* that are placed on the patient's hip [6]. The electrode tips

can be internally cooled by a saline solution, which decreases the risk of "*tissue charring*" [454]. The active tip lengths can range between 0.9 *mm* to 80 *mm* and the typical ablation pattern is cylindrically shaped along the active needle part [120]. The ablation radius is roughly 1 *cm* [6].
In the spine, electrodes with 20 *mm* to 30 *mm* long active tips can be employed [144]. With respect to our method, we did not employ ablation zone prediction and/or simulation techniques [110, 230, 400].

- In contrast, *bipolar electrodes* have two poles along their tips. Thus, no external grounding is necessary to *draw* the electricity. Moreover, saline solution is often employed between the poles go guide the applied currents [6].
- Multiprobe arrays are employed when target lesions are too large for one electrode and/or if their general shape is not cylindrical [120].
  - When monopolar electrodes are employed in arrays, they are arranged in a way that their ablation zones overlap each other. Moreover, they coagulate surrounding tissue independently.
  - When bipolar electrodes are employed in arrays, very individually shaped ablation zones can be achieved, e. g. between two non-opposing poles in two electrodes [138]. However, *currently* active poles have to be synchronized, which makes such setups technically more challenging [316].

  This is relevant in our work, since spine metastases may have to be treated via two (bipolar) RFA electrodes. Thus, in our prototype, the placement and orientation of two applicators is supported.
- Umbrella-shaped instruments enable physicians to *unfold* needle tips to create larger ablation zones with *one* electrode. However, physicians must exercise care to not penetrate nearby risk structures, such as blood vessels. It was reported that ablation zone radii between 1.5 *mm* to 2.5 *mm* can be achieved [6, 503].
  Presumably, such instruments could be employed for very soft bone metastases. However, they cannot penetrate bones, and thus, are out of the scope of this thesis.

Accurate ablation zone shaping is challenging, since nearby blood vessels function as so-called *heat sinks* that *carry* away heat. In other words, they somewhat *cool* surrounding tissue and decrease the ablation zone's size. With respect to RFAs in the spine, this is primarily done by veins in the vertebrae and the cerebrospinal fluid in the spinal canal [114]. Bone tissue also is a good electrical insulator, which further *protects* nearby nerves from being damaged [6].

5.2.3 OTHER HYPERTHERMAL TECHNIQUES

In addition to RFAs, there exist other ablation techniques that *apply* heat to induce cell death. Some of them are presented here briefly and for more details see the works of Ahmed and Chu et al. [6, 85].

MICROWAVE ABLATION. In contrast to RFAs, microwave ablation systems operate at higher energy levels of 915 MHz or 2.45 GHz [6]. Rather than relying on electrical conduction, microwaves can realign molecules which causes locally increased temperatures of around 150 $°C$ and above [6, 503]. This approach can be used to ablate tissue areas with radii around 2 cm [85]. However, such systems require higher energy inputs, and thus, thicker cables must be run through the Operation Room (OR) [6]. Moreover, no grounding pads are necessary and multiple microwave electrodes can be employed.

LASER ABLATION. Laser ablations, namely Laser-Induced Thermal Therapy (LITTs), utilize light energy to ablate tissue. On the one hand, such systems are very precise. On the other hand, they cannot penetrate tissue very well and can only be used to create ablation zones with radii of roughly 2 mm [6, 85, 294]. Typically, lesions that are larger than 3 cm to 5 cm are not treated by single laser probes [20, 294, 439]. However, by combining multiple probes and/or employing a "*pull-back procedure*" [503], elongated ablation zones can be created. Laser ablations can be used in patients for which RFAs, for example, are not feasible, e. g. due to metallic implants and/or pacemakers [129]. For intra-interventional instrument guidance, MR image guidance can be employed [503].

5.3 AN EXEMPLARY RADIOFREQUENCY ABLATION WORKFLOW

Here, a simplified clinical workflow is described for which it is assumed that an RFA is conducted to treat spinal metastases (see Fig. 5.4). This is done to present the current clinical workflow, for example w. r. t. instrument guidance in- and outside of patients or w. r. t. cognition-supporting visualization techniques for needle-pathway planning, but also to motivate our work in the following two sections. Furthermore, note that some of the cited methods in this section specifically focus on screw insertions in the spine. From a general perspective, they are, however, very similar to each other in the aspects that this section and our work focuses on, for example the definition of clinically feasible pathways.

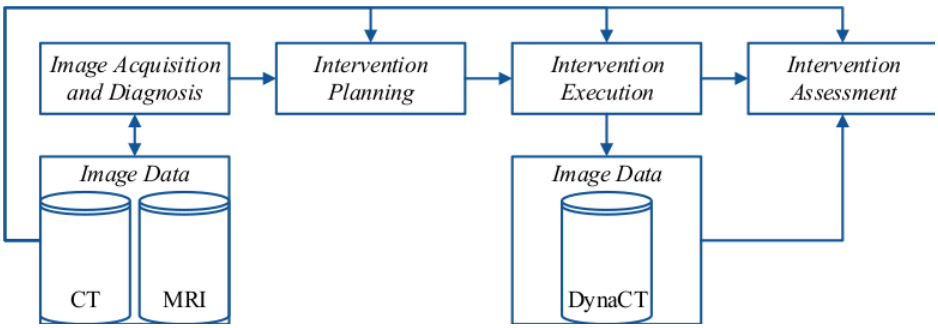

Figure 5.4: Simplified overview of RFAs from a clinical workflow perspective. Below, we will reuse this outline to describe our two-step risk assessment method.

Image inspired by [319, Fig. 1].

5.3.1 IMAGE ACQUISITION AND DIAGNOSIS

Bone pain is the most often occurring symptom of heavily altered bone densities and can also result in bone fractures, deformities and "*nerve-compression syndromes such as spinal-cord compression[s]*" [349] (cf. Fig. 5.21). From an image acquisition perspective, PET, SPECT, CT and MR images and combinations of them can be assessed to find the pain source [184]. For example, SPECT bone scintigraphies via ^{99m}Tc can be acquired to highlight bone lesions [123, 146]. On the one hand, they have a high sensitivity and can be employed to find bone metastases. On the other hand, however, they have a rather low specificity, since said radiotracer can also accumulate in infections and bone fractures. As mentioned before, the same applies to ^{18}F-FDG w. r. t. tumor and inflammatory tissue. In combination with conventional radiographies and/or CT images, however, the specificity of SPECT images can be increased [123].

In our setup, for diagnosis – and also intervention planning – various imaging modalities are employed, namely CT, MRI T_1 with and without contrast agent, MRI T_2 and MRI STIR (see Fig. 5.5). This modality combination is assessed via differential diagnoses to

- re-assess the patient's current cancer staging or
- to conclude about the primary tumor in patients that have no history of cancer [373].

On the one hand, CT images are assessed w. r. t. bone density and/or fracture patterns within (remaining) bone tissue. In contrast, MR sequences are primarily assessed w. r. t. intra-sequence image contrasts. For example and as mentioned before, kidney carcinomas tend to result in osteolytic bone density patterns which can result in heavily altered (*destroyed*) vertebral bodies. T_1 images often show decreased intensities in affected vertebrae, since

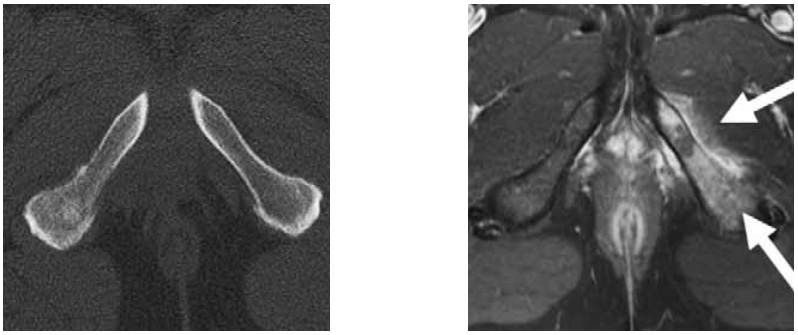

(a) CT **(b)** MRI T_1

Figure 5.5: Physicians typically assess bone lesions and/or metastases in CT and MR images via differential diagnosis. This combination is beneficial, since lesions can be occult in one modality, whereas they can be very prominent in the other one [146] **(a–b)**. Here, the primary cancer was unknown.

bone marrow is *replaced* by metastatic tissue (fat is bright in T_1) [279]. Moreover, T_2 and STIR images also often show an altered and overall heterogeneous tissue composition with the STIR image further pointing to a water-blood mix in affected vertebrae [496]. Physicians also look for cases of "*extra-compartmental*" disease patterns [479], i. e. when the metastases *grew* into nearby structures, such as the spinal cord, aorta, fatty and muscle tissue, since this heavily influences diagnoses and treatment options [349]. Subsequently, if one or multiple lesions were found, biopsies are conducted to conclude about the origin of the targeted lesions [40, 340, 373]. Depending on their outcome and other aspects, such as the primary tumor's site of origin and the actual disease pattern, scoring systems can be used to decide which type of treatment is feasible and can be conducted [477, 479].

5.3.2 DISCUSSION – TREATMENT OPTIONS

Common treatment options are external radiotherapy, chemothrapy, surgery and combinations of them [88, 166, 340, 373]. There also exist drug treatments, e. g. via *biophosphonates* [90], which momentarily cause "*programmed cell death*" in osteoclasts [292]. Thus, osteolytic disease progression can be halted, but, overall, "*the cancer continues to progress*" [292]. Due to their radical nature, surgeries, such as vertebral resections, are often considered *the last option*. Moreover, patients with bone metastases can be in an overall bad condition which renders surgeries often unfeasible. When surgeries are conducted, however, they are typically accompanied by subsequent vertebral augmentation [32], for example via

- vertebroplasties, which are procedures during which bones are filled up with a cement-like substance or
- kyphoplasties, which additionally employ balloons prior to filling to increase control over the cement's flow behavior.

This is done to restore structural integrity of the spine. With respect to the degrees of invasiveness, ablations are in between radio- or chemotherapies and surgeries, since they require pathway creation via bone hammering and/or drilling, but affect tissue more locally.

In most patients with bone metastases, RFAs are conducted for palliative reasons, e. g. to reduce back pain, whereas curative prospects are rarely realistic [88, 378]. As Lutz et al. report, "*external beam radiotherapy continues to be the mainstay for the treatment of pain and/or prevention of the morbidity caused by bone metastases*" [307, 429]. However, w. r. t. short-term pain relief ($< 1\ yr$), RFAs also showed promising prospects, but with yet unknown long-term implications [281]. Pain relief after cryo- and RFs-based interventions was reported to set in within $24\ h$, whereas radiation and chemotherapy can even fail to achieve pain relief in some patients [357, 413]. Presumably, this is the case since ablations alter (pain-inducing) tissue *instantly*, whereas other methods require time to show results [480]. Moreover, given that a radiation therapy is conducted successfully, it has to be assessed what happens to the lesion, e. g., if it breaks and results in a fracture. Therefore, vertebral augmentation can also be used for RFAs, since pathways can subsequently be used for cement and/or balloon insertion, which is not possible straightforwardly with external radiation therapies [427].

5.3.3 GENERAL CHALLENGES IN SPINAL INTERVENTIONS

Interventions in the spine, especially w. r. t. bone hammering and/or drilling, require craftsmanship (cf. Fig. 5.4). For RFAs, physicians create pathways during manual hammering or drilling [40], and thus, they require a lot of force to penetrate bone tissue to subsequently insert the RFA electrodes. Another example are screw insertions, e. g. for spinal corrections and/or fixations. Generally, any type of intervention in the spine is spatially challenging. Transpedicular pathways, i. e. through the pedicle(s), are preferred, since this maximizes remaining structural integrity [79].Typically, however, this is only feasible in lumbar and certain thoracic vertebrae, since their pedicles have enough cancellous *buffer* tissue around to-be-inserted pathway-creating instruments. For example, pedicle dimensions roughly range between

- 4 *mm* to 6 *mm* in cervical vertebrae [296], excluding the atlas and axis vertebrae,
- 5 *mm* to 8 *mm* in thoracic vertebrae [101, 521, 520] and
- 9 *mm* to 18 *mm* in lumbar vertebrae [84, 229].

Note that it is challenging to provide more precise information here, since pedicle measurements depend on various factors, such as

- patient-specific information, such as age, sex, height, and ethnicity,
- measurement-specific information, i. e. if image data or cadavers were examined,
- cohort-specific limitations, i. e. how big, and thus, how representative the assessed specimen w. r. t. all individuals are and
- morphology-specific information, i. e. if the
  - inner and/or outer pedicle dimensions were measured, i. e. with and/or without the cortical hull and
  - if the pedicle width and/or height was measured.

With respect to patient-specific information, Yu et al. reported that "*male, taller and heavier specimens have bigger pedicles*" [521] (cf. [160]). Due to these spatial restrictions, midthoracic and cervical vertebrae are often accessed parapedicularly, i. e. along but outside of the pedicle(s), and in a laminar manner, i. e. through the laminae, respectively [250, 304]. Note that other spine diseases, such as scolioses, can additionally alter vertebra morphology considerably [288, 367].

As discussed in more detail below, various visualization techniques aim to minimize the insertion depth and/or pathway length of instruments (cf. Tab. 5.2). In organs such as the brain or liver, the risk of *breaking through* to injure subsequent (risk) structures is rather low. Still, if this *risk* is deemed to be too high, after careful consideration, longer pathways can be chosen by entering the target organ from another surface region. In vertebrae, this is challenging due to the aforementioned spatial constraints and the necessity to penetrate the vertebra's surface as perpendicular as possible to prevent bone chipping or comminution.

Moreover, pathway-creating instruments have to be inserted into metastases which can bring them very close to the front side of vertebrae, e. g. near the lungs or abdominal aorta.

NECROSES DUE TO BONE DRILLING. During drilling, bone tissue heats up, which can result in irreversible osteonecroses. This takes place around 47 $°C$ [21]. Moreover, cytotoxic reactions in the spinal cord manifest around 44 $°C$ [114, 516]. Although tested in porcine nerves, temperatures between 60 $°C$ to 70 $°C$ can cause full functional loss in nerves in around five minutes [249]. In practice, however, some of these key values can be overshot. For example, Augustin et al. [21] reported up to 55.5 $°C$ during drilling in porcine femurs (ex vivo), whereas Eriksson et al. [121] reported up to 96 $°C$ in human femurs (in vivo, plate-based hip fixation). To measure temperatures, for both works, so-called thermocouples were used. Measuring temperatures during interventions, however, is more challenging, since, e. g., MR-based thermometry may not be employable due to magnetic materials (cf. [404]). This can be addressed, e. g., by decreasing the drill's feed rate and diameter, by employing two-step drills and/or by applying external colling via saline and/or water [21, 114, 121, 491]. Additionally, to decrease the number of drilling-related animal fatalities, bone-like plastics can be used for drilling experiments [126]. With respect to the transferability of interspecies-related results, note that human, dog and porcine bones were reported to be very similar in regard of bone tissue composition [5]. For more information about bone drilling, see the article from Pandey and Panda [366].

IMPLICATIONS FOR THIS THESIS. Vertebrae typically have more trabeculae (*small beams*) than, for example, long bones in their elongated parts, and thus, should require higher drilling forces (cf. [125]). However, the heads of femora also have many trabeculae and drilling through them will result in very high temperatures, even with saline-based cooling [87, 121]. Presumably, in patients with bone metastases, pain management in a palliative context outweighs small drilling-related necroses. However, external cooling should always be applied [21]. With respect to our drilling experiments, conserved vertebrae were used, and thus, drilling-related necroses were not an issue.

5.3.4 INTERVENTION PLANNING

In the following, visualization techniques are presented that aim to offer cognitive support during intervention planning, i. e. to find low-risk instrument pathways. Note that although such techniques exist, in actual practice, intervention planning is typically focused on the visual exploration of the diagnostic images alone. In other words, no refined image processing and/or analysis, (risk) visualization or interaction facilities are employed and the process of finding *good* pathways is primarily based on the experience of the physicians.

Finding *good* pathways is done w. r. t., for example, risk structures that must not be injured during interventions. Such structures can be labeled during planning and are then later used during intervention execution to enhance intra-operatively acquired images. This entails image registration, which is discussed in more detail below. Beforehand, visualization techniques can be employed that convey *risk*. *Risk*, however, is challenging to define and is often a combination of various aspects such as

- safety margins to nearby risk structures,

Table 5.2: Combinations of risk aspects in needle-based related methods. Parenthesized marks indicate that respective aspects were discussed but not yet included.

		Risk Aspects					Risk Coding
Category	Citation	*Safety Margin*	*Pathway Length*	*Instrument Diameter*	*Angle*	*Ablation Zone*	low → high
Mesh	Baegert et al. [26]	×	×		(×)	×	
	Zombori et al. [530]	×	×		×		
Projection	Navkar et al. [356]	×	×	×			
	Rincón-Nigro et al. [405]	×	×				
Map	Herghelegiu et al. [187]	×		×	(×)		
	Rieder et al. [403]					×	
Mesh & Volume	Our method	×	(×)	×			

Table originally published in Computers in Biology and Medicine [319, Tab. 1].

- the pathway length between an entry and target point,
- the instrument's diameter,
- the insertion angle relative to a context structure's surface or
- the ablation zone that was or will be ablated.

Some techniques employ weighting functions to assign varying degrees of importance to each aspect, which makes them more tailorable to certain application scenarios [26]. Table 5.2 shows related methods and depending on their implementation they were assigned to one of the following three categories: Risk is either presented

- on a surface mesh (cf. Sec. 3.4),
- by an outward projection or
- in a map-like presentation in an additional viewer (cf. Sec. 4.5.2).

MESH-BASED TECHNIQUES. For (surface) mesh-based techniques, risk is conveyed via vertex colorization. Baegert et al. [26] presented a technique that utilizes a sequential brightness scale to visualize risk to support liver tumor ablations (see Fig. 5.6a). This is done, for example, w. r. t. the instrument's insertion depth, which is typically aimed to be minimized. Light areas are intended to represent more safe insertion regions, however, the dark areas are more attention-drawing w. r. t. the light body surface. In contrast, Zombori et al. [530] utilize a sequential green-to-red color scale in the context of stereo-electroencephalographies (see Fig. 5.6b). Such studies are conducted by inserting electrodes into deep-seated brain areas to locally measure brain activity, e. g. in patients with epilepsy. During electrode insertion, risk structures, such as blood vessels, must not be injured. Moreover, the insertion angle should be maximized to approximately 90° w. r. t. the skull's surface to support skull drilling before electrode insertion. The authors employ a multi-hue sequential color scale to depict many *degrees of riskiness*. However, at a certain point, adjacent degrees become impossible to be distinguished.

PROJECTION-BASED TECHNIQUES. Projection-based techniques also encode risk via surface meshes, but the underlying image-generation approach w. r. t. safety margins

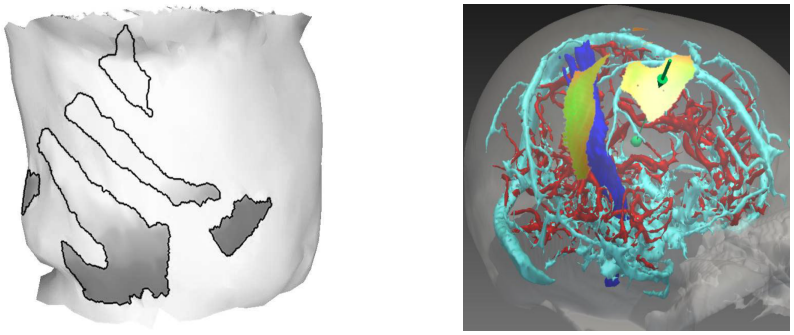

(a) **(b)**

Figure 5.6: For mesh-based methods, risk is visualized by color-coding vertices of the context structure's surface mesh. Baegert et al. [26] employ a grayscale to depict risky regions for instrument insertion with darker regions being more risky **(a)**. In contrast, Zombori et al. [530] employ a sequential green-to-red color scale with red representing pathways of high risk **(b)**.

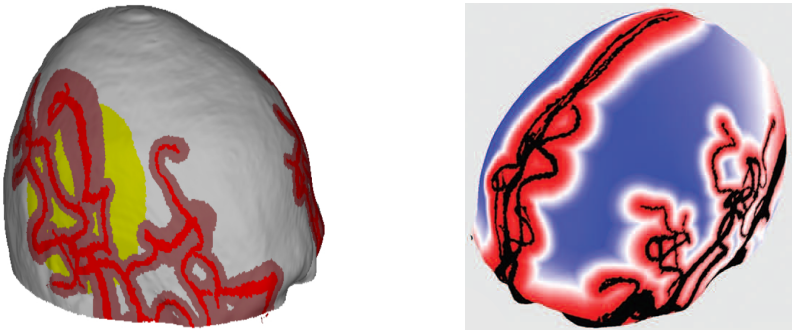

(a) **(b)**

Figure 5.7: For projection-based techniques, users also define a point inside a target structure. Subsequently, surface patches are color-coded in a ray casting-manner w. r. t., for example, safety margins and intersections with risk structures. Navkar et al. [356] depict their "*access maps*" rather categorically, i. e. by assigning one color to each risk aspect **(a)**. In contrast, Rincón-Nigro et al. [405] combine all risk aspects and present them with a diverging color scale **(b)**.

is different. For both types of techniques, users define target points inside the context structure, e. g. inside a lesion. For mesh-based techniques, context structure vertices are tested *inwards*, i. e. pathways are sampled and for each sample point safety margins to risk structures are evaluated. Subsequently, if safety margins are undershot, respective vertices are color-coded or even omitted. In contrast, for projection-based techniques, safety margins are tested *outwards* in a ray-casting manner. When margins are undershot, respective vertices are *just* color-coded w. r. t. the utilized color scale, e. g. red. In case of intersections, however, surfaces are represented via *casted shadows*.

In Figure 5.7, the works of Navkar and Rincón-Nigro et al. [356, 405] are depicted. Note that the work of Rincón-Nigro et al. is a GPU-based extension of the work of Navkar et al.. Rincón-Nigro et al. [405] combine all risk aspects via importance weights and visualize them with one diverging blue-white-red color scale. Due to white being the pivot color, more or less risky pathways are depicted with a high contrast between each other. In contrast, Navkar et al. [356] separate their employed risk aspects and employ a categorical color scale with one color representing one aspect, i. e. red for safety margins and yellow for short pathways. As depicted, their methods focus on neurosurgical interventions.

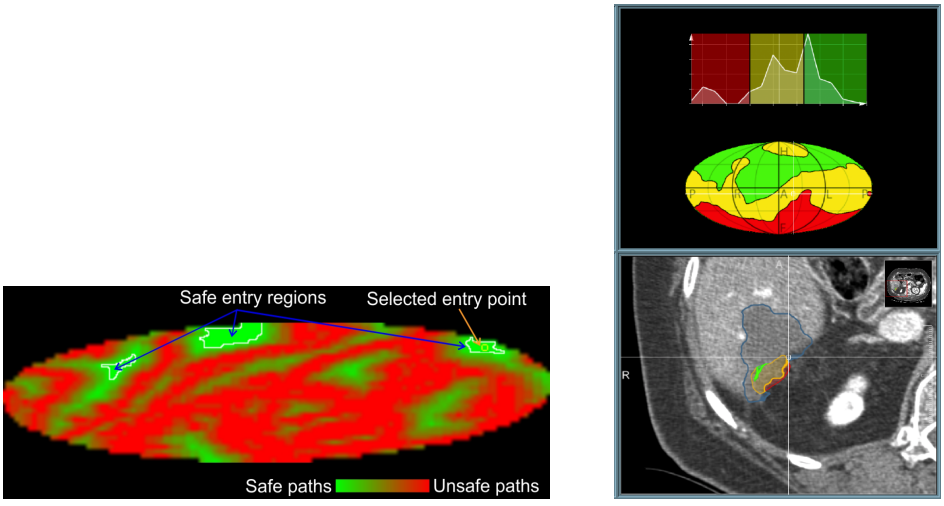

(a) **(b)**

Figure 5.8: For map-based pathway visualizations, it is assumed that they are depicted in an additional viewer. Herghelegiu et al. [187] presented their "*entry points stability maps*" that require users to define a target point and an entry region on the context structure's surface **(a)**. Subsequently, pathways are evaluated and color-coded in an outward projection-like manner. Rieder et al. [403] utilize the Mollweide projection to unfold ablation and tumor tissue to generate *real* maps **(b)**.

MAP-BASED TECHNIQUES. Here, map-based techniques are defined as techniques that depict risk in an additional viewer. However, note that the previously presented techniques can also be regarded as anatomically shaped "*access maps*" [356]. The "*BiopsyPlanner*" system by Herghelegiu et al. [187] utilizes an elliptically shaped green-to-red color-coded map to assist deep-seated brain biopsies. For this method, users define a target point inside the context structure and a surface area, e. g. on a DV-rendered skull. Thus, the authors exploit expert knowledge and experience w. r. t. typically employed pathways for certain lesion locations. Moreover, this limits computation times, since risk only has to be evaluated for a small surface area. This technique can also be regarded as a projection-based method, since rays between said target point and surface area are sampled and tested w. r. t. proximity and intersections, which results in the blood vessel-shaped red regions. Rieder et al. [403] utilize the *Mollweide* projection to unfold necrotic tissue to enable physicians to assess ablation zones (cf. Sec. 4.5.2).

For the liver, there exists some related work which is focused on the evaluation of *risk* for surgeries, i. e. tumor tissue resections. For example, Peitgen et al. [371] presented a method to enhance conventional DVRs by blood vessel and liver lobe and/or segment information. Later, Hansen et al. [172] proposed so-called "*risk maps for liver surgery*" (cf. Fig. 4.8a). Here, arbitrarily shaped planes can be placed inside an organ model, such as the liver, which are then utilized to plan tumor resections w. r. t. to-be-resected organ parts and safety margins to risk structures, such as blood vessels. Note that this approach is not listed in Table 5.2 since it is focused on surgeries. Additionally, Hansen et al. [171] evaluated how much impact 3D visualization techniques and model-based risk analysis methods have, e. g. to alter surgical strategies. The authors could show that "*model-based risk analysis enhances the awareness of surgical risk in the planning stage*" [171], which we also try to achieve with our methods. Moreover, there also exist methods that aim to predict post-surgery morbidity and mortality rates [194].

COMBINATIONS WITH GRAPH PLOTS. Some of the aforementioned visualization techniques, for example those of Herghelegiu and Zombori et al. [187, 530], are combined with graph plots (see Fig. 5.9). Typically, such graphs focus on safety margins and are generated by pathway sampling. Subsequently, at each sampling point, the minimum distance to risk structures is plotted. Overall, this enables users to assess pathways at varying LODs. From a workflow perspective, first, users would use one of the aforementioned techniques to acquire a set of low-risk pathways. Note that w. r. t. abstraction, various risk aspects are often compiled into one number that is represented by a color. Consequently, pathways can be represented as being less risky w. r. t. user-defined safety margins along their complete length. Subsequently, graph presentations can be employed to convey more insights. For example, physicians may observe that a chosen pathway *just* adheres to their pre-defined safety margins, which may lead them to re-evaluate their decision. Herghelegiu and Zombori et al. [187, 530] combine their aforementioned techniques with such graph-like representations. Consequently, this makes their methods more versatile w. r. t. intervention planning and execution, since their graph plots can be enhanced by, for example, the instrument's current position inside the patient and/or important land-

marks, such as the "*tumor entry point*" (cf. [185]). However, this would require instrument tracking, which is discussed below.

IMPLICATIONS FOR THIS THESIS. Originally, in [320] we proposed a projection-based map-like visualization concept (see Fig. 5.10a). Here, users would have to define a target point inside a vertebra and segment the targeted pedicle's cross section. With respect to the instrument's diameter and safety margins, an access map would be generated via pathway sampling between its pixels and the target point [187]. The angles θ and φ represent the horizontal and vertical rotation axes of instruments, respectively, and thus, each access map pixel ($\approx$ pathway) could be written as a triple (TP, θ, φ). Similar to Rieder et al. [403], a categorical traffic light metaphor would be used to assist the process of distinct, clinical decision making. With respect to the instrument, the access map's borders would always be red to decrease the risk of bone chipping at the pedicle's corticalis.

However, according to Table 5.2, for its extension, we employed a combined mesh- and volume-based visualization approach (cf. [319] and [320]). Generally, projection-based approaches are easy to understand and depict intersections between projection rays (potential pathways) and inlying structures, such as blood vessels, in a straightforward manner. However, since such cases are not entailed in our clinical scenario, a novel approach was developed (cf. Sec. 5.5). Utilizing a volume-based approach was inspired by distance fields that are used, for example, to render and/or control smoke in computer

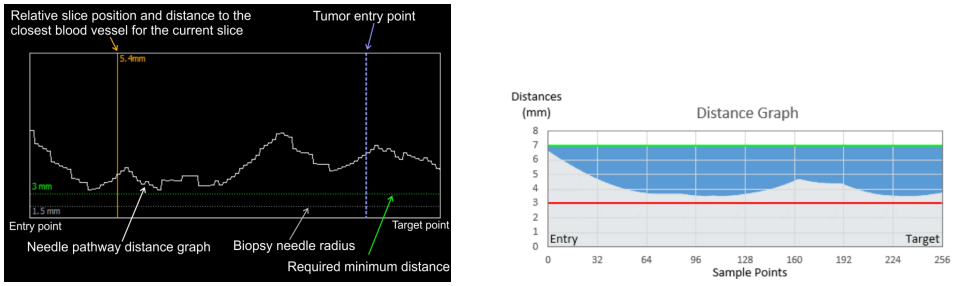

(a) Herghelegiu et al. [187] **(b)** Zombori et al. [530]

Figure 5.9: In addition to risk visualization, Herghelegiu and Zombori et al. [187, 530] also employ graph plots of chosen pathways. This is done to enable physicians to assess potential pathways in more detail, e. g. to not only assess a pathway as a whole but, for example, to assess safety margins at various sampling points. As depicted in Subfigure **(a)**, these plots can be further enhanced by *pathway landmarks*, e. g. when an instrument enters tumor and/or lesion tissue. In contrast, Zombori et al. [530] employ a more simple presentation w. r. t. the pathway's length and sample point-specific safety margins to, e. g., blood vessels.

graphics [517]. Note that the degree of abstraction is rather high for such approaches [501]. However, we consider the resulting simplification as cognitively beneficial during pathway planning when embedded in a more realistic context. As discussed below, the proposed two-step method is not limited to a certain anatomical site as long as

- (risk) structures can be segmented and presented via IVR,
- 3D distance field transformations can be employed and

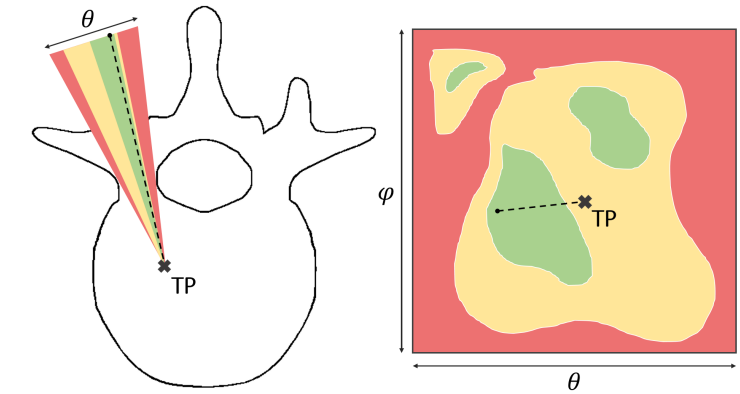

(a)

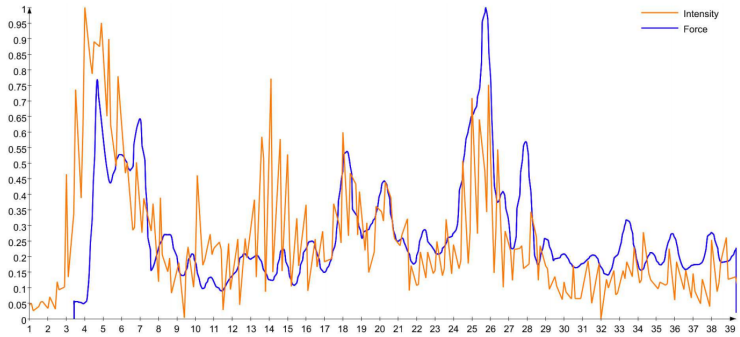

(b)

Figure 5.10: In combination, both subfigures show the inspiration from the works of Herghelegiu and Zombori et al. [187, 530]. In [320], we presented a risk map concept to support instrument insertions into vertebrae in a transpedicular manner **(a)**. Here, users would have to define a target point and segment a pedicle's cross-section to generate said map presentation via outward ray casting. With respect to safety margins and the instrument's diameter, a traffic light color-coding would visualize a pathway's *risk*. In Subfigure **(b)**, a graph plot depicts our early drilling experiment results. Note that the systematic misalignment is due to a decreased feed rate at the corticalis to allow for spudding (dt. *Anbohren*).

- structure densities can be derived from image intensities.

Furthermore, we also employ graph plots to present image intensities w. r. t. drilling forces (see Fig. 5.10b). In the respective publication, we were able to relate image intensity changes to drilling force changes, but not the other way around [320]. However, the results of our drilling experiments will be discussed in Section 5.5.5 in more detail.

5.3.5 INTERVENTION EXECUTION

Since RFAs are an image-guided type of intervention, an image guidance system has to be initialized prior to pathway creation. Note that here only a rough overview of an RFA intervention is provided and that technical details, such as intra-operative imaging devices, are discussed in more detail below. In the setup of our clinical colleagues, *CAScination* (CAScination AG, Bern, Switzerland) and Siemens *syngo DynaCT* flat-panel C-arm-mounted CT imaging systems are used to provide intra-operational instrument navigation support [107, 372]. First, optical markers are placed on the patient which are used as reference landmarks for instrument tracking and navigation. Typically, image acquisition is performed under patient apnea in roughly $10\,s$ to $20\,s$ to eliminate breathing motion artifacts. Subsequently, to-be-inserted instruments are calibrated w. r. t. the tracking system and the pathway creation can begin, e. g. by hammering or drilling through the targeted pedicle(s) [40]. This process is supported by 3D visualizations, e. g. of the skin, skeleton and aforementioned markers. With respect to the visualization techniques of the proposed two-step method (read below), such presentations could be enhanced by our findings. After pathway creation, RFA electrodes are inserted and the actual ablation process begins. With respect to the targeted lesion's size, sometimes both pedicles have to be penetrated prior to the ablation. After the ablation is finished, vertebral augmentations can be conducted to restore (some) structural integrity in the vertebra. For this, the already created pathways can be utilized to insert bone cement-guiding instruments.

PHYSICAL SUPPORT. As discussed before in the context of image registration, external fixations can be used to guide instruments. In contrast to needle-based RFAs, screw insertions typically require physicians to surgically reveal the targeted vertebrae [79]. On the one hand, this makes them generally more invasive than RFAs, but on the other hand, since the spine is (partially) exposed, there are no occlusion problems and physicians can work more *freely*. For such executions, Lu et al. [303, 304] presented a segmentation-based method to create small patient-individual drilling guides that can be put on real bones to offer instrument guidance. Presumably, these guides were 3D printed. Lieberman and Togawa et al. [287, 476] presented their "*SpineAssist*" device that requires smaller incisions. Here, multiple rods are screwed or hammered into adjacent vertebrae between which *plastic bridges* are mounted that offer guidance. The device itself is a small robot that automatically drills w. r. t. registered diagnostic CT and intra-operational fluoroscopy images. For spine biopsies, there also exist drills that enhance the physician's physical abilities to bring biopsy needles into bone marrow [40].

Furthermore, there also exist tools that offer tactile feedback during, for example, wound suturing. Typically, students learn stitching with special training models or with other non-

anatomy items. During manual stitching, with or without clamp support, there is no to little tactile attenuation. To provide such feedback cues in (tele-)robotic setups, there exist force feedback-enhanced clamps [353, 436]. This is especially important for softer needles, since their head's shape heavily influences the intended stitching direction [493]. With respect to hammering and drilling, especially hard tissue, e. g. sclerotic metastases, can result in pathway shifts. Thus, ablation and/or radiation zones are often $5\,mm$ to $10\,mm$ larger than the actual lesions to guarantee a full ablation of suspicious tissue and to account for pathway inaccuracies [6, 240, 508]. Similar force feedback facilities are also beneficial during bone drilling, e. g. to decrease the risk of bone penetration in medial direction which could result in fatal injuries of the aorta and/or lungs [204, 280, 507]. With respect to Step 2 of the proposed two-step method, drilling force profiles aim to offer additional support during bone drilling, i. e. for drill position validation.

INSTRUMENT GUIDANCE ON THE OUTSIDE. To provide (image-based) instrument guidance, instruments and artificial landmarks have to be tracked [228, 237, 372]. Typically, this is done via optical markers that are momentarily glued on the patient, whereas instruments often provide their own fixated markers at their upper ends. Since cameras are calibrated and registered w. r. t. other devices in the OR, tracking accuracy in optical systems is typically high [381]. However, optical tracking fails in cases of occlusion, e. g. if operation staff or patient tissue breaks line of sight to the instruments. Since instrument geometry is fixed, and thus known, estimations about the instrument's tip can be presented on screens near the patient table. For flexible instruments, such as catheters, typically, such support cannot be provided. In contrast, there also exist electromagnetic tracking devices. Although occlusion problems do not apply here, such systems are virtually impossible to use in certain setups due to metal- and electricity-related interferences, for example by surgical instruments or intra-operative imaging devices, such as MRI scanners [381].

There also exist augmented reality approaches that enable physicians to keep their eyes on the patient in front of them [170, 185, 330]. Furthermore, since augmenting information is computer-generated, occlusion problems, for example w. r. t. blood vessels behind an organ, can be pointed out to physicians. Furthermore, depth cues can be provided to minimize the risk of overshooting instruments [185] (cf. [280]).

INSTRUMENT GUIDANCE ON THE INSIDE. Instrument tracking and/or navigation support inside of patients can be provided via intra-operative imaging devices [515]. This entails (multimodal) image registration, since pre-operative scans are typically acquired via *closed* machines, whereas ORs have to be more *open* to enable unhindered patient access [331]. For example, C-arm-mounted imaging devices are often employed to acquire fluoroscopies or DynaCT images. Since both modalities are based on X-rays, metallic instruments and administered contrast media result in good contrast w. r. t. patient tissue. DynaCT images, however, are volumetric, whereas fluoroscopies are (bi-)planar. However, US and MR imaging can also be employed [265, 372]. Ultrasound images have a high temporal resolution, and thus, they can be used to *track* organ motion [372]. However, their spatial resolution is low and physicians have to be experienced to *read* them. Magnetic Resonance Imaging has good soft tissue contrast, and thus, is highly feasible for instrument

navigation in soft organs, such as the liver [9]. A downside is that MRI cannot be used in some patients, e. g. in patients with tattoos, peacemakers or certain alloy-based implants [10, 239, 247]. Instrument-wise, this can be addressed via titanium- and/or ceramic-based instruments [228, 239]. However, titanium-based alloys, i. e. metal mixtures, can still be magnetic, while ceramics can be very brittle under certain conditions, which may render them unfeasible for bone hammering. In any case, some organs are comprised by (breathing) motion, which has to be considered during interventions [149, 308]. In combination, various information can be presented to the physicians, namely

- pre-operative scans and/or key features from intervention planning, such as intended screw placement or to-be-ablated tissue volumes (cf. [467]),
- intra-operatively acquired images that show current instrument placement w. r. t. inner patient anatomy and aforementioned key features and
- 2D and/or 3D renderings that offer further guidance, e. g. via overview-providing depictions of patient images and instrument orientation to support navigation tasks.

5.3.6 INTERVENTION ASSESSMENT

With respect to the proposed two-step method, intervention assessment is out of the scope of this work. However, in clinical practice, post-operative CT and/or MRI scans are acquired to examine the treatment outcome [144, 403]. This is done by image-based assessment of necrotic tissue, i. e. if all tumor tissue was ablated successfully. This is assessed with great care, especially around the boundaries of ablation zones, to minimize the risk of reoccurring cancer tissue [240]. Similar to safety margins during therapy planning, Wang et al. reported that "*an ablation zone with a minimal margin uniformly larger than* 5 *mm 4–8 weeks postablation CT is associated with the best local tumor control*" [508]. To offer computer assistance in this field is challenging, since, e. g., image registration has to be performed w. r. t. – potentially intervention-induced – organ deformations. Presumably, for ablations of spinal metastases, post-interventional pain assessment is more important than image assessment to conclude about a positive intervention outcome.

5.3.7 BACKGROUND ON ROBOTS IN MEDICINE

Overall, robots have many application scenarios, for example in construction, forestry and hazardous situations [444]. Basically, robots are typically designed in a way that they surpass human capabilities in at least one aspect, for example, precision, speed and/or strength. In medicine and health care, robots also have many application areas, for example in rehabilitation scenarios, such as assisted walking training, or to assist individuals with severe degrees of disability at everyday tasks, such as drinking or eating [444, Ch. 64]. Employing robots for interventions has many potential benefits, such as increased patient safety due to an increased accuracy during instrument insertion, for example due to scaled, constrained and tremor-free motions [36, 102, 158]. However, robotic assistance is rather about enhancing human capabilities than replacing them, since robots often only perform better in a small set of tasks within a certain range of parameters, whereas humans can more easily improvise. The most well-known robot systems are the da Vinci systems that

are used in a teleoperated manner, e. g. with its operator(s) in another room or even facility (see Fig. 5.11). For more information about robots and robotic systems, see the "*Springer Handbook of Robotics*" [444].

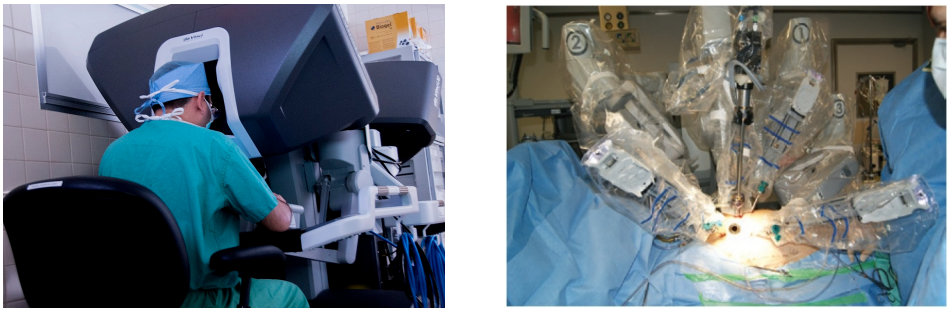

(a) **(b)**

Figure 5.11: The *da Vinci Surgical Systems* (Intuitive Surgical, Sunnyvale, California, US) are used in a teleoperated manner, i. e. they are *indirectly* controlled by their operators, e. g. from another room **(a)**. Meanwhile, various instruments, such as clamps, needles and endoscopes, are employed to treat the patient **(b)**. Here, a coronary artery bypass intervention was conducted [375].

Figure 5.12: The *KUKA LBR* (KUKA AG, Augsburg, Germany) was originally designed to be employed in industrial settings, e. g. for assisted wielding or automated assembling of small parts [56]. In the context of this thesis, it is intended to be used in a collaborative manner, i. e. by enhancing the operating physician's physical abilities, for example during drilling.

IMPLICATIONS FOR THIS THESIS. In contrast, for our work, a KUKA lightweight robot is intended to be used (see Fig. 5.12). This robot is intended to be operated in a collaborative manner, i. e. the robot and its operator insert instruments together [56, 173]. Starting from "*the worker's third hand*" concept by Bischoff et al. [56], Hanses et al. [173] presented a collaborative robot-interaction concept to assist physicians during interventions in the spine. Here, the operator would hand-guide the robot along a predefined and constrained path to, for example, insert a robot-mounted drilling device. To ensure that the robot would only be used in such a manner, a tactile floor mat would be placed in front of the patient table to enforce a collaborative instrument insertion. With respect to safety, the robot's range of motion must be constrained to not harm operation staff and the patient or to damage other OR facilities, such as imaging or tracking devices. With respect to safety margins, this will be discussed in detail in the following section (cf. [R6] below).

5.4 REQUIREMENT ANALYSIS FOR COMPUTER- AND ROBOT-ASSISTED RFAS

Here, our requirement analysis and prototypical implementation for computer- and robot-assisted spinal RFAs is presented [325]. Overall, the findings described in this section are intended to further enhance workflows such as the one presented in the previous section. Note that the prototypic implementation was intended to be used by our colleagues as an easy to customize software framework and interface for their technical setup. However, the requirements themselves are worded and discussed as general as possible.

5.4.1 CONTRIBUTIONS

The key contributions are as follows:

- A requirement analysis for computer- and robot-assisted RFAs in the spine.
- A partial and prototypic implementation of these requirements.

There was no subsequent evaluation, however, the requirements were obtained by interviewing robotic experts and a neuroradiologist in *think aloud* settings. All interviewees co-authored the respective publication.

5.4.2 REQUIREMENT LISTING

Here, the aforementioned eight requirements are listed.[2] The software prototype should

[R1] enable the 2D segmentation of risk structures, such as the spinal canal and/or cord,

[R2] support the placement and orientation of one or two applicators that represent to-be-inserted instruments, such as drills or cannulated trocars,

[R3] present the imported image data via 2D and DVRs,

[R4] superimpose said renderings with segmentations and applicators,

[R5] visually indicate the employed robot's current operation mode, namely

[2] Note that in the original publication nine requirements were presented [325]. The former requirements [R2] and [R3] addressed the placement and orientation of one and two applicators, respectively. For simplification reasons, here, both requirements were merged into [R2].

- collaborative insertion of an instrument,
- tactile floor map is *triggered* to enable insertion,
- target position within vertebra is reached,
- position holding of an instrument w. r. t. patient's breathing motion and/or
- combinations, e. g. insertion is enabled without actual insertion,

[R6] consider two types of safety margins, namely

- the proximity to previously segmented risk structures and
- the proximity to interventional staff and other devices in the OR,

[R7] depict the HUs and drilling forces along the applicators' pathways to convey to-be-expected resistances and

[R8] convey information about the patients' respiratory motion.

5.4.3 REQUIREMENT IMPLEMENTATION

Form a clinical workflow perspective, the aforementioned requirements were divided into three GUI groups [173], namely

- *Data Import*, where image data can be imported and examined (see Fig. 5.13),
- *Planning*, where, e. g., pathways can be defined and evaluated (see Fig. 5.14) and
- *Intervention*, which is intended to be used during actual intervention to, for example, assess lesion shifts during breathing motion (see Fig. 5.16).

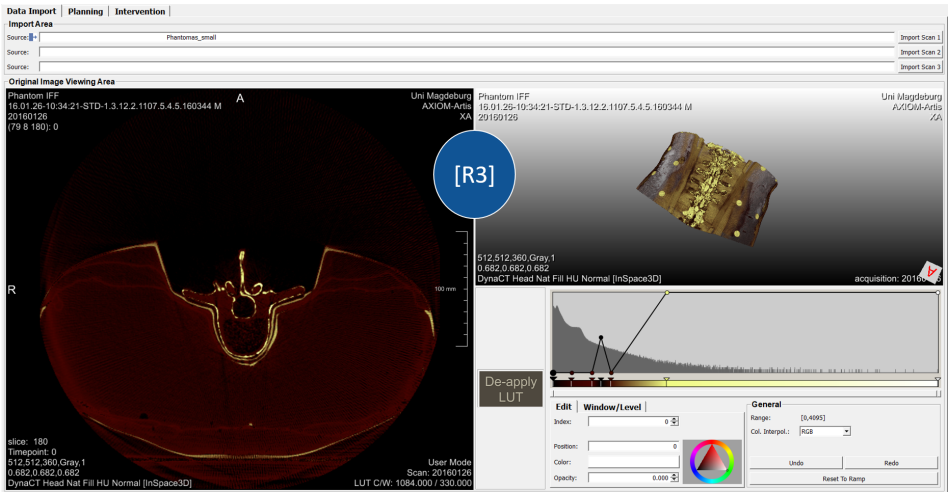

Figure 5.13: In this GUI tab, users can import and assess image data. Here, a CT phantom data set was imported. Note the dots on the *skin* that are intended to be used as a reference coordinate system during instrument tracking [372].

Similarly published in [325], but adapted for this dissertation.

In the following, the prototypic realization of said requirements is described w. r. t. these groups and the aforementioned *requirement tokens* [R1] to [R8]. As mentioned before, the prototype was implemented in *MeVisLab 2.8.2* [406].

DATA IMPORT. Here, image data is imported and assessed in 2D and 3D [R3] (cf. Fig. 5.13). Moreover, LUTs can be defined and applied to all viewers in the prototype. This GUI tab can either be used during intervention planning or prior to intervention execution to import image data.

PLANNING. Requirements to support intervention planning were conceptually implemented in the planning tab (see Fig. 5.14). This tab is focused on 2D and 3D viewers that can be used to position and orientate up to two applicators [R2]. Moreover, the 2D viewers can be used to segment risk structures, such as the spinal canal and/or cord [R1]. With respect to axial slices, the vertical interpolation of adjacent in-slice segmentations into a 3D mesh is done via the "*CSOConvertTo3DMask*" module in MeVisLab [406, 489]. Linked views are employed to update alterations in all viewers [R4]. The applicators and segmentations can be regarded as key features of the visualizations in the context of 2D and 3D presentations of the original images.

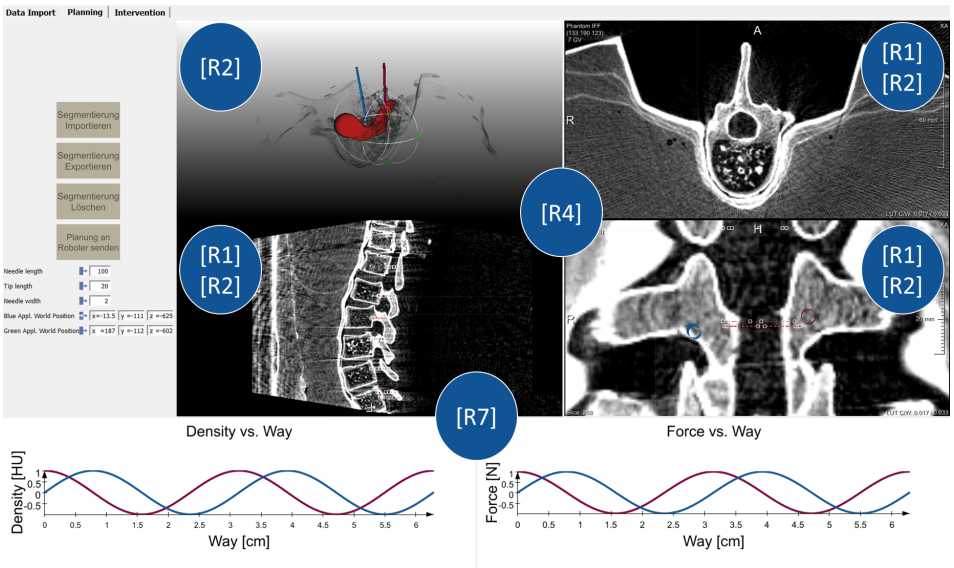

Figure 5.14: In the *Planning* GUI tab, users can position and orientate up to two applicators, here depicted in red and blue. Risk structures, such as the spinal canal, can be segmented and used to superimpose all 2D and 3D viewers. On the left, instrument features and segmentation masks can be altered and managed, respectively. At the bottom left, a graph plot depicts the HUs along both applicators (cf. Fig. 5.15). The graph on the bottom right is intended to depict estimated drilling forces that are derived from the pathways' HUs. Here, for the prototype, default graph plots were used, i. e. of the sine and cosine functions.

Similarly published in [325], but adapted for this dissertation.

On the left, various interaction facilities are listed, e. g., to import and export segmentation masks or to alter the to-be-employed instrument's geometry, for example w. r. t. their diameter. On the bottom, two graphs are plotted. In the left graph, two lines represent the HU-related tissue densities along their respective color-coded applicators [R7]. These HU profiles can be obtained via an adapted 3D Bresenham algorithm to obtain key points between the user-defined instruments' start and end points [66] (see Fig. 5.15). This is done to convey a first impression of how much structural resistance physicians have to expect during instrument insertion. Here, strong slopes would indicate tissue transitions, e. g. from muscles into bones. The graph on the bottom right is intended to depict estimated drilling forces in Newton from said HU profiles [R7], which will be discussed in the next section (cf. [319]). If feasible pathways are defined, they can be sent to the robot.

The Bresenham algorithm, in contrast to linear interpolation, has the advantage that it can be exploited to return an ordered list of 3D integer coordinates that do not entail subsequent (tri-)linear interpolation of voxel values. However, assuming an isotrope voxel grid with the size of $1\,mm$, the distance between adjacent key points varies between 1, ≈ 1.41 ($\sqrt{2}$) and $\approx 1.73\,mm$ ($\sqrt{3}$). This results in the uneven up- and downward slopes (cf. Fig. 5.15). In contrast, linear interpolation results in an even spacing between key points, but is less efficient w. r. t. memory management (float vs. integer) and computational effort (multiplications vs. additions). For modern computers, this difference is marginal and the actually employed approach can be regarded as a design choice. From a user perspective, and if not indicated otherwise, e. g. in plots with logarithmic scales, equidistant spacing between control points is preferable, though.

X-ray-based images depict the radiodensity of tissue and not their *strength*. In humans, bone density and/or strength is assessed via Bone Mineral Densities (BMD) values which denote how well-mineralized *our* bones are. Typically, BMD values are obtained via DXAs, i. e. two X-ray acquisitions with different eV settings, since varying energy levels result in different absorption-to-scattering ratios. This can be used to obtain the bones' mineral composition and strength. However, Schreiber et al. [432, 433] found a linear relationship

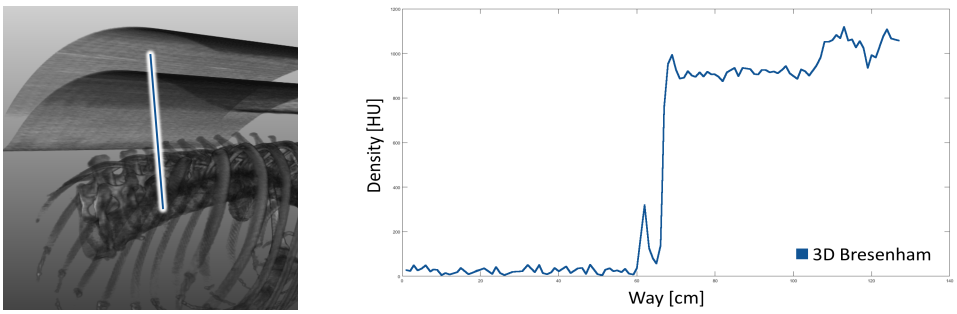

(a) **(b)**

Figure 5.15: After pathway definition **(a)**, HU profiles can be created to convey a first impression of structural resistance during instrument insertion **(b)** [R7]. For this, a 3D variation of the Bresenham algorithm can be used [66]. For presentation purposes, the pathway was enhanced although it should lie somewhere *in* the DVR.

(r^2 = 0.44) between BMD and HUs, and thus, CT images can be employed to convey a drilling density profile. Moreover, CT and DynaCT images have different "*Delta HUs*" [452], i. e. the contrast resolution of DynaCT images is worse, which renders this modality unfeasible for certain purposes, e. g. stroke imaging.[3] This mostly results in differences around 10 HUs, which is negligible. Thus, DynaCT-based HU curve plots are feasible to convey a first impression about the structural resistance along potential pathways.

INTERVENTION. The last GUI tab is intended to be used during actual interventions (see Fig. 5.16). Here, various 2D and 3D viewers are employed to assist physicians cognitively. Certain key features, i. e. previously defined pathways and segmented risk structures, are imported from the *Planning* tab. Although two pathways and/or applicators should be supported, only one pathway is depicted here, since, during interventions, multiple pathways are created in a subsequent manner.

DRILLING FORCES GRAPH PLOT. At the bottom of Figure 5.16, two plots depict information about the currently created pathway and patient breathing, respectively. In the bottom left plot, two curves are depicted (see Fig. 5.17). The estimated drilling forces are presented as a stippled curve, which is done to present them less prominently, i. e. to provide a visual context for the *currently* measured drilling forces which are represented

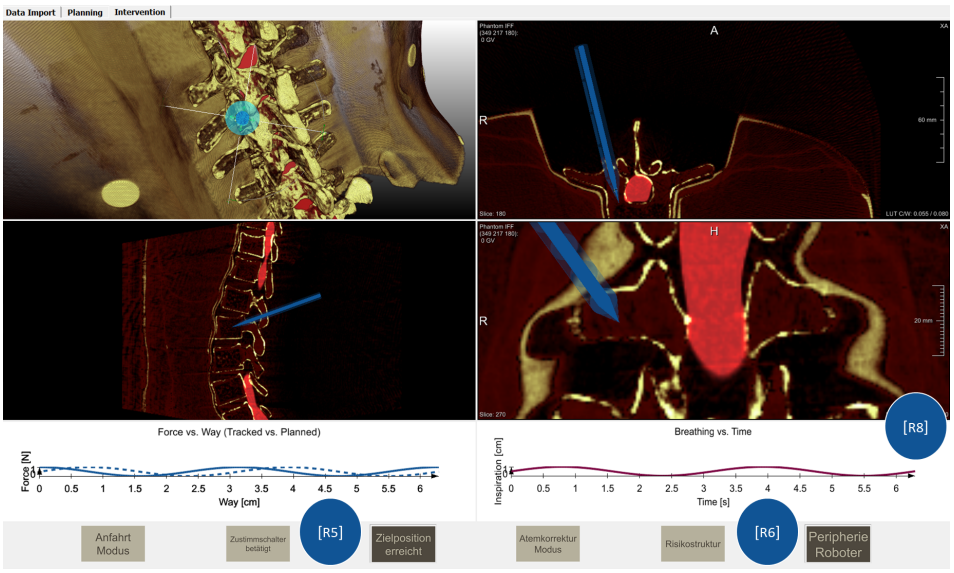

Figure 5.16: Here, multiple 2D and 3D viewers are also used to depict the key feature-enhanced images. Moreover, the pathways are enhanced by *halos* to depict eventual displacements during drill insertion [29]. The graphs below depict estimated and measured drilling forces and anatomical displacements, respectively w. r. t. tracked patient breathing motions. The indicators at the bottom depict the robot's mode and proximity to inner and outer risk structures.

Similarly published in [325], but adapted for this dissertation.

[3] These differences are even greater when comparing CT and fluoroscopy images [452].

by a solid curve. These forces (resistances) are measured with a robot-mounted pressure sensor (cf. Fig. 5.20). Our idea was to offer the robot's operator a visual feedback on one of the screens if the estimated and measured drilling profiles are too different, since the drill might not be guided along its intended pathway anymore. Additionally, w. r. t. the planned and actual drill orientations, this would be indicated by the color-coded *halos* around the applicators in the 2D and 3D viewers with the planned path being rendered more transparent [29]. Consequently, the robot could block further insertion and the software could prompt the robot's operator to confirm the current pathway, for example, by acquiring an additional scan, to unlock cooperative drill insertion again. Below that graph, GUI elements indicate the robot's currently active mode [R5], e. g. if the robot's operator stands on the aforementioned tactile map or if the target point was reached.

BREATHING MOTION GRAPH PLOT. The bottom right graph is intended to be used to track the patient's breathing motion [149, 308] [R8]. Typically, diagnostic images are acquired with patients lying on their back (supine position), whereas they lie face-down during spine interventions (prone position). Similar to the aforementioned breathing motion artifacts [169], this can result in positional changes around $2\,mm$ of vertebrae in anteroposterior direction [197]. Thus, patient movement w. r. t. breathing should be tracked and utilized by the robot to ensure accurate drill insertion. From a patient's perspective, cushions, pads and belts can be utilized to impair their mobility and reduce anatomical displacements [139]. Moreover, this makes image registration necessary to align pre- and intra-operative images w. r. t. key features. The two rightmost indicators at the bottom depict the instrument's proximity to inner and outer risk structures [R6]. As mentioned before, inner risk structures are imported from the *Planning*. Outer *risk structures*, such as operation staff and other devices in the OR, should be kept out of the robot's range of motion to minimize the risk of dangerous situations [173].

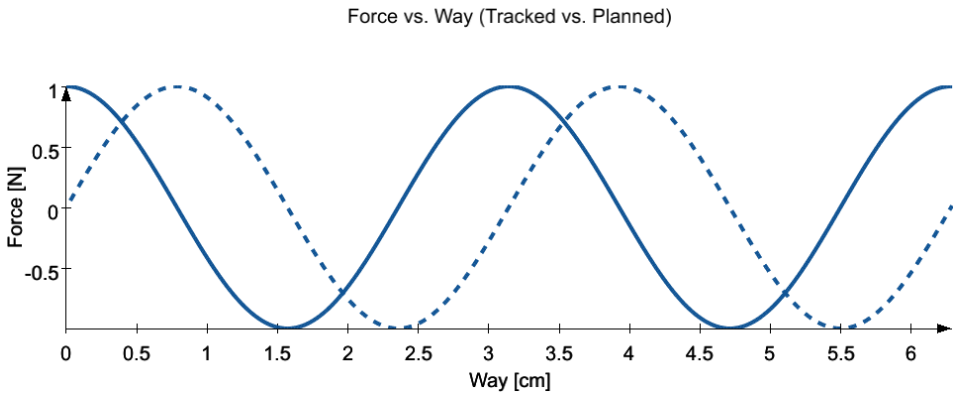

Figure 5.17: A detailed depiction of the graph plot from Figure 5.16. The stippled graph is intended to depict the estimated drilling forces, whereas the solid graph is intended to depict the *currently* measured forces during interventions. Thus, the estimated forces provide a visual context without drawing too much attention.

Similarly published in [325], but adapted for this dissertation.

5.4.4 EXTENSION-RELATED OPEN IDEAS

One limitation of the presented prototype was that no multimodal medical image data could be employed. This was not an issue, since it was more important that a customizable prototype was implemented. Another limitation was that certain risk aspects, such as inner safety margins, could not yet be considered during pathway definition [R6]. To offer cognitive support during planning and/or execution, we continued to work on methods to find *good* pathways and to present their respective *risk* in more sophisticated ways. The initial idea to create 2D access maps w. r. t. pedicles was dropped, since projection-based approaches are typically used in cases of embedded structures that can *occlude* target structures [320] (cf. Fig. 5.10a). With respect to bone drilling, the initial approach was to employ only a small set of HUs along pathway sampling points to predict drilling forces (cf. Fig. 5.10b), which resulted in promising first results. However, we were not able to derive drilling force changes from image intensity changes, which is a key feature to provide drilling force estimations during intervention planning and physical support during intervention execution (cf. Figs. 5.14 and 5.16). However, these limitations were addressed in our extended work, which will be presented in the next section.

5.5 A TWO-STEP RISK ASSESSMENT METHOD FOR RFAS IN THE SPINE

In this section, we present and discuss our two-step risk assessment method [319].

5.5.1 CONTRIBUTIONS

The key contributions of the proposed two-step method are as follows:

- Step 1 primarily aims to offer cognitive support during pathway definition and instrument insertion by combining the aforementioned inner risk aspects, namely *safety margins*, *pathway length* and/or *insertion depth* and the diameters of the to-be-inserted instruments, e. g. of cannulated trocars or drills (cf. Tab. 5.2). Said support is offered by the proposed *on-mesh* and *in-volume* visualization techniques.
  - In contrast to other mesh-based visualization methods (cf. Tab. 5.2), our on-mesh technique also employs the instrument's diameter as a risk aspect.
  - The in-volume technique employs 3D distance fields to convey safety margin-related *risk*, which is a novel approach.
  - These methods were evaluated by two neuroradiologists (cf. Sec. 5.5.6).
  - With respect to the evaluation results, an enhancement of standard 2D images via 3D safety margins from the in-volume method is superior to the conventional assessment of various 2D perspectives.
- In the context of Step 2, we propose the so-called Stiffness Criterion ρ that can predict drilling force changes from HU changes within a range of $\pm 1\ mm$. This is done by analyzing the local distribution and homogeneity of HUs. These findings could be used for manual, but especially robot-assisted bone drilling, i. e. by offering an additional feature for instrument position validation during interventions. However, these findings were not yet evaluated.

5.5.2 INTRODUCTION AND MOTIVATION

Most aspects were discussed in the previous sections, and thus, here, only a brief recap is provided. *Our* bone health is maintained through a balanced communication and interaction between different bone tissue cells, which can be disturbed by cancer cells. This can result in spinal bone metastases, which can cause pain and/or decrease the structural integrity of affected bones. Typically, bone metastases are treated via external radiotherapy, chemotherapy, surgery or combinations of them [88]. Additionally, RFAs can be employed, which are an image-guided and minimally invasive type of intervention. In patients with bone metastases, however, they are rather conducted for pain management purposes and curation is rarely possible. Radiofrequency ablations were reported to result in quick short-term pain relief and can be combined with augmentation strategies to re-establish spine stability in cases of fractures [281, 413, 427]. However, interventions in the spine are spatially challenging, and thus, the main goal of this work was to develop means to support the intervention planning and execution of spinal RFAs w. r. t. pathway definition and creation, and potential instrument position validation during robot-assisted interventions. Over the course of the next sections, the proposed two-step method is presented w. r. t. the previously described clinical workflow (see Fig. 5.18).

5.5.3 STEP 1 – RISK VISUALIZATION

In our previous work, we presented a projection-based map-like approach [320] (cf. Fig. 5.10a). However, we opted for a combination of mesh- and volume-based visualization techniques, since our clinical context does not include cases with inlying structures and the utilization of volumetric information enables us to present safety margins in all directions at the same time [517] (cf. Sec. 5.3.4). However, a major advantage of projection-based techniques is the overall easy to understand approach w. r. t. visualizing intersections between (unfeasible) pathways and risk structures.

With respect to preprocessing, first, the image sources are aligned via rigid or affine (scaled) registration. Then, segmentations of the (remaining) vertebra, the metastasis and the spinal cord are acquired. For Case 1 and Case 2 presented in the original paper and in this thesis (read below), the segmentations were carried out by an image processing expert using a multi-label live wire approach. The vertebrae were segmented using DynaCT images, whereas the spinal cord and bone metastases were segmented using MR images. In contrast, the segmentations for Case 3 were acquired manually by the author of this thesis via thresholding and 3D region growing from CT images (cf. [263]).

5.5.3.1 INTENDED VISUALIZATION WORKFLOW

Similar to the current clinical workflow, a pathway is searched for and defined in three 2D orthogonal slice viewers during intervention planning via two points (clicks). Subsequently, the pathway would be assessed using the proposed in-volume and in-mesh visualization techniques. For two reasons, these techniques are intended to be used iteratively, i. e. the assessment begins with the in-volume technique. First, the technique implicitly depicts multiple pathways and their surroundings simultaneously. Thus, the process of finding low-

risk pathways can be sped up. Secondly, although only safety margins to risk structures are depicted via the in-volume technique, this is the most important risk aspect in this context. Other aspects, such as the insertion depth, can be evaluated subsequently.

5.5.3.2 IN-VOLUME VISUALIZATION

For the in-volume technique, first, pathways are enlarged to create cylinders or ellipses with a diameter of, e. g., $10\,mm$. For ellipses, this diameter denotes the *thickest* mid-cross-section, and thus, distance field computation is faster for them than for cylinders. In the final presentation, said cylinders or ellipses are cut out from all DV-rendered segmentations to create virtual paths into targeted metastases (cf. Fig. 5.21). Then, all risk structures'

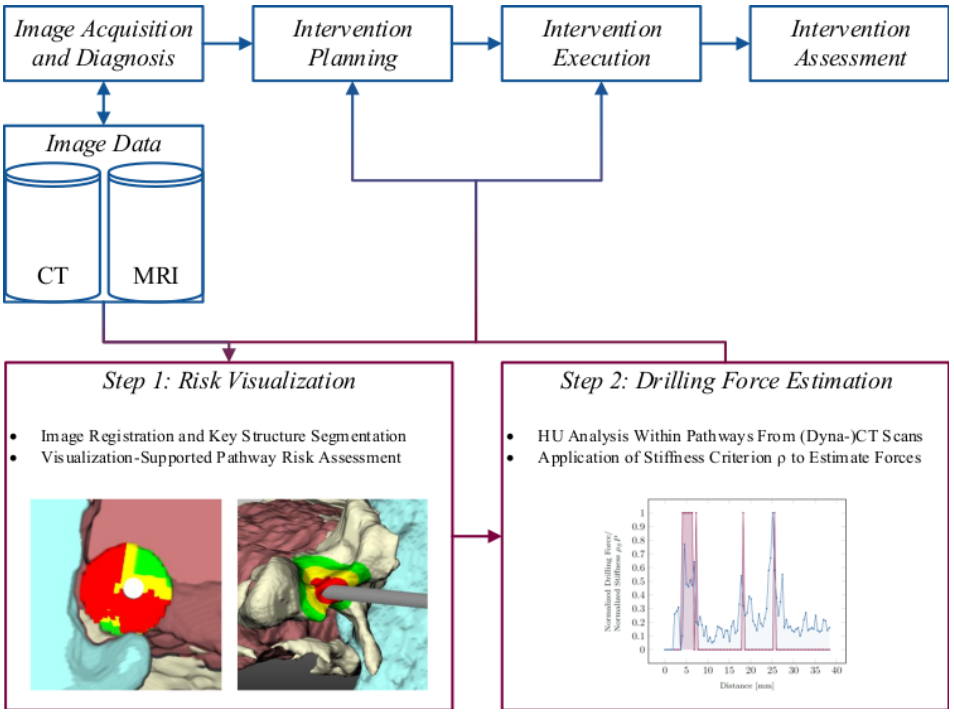

Figure 5.18: The simplified clinical workflow from Figure 5.4 w. r. t. the proposed two-step method. For presentation purposes, the intra-operatively acquired DynaCT images were omitted. For Step 1, first, CT and MR images are registered, and subsequently, segmentations of the spinal cord (blue; MRI), the metastasis (red; MRI) and the remaining vertebra (brown; CT) are obtained. These segmentation masks are then used for the on-mesh and in-volume visualization methods to find low-risk pathways. For Step 2, the HUs along said pathways are used to derive and estimate drilling forces. The results of both steps aim to offer cognitive and physical assistance during intervention planning and execution. For a better depiction of the graph plot in Step 2, see Figure 5.26.

Image similarly published in Computers in Biology and Medicine [319], but adapted for this dissertation.

Table 5.3: Visualization parameters (upper table) and equations (lower table) to construct the respective transfer function's key points for the proposed visualization techniques (cf. Fig. 5.19). Abbreviations: HR and LR are the high and low risk proximity thresholds, SO and RO are the structure and risk visualization opacities and D denotes the instrument's diameter.

Count	Name	Abbreviation	Visualization Method	Default Values
3	Risk Colors		in-volume & on-mesh	red, yellow, and green
1	Structure Color		on-mesh	red, yellow, and blue
2	Risk Thresholds	HR & LR	in-volume & on-mesh	5 mm to 10 mm or 1 mm to 3 mm
2	Opacity Values	SO & RO	in-volume & on-mesh	0.5 and 1
1	Instrument Diameter	D	on-mesh	3 mm

Method	Transfer Function Key Point Equations					
in-volume	$(0,\ 1)$	$(HR,\ 1)$	$(\frac{HR+LR}{2},\ 1)$	$(LR,\ 1)$		
on-mesh	$(0,\ RO)$	$(HR+\frac{D}{2},\ RO)$	$(\frac{HR+LR+D}{2},\ RO)$	$(LR+\frac{D}{2},\ RO)$	$(LR+\frac{D}{2}+\epsilon,\ RO)$	$(maxDistance,\ SO)$

Table originally published in Computers in Biology and Medicine [319, Tab. 2].

segmentation masks are merged. Subsequently, a 3D voxel-based Euclidean unsigned distance field is calculated between this combined mask and the pathway voxels via

$$I_{DF}(x,y,z) = \min_{Vol_{PW}, Vol_R} \left(\sqrt{(x_{PW}-x_R)^2 + (y_{PW}-y_R)^2 + (z_{PW}-z_R)^2} \right) \tag{5.1}$$

with $I_{DF}(x,y,z)$ being the resulting distance field voxel values, Vol_{PW} being the pathway voxel coordinates for which distance values are computed, and Vol_R being the voxel coordinates of the combined risk structure segmentation masks [517]. For example, given that for $Vol_{PW} = \begin{pmatrix}1\\1\\1\end{pmatrix}$ the nearest corresponding *risk voxel* would be $Vol_R \begin{pmatrix}2\\2\\2\end{pmatrix}$, $I_{DF}(1,1,1)$ would be evaluated to $\sqrt{(1-2)^2+(1-2)^2+(1-2)^2} = \sqrt{3}$. Note that, since voxel sizes might not be isotropic, the distance values might have to be corrected w. r. t. the voxel dimensions. Here, the only risk structure is the spinal cord, but as discussed below for Case 3, the technique also works with merged segmentation masks (cf. Sec. 5.5.5). Similar to Tappenbeck et al. [468], a distance-based TF and traffic light-like green-yellow-red color-coding are employed to support the process of distinct clinical decision making (see

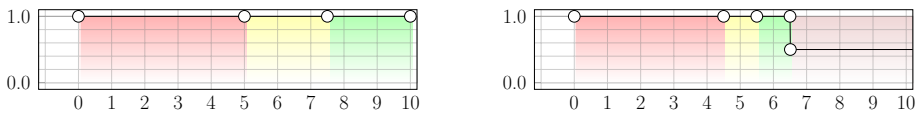

(a) In-Volume TF **(b)** On-Mesh TF

Figure 5.19: Exemplary in-volume **(a)** and on-mesh TFs **(b)** w. r. t. the visualization parameters (cf. Tab. 5.3). The x-axes show distances in millimeters, while the y-axes denote key point opacities. Note that the color-coding in the on-mesh TF beyond the key point at 6.5 mm denotes the color of the respective structures (cf. Fig. 5.23).

Images originally published in Computers in Biology and Medicine [319, Fig. 2].

Fig. 5.19a). At most, users are required to define seven parameters to define in-volume TFs. However, by employing the default values from Table 5.3, generally, less interactions are necessary. Said parameters were acquired in collaboration with our clinical colleagues and/or interviewees.

Given that an unfeasible pathway was defined, it can be re-oriented. This can be done efficiently, since, e. g., the *enlarged voxel cylinders* implicitly depict various pathways simultaneously. In contrast, if a feasible pathway was found, it can be assessed in more detail via the on-mesh method and then via the findings related to Step 2. This reflects the aforementioned workflows of related methods, i. e. that first multiple potential pathways are evaluated and after careful consideration one pathway is assessed in more detail.

5.5.3.3 ON-MESH VISUALIZATION

Subsequently, the on-mesh technique enables users to assess the chosen pathways, for example, w. r. t. the instrument's insertion depth. To do so, first, the segmentation masks are converted into surface meshes [25, 299]. Then, the absolute, minimum and unsigned Euclidean distance between each vertex of said surface meshes and the instrument's pathway are computed. This was done by using the "*WEMSurfaceDistance*" module in MeVisLab [406]. Note that this module requires two surface meshes to compute distances, and thus, the pathway (line) had to be translated into a Bresenham-like 3D mesh representation. With respect to the source images' voxel resolution, this typically results in inaccuracies on the submillimeter scale, which are negligible. The resulting distance values are assigned to the segmented structures' surface mesh vertices which become color-coded during rendering (cf. Fig. 5.23). For the color-coding, a transfer function is employed which has to be defined w. r. t. the instrument's radius to not *omit* high risk regions in close proximity to the virtual applicator (see Tab. 5.3).

PATHWAY LENGTH VS. INSERTION DEPTH. Note that the proposed on-mesh method does not employ the instrument's length as a risk aspect, since vertebrae lie near the skin of *our* back, i. e. targeted lesions lie well within the to-be-inserted instruments' range. Thus, the on-mesh method is rather focused on depicting the insertion depth, i. e. how much *bony buffer* in medial direction hinders instruments to break through. This perspective was not addressed by related methods (cf. Tab 5.2), since their clinical applications (liver and brain) were not comprised by such issues. However, here, this aspect is important.

INSTRUMENT DIAMETER. Note that the instrument's radius is employed for the on-mesh, but not for the in-volume color-coding (cf. Tab. 5.3). The reason is that for the in-volume technique *absolute* distance values are color-coded, whereas *relative* distance values are color-coded via the on-mesh technique. In other words, for the in-volume method, pathway voxels are visualized w. r. t. their absolute distances to risk structures which do not change as long as the set of risk structures does not change. Thus, they are independent from instruments and their orientation. The distance values employed for the on-mesh technique, however, directly depend on the instrument's placement and orientation, and thus, have to be corrected for the final presentation.

5.5.4 STEP 2 – DRILLING FORCE ESTIMATION

Under the supervision of our clinical colleagues, we conducted drilling experiments on ten lumbar and five thoracic vertebrae (cf. *Division of Work* chapter). Since we had no access to fresh bones, fat-free and dried vertebrae were used. Note that no vertebra had anatomical abnormalities due to metastases. To evaluate said experiments, DynaCT scans were performed before and after drilling: The acquisition time was set to $10\,s$ and the reconstructed data sets had an isotropic voxel size of $0.46\,mm$. As discussed before, the use of DynaCT instead of CT images has only little to no influence in bone imaging.

Figure 5.20 depicts the drilling experiment setup with the respective drilling parameters being listed in Table 5.4. The vertebrae were fixated and a dynamometer-mounted hollow drill was employed to create transpedicular pathways. The drill had an outer diameter of $3\,mm$ to mimic the biopsy needles that our clinical colleagues employ for initial pathway creation into vertebrae [40].[4] Except at the vertebrae's corticales, the feed rate was set to $2\,mm/s$. In contrast, at the corticalis it was lowered to $1\,mm/s$ to allow for surface

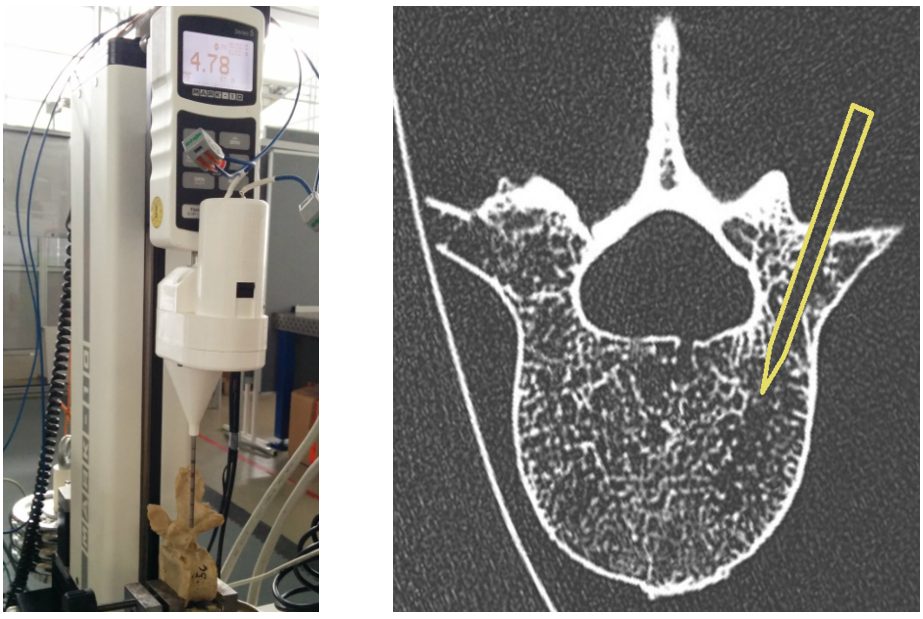

(a) **(b)**

Figure 5.20: The drilling setup was composed of a *Mark-10 Force Test Stand ESM301* (Mark-10 Corporation, New York, USA) and a *Mark-10 M5-20 Force Gauge* **(a)**. On the right, a post-drilling DynaCT-scanned thoracic vertebra is depicted **(b)**. The drilling pathway was enhanced for presentation purposes.

[4] They use the *Arrow OnControl Powered Bone Access System* (Teleflex, Wayne, Pennsylvania, USA).

Table 5.4: Parameters for the drilling experiments. At the corticalis, the feed rate (dt. *Vorschub*) was lowered to allow for spudding (dt. *Anbohren*). Since a hollow drill was used, the column *Drill Diameters* denotes the drill's inner and outer diameters.

Parameter	Feed Rate	Measurement Frequency	Drill Diameters	Rotations	Nominal Torque
Value	$1\,mm/s$ to $2\,mm/s$	$1\,kHz$	$2\,mm$ to $3\,mm$	$420\,R/min$	$1.75\,N\,m$

Table originally published in Computers in Biology and Medicine [319, Tab. 3].

spudding. With respect to the aforementioned isotropic voxel size and force (resistance) measurement frequency, approximately 230 measurements per voxel were acquired.

In order to estimate drilling forces from image intensities, the drilling hole voxels were analyzed. Thus, first, a 3D region growing is seeded in the drilling hole of the post-drilling DynaCT scan (see Fig. 5.20b). Although the principal shape and/or direction of the pathway can be segmented in such a manner, the results are typically accompanied by a large amount of over-segmentation artifacts, since the region growing *bleeds* into adjacent airy voxels in between the trabeculae of the spongiosa. Subsequently, a Principal Component Analysis (PCA) is applied to the pathway segmentation with the eigenvector corresponding to the largest eigenvalue representing the drilling pathway. Since the drill's outer diameter is known, a cylinder around this eigenvector can be defined to segment the bone tissue voxels in the pre-drilling DynaCT images. However, this entailed rigid image registration to align the vertebrae from before and after drilling. Finally, the inlying image intensities could be analyzed, which is discussed in Section 5.5.5.2. With respect to the proposed two-step method, instead of this preprocessing pipeline, the user-defined pathway from Step 1 can be employed to segment to-be-drilled-through bony tissue.

5.5.5 RESULTS

In this section, the results of Step 1 and Step 2 are presented.

5.5.5.1 RESULTS FOR STEP 1 – THREE CASE DESCRIPTIONS

To assess the capabilities of the aforementioned in-volume and on-mesh visualization techniques, they were applied to three cases. The first two cases are real, i. e. they were applied to image data from actual patients that received spinal RFAs for metastases treatment. The last case is *staged* and is intended to present the versatility of the proposed combination of visualization techniques, i. e. that they are not limited to the spine and can potentially be employed for other context organs as well, such as the lungs (cf. Fig. 5.24). Note that for Case 1 and Case 2 the gray applicators represent pathways that were actually created during the respective RFA interventions. For the figures in this section, they were reconstructed manually. The case descriptions were provided by Interviewee 2 (cf. Sec. 5.5.6).

CASE 1. A 59-year-old male with recurrent kidney cancer on the right side infiltrated the liver, the right adrenal gland and the first lumbar vertebra on the right side. The patient presented himself with heavy pain in his lower back and right hip. MR images revealed a

lesion in said lumbar vertebra and its right pedicle. These images revealed that the patient was at a high risk of spinal cord compression. The patient was reported to be in a poor condition, and thus, it was decided to perform a RFAs the next day. This decision was made in a tumor board conference consisting of neurosurgeons, radiotherapists, oncologists and neuroradiologists and was agreed on by the patient. Two days after the intervention, additionally acquired MR images revealed that the aforementioned spinal cord compression was reduced. Moreover, the patient reported having less pain.

Figure 5.21 depicts the results when the in-volume technique was applied to the patient's image data. For the color-coding, the TF from Figure 5.19a was employed. The spinal cord was set to be the only risk structure with the high and low risk thresholds set to $HR = 5\,mm$ and $LR = 10\,mm$ (cf. Tab. 5.3). Consequently, the color-coding intervals are as follows: **High risk** from $0\,mm$ to $5\,mm$, **medium risk** from $5\,mm$ to $7.5\,mm$ and **low risk** from $7.5\,mm$ to $10\,mm$. The cut-away ellipse's diameter was set to $10\,mm$.

The pathway in Figure 5.21a is the actual pathway that was employed during the intervention. With respect to the low risk color-coding threshold of $10\,mm$, said figure depicts that the instrument was inserted more than $10\,mm$ away from the spinal cord. Note that although transpedicular pathways are typically preferred, here, the right pedicle was completely destroyed by the metastasis. To depict the technique's capabilities, a deliberately ill-placed pathway was defined in close proximity to the spinal cord (see Fig. 5.21b). Here, one key feature of the in-volume technique is depicted: Each color-coded pathway voxel represents the absolute and minimum distance between *this* voxel and all risk structure

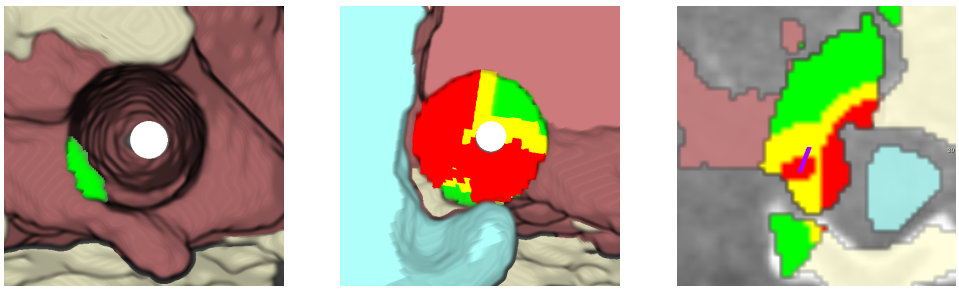

(a) **(b)** **(c)**

Figure 5.21: The results of the in-volume technique for Case 1. Subfigure **(a)** depicts the actual pathway that was used during the intervention. Since the instruments were inserted more than $10\,mm$ away from the spinal cord, another virtual pathway was defined that was deliberately placed in close proximity to the cord **(b)**. The small hook represents the patient's spinal cord compression, which results in the stair-like high risk color-coding in the bottom left of the ill-placed pathway. In Subfigure **(c)**, the 3D safety margin information is used to enhance the original 2D images. Here, the pathway has sufficient in-plane (lateral) distance to the spinal, however, the user-defined high risk safety margin of $5\,mm$ is still undershot in inferior direction (cf. Tab. 5.3), which cannot be depicted in a typical 2D viewer.

Images originally published in Computers in Biology and Medicine [319, Fig. 5].

segmentation voxels. In other words, the color-coding depicts the minimum distance w. r. t. all directions simultaneously. Since the patient had a spinal cord compression, the in-volume technique *directly* shows that a pathway correction in top-right direction would result in more feasible pathways w. r. t. the low and high risk safety margins.

Note that the spinal cord and metastasis in Figure 5.21b have *flat* back surfaces, since the 3D viewer is linked to a 2D viewer that translates a cut-away plane during image stack slicing (see Fig. 5.22). This can result in the pathway not being cut perpendicularly, since, typically, pathways are not perfectly axis-aligned. However, this is not an issue, since instruments are almost always inserted *from behind*, i. e. they are often somewhat axis-aligned. Moreover, even when the pathways' cross-sections might not be perfectly circular, the inlying distance values depict absolute distances which are independent from the cross-section's shape. If necessary, this could be addressed via Multiplanar Reformations (MPRs) of the 2D images along the 3D pathway.

CASE 2. A 75-year-old male with kidney cancer on the left side presented himself with partial paralysis of his left leg, lower back pain, and pain in his left leg. MR images

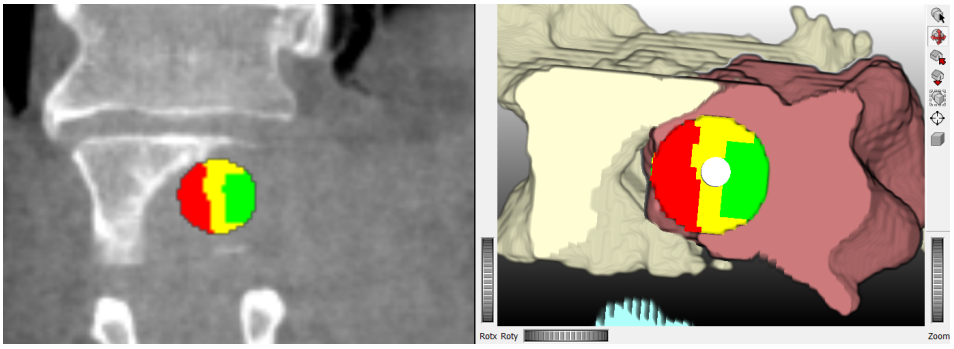

(a)

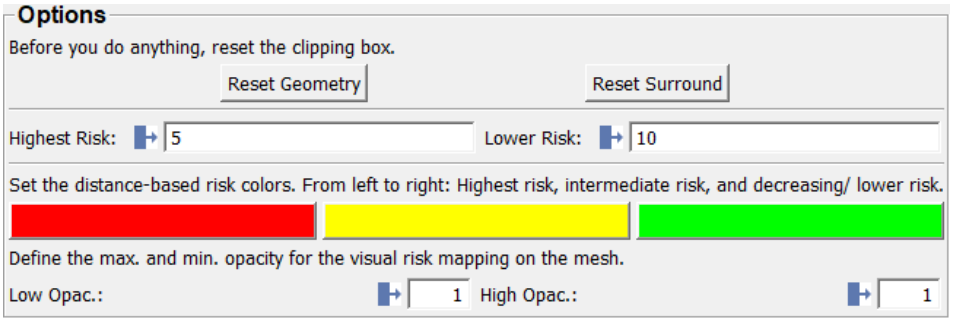

(b)

Figure 5.22: Screenshot from the GUI. During the assessment of the in-volume technique's results, users can slice through a 2D viewer **(a, left)**. Consequently, a cut-away plane is translated through the DV-rendered in-volume scene to reveal the pathway's current cross-section **(a, right)**. With respect to Table 5.3, users can alter various visualization parameters which updates the presentation in real time **(b)**. Note that the 2D in-volume enhancement is optional, and thus, users can only assess the original and unaltered image source.

revealed a suspicious lesion in the fifth lumbar vertebra and its left pedicle. No spinal compression was found. An additional CT scan was performed to assess the known kidney cancer and to search for additional metastases, but no such lesions were found. The patient was discussed in a tumor board and it was decided to perform an RFA with a subsequent radiation therapy. Afterwards, the patient reported that he was elevated from local pain.

Figure 5.23 depicts the results when the on-mesh technique was applied to the patient's image data. For the color-coding, the TF from Figure 5.19b was employed. The high and low risk thresholds were set to $HR = 1\,mm$ and $LR = 3\,mm$, and thus, the color-coding intervals are as follows: **High risk** from $0\,mm$ to $2.5\,mm$, **medium risk** from $2.5\,mm$ to $3.5\,mm$ and **low risk** from $3.5\,mm$ to $4.5\,mm$. Note that the instrument's diameter was set to $3\,mm$. In contrast to the aforementioned case, here, the instruments could be inserted through the left pedicle. To visualize the insertion depth ($\approx$ pathway length), in Figure 5.23b the TF was also applied to the metastasis' surface mesh, since it made up the majority of the remaining vertebra. During planning, this would enable physicians to conclude about the proximity to the vertebra's surface in medial direction which is an important key feature

- during instrument insertion to lower the risk of *breaking through* and
- during the RFA itself to not ablate non-targeted structures *in front*.

Generally, bone is a good electrical insulator [6]. However, as depicted, the metastasis also destroyed parts of the vertebra's front face.

CASE 3. As mentioned before, this case is *staged*, i. e. it was created to highlight the proposed visualization techniques' versatility. Typically, small lung nodules are treated

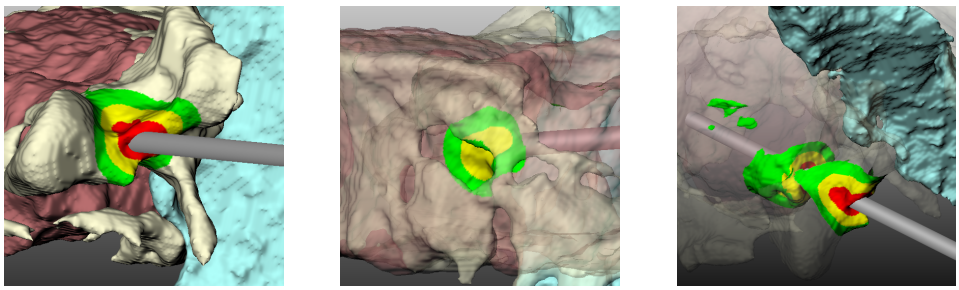

(a) **(b)** **(c)**

Figure 5.23: The results of the on-mesh visualization technique for Case 2. For all subfigures the high and low risk thresholds were set to $1\,mm$ and $3\,mm$ (cf. Tab. 5.3). When the applicator enters surface meshes, target-like color patterns are created **(a,c)**. As depicted in Subfigure **(b)**, the technique also visualizes the insertion depth, i. e. how close a to-be-inserted instrument would get to the targeted vertebra in medial direction. The color-coding can be applied to all surface meshes **(b–c)**. Here, it was applied to the vertebra and metastasis. Moreover, the surface opacities can be decreased to enable physicians to assess the instrument's positioning and orientation inside the targeted structures.

Images originally published in Computers in Biology and Medicine [319, Fig. 4].

via resections if not contraindicated otherwise, e. g. if patients would be left with roughly 35 % to 40 % of their lung volume [201, 215, 282, 291]. However, ablations are also done more frequently, e. g. in patients that would not tolerate or agree on surgical interventions [103, 114]. In Figure 5.24, an image series depicts the results when the in-volume and on-mesh methods were applied to said patient image data. The high and low risk thresholds are equal to before, i. e. 5 *mm* and 10 *mm* for the in-volume method and 1 *mm* and 3 *mm* for the on-mesh method. The segmentation masks were acquired manually via region

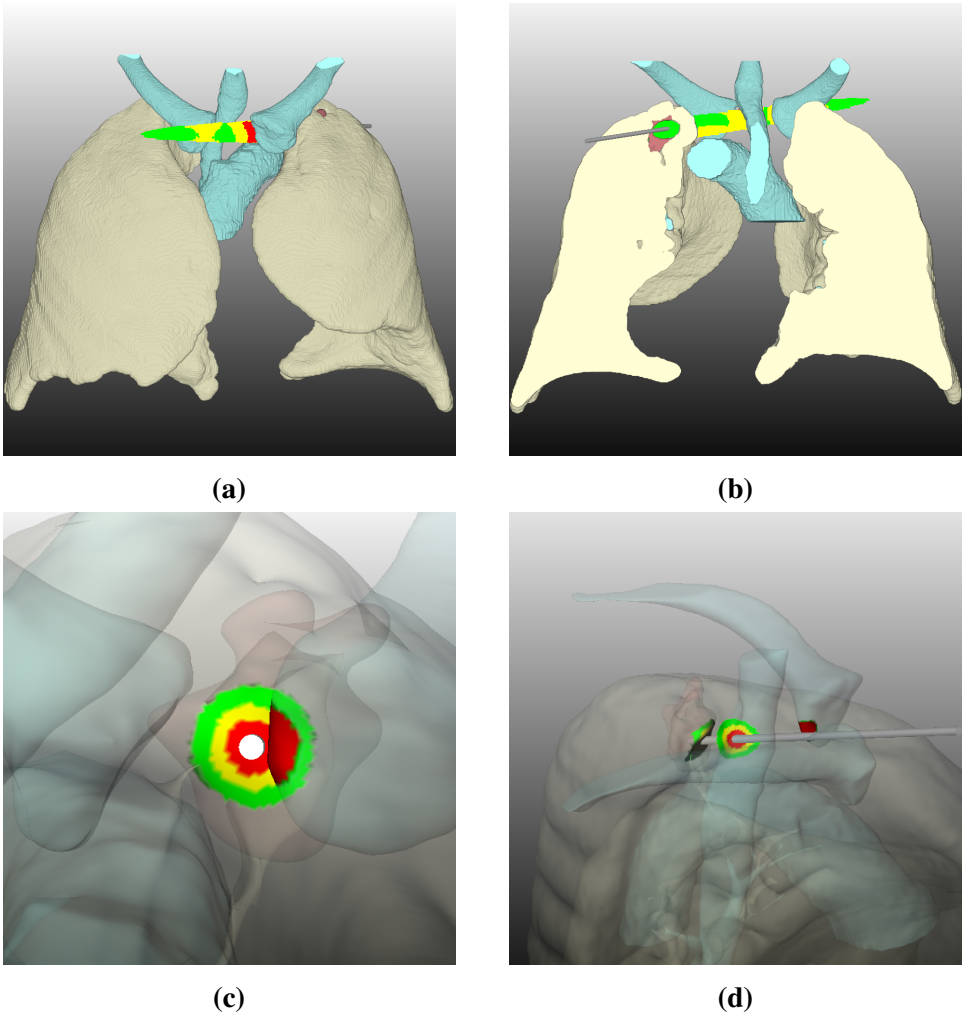

(a) **(b)**

(c) **(d)**

Figure 5.24: An image series that is intended to present the versatility of the proposed visualization techniques. Subfigures **(a–b)** depict the results of the in-volume method. Here, the risk structures (blue) are the trachea and primary bronchi, the aorta and the claviculae. For presentation purposes, the full elliptic cut-away distance field pathway is presented. With respect to the pathway's risk, it was placed near to the left clavicle. Subfigures **(c–d)** depict the results of the on-mesh method. Here, the red color-coding on the left clavicle also reveals its proximity to the to-be-inserted instrument.

The original medical images were provided and used here with permission by Philipp Genseke.

Table 5.5: Computation times for processing. For Case 1 and 2, the spinal cord was the sole risk structure. In contrast, for Case 3, the trachea and primary bronchi, the aorta and the claviculae were used as risk structures. Due to performance reasons, elliptically-shaped pathways were used for the in-volume technique (10 *mm* mid-section). The computational times were averaged for five executions.

	Case		
	C1	C2	C3
In-Volume			
# Voxel Risk Structure(s)	38 755	212 084	372 487
# Voxel Pathway	30 408	139 002	77 370
Time [s]	0.83	8.60	2.86
On-Mesh			
# Vertices All Structures	272 928	881 402	631 660
# Vertices Pathway	688	1504	1412
Time [s]	4.01	12.84	9.14

growing and thresholding of CT images (cf. [263]). Note that the depicted pathway is rather unrealistic, since it would have to be created through the ribs and/or sternum, whereas pathways through the upper left chest would be shorter.

PERFORMANCE. Including image registration and surface mesh generation, the proposed visualization techniques require roughly 10 *min* to 20 *min* preparation. However, this heavily depends on the users' experience and the segmentation masks' quality. In Table 5.5, the computation times for the in-volume and on-mesh technique are shown. They were acquired using an i5-2500 processor with 3.3 *GHz*.

5.5.5.2 RESULTS FOR STEP 2 – DERIVING DRILLING FORCE CHANGES FROM IMAGE INTENSITY CHANGES

The main goal of this step (in the future) is to provide means for drill position verification during robot-assisted bone drilling. Since RFA is an image-guided type of intervention, the relationship between image intensities, e. g. HUs, and drilling forces has to be analyzed. As discussed before, these relationships are not yet fully understood, since drilling and/or breaking experiments are often conducted in other species and in combination with bone conservation, it is challenging to directly translate findings [5, 238, 301]. First, we compared drilling force and image intensity changes along drilling paths in DynaCT images [320] (cf. Figs. 5.10b and 5.20). We followed the notion that increasing HUs are the only necessity for increasing drilling forces, i. e. when image intensities increase, drilling forces should also increase and vice versa. However, at many sampling points along reconstructed pathways, this resulted in false predictions. Additionally, instead of analyzing only one HU per sampling point, we analyzed averaged HUs in cross-sections around each sampling point (*disks*). This addressed the issue only partially and we came to the conclusion that high HUs are not the only prerequisite for high drilling forces.

CYLINDER SEGMENTS. While keeping the approach of utilizing more key values per sampling point, we derived a more sophisticated approach: Instead of *disks*, we employ small cylindrical cross-sections around sample points with each cylinder divided into six uniformly shaped segments (see Fig. 5.25). Subsequently, for each segment, the average HU was computed. This was done since we assumed that drills do not only have to work against bone tissue just in front of them, but against a larger volume of bone tissue. We set the *depth* of these cross-section cylinders to be around three times the isotropic voxel size, i. e. $1.4\,mm$. Subsequently, we defined a *stiffness criterion* called ρ which is used to categorize cross-section cylinders and their segments: A segment SE within a cross-section cylinder of the sample point is considered *stiff* if its average HU μ_{SE} is

$$\mu_{SE} > 0.8 \cdot IS_{max} \tag{5.2}$$

with IS_{max} denoting the highest HU within the assessed vertebra's spongiosa. Note that since conserved bones were used for the drilling experiments, i. e. bones that were freed from fat and dried, the spongiosa contains air (voxels). They do not contribute to the bones' stiffness, but they are included in the reconstructed drilling pathway. Thus, an additional lower threshold for μ_{SE} was defined via

$$\mu_{SE} < 0.1 \cdot IS_{max} \tag{5.3}$$

to filter voxels and/or segments with only little structural relevance. Now, the aforementioned stiffness criterion ρ_{SP} can be employed to analyze if a sampling point (SP) can be considered stiff:

$$\rho_{SP} = \begin{cases} 1, & \text{if } \left(\sum^{\#SE} \mu_{SE} > 0.1 \cdot IS_{max} = 6\right) \wedge \left(\sum^{\#SE} \mu_{SE} > 0.8 \cdot IS_{max} \geq 3\right) \\ 0 & \text{else} \end{cases} \tag{5.4}$$

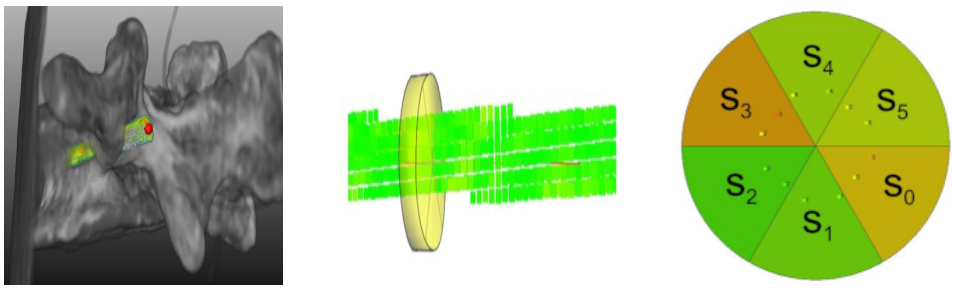

(a) **(b)** **(c)**

Figure 5.25: Subfigure **(a)** depicts a virtual drilling pathway w. r. t. a DV-rendered lumbar vertebra. Here, we employed small cylinders along a pathway to analyze inlying HUs **(b)**. To further increase the number of key values per sampling point, each cylindrical cross-section is partitioned into six segments **(c)**. Relative to IS_{max} within the spongiosa, the segments are color-coded with green representing small average values and red representing high average values.

Images originally published in Computers in Biology and Medicine [319, Fig. 6]. The images were reprinted with permission by Simon Adler and Magnus Hanses.

The graph curves in Figure 5.26 depict the results when ρ is applied to a (normalized) drilling force profile: In simplified terms, a sampling point – or rather the surrounding bony tissue – is considered *stiff* if all segments contain relatively high HUs. Consequently, if all conditions are fulfilled, higher drilling forces are necessary to maintain the *current* feed rate, e. g. of $2\,mm/s$. Using this criterion makes it possible to *predict* high drilling force changes from HUs with an inaccuracy of less than $\pm 1\,mm$. Potentially, this criterion could be used for drill position verification by analyzing if predicted drilling force peaks match with *currently* measured drilling forces. This will be discussed in more detail below.

5.5.6 EVALUATION

In this section, it is described how the in-volume and on-mesh techniques were evaluated.

INTERVIEW SETUP. The proposed visualization techniques were evaluated by two neuroradiologists. Interviewee I2 co-authored the respective publication [319]. They were interviewed using interactive questionnaires via document-embedded 3D IVR viewers and other interactive elements, such as check and text boxes. For this, the TEX packages

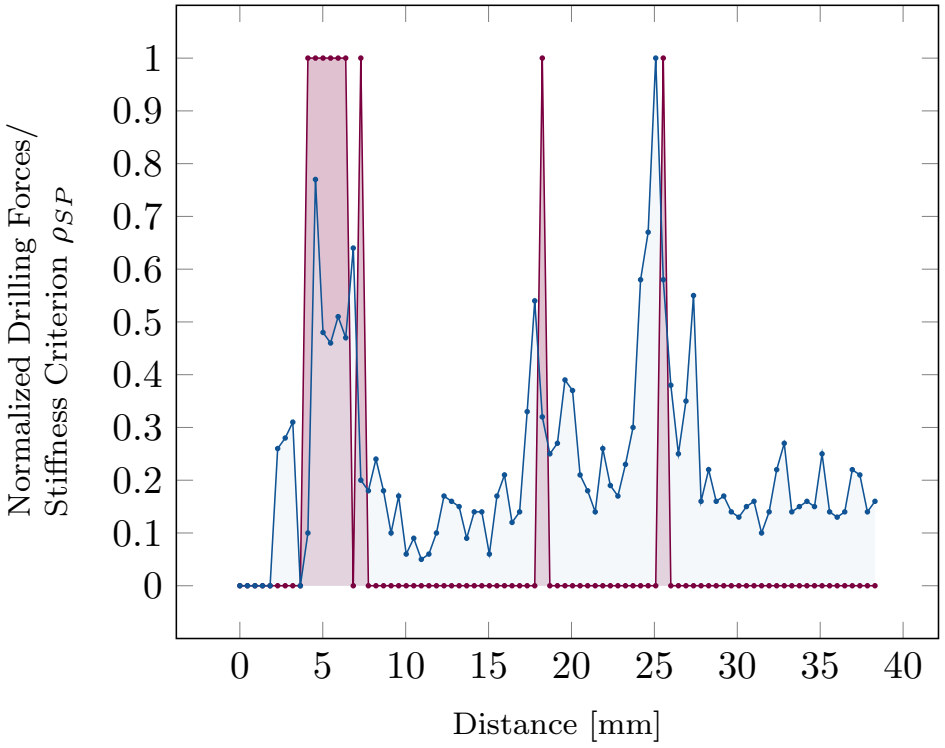

Figure 5.26: Measured and normalized drilling forces compared with the sample points' stiffness ρ_{SP} along a drilling pathway.

Image originally published in Computers in Biology and Medicine [319, Fig. 7] and reprinted with permission by Simon Adler and Magnus Hanses.

[5] `hyperref`: https://ctan.org/pkg/hyperref?lang=de and `media9`: https://ctan.org/pkg/media9?lang=de, both last accessed October 22, 2019

Table 5.6: The results of the evaluation via interactive questionnaires and a think-aloud interview of two neuroradiologists. The numbers are denoted in years.

	Interviewees	
	I1	I2
Part 1 – General Questions		
Gender	m	m
Age	49	29
Experience with Planning and Performing RFAs	12	4

	In-Volume				On-Mesh			
	C1		C2		C1		C2	
	I1	I2	I1	I2	I1	I2	I1	I2
Part 2 – Visualization Features								
Q1								
Q2								
Q3								
Part 3 – Clinical Feasibility								
Intervention Planning								
Intervention Execution								
Intervention Validation								

Legend: −− | − | ∘ | + | ++

Table originally published in Computers in Biology and Medicine [319, Tab. 4].

`hyperref` and `media9` were employed.[5] Additionally, I1 was interviewed in an informal think-aloud setup, whereas I2 provided additional written feedback. With respect to the interactive questionnaires, first, the interviewees were instructed how to use the 3D viewer, e. g. how to rotate depicted surface models. Similar to Figure 5.23, surface models of the remaining vertebrae, metastases and spinal cords were shown, however, without the respective applicators. The in-volume and on-mesh visualization results were presented via screenshots. They answered questions using a five-item Likert scale (- -, -, ∘, +, ++). The questionnaires were divided into three parts.

PART 1 – GENERAL QUESTIONS. First, the interviewees were asked about their clinical experience (see Tab. 5.6).

PART 2 – VISUALIZATION FEATURES. Subsequently, the interviewees were asked about visualization-specific features and capabilities:

Q1 How easy to understand is the respective visualization method?

Q2 In-Volume only: How sensible and useful do you rate the three-dimensional encoding of the correction direction?

Q3 On-Mesh only: How sensible and useful do you rate the usage of transparencies?

PART 3 – CLINICAL FEASIBILITY. For the last part, the interviewees were asked to rate the methods' feasibilities w. r. t. RFA-related tasks (cf. Fig. 5.18).

5.5.7 DISCUSSION

In this section, shortcomings and ideas how to address them will be discussed.

LIMITING PREPROCESSING. Both interviewees stated that, for each patient, manual image registration and key structure segmentation would be too time-consuming. Thus, employing (semi-)automatic methods would be a valuable addition to the proposed visualization techniques. For example, Rak et al. [388] published a survey article on image analysis methods in the spine, including the localization, segmentation and extraction of vertebrae or the spinal cord. To automatically segment spinal metastases, the method of Hille et al. could also be employed [192].

IN-VOLUME PERFORMANCE. There are two principal ways to employ the distance field computation for the in-volume technique. On the one hand, and as shown in Figures 5.24a and 5.24b, the pathway can be extended into an elongated ellipse or cylinder. Subsequently, the distance field is only computed for voxels in this shape. On the other hand, the distance values can also be computed between the risk and the non-risk structure sets – or even within the whole volume – with the pathway being subsequently used to *filter* and/or mask the non-risk structure-shaped distance field. This can be done since it is guaranteed that a pathway will be created through non-risk structures, i. e. through the context organ and the targeted lesion. The main downside of this is that the computation times are higher. For example, for Case 3, when the combined lung parenchyma and lesion mask is used, distance field computation requires 113.18 *s* on average for five executions (7 702 944 voxels). However, the masking between pathway and the distance field volume only requires seconds, which is faster than re-computing the distance field repeatedly.

3D SAFETY MARGINS IN 2D. The general challenge during slice-based image assessment is to find feasible pathways for the to-be-inserted instruments. This is depicted in Figure 5.21: When the ill-defined pathway would be assessed in 2D without any enhancements, presumably, it may be corrected in lateral direction due to its in-plane proximity to the spinal cord. However, it would still be too close in inferior direction due to the patient's spinal cord compression and, overall, due to the strict spatial constraints in the spine, pathway corrections in lateral direction are only feasible to a certain degree. In contrast, the proposed in-volume method *directly* proposes a correction in top-right direction, which could speed up an iterative pathway correction process. Both experts acknowledged the potential of this approach, however, it has to be evaluated in terms of efficiency.

EVALUATION. Both interviewees reported that the visualization methods are easy to understand. However, their opinions regarding visualization-specific features differ. For

example, I1 considers the use of transparencies for the on-mesh method to be beneficial, since they allow for a quick assessment of the instruments' orientation within targeted lesions (cf. Figs. 5.23b and 5.23c). The second interviewee, however, reported that transparent surfaces did not provide benefits for him. In contrast, I2 reported that the in-volume method is superior to the conventional 2D slice-based assessment, since distances between the currently assessed drilling pathway and risk structures are encoded in all directions at once. Interviewee I1, however, argued that the in-volume results are visually complex, which requires some time to be *read*. Both experts stated that the proposed visualization techniques are feasible for their intended purposes, i. e. intervention planning and execution, but they also mentioned that their true usefulness would have to be assessed in a real clinical setting. With respect to intervention validation, the assessment of necrotic bone tissue is important, which is out of the scope of the proposed method (cf. [403]). Furthermore, I2 noted that the techniques could also be employed in an educational setup, such as in student seminars. Moreover, the proposed methods could also be employed in visualization-enhanced intervention reports, e. g. to document intervention executions.

DRILLING FORCE ESTIMATION. With respect to Step 2, the so-called stiffness criterion ρ was introduced to derive drilling force peaks from HUs. Hammering and drilling are unique tasks to bring instruments into target (context) structures, which typically is not required in softer structures, such as the liver. Additionally, bone metastases can result in very heterogeneous disease patterns (cf Figs. 2.2b). Therefore, knowledge about suspiciously dense or loose bone tissue along instrument pathways is an important key feature. With respect to the introduced criterion, we could show that *strong* drilling force changes depend on the homogeneity and overall high tissue density within a certain depth *in front* of instruments. However, note that respective parameters, such as the cross-section's depth, the density thresholds and the number of segments, were acquired by observations alone and that further research is required to examine their relationships.

BONE CONSERVATION AND DRILLING. For the drilling experiments and subsequent analysis, conserved vertebrae were used. During conservation, the physical properties of bones change and it can be expected that higher drilling forces are required for fresh bones [21, 121]. However, there exists no data that describes how these changes relate to drilling forces. This knowledge could be used to understand if conserved vertebrae can be utilized to reliably predict drilling forces and drilling force changes in fresh bones.

ABSTRACTION AND COLOR-CODING. With respect to the abstraction theory of Viola and Isenberg [501], the final presentations only introduce a rather low degree of geometric abstraction. This preserves geometric features which are important during intervention planning and execution, for example how well-preserved the targeted pedicles are or if the spinal cord is damaged (cf. Figs. 5.21b and 5.23a). Similar to our floor maps, a simple diffuse shading was employed, which results in a moderately high degree of photometric abstraction. Since no temporal image data was employed, e. g. to simulate ablations, no temporal abstraction was introduced. Scale-wise, since gross anatomy is depicted, both visualization methods are on the *upper end* of the abstraction scale axis. With respect to the color-coding, a qualitative (categorical) traffic light-like color scale was employed to

assist clinical decision-making. On the one hand, this limits the methods' *expressiveness* w. r. t. safety margin-related *risk* for pathways *in between* two risk categories, e. g. that could still be considered being somewhat *safe* (between green and yellow) (cf. [187, 530]). On the other hand, safety margins in clinical practice are often *fixed*, e. g., for to-be-ablated or -irradiated lesions the target volume is *X mm* larger than the actual lesion [508]. Thus, we employed a (customizable) categorical three-element color scale, for which default visualization parameters can be re-used for other cases (cf. Tab. 5.3).

EXPLICIT VS. IMPLICIT MEASUREMENTS. During all intervention steps, explicit size and distance measurements are important key features, for example, to ascertain the targeted lesion's size or to measure the (minimal) distance between lesions and adjacent risk structures (cf. [415]). Radiological workstations provide such facilities. In contrast, the proposed visualization techniques (photometrically) *abstract*, i. e. compile, multiple distances into one of three color-coded distance categories. They can be adapted to visualize safety margins on the submillimeter scale (cf. Fig. 5.22), however, this *degree of explicitness* is limited. If the techniques would be evaluated in a clinical setting, explicit measurements should be provided to potentially raise user acceptance w. r. t. facilities that they are used to and/or require (cf. [171]), while the proposed techniques are offered as an additional representation to depict distance-related information in a condensed manner. This also applies to the subsequent reporting of findings and/or the outcomes of interventions. With respect to the proposed floor maps, here, visualizations are also employed to cognitively assist physicians by enhancing established facilities rather than replacing them.

CLINICAL APPLICABILITY. The proposed two-step method's clinical applicability w. r. t. RFA-related tasks would have to be evaluated in a *real* clinical setting. The presented methods and techniques could be used during intervention planning and execution to support physicians during pathway definition and creation. However, in its current state, the method is more feasible to provide cognitive support by providing additional key features during intervention planning, i. e. by visualizing pathway *risk* w. r. t. a certain combination of risk aspects and by providing a rough estimation of the forces to be applied during drill insertion w. r. t. the pathway's extent. It was shown that the in-volume and on-mesh methods could also be applied to other organs, such as the lungs. Moreover, these visualization methods can also be employed to support other needle-based interventions or tests, e. g. biopsies, as long as

- the set of risk aspects is identical and
- the instruments to be employed are rigid.

With respect to Step 2, instruments with ruler marks could be used to raise awareness for bone tissue compartments with varying densities w. r. t. the instruments' extents. Given that force peaks could reliably be estimated, the stiffness criterion ρ could be used in a robot-assisted setup for instrument position validation. Moreover, a robot could potentially be equipped with various additional tools, for example with a thermal sensor and cooling system, to minimize the risk of drilling-related necroses in healthy bones.

MULTIMODALITY. With respect to the scope of this thesis, multimodal medical image sources are utilized for the proposed two-step method but in a limited way. Since DVR of MR images is challenging, segmentation masks for Step 1 were employed (cf. Figs. 5.13 and 5.25a). However, MR images could be further utilized, for example, to visualize other types of soft tissue, such as the skin and muscles, *in front* of the vertebra to provide an enhanced spatial context. In contrast, the in-volume technique could be coupled stronger to Step 2, for example, by depicting high density compartments along pathways. Especially w. r. t. manually conducted interventions this could be a useful key feature to raise awareness about highly dense tissue compartments at the border of a pathway that could displace instruments in an unfavorable direction.

5.6 SUMMARY

In this chapter,

- a requirement analysis and prototypical implementation for computer- and robot-assisted RFAs and
- a two-step risk assessment method for pathway definition and creation

in the spine were presented. Intervention planning, i. e. the process of finding clinically feasible pathways w. r. t. the patient's metastatic disease pattern, is primarily based on the physicians' experience when assessing diagnostic image sources. Thus, we aimed to offer cognitive assistance to find *good* pathways, e. g. by enhancing diagnostic and/or intra-operative 2D images by 3D information. During RFAs in the spine, currently, only little to no physical assistance can be offered to physicians (cf. [40]). Thus, robotic assistance would offer promising prospects, such as tremor-free and constrained motions [173, 444]. With respect to the aforementioned limitations, some work has to be done, e. g., to make pathway planning more interactive and to deepen *our* understanding of how image intensities can reliably be used to predict drilling forces. However, the presented findings can already provide assistance in manually conducted needle-based interventions, although robotic assistance has to be researched more. Moreover, an in-depth evaluation of how

- different types of metastases,
- RFA electrode positioning and currents,
- post-ablation evaluated necrotic tissue and eventually remaining metastatic tissue

relate to each other, would be very beneficial for all RFA-related topics.

The next chapter focuses on SIRTs, which are also a type of treatment in interventional radiology. In contrast to RFAs for which electric currents are used to affect tissue, in SIRTs, radioactively labeled microspheres are employed to embolize the subsequent blood vessel network and to irriadiate tissue in close proximity to microsphere accumulations [398].

6 ILLUSTRATIVE VISUALIZATIONS FOR SIRTS IN THE LUNG

SELECTIVE Internal Radiation Therapy (SIRT) is an image-guided and minimally invasive type of intervention in radiology. Such interventions are also called *radioembolizations*, i. e. a combination of an embolization, which is the process of virtually creating an artificial vessel occlusion to cut off tumor tissue from nutrition supply, and a subsequent local radiotherapy [503]. Typically, SIRTs are conducted in the liver [376], but there also exist advances to use them for renal carcinomas [455], or metastases in the lung [398]. There are other types of radiation therapies, such as external beam radiotherapy or brachytherapy, and the basic idea is that some type of radiation, e. g. from X-rays or (natural) radioactive material, is used to locally destroy cancerous tissue. In SIRTs, the embolization material is radioactively marked, for example via ^{90}Y, which subsequently irradiates surrounding (tumor) tissue. This media consists of small resin- or glass-based microspheres that are employed via catheters which have to be maneuvered through blood vessels near the target lesion(s) [232]. Most commonly, SIRTs are employed to treat carcinomas and/or metastases in patients that cannot undergo surgeries, e. g. if they would be left with an insufficient lung capacity [148, 486], for whom there exist no other treatment options, such as chemotherapies [398], or who did not show positive treatment responses [232]. Another limiting factor is the disease pattern, since various types of interventions in the lung, such as RFAs or brachytherapies, are limited to a certain lesion number ($\lesssim 3$) and lesion size ($\lesssim 3\,cm$) [398]. Moreover, SIRTs are most commonly conducted in a palliative setting, i. e. "*to relieve symptoms and, if possible, prolong survival*" [207], although they were also reported to *downgrade* liver carcinoma to make them resectable [207].

The techniques presented in this chapter aim to provide cognitive support for PET hotspot and blood vessel assessments in the lung to plan and evaluate SIRT interventions. Typically, lung diagnostics are conducted via high-quality CT images, but also via combined PET/CT images that show physiological abnormalities in their morphological context. To cognitively support physicians during the assessment of such abnormalities, e. g. to relate PET hotspots to their respective lung lobe(s), 3D visualization techniques can be employed. With respect to the techniques presented in Chapter 3, most authors employ DVR techniques that somehow decrease the visibility of occluding anatomy *in front* of hotspots. Here, an illustrative IVR approach was chosen to exploit the generally high degrees of simplification and/or abstraction to provide spatial exploration support *at a glance* [501]. To do so, we propose a technique for which OITs with enhanced boundaries and silhouettes are combined in an interactive manner. Thus, PET hotspots can be revealed interactively while boundaries between adjacent structures preserve spatial relationships,

even if the visibilities of context structures are heavily decreased. Note that in the context of this chapter there exist two types of PET hotspots, namely

- ^{18}F-PET hotspots, which are assessed during (initial) diagnoses and follow-up assessments to evaluate treatment responses and
- ^{90}Y-PET hotspots, which are examined during intervention assessment to evaluate if the ^{90}Y-labeled microspheres reached their intended destination.

The technique was evaluated by five clinical and four medical visualization domain experts w. r. t. its perception-related capabilities to distinguish lung lobes and to render PET hotspots clearly visible in their morphological context.

Since SIRTs are catheter-based interventions, during intervention planning, physicians have to plan how they will have to maneuver catheters to employ the radioembolization media. Thus, physicians evaluate CT and DSA images to gain knowledge about eventual blood vessel abnormalities that might complicate catheter guidance. Typically, diagnostic (standard-dose) CT images are used to do so, since they have good contrast between lung blood vessels and adjacent parenchyma. In contrast, the aforementioned CT scans from the combined PET/CT images are acquired in so-called *low-dose* mode and are typically only used for attenuation correction purposes (cf. Sec. 2.2.1). Here, low-dose denotes that the patients' radiation exposures are roughly decreased by 75 % to 80 % when compared to standard-dose CT acquisitions [470]. Image matrix- and voxel size-wise, both image stack types are roughly comparable with the low-dose images having a slightly worse resolution. The main difference, however, is that the X-ray tube's current is significantly lower, e. g. ranging from 40 mA to 80 mA for low-dose images and from 200 mA to 400 mA and more for standard-dose images, which results in increased image noise. In combination with standard kVp settings ranging from 120 keV to 140 keV, these settings result in relatively low soft tissue contrast (cf. Sec. 2.1.2).

Thus, the qualitative assessment and segmentation of lung blood vessels can become challenging. With respect to segmentation and/or enhancement approaches to support intervention planning, straightforward methods typically lead to under- or over segmentation artifacts, e. g. by excluding blood vessel or including lung parenchyma voxels. Most (blood) vessel segmentation methods segment and/or enhance vessels in diagnostic and/or contrast-enhanced CTA, Magnetic Resonance Angiography (MRA) or retinal photographies [137, 339, 426]. In the context of our collaboration with the local University Clinic for Nuclear Medicine in Magdeburg, we also had access to diagnostic CT images which could have been used to carry out blood vessel segmentations and subsequent visualizations. However, since blood vessels were also intended to be visualized via the aforementioned visualization technique, this would have resulted in the necessity to register the aforementioned PET images with these CT images, which would have complicated the processing pipeline. Thus, an image processing method was developed to enhance blood vessels in low-dose CT images, which we called the LANCELOT method (**L**ung Vessel Enh**ance**ment for **Lo**w-Dose C**T**) [97, 283]. Note that, since this thesis is focused on visualization techniques, this part will only be reflected on briefly.

This chapter is structured as follows: First, backgrounds on the human lung w. r. t. its gross anatomy and cancer biology are provided (Sec. 6.1). Subsequently, it is explained how SIRTs are conducted from a clinical workflow perspective (Sec. 6.2). In Section 6.3, the aforementioned illustrative visualization technique and the LANCELOT method will be presented. Finally, this chapter is concluded with a short summary (Sec. 6.4).

This chapter is based on:

[323] **Merten, N.**, Glaßer, S., Lassen-Schmidt, B., Großer, O. S., Ricke, J., Amthauer, H., and Preim, B. "Illustrative PET/CT Visualisation of SIRT-Treated Lung Metasteses." In: *Proc. of Eurographics Workshop on Visual Computing in Biology and Medicine*. 2016, pp. 99–104

[324] **Merten, N.**, Lawonn, K., Genseke, P., Großer, O. S., and Preim, B. "Lung Vessel Enhancement in Low-Dose CT Scans – The LANCELOT Method." In: *Proc. of Bildverarbeitung für die Medizin*. 2018, pp. 347–352

6.1 BACKGROUND ON THE HUMAN LUNG

Here, brief overviews about the human lung, its functions and cancer-related topics are provided. For more information, see [314, Ch. 24] and [424, Ch. 23].

6.1.1 GROSS ANATOMY – THE LUNG

Our lungs are parts of *our* respiratory system, which also includes, e. g., the nose, trachea and bronchi. The lung itself is a rather soft organ that is traversed by arteries, veins and airways with an average total air capacity of roughly 4 *l* to 6 *l* in healthy adults (see Fig. 6.1).

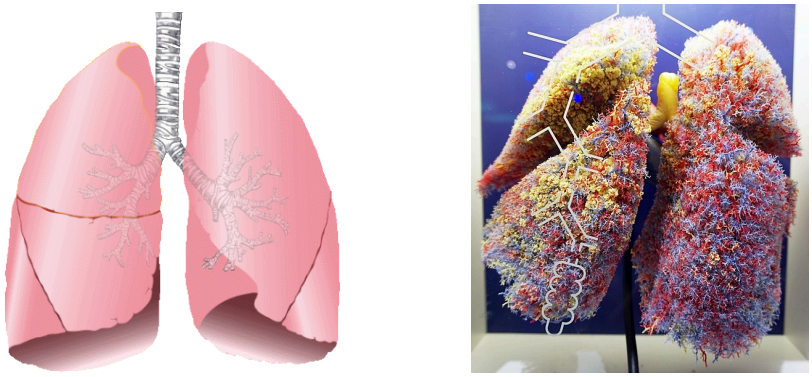

(a) **(b)**

Figure 6.1: Subfigure **(a)** depicts a stylized presentation of the human lung with the trachea and some bronchi in the middle. On the right, a – presumably plastic-based – cast of the lungs from a posterior viewpoint is depicted **(b)**. The red, blue and yellow entities are pulmonary arteries, veins and airways and/or alveoli, respectively.

The pulmonary arteries transport de-oxygenated blood from the heart to the alveoli and the capillaries embedded therein [424]. Here, carbon dioxide is exchanged with oxygen through a very thin membrane near the pulmonary arteries (gas exchange). Subsequently, the oxygen-enriched blood is sent back to the heart via the pulmonary veins from where it gets distributed through the body. Similar to the myocardial arteries that supply the heart with nutrients and oxygen, the so-called bronchial arteries "*usually originate from the proximal descending thoracic aorta*" and supply other pulmonary structures, such as pulmonary arteries, with nutrients and oxygen [505]. The de-oxygenated blood from the bronchial veins "*flows into the pulmonary veins, bypassing the rest of the systemic circuit and diluting the oxygenated blood leaving the alveoli*" [314]. Additionally, the lung is traversed by lymphatic capillaries [424]. As Saladin states, "*the lungs have a more extensive lymphatic drainage than any other organ in the body*" to keep the alveoli dry and functioning [424]. Presumably, this is the reason that thoracic metastases manifest often (≈ 40 % to 45 %) in patients with lung cancer [213, 315, 336] (cf. Ch. 7).

6.1.2 GROSS ANATOMY – LUNG LOBES AND SEGMENTS

As depicted in Figure 6.1a, the lungs typically consist of five lobes, with three lobes comprising the right and two lobes comprising the left lung. Note that although it is rather rare, some individuals miss the right middle lobe [487] or have a mirrored lung arrangement [210, 289] (situs inversus, incidence roughly 1:10 000). The lobes are separated by so-called fissures and, w. r. t. lung functionality, are distinct compartments (see Fig. 6.2). For the left lung, e. g., the primary bronchi, i. e. the "*air tubes*" after the trachea splits up at the carina (dt. *Schiffskiel*), branch out into superior and inferior secondary bronchi [424]. Note that the main bronchi are asymmetrical, i. e. the right main bronchus is roughly 2 *cm* to 3 *cm* long, whereas the left main bronchus roughly measures 5 *cm* [424]. This asymmetry is also reflected by the lungs itself, with the right lung typically being broader and the left lung being longer [313]. Subsequently, the secondary bronchi branch into tertiary bronchi which "*ventilate[s] one functionally independent unit of lung tissue called a bronchopulmonary segment*" [424]. Typically, the left lung consists of eight segments, whereas the right lung

Figure 6.2: A normal, i. e. healthy, formalin-preserved lung that was resected during autopsy. The prominent *valley* between the lung lobes is called a fissure.

Table 6.1: Primary lung carcinomas have very high incidence and mortality rates. In Subtable **(a)**, estimated new cases and deaths for 2019 w. r. t. the four *most common* primary cancer sites are listed [445]. Primary lung carcinomas can also result in distant metastases. Common *target organs* are listed in Subtable **(b)** [336].

(a)

Primary	New Cases	Deaths
Digestive System	328 030	165 460
Genital System	295 290	65 540
Breast	271 270	42 260
Lung	228 150	142 670

(b)

	[%]
Liver	34.3
Adrenal Glands	32.6
Brain	25
Bones	14.9

consists of ten segments [424]. In addition to the primary bronchus being wider and more vertically proceeding than the left primary bronchus [424], presumably, the right lung contributes more to the oxygen intake than the left lung (cf. [519]).

6.1.3 LUNG CANCER BIOLOGY AND METASTATIC DISEASES

As with any other type of cancer, lungs can also develop cancerous and/or metastatic diseases. For the lungs, there exist four major types of cancer [92, 127], namely

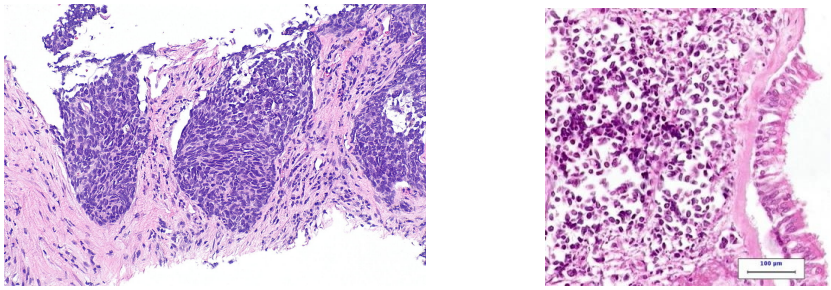

(a) Non-Small Cells **(b)** Small Cells

Figure 6.3: Depictions of non-small **(a)** and small **(b)** cell lung cancer cells. The names reflect cell morphology with the cells on the left being larger. Small cell lung cancer is also called "*oat cell carcinoma*" which "*gets its name from its small, densely packed oat-grain-like cells*" [127]. No scale was available for Subfigure **(a)**.

Table 6.2: An estimation of new lung metastasis w. r. t. certain primary cancers.

Primary Carcinoma	Incidence of Lung Metastases [%] [3]	Number of Autopsy Cases [3]	Estimated New Cases 2019 [445]	Estimated (New) Lung Metastases 2019
Breast	77.2	167	271 270	209 420
Kidney	65	34	73 820	47 983
Lung	46.9	160	228 150	107 002
Rectum	38	87	44 180	16 788

The numbers of the 1st and 2nd column were reprinted by permission of John Wiley and Sons (Source: Herbert L. Abrams, Robert Spiro, Norman Goldstein, Metastases in carcinoma. Analysis of 1000 autopsied cases, Cancer) [3, Tabs. 1, 2, 5, 10 & 13]. The numbers in the 3rd column were reprinted by permission of John Wiley and Sons (Source: Ahmedin Jemal, Kimberly D. Miller, Rebecca L. Siegel, Cancer statistics, 2019, CA: Cancer Journal for Clinicians) [445, Tab. 1].

- Adenocarcinomas, which "*begin[s] in the smaller airways and the alveoli*" and "*make up about* 40 % *of all lung cancers*" [127],
- Squamous Cell Carcinomas, which "*are centrally located in the larger airways*" [92] and make up about 30 % of all lung cancers,
- Large Cell and/or Giant Cell Carcinomas, which also "*usually start in the smaller airways*", get their name from their comparatively large cells and "*comprise about* 10 % *of all lung cancers*" [127] and
- Small Cell Carcinomas that "*usually develops[s] in the [...] bronchial airways*" [127].

Moreover, there exists a general differentiation into

- Non-Small Cell Lung Cancers (NSCLCs) (adeno-, squamous cell, large and giant cell carcinomas), with their respective cells having a "*usual doubling time*" of about 30 *days* to 180 *days* [127] (see Fig. 6.3a), i. e. they typically grow *rather* slowly, and
- Small Cell Lung Cancers (SCLCs), with their respective cells typically having a very short *doubling time* of roughly 30 *days*, which makes this type a "*particularly aggressive form of cancer that spreads quickly*" [127] (see Fig. 6.3b).

NSCLCs make up roughly 75 % to 80 % of all lung cancer cases [92, 127]. However, on a cellular scale, lung cancer can be heterogeneous and "*tumours are sometimes categorized as 'adenosquamous carcinoma'*" when they have mixed disease patterns [92]. The numbers listed in Table 6.1 show that although primary cancers from the respiratory system do not have the highest incidence rates, the respective mortality rate is very high. With respect to metastases that originate from primary lung cancer, Table 6.1 denotes that the liver, adrenal glands and the brain are the most common target organs [336]. Additionally, lung cancer also tends to spread into other parts of the lungs, e. g. into different lobes, and thus, lung metastases from primary lung cancer are also common (≈ 45 %) [3].

Similar to bone metastases, it is also more likely that carcinomas from other organs result in lung metastases than that primary lung carcinomas develop. This is shown in Table 6.2,

where the works of Abrams et al. [3] and Siegel et al. [445] are combined to estimate new cases of lung metastases. Note that these numbers are a rough estimation, since, for example, the numbers provided by Siegel et al. [445] are also estimations. However, assuming that the numbers would be accurate, the ratio between lung carcinomas and lung metastases from foreign sites roughly lies between 1 to 1.5/2.

IMPLICATIONS FOR THIS THESIS. These high incidence and mortality rates show the importance of detecting and treating lung carcinomas and metastases at an early stage. Due to the fast growing rates and often cancer-unspecific symptoms, such as coughing or breathing issues, initial screening can often reveal already advanced diseases, which may render curative prospects unrealistic. With respect to lung cancer imaging (and screening), false-positive diagnoses are a common problem in (low-dose) CT image (and radiography) assessments. For example, Croswell et al. [96] reported that the false-positive rate for low-dose CT images ranges from 21 % to 33 %, which not only results in patient burden (cf. [305]), but also in increased costs due to re-testing and eventually unnecessary follow-up interventions. Thus, there exists a high research interest to provide physicians with computer-assisted support, e. g. to detect and segment lung structures and suspicious nodules, to derive treatment decisions, and to plan and evaluate interventions. For such methods, typically, diagnostic (standard-dose) CT images are used. We assumed that SIRTs would be planned, employed and assessed in a palliative setting with combined PET/CT images being the *primary modality*. Moreover and as mentioned before, we had access to diagnostic CT images, but we wanted to assess how low-dose (low-contrast and high-noise) CT images can be employed for said purposes. Thus, the proposed illustrative visualization technique and the LANCELOT method use low-dose CT images to provide cognitive support during diagnoses, intervention planning and intervention assessment.

6.2 AN EXEMPLARY SELECTIVE INTERNAL RADIATION THERAPY WORKFLOW

Similar to the previous chapter, here, a simplified clinical workflow is described for which it is assumed that a SIRT is conducted to treat a lung carcinoma or metastasis (see Fig. 6.4). This will be done, for example, w. r. t. various lung structure segmentation and analysis methods. Important key features are, for example, the position, size and volume of lung nodules, but also their ratio w. r. t. the surrounding parenchyma. Some of the methods presented in this section are part of the *MeVisPULMO 3D*[1] (MeVis Medical Solutions AG, Bremen, Germany) application which we had access to in the context of our SIRT-related publications [323] (cf. [312]).[2] In clinical practice, however, such sophisticated methods and/or tools are typically not used, since, e. g., nodule sizes are approximated via spherical and/or elliptical ROI segmentations (read below). Moreover, in contrast to the depicted imaging modalities, MR images can also be employed for lung diagnostics [27]. However, this section will be focused on CT, ^{18}F-FDG- and ^{90}Y-PET images that are acquired with hybrid imaging devices (cf. Sec. 2.2.1).

[1] https://www.mevis.de/en/competences/clinical-competences/lung/, last accessed November 5, 2019

[2] Note that this application was a research prototype, although newer versions are certified and distributed.

Note that the step *Image Analysis* will not be described explicitly, since related aspects will be discussed in the sections that represent the preceding segmentation steps. Nevertheless, treatment decisions and respective limitations that are typically derived from image analysis key features are briefly discussed in Section 7.4.

6.2.1 IMAGE ACQUISITION AND DIAGNOSIS

From an imaging perspective, prior to CT, chest radiography was the primary imaging modality used to screen for lung cancer and other lung-related diseases. However, lung cancer diagnoses are challenging and typically entail high false-positive diagnoses which do not only result in patient burden (cf. [305]), but also in increased costs due to re-testing and eventually unnecessary follow-up interventions. *Low-dose* is "*defined as a protocol to minimize patient radiation exposure while maintaining the performance of CT for the detection of lung nodules*" [470] and such protocols depend on, e. g., the CT scanner's kVp, tube current and rotation speed settings [391].

6.2.1.1 CT-ONLY DIAGNOSTIC PERSPECTIVE

In CT images, physicians typically search for (small) nodules which can be non-solid, partially solid or *just* solid (see Fig. 6.5). *Solidness* refers to the more or less clear delineation between a nodule and its adjacent tissue. Finding and distinguishing such nodule types is important, since the type represents a certain degree of malignancy. For example, Henschke et al. [186] reported that in their study of 233 cases, they found that for solid, partially solid and non-solid nodules the malignancy was ascertained in 7 %, 63 % and 18 %,

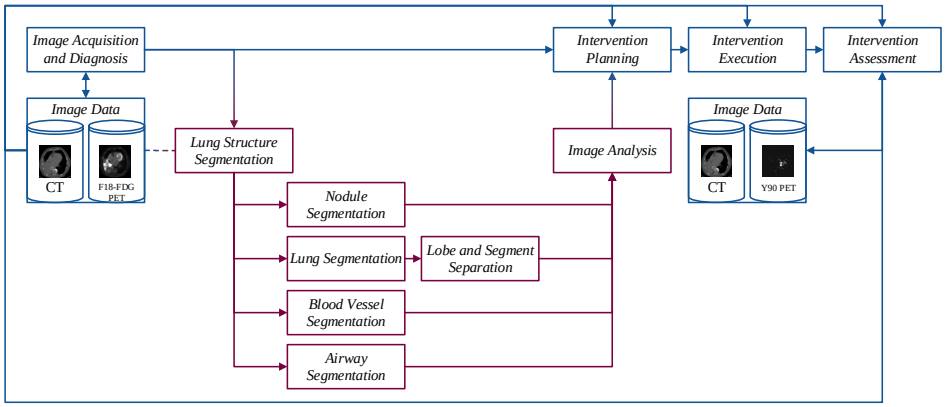

Figure 6.4: Simplified overview of SIRTs from a clinical workflow perspective. With respect to this, a Lung Structure Segmentation and Image Analysis pipeline is depicted. This outline will later be reused to describe the proposed illustrative visualization technique for PET/CT images (cf. Fig. 6.10). For presentation purposes, some of the actually employed imaging modalities are not depicted, e. g. intra-interventional DSAs or post-interventional ^{90}Y-SPECT images. Thus, this depiction is *streamlined* w. r. t. the proposed visualization technique. Moreover, post-interventional ^{18}F-FDG PET/CT images can be used to quantify and assess treatment outcomes from a morphological and physiological perspective.

respectively. Solid nodules often indicate small-cell lung carcinomas [180], whereas subsolid nodules rather indicate adenocarcinoma-related lung cancers [391]. Moreover and w. r. t. malignancy, the sensitivity also depends on the nodules' locations, i. e. perihilar (medial) nodules are more challenging to detect (36.7 %) than peripheral nodules (73.9 %) [354]. Presumably, this is due to the high degree of anatomical variability near the lungs' hila. If physicians find nodules, they assess their size and the overall disease pattern (read below). Subsequently, biopsies and/or bronchoscopies can be conducted to ascertain the malignancy and/or type of lung cancer.

There also exist other nodule types, e. g. *calcifications*, which typically point to *benign* (non-cancerous) lung diseases. However, physicians also have to assess such findings carefully, since real carcinomas sometimes mimic the appearance of calcifications [234].

6.2.1.2 PET/CT DIAGNOSTIC PERSPECTIVE

The combination of CT and PET images has the major advantage that morphology and physiology can be assessed *simultaneously*. This is done since lesions and/or nodules that appear suspicious might not behave suspiciously. However, if they behave suspiciously, i. e. when they show an abnormally increased radiotracer uptake, this can indicate malignant lesions. As mentioned in Chapter 2, ^{18}F-FDG has a low specificity since it gets accumulated in all types of tissue that have an increased number of glucose (GLUT) receptors, which includes tumor and inflammatory tissue (cf. [113]). However, this results in an overall high sensitivity of PET images. Other downsides are the typically *low* image matrix and pixel resolutions of PET images which make it challenging and/or impossible to find very small lesions, e. g. $\lesssim 4\,mm$. In clinical practice, PET/CT images are often assessed in four-viewer GUI setups (cf. Fig. 2.14c) that depict unaltered and fused images next to each other (see Fig. 6.6). This enables physicians to assess each image stack individually and in unison.

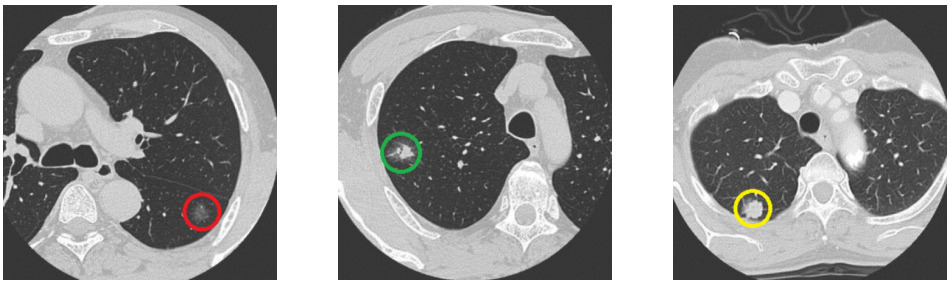

(a) Non-Solid **(b)** Partially Solid **(c)** Solid

Figure 6.5: Depictions of three lung nodule types. *Solidness* describes how well delineated a nodule is w. r. t. adjacent tissue. Non-solid nodules, e. g., appear like *soft shadows* **(a)**, whereas solid nodules are homogeneous with prominent boundaries **(c)**. Partially solid nodules typically have solid *cores* and diffuse boundaries **(b)**.

Images reprinted from Automatic 3D pulmonary nodule detection in CT images: A survey, Computer Methods and Programs in Biomedicine volume 124, Igor Rafael S. Valente, Paulo César Cortez, Edson Cavalcanti Neto et al., Pages 91–107, © 2016, with permission from Elsevier [492, Fig. 3(a–c)].

On a per-findings base, lesions and/or nodules can then be assessed and further processed, e. g. by quantifying PET image values to relate them to the individual nodules' volumes.

6.2.1.3 TNM STAGING IN THE LUNGS

Given that one or multiple malignant nodules are found, the disease has to be *staged*, i. e. certain features of the local and distant tumor tissue are quantified (measured) and categorized. Note that due to the rapid cell doubling times, even during initial diagnoses, lung cancer can sometimes be found in an already progressed state with multiple *primary* nodules and/or thoracic metastases [127]. For lung cancer staging, the TNM system can be employed with each letter describing a certain disease feature category [72]:

- T represents the primary tumor.
  - T1a The tumor's largest extent is $\leq 2\,cm$.
  - T2b The tumor's largest extent lies between $5\,cm$ and $7\,cm$.
- N represents the regional (thoracic) lymph nodes.
  - N0 No regional lymph node metastases.
  - N2 Lymph node metastases in the mediastinum on the same lung side.
- M represents distant metastases.
  - M1a Distant metastasis or metastases in the other lung.
  - M1b Distant metastasis or metastases, e. g. in the liver and/or brain.

Note that for each category the subitems describe certain exemplaric characteristics. Subsequently, all findings are combined into one final staging. For example, in cases of lung

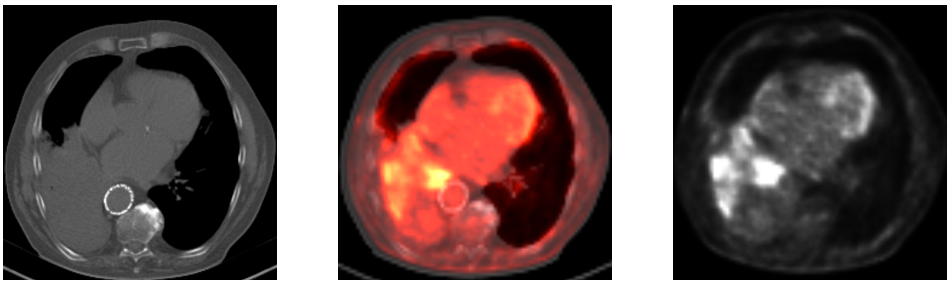

(a) CT-only **(b)** Fused PET/CT **(c)** PET-only

Figure 6.6: For PET/CT images, clinical workstations typically enable physicians to assess both image sources individually **(a,c)** and simultaneously **(b)**. For combined presentations, the PET images are color-coded and then used to superimpose CT images. Here, a black-red-yellow-white color scale was employed with bright image regions representing anatomical regions with increased metabolic activity. Such techniques are somewhat map-like, since the CT images are used as a *base map*, whereas the PET images are used as a *theme map* (cf. Ch. 4).

The original medical images were provided and used here with permission by Philipp Genseke.

cancer with distant metastases, e. g. in the liver, the staging is always IV [72] (cf. [119, 364]). With respect to this, certain treatment and/or intervention decisions are more or less feasible, e. g. treatment risk and outcome prospects do not align.

6.2.2 LUNG STRUCTURE SEGMENTATION METHODS

For diagnostic, treatment planning and evaluation purposes, physicians have to assess various key features, such as the patient's current lung functionality, parenchymal volume, nodule position and dimensions and blood vessel morphology, for example w. r. t. catheter access. With respect to the proposed IVR visualization support, presentations should convey nodules or PET hotspots in their morphological context, i. e. which lung lobe(s) contain them, and w. r. t. SIRTs, which blood vessels have to be used to access them. Thus, segmentations of the nodules and/or hotspots, the parenchyma and blood vessels have to be carried out. Furthermore, airways can also be segmented and visualized to provide orientation support as anatomical landmarks. In the following, various computer-assisted structure segmentation and analysis methods for the lungs are presented, but as mentioned before, sophisticated segmentation and analysis methods are rarely used while radiologic workstations only provide basic measurement and (manual) segmentation facilities.

As mentioned before, clinical workstations often only provide basic tools to *measure* nodules. For example, nodule sizes are typically approximated with (one) diameter of spherical and/or elliptical ROIs, while their volumes are often approximated w. r. t. the image source's slice thickness or by computing the respective *sphere*'s enclosed volume. Note that something similar is done in nuclear medicine workstations, e. g. to derive quantified key values from PET images (cf. Ch. 7). Thus, assessments can become inaccurate, since they heavily depend on the physicians' experience, image quality, image presentation (windowing) and the *fineness* of their tools. These measurements, however, affect various clinical aspects, such as diagnoses, stagings, treatment decisions and treatment evaluations. Therefore, more accurate measurements, e. g. via segmentation and image analysis methods from lung lobes and nodules embedded therein, can benefit these aspect, for example to more accurately quantify treatment responses w. r. t. radiation- and/or chemotherapies.

6.2.2.1 NODULE SEGMENTATION

For diagnoses, the size and/or volume of suspicious nodules must be ascertained. In other words, quantitative key values and/or features have to be derived from images. Such features are important for diagnoses, staging and treatment and/or intervention planning, e. g. for radiation therapies [169, 429]. However, images are not *perfect* since they typically exhibit partial volume effects and boundary-related *uncertainties*, and thus, it can be challenging to carry out accurate measurements. Especially for small lesions and due to contrast-enhancing (thresholding-like) windowing between nodules (*bright*) and parenchyma (*dark*), this often results in experts overestimating lesion dimensions [136, 262, 514]. In solid nodules, *straightforward* segmentation approaches, e. g. via thresholding and/or region growing, can lead to good results, but they are often compromised by over segmentation artifacts, since nodules are typically *connected* to blood vessels and/or the pleura. Thus, there exist methods that separate nodules from adjacent blood vessels.

For example, Kuhnigk et al. [262] employ Euclidean distance fields and connectivity information in an automated segmentation and image (nodule) analysis framework, e. g. to analyze if blood vessels end in or pass through nodules. From an algorithmic perspective, this is done to enhance region growing-based and/or morphological erosion methods, e. g. to find *good* thresholds and filter kernel radii. The authors also exploit expert knowledge to correct eventual unfavorable segmentation results, i. e. by letting users manually correct filter kernel radii, e. g., to address "*anatomical anomalies, imaging or motion artifacts, or conditions related to other [parenchymal] diseases*" [262]. There also exist more recent deep learning-based nodule detection [216] and classification methods [86, 205].

IMPLICATIONS FOR THIS THESIS. For the proposed illustrative visualization technique, PET hotspots are visualized in the context of the lung. These hotspots are surface meshes that are created via thresholded ^{18}F- or ^{90}Y-PET images [136]. Thus, metabolic hotspots (^{18}F) or radiation *patterns* of radioembolization media (^{90}Y) are visualized. On the one hand, morphology-based nodule visualizations are not addressed (cf. [55, 262]). On the other hand, however, this is not an issue, since instead of *real* nodules PET hotspots are assessed in their morphological context. In other words, it is a different perspective.

6.2.2.2 LUNG SEGMENTATION

The analysis of lung parenchyma is important to, e. g., plan surgeries w. r. t. the patient's lung functionality to be remaining. This can be done by segmenting lung parenchyma and subsequently deriving volumetric- and functionality-related information [263, 269, 511]. For our work, lung lobes are segmented and translated into surface meshes to provide an anatomical context. Straightforward approaches, such as threshold-based region growing in *air-like* and soft tissue anatomy including the trachea, bronchi and parenchyma, can also lead to feasible results [268]. Some approaches, however, result in parenchyma segmentation masks with holes, which can be addressed via spherically-shaped morphological

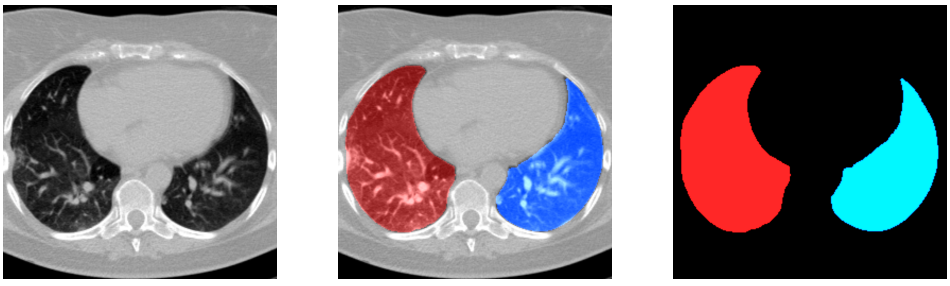

(a) **(b)** **(c)**

Figure 6.7: Separated lung parenchyma segmentation masks **(c)** that were created from a CT image stack **(a)** employing the threshold-based region growing approach described by Kuhnigk and Lassen et al. [263, 268]. For Subfigure **(b)**, the original image was superimposed via color-coded lung masks. The two dark (nearly horizontal and black) regions in the parenchyma represent the lungs' fissures **(a)**.

The original medical images were provided and used here with permission by Oliver S. Großer.

closing. Subsequently, to separate the lung masks, typically, a connected component analysis and labeling can be employed (see Fig. 6.7). However, due to *uncertain* lung boundaries and smooth transitions between them, unfavorably seeded region growing may *bleed* from one lung into the other, which can result in one large segmentation mask. Such *kissing lung artifacts* can be addressed by morphological opening [203].

6.2.2.3 LUNG LOBE AND SEGMENT SEPARATION

To enable more detailed analyses and visualizations, the lung masks have to be separated into individual lobes (see Fig. 6.8). Kuhnigk et al. [263] presented a fissure-orientated lung lobe separation approach (cf. Fig. 6.2 and [165]). The basic idea is that two image sources are combined: The first image is an Euclidean distance field w. r. t. pulmonary blood vessels with maxima around the fissures. These maxima are created since blood vessels *stop* around fissure boundaries, and thus, create large distances between each other w. r. t. adjacent lobes.[3] The second image is an original and unaltered CT slice which is masked with the aforementioned lung segmentation masks. Typically, in CT images, fissures are represented somewhat prominent as bright and/or medium-bright lines. In some cases, however, e. g. due to poor image quality, resolution or other parenchymal diseases, they are not visible. In combination, these two images result in good fissure estimations and/or segmentations, and if necessary, the aforementioned MeVisPulmo 3D application offers facilities to manually correct separation boundaries.

LUNG SEGMENT SEPARATION. The subdivision from lung lobes into lung segments is more challenging. As mentioned before, segments are "*functionally independent unit[s]*" [424] which have their own ventilation and perfusion subsystems. In other words, if airways and blood vessels can be segmented, lung segments can be *estimated* from lung

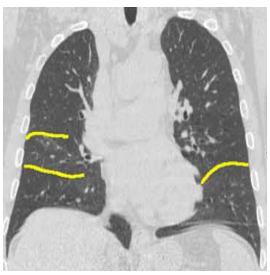

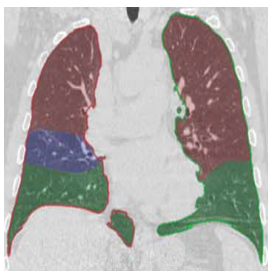

See [263, Fig. 4].

(a) **(b)** **(c)**

Figure 6.8: To separate the lung lobes, Lassen et al. [269] presented an extended version of Kuhnigk et al.'s [263] method that, for example, combines blood vessel and airway segmentations and therefrom derived distance fields to find fissures. Subfigure **(a)** shows a CT image with enhanced fissures and the color-coded result is depicted in Subfigure **(b)**. After lung lobe separation, the masks can be further subdivided into segment estimations [263] **(c)**.

[3] "*The rareness of vessels [...] allows an estimate of the fissure locations*" [264, Fig. 3].

lobes (read below; see Fig. 6.8c). Note that in contrast to lung lobes, segments are not separated morphologically, e. g. by fissures, and thus, anatomically correct lung segment segmentation typically cannot be achieved. Kuhnigk et al. [263] presented an approach that analyzes lung lobe segmentation mask voxels w. r. t. their distance to an airway segmentation mask. First, an airway mask is skeletonized and subsequently analyzed w. r. t. its branchings from the *top* of the trachea to the smallest airways. In simplified terms, after the second branching (primary bronchi → secondary bronchi), an airway *belongs* to a certain lobe and after the third branching (secondary bronchi → tertiary bronchi) it *belongs* to a certain segment. For the middle and lower right lung lobe, however, this explanation applies to the third and fourth branching, since the upper lobe's airways branch out earlier. The tertiary bronchi are used to label all lung (lobe) mask voxels w. r. t. the nearest tertiary bronchus voxel in a Voronoi diagram-like manner. This only results in rough estimations of lung segments, but other authors, such as Rikxoort et al. [494], refined this method by also employing the voxels' relative position w. r. t. lung lobe fissure segmentations.

IMPLICATIONS FOR THIS THESIS. Figure 6.7a depicts a low-dose CT image to which the lung segmentation method of Kuhnigk et al. [263] and Lassen et al. [268] was applied. To acquire separated lung lobe segmentations that were subsequently used for the proposed visualization technique, we used a MeVisPULMO 3D 3.7 prototype which was provided by our cooperation partners from MeVis Medical Solutions in Bremen. Due to poor fissure visibility, however, manual corrections had to be carried out. Lung segment estimations and/or segmentations were not employed for the proposed visualization technique and although it would be possible w. r. t. the proposed visualization technique, defining a qualitative color scale with up to eighteen well-distinguishable colors is challenging.

6.2.2.4 BLOOD VESSEL SEGMENTATION

Cancerous tissue prefers glucose over oxygen to fuel its growth, and thus, nodules are virtually always connected to lung blood vessels (cf. Ch. 2). From a clinical perspective and w. r. t. standard reporting, however, it is more important to convey in which lung lobe a nodule and/or hotspot was found in than showing which specific vessel (part) the nodule is connected with. However, for more locally acting treatments, such as SIRTs, knowledge about the blood vessel network is an important key feature, e. g. to plan catheter pathways.

There exist various blood vessel segmentation techniques to, e. g., assess suspicious blood vessel morphology and/or blood flow behavior or to treat blood vessels as key structures in risk visualizations (cf. Chs.3 and 5). Two well-known vessel segmentation methods were introduced by Frangi et al. [137] and Sato et al. [426] that calculate and evaluate the *vesselness* of structures. To do so, their methods evaluate the eigenvalues of local pixel- and/or voxel-related Hessian matrices comprising partial second order derivatives. In simplified terms, depending on the individual characteristics and relationships between the eigenvalues of these 3×3 matrices, e. g. if they are positive and/or negative, with certain combinations representing certain *findings*, e. g. if a bright structure was found *in front* of a dark background. For example, for bright tubular structures in front of dark

backgrounds, the eigenvalues λ_1, λ_2 and λ_3 with $|\lambda_1| \leq |\lambda_2| \leq |\lambda_3|$ should fulfill the following conditions and relationships [137]:

$$\begin{aligned} \lambda_1 &\approx 0 \\ \lambda_2 &\ll 0 \\ \lambda_3 &\approx \lambda_2 \end{aligned} \tag{6.1}$$

Since vessels can have varying diameters, multiple *scales*, i. e. filter sizes, are combined. Although these and related approaches typically lead to good results, the authors primarily employed contrast-enhanced image sources, e. g. DSAs, CTAs or MRAs. As Moccia et al. [339] report in their recent review article on "*blood vessel segmentation algorithms*", this is a general trend and most methods are tailored to such images. For non-contrast-enhanced CT images of high quality, region growing can also lead to good results [264].

IMPLICATIONS FOR THIS THESIS. In addition to PET hotspots, we aimed to further enhance the proposed illustrative visualization technique to depict blood vessels to provide navigation and orientation support during the intervention planning and execution of SIRTs. In diagnostic CT images, pulmonary blood vessels typically have a good contrast when compared to surrounding tissue. However, in low-dose CT scans, such tissue transitions are not clear, e. g. blood vessels that are compromised by breathing motion artifacts or image noise have *rather smooth* boundaries. Thus, straightforward image intensity-based segmentation approaches typically result in under- (omitted blood vessels) or over-segmentation (including parenchyma) artifacts. These artifacts can be further enhanced when surface meshes are created. This can partially be addressed by refining the mesh-creating algorithm's reconstruction quality; results are typically *cluttered* [25, 299]. This was the main motivation to work on the LANCELOT method, i. e. to enhance pulmonary arteries in low-dose CT scans [324] (cf. [97, 283]).

PULMONARY VS. BRONCHIAL ARTERIES. Ricke et al. [398] presented two cases for which they conducted SIRTs in the lung. However, the authors utilized the *bronchial arteries* to guide catheters which branch out around the aorta's descending arc and "*supply the bronchi, bronchioles, and larger blood vessels of the lung*" [424, Tab. 21.4]. Their diameters roughly range from $1.3\,mm$ to $1.5\,mm$ [519]. In contrast, *pulmonary arteries* hold blood flowing from the heart to the lungs with diameters ranging from $30\,mm$ (branch origin) to $10\,\mu m$ (near capillaries), which makes them generally larger [198, 314, 484]. In other words, in contrast-enhanced and/or high-resolution CT images, bronchial arteries are barely visible, whereas they are typically not visible in low-dose CT images [519]. If bronchial arteries are used for catheter guidance, this renders the proposed illustrative PET/CT image visualization technique and the LANCELOT method somewhat *unfeasible* for SIRT-related intervention planning, since pulmonary arteries are enhanced and visualized. On the other hand, however, cancerous nodules are also often connected to pulmonary blood vessels, which makes both methods still feasible if pulmonary blood vessels are used for catheter guidance. Furthermore, if bronchial arteries are visible on CT images and *good* segmentations could be carried out, both techniques still could be applied. Although not evaluated, both techniques could also be applied to other anatomical

sites, e. g. the liver, since it is also composed of multiple lobes, or other fine blood vessel networks, e. g. in the brain.

6.2.2.5 AIRWAY SEGMENTATION

Due to the typically high contrast between the airways and surrounding tissue, a threshold-based region growing often suffices to create segmentation masks of the trachea and subsequent airways. Subsequently, the segmented airways can be employed to create rough segmentation masks of lung segments, i. e. by skeletonizing airway masks and analyzing the number of branches. Additionally, such airway masks and skeletons (key frames) can further be utilized to create virtual bronchoscopies [47, 75, 381].

IMPLICATIONS FOR THIS THESIS. We carried out airway segmentations via threshold-based region growing. For the proposed visualization technique within this chapter and the map-based *Lymph Node Maps* in the next chapter, the trachea and main bronchi are utilized as anatomical landmarks which are aimed to provide orientation support. Here, however, the trachea was reported to provide only little support (read below).

6.2.3 CHALLENGES FOR LUNG CANCER INTERVENTIONS

Interventions in the lung are accompanied by certain *risks*. For example, for radiation-based therapies, which also includes SIRTs, an increased exposure of healthy tissue can result in toxic reactions, and thus, in a reduction of lung functionality. However, such damages can resolve themselves over time, but may also become chronic [95]. For needle-based tests and/or interventions, lung parenchyma has to be penetrated. In contrast to bones, this is much easier due to the lungs' soft tissue. It may happen, however, that the lung collapses or that various *foreign bodies*, such as air, water or blood, accumulate between the lungs' surfaces and pleura which can result in infections [127]. Although lungs can re-expand themselves, external drainage is sometimes necessary. However, Ferreiro et al. [127] also reported that adenocarcinomas, "*in many cases, seem[s] to arise at the site of old scars*", which could be an additional long-term risk factor for needle-based interventions.

With respect to SIRTs, catheters have to be guided through complex blood vessel networks to administer radio-labeled embolization media. The risk of vessel perforation is low, but operating physicians require craftsmanship for catheter guidance. Moreover, due to the ability of arteries to contract themselves as a pumping mechanism, catheter insertion can cause spasms or occlusions, which can result in undesirable radio media *reflux* into other anatomical sites (cf. [157]). However, spasms can be addressed by waiting.

6.2.4 INTERVENTION PLANNING

Historically, the primary target organ for SIRT interventions is the liver [157, 376, 398]. Selective internal radiation therapy is primarily conducted in palliative settings and in patients that did not show positive treatment results when exposed to other treatments. For example, Ricke et al. [398] presented two cases and reported that a post-interventional image-based evaluation revealed that targeted lung metastases (renal and colorectal origin) remained stable or showed partial remission four weeks after intervention execution [119].

During intervention planning, the target nodule and organ have to be assessed w. r. t. their size and/or volume ratio and w. r. t. the target organ's functionality, since it can be assumed that it will be (further) decreased due to the irradiation of non-target tissue [503, Sec. 2.7]. However, this damage typically is rather small, since the ^{90}Y-emitted radiation has an "*average penetration*" of $2.5\,mm$ in biological tissue "*with a maximum range of up to* $1.1\,cm$" [503]. Note that these key numbers refer to the emitted radiation itself and that *radiation zone shaping* is somehow manageable w. r. t. the amount of administered embolization media and vessel morphology. Additionally, the vascular anatomy is assessed via contrast-enhanced images, such as DSAs, to gain knowledge about eventual local abnormalities that might hinder or complicate actual interventions. Primarily, however, such images are acquired to let physicians prepare for the actual catheter navigation during interventions. Moreover and w. r. t. the tumor mass, the amount of radioactive media to be administered, and thus, the to be administered radiation dose to be administered has to be planned.

6.2.5 INTERVENTION EXECUTION

In related literature, SIRTs are also referred to as *radioembolizations*, which implies that they are a two-fold type of intervention [503]. The basic idea is that physicians navigate catheters as close as possible to targeted lesions to inject radio-labeled microspheres.[4] On the one hand, the spheres block subsequent blood vessels near and/or within tumor tissue which cuts them off from their nutrition supply. On the other hand, the adhered radioactive material irradiates surrounding (tumor) tissue which potentially increases the overall effectiveness of SIRTs when compared to standard embolizations, since tumor parts that are connected to non-embolized arteries also become affected. The microspheres' diameters range from $20\,\mu m$ to $60\,\mu m$ and with respect to the aforementioned diameters of lung-related arteries ($\lesssim 15\,\mu m$) and catheters ($\lesssim 1\,mm$; cf. [398]), presumably, only more perihilarly and/or centrally located tumor tissue can be targeted accurately, i. e. with a decreased risk of *microsphere shunting* into non-target tissue.[5] However, this may even be favorable in cases with multiple malignant nodules and/or metastases (cf. [398]).

Selective internal radiation therapies are conducted under image guidance, i. e. contrast-enhanced DSAs and/or fluoroscopies [399, 503]. The resulting and pre-interventional images are displayed on screens *over* the patient and typically show parts of the employed catheter w. r. t. surrounding and subsequent blood vessels. On-the-fly in-patient image guidance via tracking is not done since flexible instruments, such as catheters or endoscopes, are challenging to track even if their pathways are limited by vessel morphology. During radio-media administration, the so-called "*infusion technique has to be adjusted to the target vessels, the diamater and position of the catheter, and the type of microspheres used, to avoid back-spill of the particle suspencion and secondary unintentional embolization of extrahepatic vascular territories*" [503]. In other words, the administration

[4] Note that this is done manually, but there exist approaches to employ MR-sensitive catheters that can be guided in a "*remote control*"-like manner [348].

[5] https://www.bostonscientific.com/content/dam/bostonscientific/pi/portfolio-group/resources/ProductCatalog/PI%20Product%20Catalog%20Angiography.pdf, last accessed November 7, 2019

is conducted slowly, i. e. to not provoke early artery occlusion, and is somewhat further assisted by water- or saline-based fluids that flush out the microspheres from catheters. Since embolizations are permanent, i. e. embolization media remains within target tissue, tumor tissue is irradiated over a prolonged time (half life ^{90}Y: 64.2 *h*).

6.2.6 INTERVENTION ASSESSMENT

The treatment evaluation process for SIRTs is also two-fold. On the one hand, due to the aforementioned half time of ^{90}Y, PET/CT and SPECT/CT images can be acquired a day after treatment to evaluate radiation patterns w. r. t. embolization media accumulation (cf. Sec. 6.3). This is done since, once administered, it is not guaranteed that the embolization media reaches the intended lesion(s). Although this risk can be minimized by navigating catheters as close as possible towards lesions, at a certain point, catheter geometry renders further advancements impossible. On the other hand and as mentioned before, the treatment outcome is evaluated a few weeks after intervention execution. Such periods reflect the necessity of radiation therapies – and chemotherapies, for that matter – to take and show effect. This can also be done in a multimodal manner, e. g. via ^{18}F-PET/CT images, which can then be assessed w. r. t. morphological and physiological changes [119, 364].

6.3 ILLUSTRATIVE VISUALIZATION SUPPORT FOR SIRTS IN THE LUNG

In this section, an illustrative visualization technique is presented and discussed that aims to offer exploration support during intervention planning and assessment of SIRTs in the lung [323]. With respect to related visualization techniques that were presented in Chapter 3, the herein presented technique combines concepts of focus-and-context (PET in CT) and ghosted (transparencies) approaches (cf. Sec. 3.6).

6.3.1 CONTRIBUTIONS

The key contributions are as follows:

- An illustrative visualization technique for which OITs [33], silhouettes and boundary enhancements (both image space-based) are combined to visulize PET/CT images [130]. Although the methods were not novel themselves, their combination was.
- An evaluation with five clinical (two nuclear medicine physicists and three nuclear medicine physicians) and four medical visualization domain experts.

Note that the respective publication was focused on ^{90}Y-PET/CT images in an intervention assessment context. However, the technique can also be applied to other multimodal image combinations and SIRT-related tasks, e. g. to ^{18}F-PET/CT images for diagnostic and follow-up evaluation purposes.

6.3.2 INTRODUCTION AND MOTIVATION

Here, a brief recap of this chapter's contents so far is provided. Although there exist other primary carcinomas that have higher incidence rates, the mortality rate in cases of lung cancer is considerably high (cf. Tab 6.1). With respect to the actual type of lung cancer, treatmant options can be very limited due to cancer-unspecific symptoms, e. g.

coughing or breathing issues, and thus, due to an eventually already advanced disease progression during initial diagnoses. In contrast to interventions in the spine, lung cancer treatment aims for surgical resections of (suspected) tumor tissue as early as possible to minimize the risk of cancer growth and (distant) metastases. This, however, can be unfeasible due to missing patient compliance or if patients would be left with a severely decreased lung functionality [291, 355]. In such cases, less invasive interventions such as radiation- and/or chemotherapies can be conducted that come with their own risks and side effects. Thus, there exists a high interest to evaluate novel treatment options for lung cancer. One such option are SIRTs that employ catheters to embolize tumorous and/or metastatic blood vessels with a subsequent local radiation therapy. Similar to RFAs in the spine, currently, SIRTs in the lung are primarily conducted in palliative settings with limited curative prospects [398]. During diagnoses and intervention assessment it is important to accurately relate PET hotspots to their morphological origin, i. e. to evaluate abnormal physiological activities (^{18}F), or to evaluate radio-labeled embolization media (^{90}Y).

6.3.3 REQUIREMENTS

The aim was to develop an illustrative visualization technique that could provide orientation and evaluation support for PET/CT images. An illustrative IVR approach was chosen to exploit the generally high degrees of simplification and/or abstraction to provide spatial exploration support *at a glance* [501]. As discussed in Chapter 3, PET information is often deeply embedded in its morphological context, and thus, transparencies should be employed to reveal them. However, increased context transparency also results in decreased visibility, and thus, boundary enhancements and silhouettes were employed to preserve and/or highlight shape details of context structures. From this, the following two requirements were formulated: The visualization technique should

[R1] present all lung lobes in a manner which makes them clearly recognizable and

[R2] present segmented PET hotspots in a manner which makes them clearly visible.

6.3.4 INTERMISSION – COGNITION OF TRANSPARENCIES

Rather than perceiving transparencies *directly*, *we* interpret adjacent lightness differences as transparent layers [448] (see Fig. 6.9a). In other words, "*physical transparency is neither necessary nor sufficient for phenomenal transparency*" [448]. Generally, transparent layers *in the front* darken objects behind them. This effect can be interrupted rather quickly if, for example, local discontinuities (misalignments) are introduced via translations and/or rotations [8, 13, 448] (see Fig. 6.9b). Furthermore, such interruption can be further enhanced in geometrically complex objects, i. e. if locally large shape differences are aligned with transparent borders. As a result, discontinuities are dissected into multiple parts [448].

IMPLICATIONS FOR THIS THESIS. The perception of transparencies – with and without the involvement of color (cf. [115]) – is a challenging field of research. As mentioned before and discussed in more detail below, high PET image intensities are employed to represent lung nodules, i. e. anatomical regions with high metabolic activities or accumulation volumes of embolization media. In contrast to the aforementioned works that discuss *phe-*

nomenal transparencies with a certain focus on boundary conditions, here, PET hotspots are fully embedded into lung parenchyma [8, 13, 447, 448]. Note that in clinical practice, however, lung cancer can extend into the lungs' pleura and/or chest wall (TNM T2 and above; cf. [72, p. 263]), i. e. *leaving* the parenchyma, but the available image sources did not include such cases. In other words, shape- and position-related transparency discontinuities are not an issue here. Furthermore, to address eventual color-related visibility artifacts regarding the PET hotspots' visibility, i. e. they *disappear* when depicted in a similar color than the encompassing lung lobe, they are presented in gray. Although this does not draw user attention, which is a typical goal in (multimodal) visualizations, it minimizes color-related visual clutter.

Figure 6.9: Due to the geometrical arrangement of the four rectangles, it appears that the two rectangles in the middle form one transparent layer **(a)**. If this regular arrangement is interrupted, the transparency effect is also interrupted **(b)**.

Image **(a)** was inspired by [448, Fig. 1(b)], whereas Image **(b)** was inspired by [448, Fig. 2(b)].

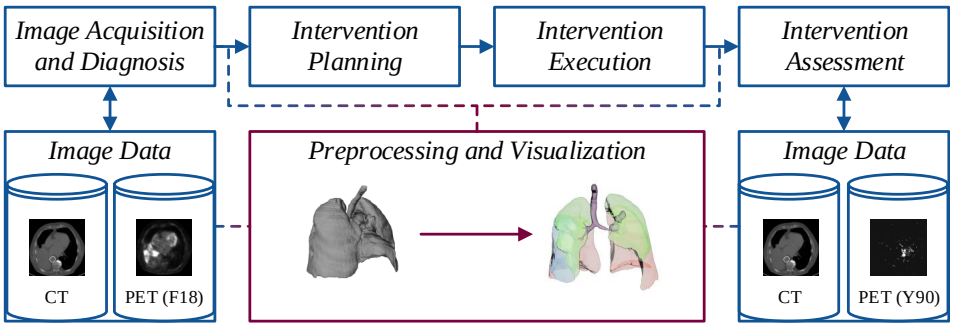

Figure 6.10: The simplified workflow from Figure 6.4 w. r. t. the proposed illustrative visualization technique. The PET/CT images are first preprocessed to extract visualization-related key features and anatomical landmarks, i. e. the trachea, lung lobes and PET hotspots (cf. Fig. 6.11). Subsequently, they are visualized by combining OITs, boundary enhancements and silhouettes (cf. Fig. 6.12).

The original medical images were provided and used here with permission by Oliver S. Großer.

6.3.5 IMPLEMENTATION

The implementation consists of two steps, preprocessing and visualization (see Fig. 6.10).

PREPROCESSING. The main goal of the preprocessing step is to carry out segmentations of certain key features and anatomical landmarks, i. e. from the PET hotspots (≈ lung nodules), the lung lobes and the airways consisting of the trachea and main bronchi. Note that the pulmonary blood vessels were also segmented via thresholded region growing, however, this is discussed in more detail below (cf. Fig. 6.17). Figure 6.11 depicts the preprocessing pipeline that was employed to acquire segmentation masks of the aforementioned structures. Computed tomography images are processed in the *Mevis PULMO 3D* prototype to carry out lung fissure-oriented segmentations of the lung lobes and the airways. Since low-dose CT images were used, straightforward thresholding of *air voxels* is challenging, and thus, the airway segmentation masks primarily consist of voxels that represent the trachea, main and secondary bronchi. In contrast, the PET images are thresholded, i. e. high-pass filtered, to create one or multiple hotspots. Note that this thresholding was not motivated clinically and was primarily carried out for the subsequent evaluation (cf. [136]). Subsequently, surface meshes were generated using the *WEMIsoSurface* module in MeVisLab [25], which were then further processed in the visualization step.

Due to the *poor* resolution of the low-dose CT images along the third axis (slice thickness $\approx 3\,mm$), these resulting surfaces were comprised by heavy staircase artifacts, i. e. *bumpy*, hard to interpret surfaces. Thus, a Laplacian smoothing with factor 0.6 ($\in [0, 1]$) was applied for forty iterations. These values were chosen to preserve the general shape of the

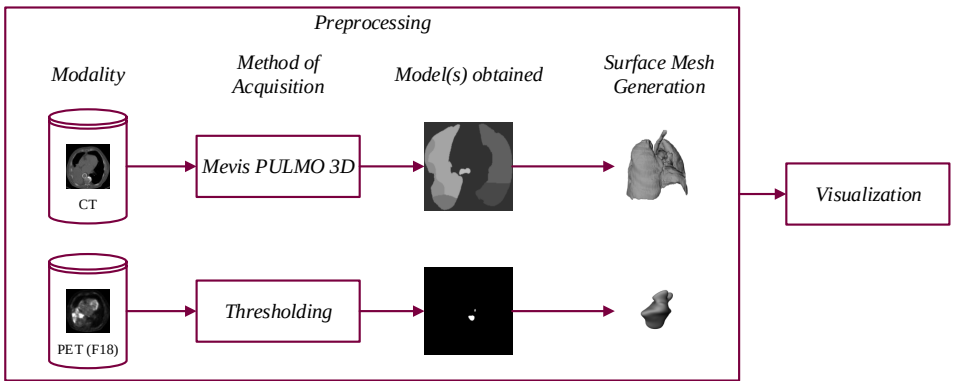

Figure 6.11: The preprocessing pipeline to acquire segmentation masks of the trachea, lung lobes and PET hotspots. The *Mevis PULMO 3D* prototype carries out a fissure-oriented lung lobe segmentation and separation [263, 269], whereas the airways and PET hotspots are acquired via thresholded region growing or just thresholding, respectively. Subsequently, surface meshes are generated [25].

structures (moderate factor), while *slowly* and iteratively removing said artifacts (many iterations). This results in minor spatial inaccuracies, which are negligible here.

COLORS. For the visualization of the aforementioned surface meshes, OITs, boundary enhancements and silhouettes are employed. To do so, per-pixel colors, surface normals and depth buffer values are combined in a multi-pass rendering approach. The colors are processed via per-pixel lists that were introduced by Barta et al. [33]. In simplified terms, for each pixel a list of scene objects, e. g. the lung lobes and airways, is created that *correspond* with *this* pixel. Each entry consists of the corresponding objects' per-pixel depth values, colors and opacities. In an additional rendering pass, these lists are sorted w. r. t. the depth values to create an accurate *back to front* blending. Sorting is necessary, since the arrangement of scene objects w. r. t. the scene camera is typically unclear due to interactions, i. e. color blending has to be re-computed for each frame. For sorting, the *insertion sort* algorithm was employed. This is not the fastest sorting algorithm, however, here, the number of objects, and thus, the number of per-pixel list entries is limited and typically rather low, which also guarantees interactive frame rates. After color and alpha blending, the resulting color is combined with the boundary and silhouette enhancements.

BOUNDARY ENHANCEMENTS AND SILHOUETTES. Mesh normals and depth buffer values are used to create image space-based boundary enhancements, e. g. around the lung lobes, and silhouettes that enhance shape features of surfaces, even if they are presented more transparent. To do so, the methods of Fischer et al. [130] were employed. The basic idea is that normals and depth buffer values are written into Framebuffer Objects (FBOs),

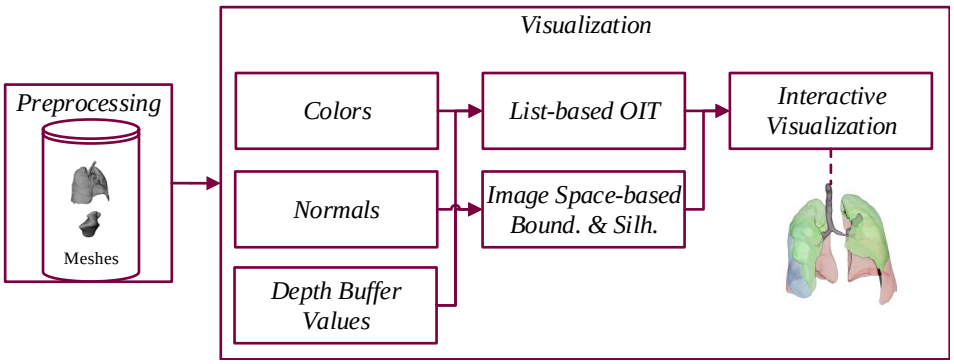

Figure 6.12: The visualization pipeline that presents the previously acquired surface meshes in an interactive GUI. The colors are compiled into lists and become subsequently ordered and blended [33]. The normals and depth buffer values are employed during rendering to create image-space based boundary enhancements (depth values) and silhouettes (normals) [130]. In the GUI, users can interactively adapt structure colors and transparencies.

and subsequently, adjacent values and/or normals are combined and thresholded in a filter-like manner. To create boundary enhancements, *adjacent* depth values are compared in an N-large 2D distance (*axis-aligned cross*) around the currently processed pixel. In other words, a Sobel edge filtering-like, typically with a filter size of 3 ($N = 1$), is applied. When N is increased, thicker boundary enhancements can be created (cf. Fig. 6.16a). Subsequently, these depth differences are thresholded and if they exceed a certain limit, the pixel is considered a boundary pixel, i. e. it will be rendered darker. Silhouettes are created in a similar manner, but w. r. t. adjacent surface normals. In contrast, however, pixels are regarded as silhouette pixels if they are somewhat homogeneous w. r. t. their normals, and thus, only surface areas with low curvatures are darkened. If the respective threshold is increased, silhouette *thickness* can be increased.

6.3.6 RESULTS

Visualization results of the proposed technique are depicted in Figure 6.13. The technique was primarily implemented in MeVisLab 2.8.2 using a VTK rendering pipeline with the visualization technique – or rather the respective rendering pipeline – being implemented in a tailored *vtkPolyDataMapper* module. Since a Mevis PULMO prototype was used

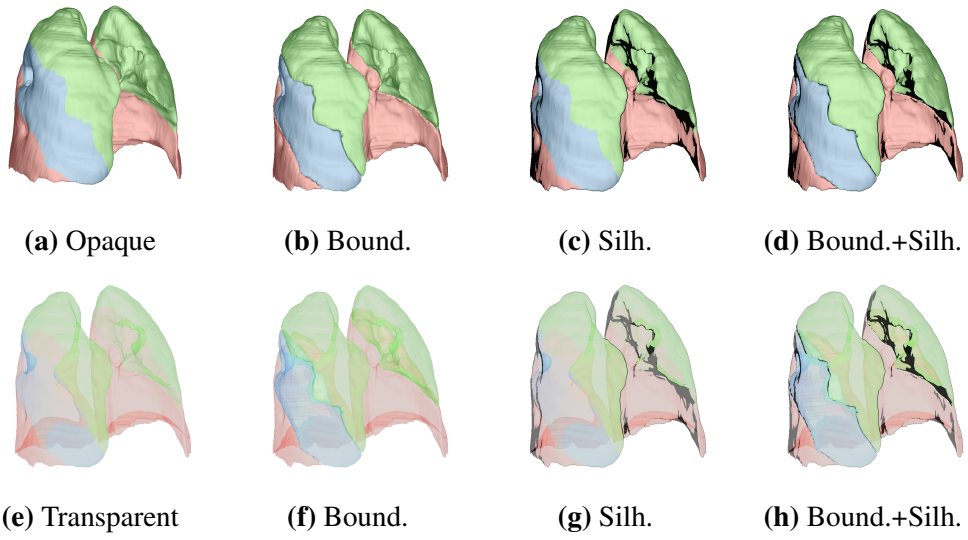

(a) Opaque **(b)** Bound. **(c)** Silh. **(d)** Bound.+Silh.

(e) Transparent **(f)** Bound. **(g)** Silh. **(h)** Bound.+Silh.

Figure 6.13: An image series that presents the results of the proposed illustrative rendering technique. The subfigures are virtually identical with the bottom row depicting lung lobes with increased transparencies. For the Subfigures **(b,f)**, boundaries (depth-dependent) were enhanced, whereas silhouettes (normal-dependent) were included for the Subfigures **(c,g)**. In the rightmost subfigures, both features are combined. These and similar images were used for the evaluation.

for parts of the preprocessing step, the generation of segmentation masks roughly takes 10 *min*, whereas the visualization itself achieves interactive framerates. With respect to the general requirements for visualizations of (multimodal) medical image data, a GUI was implemented that presents the original image data, the visualization results and interaction facilities, i. e. to change structure colors and opacities, next to each other (see Fig. 6.14).

6.3.7 EVALUATION

To evaluate the proposed illustrative visualization technique and the aforementioned requirements, five clinical (two nuclear medicine physicists and three nuclear medicine physicians) and four medical visualization domain experts were interviewed. Similar to the evaluation of the proposed risk visualization technique from the previous chapter, this was done via interactive questionnaires. In contrast, no interactive 3D viewers were employed. The interviewees were asked to answer their questions using a five-item Likert scale (- -, -, ○, +, ++) which was *quantified* from 1 (- -) to 5 (++). Note that the interviewees I5 and I6 co-authored the respective publication [323].

PART 1 – GENERAL QUESTIONS. In the first part, the interviewees were asked general questions regarding their anatomical knowledge and experience with visualization techniques for medical image data.

PART 2 – VISUALIZATION-RELATED QUESTIONS. In the second part, the interviewees were shown various visualization results to familiarize them with the proposed technique (cf. Fig. 6.13). Additionally, they were asked to rate the visibility of lung lobes and to judge the depth order of PET hotspots to evaluate the aforementioned two requirements. Subsequently, they were asked general questions regarding the anatomical

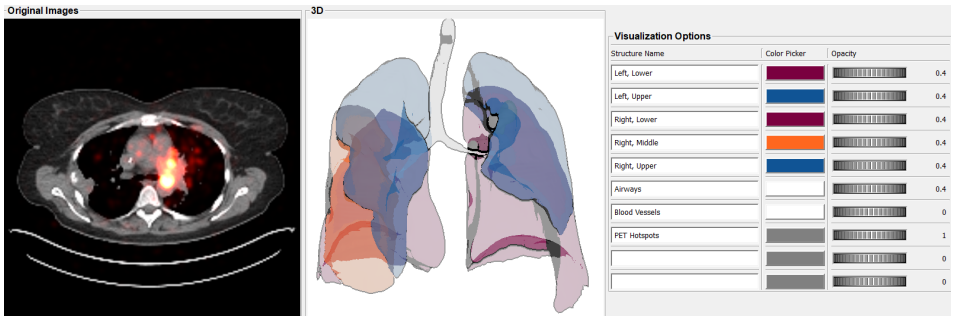

Figure 6.14: The GUI that enables users to assess the original (multimodal) medical image data **(left)** and the results of the proposed illustrative visualization technique **(middle)**. On the right, users can adapt various (visualization) parameters, i. e. the names of anatomical structures or key features, their colorization and opacities. The dark-colored image regions are a result of multiple overlapping semi-transparent surfaces of the same color. For example, the dark blueish regions around the lungs' hila highlight the lungs' concave *mold* where the heart is typically embedded in.

The original medical images were provided and used here with permission by Oliver S. Großer.

Table 6.3: The evaluation results of the proposed illustrative visualization technique via interactive questionnaires. The numbers are denoted in years.

	Interviewees								
	Clinical Experts					Visualization Experts			
	I1	I2	I3	I4	I5	I6	I7	I8	I9
Part 1 – General Questions									
Gender	w	m	m	m	m	w	m	m	m
Age	37	30	31	29	46	32	28	26	28
Anatomical Knowledge									
Experience with Visualization Techniques									
Part 2 – Visualization-Related Questions									
Q1									
Q2	–								
Part 3 – Clinical Feasibility									
Diagnosis		×	×	×					×
Therapy Planning	×	×	×	×		×			×
Interdisciplinary Communication	×	×	×	×		×	×	×	×
Doctor-Patient Consultation	×	×	×	×		×	×	×	×
Legend	−−	−	○	+	++				

correctness of the depicted surface models and the proposed combination of visualization techniques:

Q1 How anatomically correct do you rate the presented surface models?

Q2 How do you rate the combination of (order-independent) transparencies, boundary enhancements and silhouettes?

PART 3 – CLINICAL FEASIBILITY. For the last part, they were asked to estimate the proposed method's feasibility for certain clinical disciplines.

REQUIREMENT 1. To evaluate the first requirement, i. e. if all lung lobes are presented in a manner which makes them clearly recognizable, the interviewees were presented an array of visualization results which they were asked to compare row- and column-wise (cf. Fig. 6.13). For each pairing, they were asked to state which image depicts the lung lobes more clearly and/or makes it easier to distinguish the lobes from each other. The results are listed in Table 6.4. Unsurprisingly, the majority of all experts stated that more opaque depictions are more suitable to do so. However, this task rather aimed to further familiarize them with the visualization technique for subsequent questions. Subsequently, they were asked to compare the visualizations row-wise, i. e. to compare an opaque or transparent rendering with and without enhanced boundaries, silhouettes and/or both, and to rank the lung lobes' recognizability. All interviewees stated that for the transparent

Table 6.4: The evaluation results for [R1]. With respect to the results in Subtable **(a)**, the interviewees were asked to compare the visualizations from Figure 6.13 in a column-wise manner (opaque vs. transparent). The majority of interviewees rated the more opaque rendered lung lobes being more easy to be recognized. With respect to the results in Subtable **(b)**, the experts were asked to rank the lung lobes' recognizability in a row-wise manner. Boundary enhancements were reported to have a greater influence than silhouettes on lung lobe recognizability.

(a)

Clinical Experts			
Column	Opaque	Transparent	Indecisive
Opaque	4	0	1
Bound.	4	1	0
Silh.	4	0	1
Bound.+Silh.	4	1	0
Visualization Experts			
Transparent	4	0	0
Bound.	2	2	0
Silh.	3	0	1
Bound.+Silh.	3	1	0

(b)

	Clinical Experts			Visualization Experts		
Rendering	μ	σ	*med.*	μ	σ	*med.*
Opaque Renderings						
Opaque	3.8	1.3	4	3.75	0.5	4
Bound.	4.4	0.55	4	4.75	0.5	5
Silh.	4	1.22	4	3.5	0.58	3.5
Bound.+Silh.	4.6	0.45	5	4.75	0.5	5
Transparent Renderings						
Transparent	2	0	2	1.5	0.58	1.5
Bound.	3.2	0.45	3	3.25	1.71	3.5
Silh.	2	0	2	4	0	4
Bound.+Silh.	3.8	0.45	4	4	0.82	4

renderings, boundary enhancements and silhouettes influenced their decisions, but the boundary enhancements' influence w. r. t. recognizability was ranked higher. Thus, clear boundaries on objects – and a clear and/or familiar arrangement of objects – have a high influence on the object recognizability when object visibility decreases, whereas shape features, such as silhouettes, only have a minor influence.

REQUIREMENT 2. The evaluation according to the second requirement, i. e. if the segmented PET hotspots are clearly visible, was done two-fold. A small perceptual study was conducted in which the interviewees were asked to judge the depth order of multiple PET hotspots. Note that transparencies were employed to reveal hotspots in the first place, i. e. just asking the interviewees if the hotspots are perceivable would have been too simple. In 3D, depth ordering can be achieved interactively, e. g. via rotations, whereas planar presentations, e. g. in the form of printed reports, do not allow for such interactions. Thus, by letting the interviewees judge the depth order multiple hotspots, on the one hand, it is guaranteed that they actually see them. On the other hand, this made it possible to *measure* the depth perception-related influence of boundary enhancements, silhouettes and anatomical landmarks, such as the trachea, on such decisions.

First, the PET images were thresholded manually to create multiple hotspots (cf. Fig. 6.14 and [136, 332]). Similar to Figure 6.14, the interviewees were shown superimposed and color-coded PET/CT images and 3D visualizations from the proposed technique. This was done from the coronal (front to back), sagittal (left to right) and axial (bottom to

Table 6.5: The evaluation results for [R2]. The interviewees were asked to judge the depth order of two PET hotspots correctly, once with (**w.**) and once without (**w./o.**) boundary enhancements and silhouettes (**BE./S.**). Correct answers are denoted by a checkmark (✓), wrong answers with a cross (✗) and indecisiveness via **ind.**. Subsequently, they were asked to state if they used the trachea (**trach.**) to make their decision and how strong they rate the influence (**infl.**) of it and the visualization technique in general. Similar to before, statistics **(stat.)** were derived. Boundary enhancements and silhouettes were reported to have only moderate influence.

Clinical Experts								Visualization Experts							
w./o. BE./S.			Trach. Used?		Trach. Infl. Stat.			w./o. BE./S.			Trach. Used?		Trach. Infl. Stat.		
✓	✗	ind.	Yes	No	μ	σ	*med.*	✓	✗	ind.	Yes	No	μ	σ	*med.*
11	3	1	6	9	4.2	0.98	4.5	8	2	2	2	10	2	1.41	2
w. BE./S.			BE./S. Infl.?		BE./S. Infl. Stat.			w. BE./S.			BE./S. Infl.?		BE./S. Infl. Stat.		
✓	✗	ind.	Yes	No	μ	σ	*med.*	✓	✗	ind.	Yes	No	μ	σ	*med.*
10	3	2	3	12	3.7	0.58	4	9	2	1	1	11	3	0	3

top) perspective with and without boundary enhancements and silhouettes, which results in six presentations per user. For each presentation, they were asked

- which hotspot appears nearer,
- if they used the trachea as an anatomical landmark, and if so, how strong they rate its influence, and
- if boundary enhancements and silhouettes influenced their decision, and if so, how strong they rate their influence.

The respective results are listed in Table 6.5. As expected, more clinical than visualization domain experts used the trachea for their decision. Boundary enhancements and silhouettes were reported to only have a moderate influence on decisions and most experts judged the depth ordered hotspots correctly. However, there was one sagittal arrangement that no expert evaluated correctly (read below).

6.3.8 DISCUSSION

In this section, shortcomings and ideas how to address them will be discussed.

LIMITING PREPROCESSING. Preprocessing roughly takes 5 *min* to 10 *min* (cf. Fig. 6.11). Although two separate applications were used for preprocessing, most of the underlying methods are automated. The most time-consuming step is the manual correction of lung lobe separations in cases where fissures are not depicted clearly.

PET THRESHOLDING. As mentioned above, PET images are thresholded to create two separate hotspots, disregarding any clinical meaningfulness. As discussed by Foster et al. [136], there exist various PET image segmentation methods, e. g. adaptive thresholding

for lung cancer or lung inflammation imaging. From a workflow perspective and instead of thresholding *raw* PET image intensities, users could also threshold SUVs to create hotspots. In simplified terms, SUVs *quantify* ^{18}F-PET image intensities by including various parameters, such as the radioactive decay of ^{18}F and patient-specific parameters, such as their weight. This is done, e. g., to evaluate treatment outcome from a physiological point of view [364]. However, this has to guarantee quasi-identical imaging protocols, since imaging-related parameters, such as the amount of administered radiotracer, waiting times between administration and image acquisition, and patient-related parameters, such as the blood glucose concentration, affect the resulting PET images. The quantification of PET images was not applied here, but will be discussed in more detail in the next chapter.

EVALUATION. On the one hand, the evaluation confirmed both requirements w. r. t. the employed combination of transparencies, boundary enhancements and silhouettes. On the other hand, however, this combination was reported to only offer a small perceptual benefit for depth ordering tasks. In one particular case, depth perception was distorted (read below). When comparing boundary enhancements and silhouettes, boundary enhancements were reported to have an overall bigger impact on the object recognizability when their visibility is decreased. Visualization domain expert I6 stated that annotations could provide a benefit, i. e. by labeling PET hotspots from *Hotspot 1* to *Hotspot N*, for example. Alternatively, hotspots could also be color-coded. Introducing additional colors, however, could result in visual clutter since hotspots are virtually always *occluded* by color-coded context geometry which could distort the color perception. Another interviewee (I9) stated that totally black silhouettes (cf. Figs. 6.13 and 6.16b) are *too strong* and omit which structure they belong to. Thus, we later adapted the method w. r. t. the last multi-pass rendering step by combining both enhancements with the respective structure color (cf. Fig. 6.15b and [453]) instead of just *adding* them (cf. Fig. 6.16b).

INCORRECT DEPTH ORDERING. There was one presentation of hotspots for which all experts judged the depth order incorrectly (see Fig. 6.15a). All experts stated that the lower right hotspot appears nearer although, geometrically, the upper left hotspot was closer to the scene camera. Presumably, this is due to the hard black silhouette on the bottom right hotspot which artificially brings it closer to the user. This effect could be explained by Puerta [384] who described how *we* use shadows as depth perception cues, i. e. said shadow brings the lower hotspot artificially closer to the scene camera. Although this was not evaluated further, it would be interesting to see if eventual insights could be employed to, e. g., create *good* presentations (screenshots) for on-paper reports (cf. Ch. 7).

BOUNDARY AND SILHOUETTE THICKNESS. The thickness and/or strength of boundary enhancements and silhouettes can be altered by adapting the filter sizes for depth values and normals and respective thresholds. Thicker boundaries are beneficial to visually separate lung lobes and other structures. However, image space-based boundary thickness depends on thresholding adjacent depth buffer values and should be controlled, i. e. to not *overemphasize* structure boundaries, which could be distracting (cf. Fig. 6.16a). The same applies to silhouettes, which can become very *strong* quickly (cf. Fig. 6.16b). Such effects, however, can partially be addressed via color-coded silhouettes (cf. Fig. 6.15b).

TRANSPARENCIES AND SILHOUETTES. When comparing the work of Fischer et al. [130] with the proposed method, there are two key differences. First, we employ *real* transparent and/or translucent surfaces via OITs to reveal underlying key features. In contrast, Fischer et al. [130] employ a multi-depth peeling approach to reveal and render multiple layers of geometry. This has to be done *explicitly*, i. e. each geometry layer requires its own rendering pass, whereas OITs can handle a user-defined amount of transparent layers *directly*. However, the employed method of Barta et al. [33] requires developers and/or users to predefine the size (length) of the aforementioned fragment lists, i. e. memory has to be reserved. If this list size is too low, major rendering artifacts are created when many transparent surfaces overlap. Secondly, the presented results do not employ halftoning via stippled textures to emphasize surface curvatures which was done to minimize visual clutter. When employing multiple transparent layers, there will often be *loud* image regions which could be further emphasized by an additional (texture) layer. In other words, transparencies were employed to reveal key features, such as PET hotspots, and an additional layer could occlude or draw attention away from them.

ABSTRACTION AND COLOR CODING. As discussed in Chapter 3 and Section 4.2, illustrative visualizations are typically accompanied by somewhat high degrees of geometric and/or photometric abstraction [501]. On the one hand, the final presentations are often *simple*, i. e. they provide *good* overviews without being too distracting. On the other hand, however, these abstractions and/or simplifications render such techniques rather *unfeasible* for certain clinical tasks, e. g. therapy planning for radiation therapies, since spatial relationships (details) have to be preserved in such contexts (cf. [341]). Here, an illustrative approach was chosen to provide orientation and assessment support w. r. t.

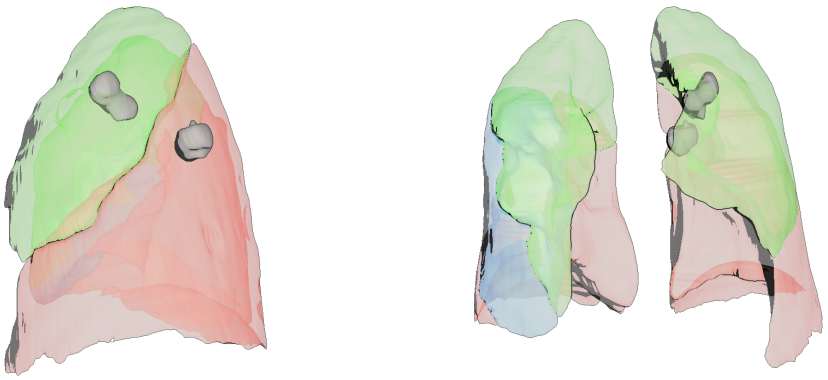

(a) **(b)**

Figure 6.15: For one presentation, all interviewees gave an incorrect answer when asked to judge the depth order of the PET hotspots **(a)**. They stated that the lower hotspot appears closer (cf. evaluation of [R2]). Subfigure **(b)** shows, however, that the upper hotspot is closer. Presumably, this is due to the black silhouette on the smaller hotspot.

The original medical images were provided and used here with permission by Oliver S. Großer.

certain key structures and features, whereas details can be assessed in 2D color-coded superimposition presentations (cf. Fig. 6.14). Per default, the lung lobes are color-coded via a categorical red-blue-green color scale which can be tailored to the users' preferences [263, 269]. Typically, PET hotspots and anatomical landmarks are presented in grayscale to limit the overall number of colors and the risk to unnecessarily draw user attention. With respect to photometric abstraction, boundary and silhouette enhancements were included to visually enhance edge and shape features even when the visibility of the respective objects is considerably decreased (cf. [276]).

ALTERNATIVE CLINICAL APPLICATIONS. The main focus of this method was to assist intervention planning and assessment of SIRTs in the lung. However, the method's general principle can virtually be applied to any other surface model or combination of surface models. Due to the IVR approach, other combinations of multimodal image data, for example MRI and SPECT, are possible, too. On the other hand, image sources typically have to be registered and target structures and key features have to be segmented.

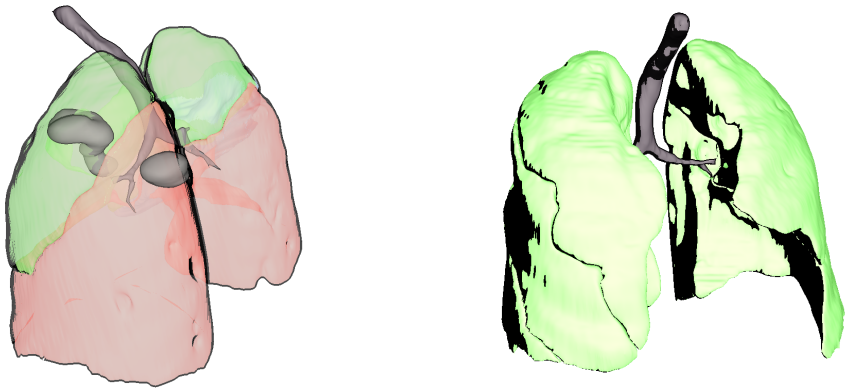

(a) **(b)**

Figure 6.16: The thickness and/or strength of boundary enhancements and silhouettes can be altered by altering the Sobel filter-like lookup neighborhood and normal thresholding, respectively. Stronger boundary enhancements emphasize the illustrative character of the proposed technique with thicker boundaries somewhat mimicking brush strokes **(a)**. If the normal-related threshold is increased [130], i. e. more curved surfaces are considered to be enhanced by silhouette features, the resulting silhouettes can become *very strong* **(b)**. This impression can partially be addressed by color-coded silhouettes (cf. Fig 6.15b).

6.3.9 AN OPEN EXTENSION – INCLUDING BLOOD VESSELS

The original goal of the proposed technique was to provide support during SIRT intervention planning and intervention assessment (cf. Fig. 6.14). Especially during intervention planing, blood vessels are an important key feature which was not yet considered. As discussed before, in comparison to diagnostic CT images, low-dose CT images often have a lower image quality, i. e. they typically contain higher degrees of image noise, which makes the employment of straightforward segmentation techniques, such as thresholding or region growing, challenging. There exist various segmentation methods to segment vessels, e. g. by estimating a structure's *vesselness* [137, 426], but these techniques are primarily applied to diagnostic and/or contrast-enhanced images or (retinal) photographies [339]. To fulfill the original goal, we worked on a blood vessel enhancement method for the lung. This method, namely the LANCELOT method (**L**ung Vessel Enh**ance**ment for **Lo**w-Dose C**T**) (cf. [97, 283]), was a first prototypical approach. Although the first results were promising, overall, they are too prototypical to be presented in detail which is why the method is only discussed briefly below.

Moreover, note three things:

- The method was inspired by the case report of Ricke et al. [398]. Here, the authors employed microcatheters which were guided through *bronchial arteries*, i. e. very small blood vessels which typically are not visible on CT images. The LANCELOT method, however, enhances *pulmonary blood vessels* and other *stick*-like structures. Thus, if bronchial arteries would be depicted, they would also be enhanced.
- In addition to low-dose CT images which were acquired during combined PET/CT scanning procedures, we had access to diagnostic CT images. With respect to certain acquisition parameters, such as the kVp setting of the scanner, such CT images

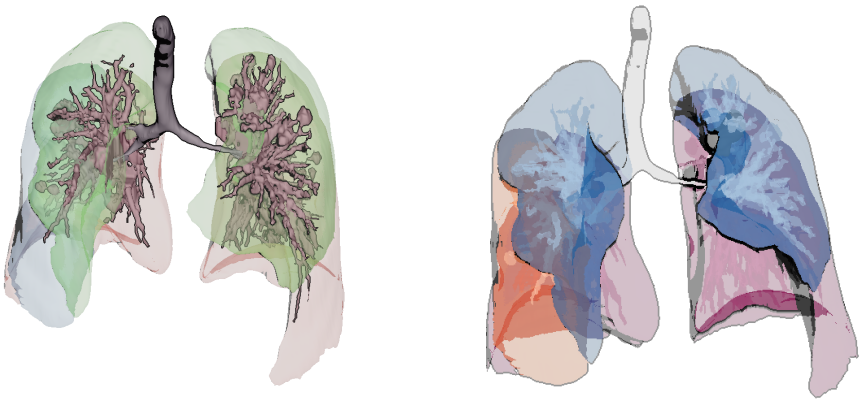

Figure 6.17: The proposed visualization technique with blood vessels. Due to the *poor* image quality of low-dose CT images, under-segmentation, e. g. represented by short and/or early terminating blood vessels, and over-segmentation artifacts, e. g. around the lung hila, are typical in straightforward segmentation approaches.

The original medical images were provided and used here with permission by Oliver S. Großer.

typically have better contrast between blood vessels and lung parenchyma. Given that image registration would be employed, blood vessels could be *transferred* from diagnostic to low-dose CT images. This was not done since we tried to *get the most out of* low-dose CT images, since "*the radiation exposure with low-dose CT is approximately 20%–25% that of diagnostic CT*" [470], although the diagnostic value of standard-dose CT images cannot be superseded.

- The LANCELOT method is an adaption and combination of the image contrast-enhancing methods of Czerwinski et al. [97] to detect and enhance "*lines in speckle imagery, such as that produced by synthetic aperature radar (SAR) or ultrasound techniques*" and the method by Li and Mould [283], who used their method to convert photographies into black and white images. The main similarity is that all three methods employ *stick filters* to enhance *stick*-like (*straight*) lines. The main differences are
  - the clinical context,
  - an iterative application of stick filtering (j) and
  - a scaled instead of an absolute enhancement of stick-like structures (s).

CONTRIBUTION. The key contribution of the LANCELOT method is that it enhances blood vessels in low-dose CT images. In contrast to other methods, such as from Frangi et al. [137] and Sato et al. [426], no contrast-enhanced images are employed. The method was evaluated by a medical technical assistant and a nuclear medicine assistant doctor.

IDEA AND CONCEPT DESCRIPTION. Due to the *poor* and/or noisy contrast between blood vessels and surrounding lung parenchyma in low-dose CT images, straightforward segmentation and/or enhancement methods rarely lead to good results. When applying more refined methods, such as *vesselness*, bilateral and/or anisotropic filtering, the results could be slightly improved, but method-specific artifacts still occurred (cf. Fig. 6.19). The motivation for the presented approach was somewhat two-fold: We knew about certain contrast-enhancing methods of lines and/or stick-like structures in images and we wanted to assess how well-suited they are for (blood) vessel enhancement in low-dose CT images [97, 283]. From a *macroscopic* perspective, however, blood vessels typically do not have stick-like shapes. Still, locally, they can be somewhat approximated (*abstracted*) as such.

METHOD DESCRIPTION. Here, the method's processing pipeline is described (see. Fig. 6.18). Given an image I, first, a 2D Gaussian smoothing $G(x;\sigma)_m$ is applied which results in the smoothed image I_G with m denoting the filter size (cf. Fig. 6.18). Due to this smoothing, blood vessels become *thicker*, and image intensity-wise, their *core* becomes more homogeneous. Subsequently, 2D stick filter kernels $(S_i)_m$ are created with the Bresenham algorithm which results in $\left(4 \times \frac{m-1}{2}\right)$-many individual filter kernels [66]. Similar to the reference methods by Frangi et al. [137] and Sato et al. [426], we also *synchronize* smoothing and stick filtering by setting $\sigma = m$. For each pixel $I(x)$ and its neighborhood $I(x)_m$, all stick filters $(S_i)_m$ are applied separately via convolution ($\star$) to compute δ_i via

$$\delta_i = |(I(x)_m \star (S_i)_m) - I_G(x)_m| \tag{6.2}$$

Since the LANCELOT and related methods are so-called *maximum response approaches*, afterwards, the maximum δ_i, namely $\max \delta_i$, is ascertained. It is challenging to denote typical values for δ_i and $\max \delta_i$. For example, for an image stack with $I(x) \in [-2048, 2724]$ and $m = 3$ the method roughly resulted in $\max \delta_i$ values $\in [0, 1360]$. Subsequently, $\max \delta_i$ is transformed w. r. t. $I(x)$ and $I_G(x)$ via

$$\max \delta_i = \begin{cases} s \max \delta_i & , \text{if } I(x) > I_G(x) \\ 0 & , \text{if } I(x) = I_G(x) \\ -s \max \delta_i & , \text{if } I(x) < I_G(x) \end{cases} \tag{6.3}$$

The first condition is fulfilled if the unaltered pixel $I(x)$ is brighter than $I_G(x)$. This is the case, e. g., if the *kernel pixel* $I(x)$ is much brighter than its neighborhood (*peak*). In contrast, w. r. t. the 3rd condition, if $I(x)$ is very dark while being surrounded by a very bright pixel neighborhood (*halo*), $I_G(x)$ becomes brighter. Note that the second condition is only fulfilled if $G(x;\sigma)_m$ if all $I(x)_m$ have the same value. The scaling factor s can be used to further increase the iteration-specific contrast enhancement of stick-shaped structures. For the images in this thesis, s was defined between 10 and 20, but smaller values around 5 can also achieve good results.

δ_i and $\max \delta_i$ are also images that depict a certain filter response w. r. t. S_i and the maximum of all filter responses respectively combined. Thus, $I(x)$ can be *updated* via

$$I^j(x) = I^{j-1}(x) + \max \delta_i(x) \tag{6.4}$$

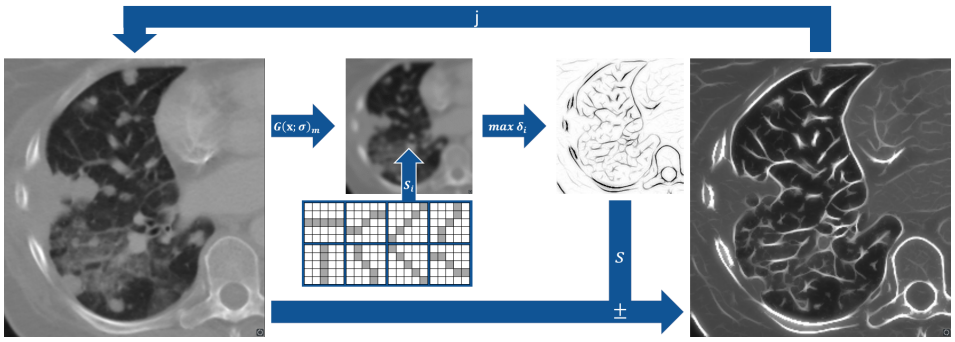

Figure 6.18: The LANCELOT method's workflow. First, thorax CT images are filtered via Gaussian smoothing $G(x;\sigma)_m$. Subsequently, per image region (pixel neighborhood), various *stick* kernels $(S_i)_m$ are applied. Here, σ and m, i. e. the degree of smoothing and stick size, were set to 5. The maximum δ_i, i. e. the *best-fitting* stick filter response, is scaled via s and is then added to or subtracted from the original image. This results in enhanced stick-like structures. Note that the filter results were inverted for presentation purposes.

Table 6.6: Computation times for processing five data sets with the methods of Frangi et al. [137], Sato et al. [426] and the LANCELOT method. The in-plane image matrix size always was 512×512 pixels and the denoted computation times were averaged for five executions. Note that although the methods of Frangi and Sato could process 3D image stacks, all methods were applied in a slice-based manner. The stick filter size m was set to 7.

			Computation Times [s]		
Data Set	# Slices	Slice Thickness	Frangi et al. [137]	Sato et al. [426]	LANCELOT
1	117	3	3.25	6.45	34.49
2	117	3	3.24	6.84	34.10
3	108	3.75	2.98	5.83	31.25
4	107	3.75	2.97	5.81	31.89
5	63	5	1.75	3.44	18.65
		Time per Slice [s]	0.05	0.03	0.29

Original table was extended by information about the data sets' slice thicknesses.

with j denoting that the stick filtering was applied j-many times with $j = 0$ being omitted for simplification purposes. For the results presented in this thesis, j was set to 3, since more iterations yielded only negligible improvements. Due to Equation 6.3, image contrast is increased with bright pixels becoming brighter and vice versa. Note that this locally increases the image region contrast around stick-like edges two-fold, since darker regions become darker, whereas adjacent brighter regions become brighter. With respect to the aforementioned image intensity ranges, repeated stick filtering applications resulted in $I^1(x) \in [-4223, 3723]$, $I^2(x) \in [-10244, 9295]$ and $I^3(x) \in [-29612, 30010]$. For demonstration purposes, s was set to 2.

RESULTS AND EVALUATION. The LANCELOT method was implemented in MATLAB (MathWorks, Natick, Massachusetts, USA) and was compared to the methods of Frangi et al. [137] and Sato et al. [426] which are implemented in the MeVisLab modules *HessianFilter* and *Vesselness*, respectively [406]. In Table 6.6, computation times for these methods are listed which were acquired with a i5-2500 processor with 3.7 GHz. An image-based comparison of the three methods can be seen in Figure 6.19. Note that the employed low-dose CT images had similar acquition parameters as the low-dose CT scans used for the National Lung Screening Trial (NLST) [470, Tab. 6], e. g. with kVp settings ranging from 120 keV to 140 keV and tube currents ranging from 40 mA to 80 mA.

INTERVIEW SETUP. The LANCELOT method was evaluated by two clinical experts, i. e. one medical technical assistant (I1) and one assistant doctor (I2). The second interviewee co-authored the respective publication [324]. The experts were interviewed in an informal think-aloud setup using on-paper questionnaires. We implemented a small evaluation-assisting prototype in MeVisLab which is a multi-viewer GUI that depicts the original images (cf. Fig. 6.7a) and the aforementioned methods' results next to each other (cf

Fig. 6.19). Various interaction facilities, i. e. cursor positions, translations, zooming and slicing, were synchronized for all viewers. Windowing, however, was not synchronized since resulting images typically have varying value ranges. The interviewees answered questions using a five-item Likert scale (- -, -, ∘, +, ++) and their answers are summarized in Table 6.7.

PART 1 – GENERAL QUESTIONS. First, the interviewees were asked about their clinical experience and knowledge about lung anatomy. Furthermore, they were asked how much experience they specifically have with CT images in general and in the context of the lung.

PART 2 – CLINICAL FEASIBILITY. For the second part, the interviewees were asked to rate the LANCELOT method's feasibility w. r. t. certain clinical disciplines. Note that *therapy planning* was meant in a general sense and not specifically aimed at SIRTs. Further comments are presented and discussed in the next section.

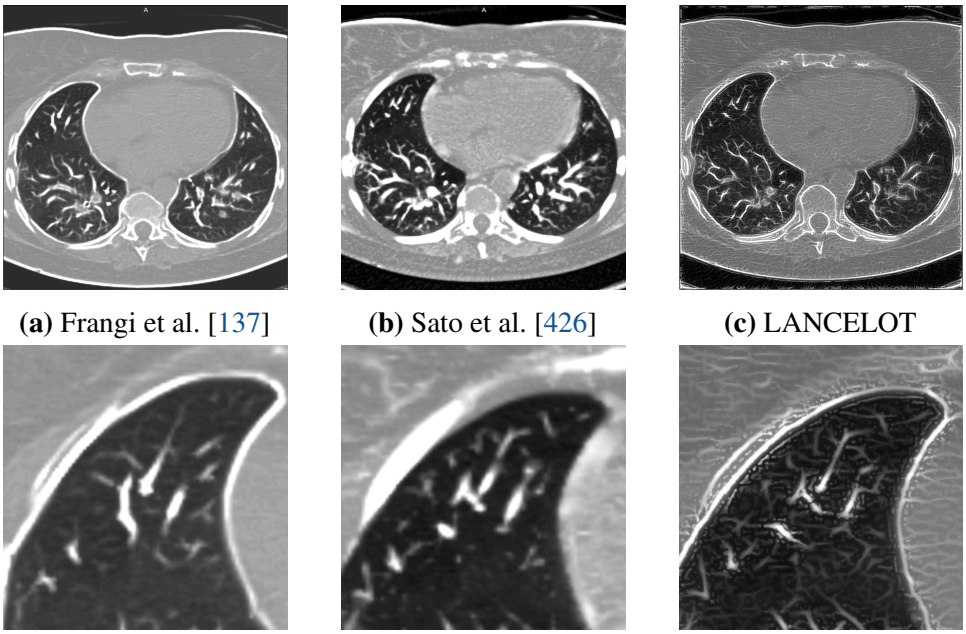

(a) Frangi et al. [137] **(b)** Sato et al. [426] **(c)** LANCELOT

(d) **(e)** **(f)**

Figure 6.19: A comparison of the methods of Frangi et al. [137] **(a,d)**, Sato et al. [426] **(b,e)** and the LANCELOT method **(c,f)**. Prior to filtering, a Gaussian blurring with $\sigma = 7$ was applied. Accordingly, m was set to 7. No multi-scaling was employed and all methods were applied in a slice-based manner. Note that the method of Frangi et al. [137] tends to enhance rather thick and medium-sized vessels **(d)**, whereas the method of Sato et al. [426] enhances medium-sized and smaller vessels **(e)**. In contrast, the LANCELOT method especially enhances smaller vessels, but may also omit very large vessels.

Table 6.7: The results of the informal think-aloud evaluation of the LANCELOT method. The numbers are denoted in years.

	Interviewees I1	I2
Part 1 – General Questions		
Gender	w	m
Age	43	30
Clinical Working Experience	21	4
Specifically for CT	8	3.5
Specifically for Lung	2	3
Anatomical Knowledge of Lung		
Part 2 – Clinical Feasibility		
Diagnosis		
Therapy Planning		
Interdisciplinary Communication		
Doctor-Patient Consultation		
Legend	−− − ○ + ++	

DISCUSSION. In this section, the LANCELOT method's results, its shortcomings and ideas how to address them will be briefly discussed.

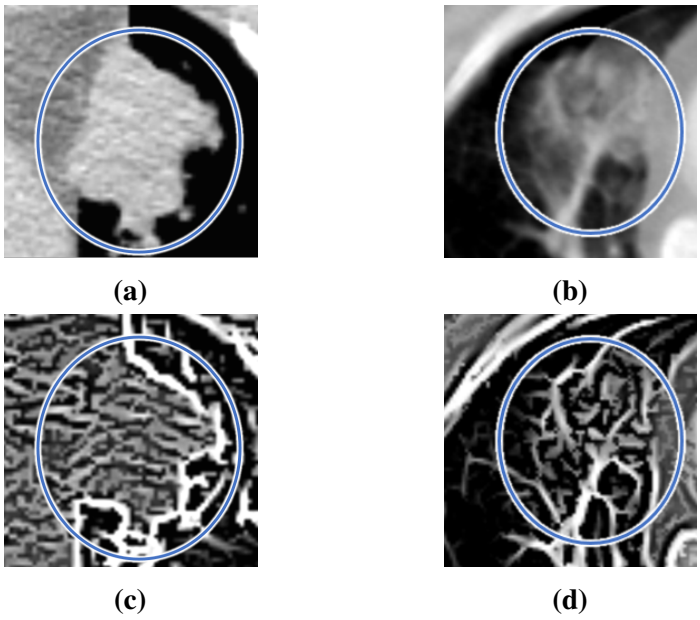

Figure 6.20: The LANCELOT method is applied to the whole image, and thus, contrast around all stick-like *structures* is enhanced. On the one hand, solid nodules become well delineated from adjacent tissue ((**a**)→(**c**)). On the other hand, however, non-solid and/or partially solid nodules become somewhat cluttered ((**b**)→(**d**)). The overall morphology of non-solid nodules is roughly preserved.

The original medical images were provided and used here with permission by Oliver S. Großer.

EVALUATION. Both interviewees stated that the LANCELOT method could improve the diagnostic- and therapy planning-related value of low-dose CT images. On the one hand, they based their statements on the fact that the LANCELOT method enhances medium- and small-sized vessels more clearly than the reference methods (cf. Fig. 6.19). This, however, is due to the single-scale application of the reference methods. The single-scale limitation was employed to make the results more comparable, since the LANCELOT method also operates on one *scale*. On the other hand and although contrast between solid nodules and adjacent parenchyma is also enhanced, the interviewees stated that the LANCELOT method is not suited for such applications (cf. Fig. 6.20 and [262]). In non-solid nodules, i. e. in nodules that have diffuse and/or missing (clear) delineations to adjacent tissue, the LANCELOT method tends to enhance *pseudo vessels*, which results in cluttered presentations (cf. Figs. 6.20b and 6.20d). Both interviewees stated that the aforementioned computational times are sufficient, although it would be desirable to speed them up (read below). Furthermore, I1 stated that the LANCELOT method could be beneficial to assist manual segmentations of blood vessels in low-dose CT images.

CLINICAL APPLICABILITY. The main motivation for the LANCELOT method was to enhance blood vessels in low-dose CT images to assist the process of finding catheter pathways during SIRT intervention planning. Some imaging protocols, such as MRAs, CTAs and DSAs, *naturally* show strong contrast between blood vessels and surrounding tissue due to administered contrast media. In contrast, low-dose CT images typically have a lower image quality and contrast than their standard-dose counterparts, which can further be enhanced by contrast media. Since both interviewees stated that enhanced blood vessels improve the diagnostic and therapy planning values of low-dose CT images, this could also apply to other anatomical regions and/or other catheter-based interventions and/or tests, such as SIRTs in the liver or cryoablations in the heart [376, 450]. However, the main limitation is that blood vessels have to be depicted as stick-like structures with a certain thickness (read below). For low-quality images with many stick-like noise, the LANCELOT method would rather not provide any enhancing-related benefit.

EXTENSION-RELATED OPEN IDEAS. The stick filtering could be extended to 3D to also enhance superiorly and/or inferiorly processing blood vessels. Currently, only in-plane stick-like image regions are enhanced, although upwards- and/or downwards-oriented sticks could potentially result in a better *fit*. Moreover, the method could be extended w. r. t. multi-scaling. This could be done in a two-fold manner: On the one hand, and in the original sense of *multi-scale* filtering, stick filters of varying lengths could be employed, i. e. by increasing m. However, (blood) vessels are not straight sticks and results for larger m, i. e. typically above $m = 9$ for standard image matrix sizes of 512×512 pixels, would rather not provide large benefits. On the other hand, not all vessels have a width (*caliber*) of one pixel and varying stick thicknesses could be used to find the *optimal* fit. This is somewhat depicted in Figure 6.19, where parts of a thicker blood vessel are omitted due to the image intensity homogeneity in the vessel's middle part.

COMPUTATIONAL PERFORMANCE. In Table 6.6, the computation times for the two reference methods by Frangi et al. [137] and Sato et al. [426] and the LANCELOT are listed.

Both reference methods are roughly 5 to 10 times faster than the LANCELOT method, since presumably the respective algorithms in MeVisLab are optimized in a parallel manner, whereas the MATLAB implementation of the LANCELOT method processes image stacks in a slice-wise manner. This could be addressed via parallel programming or by limiting the application to pre-segmented lung lobe masks (cf. Fig. 6.7).

6.4 SUMMARY

In this chapter,

- an illustrative visualization technique which combines OITs, boundary enhancements and silhouettes, and
- the LANCELOT method that enhances lung blood vessels in low-dose CT images

to assist the intervention planning and assessment of SIRTs in the lung were discussed. Similar to RFAs, intervention planning for SIRTs is primarily based on the physician's experience to assess multimodal images, for example w. r. t. various target organ compartments and potential (catheter) pathways. Thus, we aimed to enhance standard 2D PET/CT color superimpositions by illustrative 3D visualizations to cognitively support physicians

- to perceive PET hotspots in their morphological context and
- to examine *radiation patterns* during intervention assessment to evaluate if the employment of radio-labeled embolization media was successful.

Overall, the proposed technique was evaluated to be feasible for these tasks by nine clinical and visualization domain experts. Note that although the individual parts of the visualization technique were not novel themselves [33, 130], their combination and evaluation in the context of interventional radiology both were.

An open extension of this visualization technique was to visualize blood vessels to further assist the intervention planning of catheter-based interventions, such as SIRTs. Although we had access to diagnostic CT images that typically entail high contrast between blood vessels and adjacent parenchymal tissue, lung diagnostics benefit from combined PET/CT images to evaluate physiological abnormalities in their morphological context. These CT images, however, are often acquired in so-called low-dose mode, which typically leads to smoothed blood vessel boundaries, and thus, we developed the LANCELOT method to enhance them. The method was evaluated by two clinical experts who revealed its potential, limitations and possible extensions. If these limitations would be addressed, a combination of both techniques presented in this chapter could lead to an interesting combination to support intervention planning for SIRTs.

Content-wise, the next chapter concludes this thesis. Methods will also be presented in the context of the human lung, but they will be focused on the documentation and subsequent presentation of certain information, such as findings, diagnoses and the quantification of PET image intensities. Related to Chapter 4, so-called *lymph node station maps* will be presented. These maps visualize metastatic disease patterns in the thoracic region, e. g., for patients with primary lung cancer.

7 REPORT GENERATION FOR THORACIC LYMPH NODES

WHEN patients enter hospitals, they are *cataloged* in the form of printed and digital patient charts and/or reports. Charts typically contain patient-specific information, such as an anamnesis and information about current symptoms, past ailments and eventual treatments. This chapter is focused on reports which are documents that compile diagnostic- and treatment-related aspects. During hospitalization, such documents are subsequently extended via examination results, findings, diagnoses, treatment decisions, planning and/or execution details and treatment outcomes from follow-up examinations. Most reports, however, are primarily based on quasi-standardized texts and tables, e. g. by listing various key parameters from blood samples w. r. t. their typical value ranges and the actual examination results. In other words, visual representations are rarely employed. On the one hand, this reflects patients and their situations highly detailed and objectively. On the other hand, such documents do neither reflect the inherent visual nature of image-based diagnostics nor *our* capabilities to process images in seconds [394, 488].

To simplify the reporting of findings, disease patterns and diagnoses, and to support the interdisciplinary communication between clinical experts, such as between nuclear medicine physicians and thoracic surgeons, in this chapter,

- a processing pipeline to create visualization-enhanced case reports,
- various visualization concepts to abstract (stylize) PET/CT images and/or thoracic metastatic disease patterns via 2D and 3D visualizations and
- two color-coding methods for such visualizations and ROI segmentations on color-coded superimpositions of PET/CT images

are presented. Due to our collaboration with the local University Clinic for Nuclear Medicine in Magdeburg, these techniques will be focused on thoracic lymph nodes, lymph node stations and lymph node metastases in patients with primary lung cancer. These techniques were partially evaluated by two nuclear medicine physicians who also co-authored the respective publications.

Here, first, brief backgrounds about *our* thoracic lymph node system (Sec. 7.1) and the TNM staging system (Sec. 7.2) are provided [72]. This staging system was already introduced in the last chapter, and thus, here, only the lymph node-related N staging category is described in more detail. The assessment of involved lymph nodes in the context of lung cancer staging is important, since lung cancer is often found in an already progressed state, i. e. cancer cells already infiltrated local (sentinel) lymph nodes. Subsequently, related approaches w. r. t. clinical (case) report generation are presented in Section 7.3. Then, the items of the aforementioned itemization are discussed in detail, i. e.

Table 7.1: Lymph node station tokens and a rough description which anatomical region they correspond with. This particular categorization is used by the "*American Joint Committee on Cancer*", e. g. in the "*AJCC Cancer Staging Manual*" [420] (cf. Fig. 7.1).

Superior Mediastinal Nodes		**Inferior Mediastinal Nodes**	
1	Highest Mediastinal	7	Subcarinal
2R/L	Upper Paratracheal	8	Paraesophageal
3	Pre-Vascular and Retrotracheal	9	Pulmonary Ligament
4R/L	Lower Paratracheal		
Aortic Nodes		**N_1 Nodes**	
5	Subaortic	10R/L	Hilar
6	Para-Aortic	11R/L	Interlobar
		12R/L	Lobar
		13R/L	Segmental
		14R/L	Subsegmental

Table contents taken from [344, Fig. 1] and reprinted from Regional Lymph Node Classification for Lung Cancer Staging, CHEST volume 111, Clifton F. Mountain, Carolyn M. Dresler, Pages 1718–1723, © 1997, with permission from Elsevier.

- how an interactive visualization application can be used to create reports (Sec. 7.4),
- how PET/CT images can be abstracted to convey disease patterns of lung-related lymph node metastases (Sec. 7.5) and
- how they and ROIs in PET/CT images can be color-coded (Sec. 7.6), e. g. to prevent color-related redundancies and/or eventual misinterpretations in reports.

This chapter will not have a specific *Results* section and all approach-, method- and evaluation-related results will be presented in the respective sections. Still, a discussion is provided to present limitations, possible ways to overcome them and open ideas for future work (Sec. 7.7). Finally, the chapter is concluded with a short summary in Section 7.8.

This chapter is based on:

[321] **Merten, N.**, Genseke, P., Preim, B., Kreißl, M. C., and Saalfeld, S. "Maps, Colors, and SUVs for Standardized Clinical Reports." In: *Proc. of German Society of Computer- and Robot-Assisted Surgery*. 2019, pp. 292–297

[322] **Merten, N.**, Genseke, P., Preim, B., Kreißl, M. C., and Saalfeld, S. "Towards Automated Reporting and Visualization of Lymph Node Metastases of Lung Cancer." In: *Proc. of Bildverarbeitung für die Medizin*. 2019, pp. 185–190

7.1 BACKGROUND ON THORACIC LYMPH NODES

The lungs and the mediastinal region have extensive Lymph Node (LN) drainage systems. Typically, LNs are small ($\lesssim 3\,cm$) kidney-like shaped anatomical structures that have various tasks, e. g. they transport nutrients and *waste*, but also filter (external) body fluids for bacteria and/or infections [315, 424]. Lymph nodes are somewhat *clustered* w. r. t. their

anatomical origin, for example into *stations* and/or *zones* (cf. [344] and [420]). Note that these are proposed terms introduced by various research associations to group and/or distinguish LNs, e. g. with *zones* introducing another level of hierarchy for prospective and retrospective treatment-related purposes [420]. Here, we follow the nomenclature used by Mountain and Dresler [344] who group adjacent LNs into so-called LNSs (see Fig. 7.1).

Each station has a unique token, such as 2R or 7, and corresponds with a certain anatomical region, such as on the upper right side next to the trachea (2R) or beneath the carina (7) where the trachea branches into the main bronchi (see Tab. 7.1).[1] These tokens are employed to describe metastatic disease patterns from a diagnostic perspective, but also to provide rough landmark-based descriptions for treatment-related purposes. The number of LNs per station, however, can vary between individuals. For example, Schmidt Júnior et al. [431] conducted an anatomical study in 50 cadavers and resected roughly 1750 LNs in total. Typically, the right side contains more LNs. For example, in total, the authors resected 276 LNs in 2R ($mean\ count = 5.5,\ SD = 4.5$) and 55 in 2L ($mean\ count = 3.2,\ SD = 2$).

7.2 THE N CATEGORY OF THE TNM STAGING SYSTEM

Lung cancer is often accommodated by parenchymal and/or mediastinal LN metastases. For example, Milovanovic et al. [336] published an autopsy study with 175 cases with

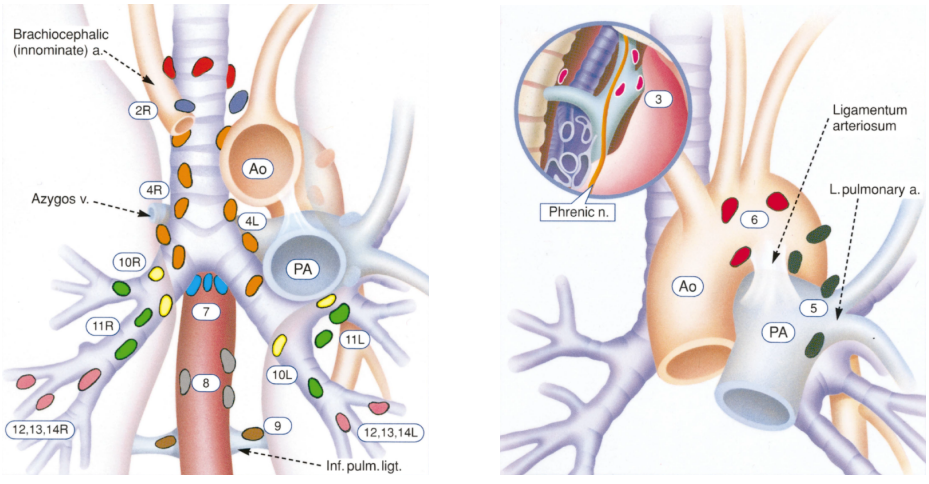

(a) **(b)**

Figure 7.1: The thoracic LNSs as introduced by Mountain and Dresler [344] (cf. [72]). Each LNS is represented as a token, e. g. 7 or 12R, and represents a certain thoracic and/or mediastinal region (cf. Tab. 7.1). Subfigure **(a)** gives a rough overview from an anterior perspective, whereas Subfigure **(b)** depicts the LNSs between the aorta (**Ao**) and pulmonary artery (**PA**) in more detail.

[1] Rarely, the left (L) and right (R) sides are abbreviated via D (dexter, right) and S (sinister, left), and

primary lung cancers for which roughly 45 % developed LN metastases around the hilum (10L/R). There also exist so-called "*skip metastases*" which are metastases that *skipped* LNs on the same lung side (N_1) and manifested themselves in more *distant* mediastinal LNs (N_2 or N_3) [72, 420]. Typically, close, so-called *sentinel* LNs become affected more often, but *skipping metastases* still appear in roughly 25 % of all cases [420].

With respect to the combination of infiltrated LNSs, an N staging is derived [72, p. 263]:

- NX An Assessment of LNs is not possible.
- N0 No LN metastases were found.
- N1 A metastasis on the same side and/or in the same lung was found.
- N2 A metastasis in the mediastinal and/or subcarinal region (e. g. LNS 7) was found.
- N3 A metastasis in the other lung and/or above the claviculae (e. g. LNS 1) was found.

The respective manual provides more details on all anatomical regions [72]. From a treatment perspective, *suspicious* LNs are rarely treated *on their own*, i. e. they are often additionally resected during nodule-related surgeries to limit disease progression [30, 282].

IMPLICATIONS FOR THIS THESIS. The main aim of the proposed visualization approaches is to convey disease patterns *at a glance*. Due to the generally quick disease progression of lung cancer, even during initial diagnoses, LN metastases are often found. Therefore, the N staging category was specifically chosen to be visualized. Moreover, the mediastinal region is somewhat *compact* and symmetrical, which renders it well-suited to employ various abstraction approaches, such as via stylized maps. The LNSs-specific classifications and/or diagnoses, namely benign, inconclusive and malign, were provided by our clinical colleagues who derived them from PET images. Thus, the proposed techniques are multimodal visualization techniques, since these physiology-related diagnoses will be somehow encoded via morphological key features and w. r. t. anatomical landmarks.

7.3 RELATED WORK FOR CLINICAL REPORTS

There exist various approaches to create and/or enhance clinical (case) reports. Birr et al. [55, 54] developed interactive reports to support the planning process of lung surgeries (see Fig. 7.2a). Similar to the interactive questionnaires that we employed for evaluations for the previously presented techniques, the authors employ reports that depict 2D presentations of original images next to interactive 3D viewers. To do so, geometric objects, e. g. given in the `.obj`, `.stl` or `.wem` format, can be exported in the `.u3d` format. This can be done via the *WEMSaveAsU3D* MeVisLab module [406]. Subsequently, these files can be embedded into Portable Document Format (PDF) files, e. g. via the `media9` LaTeX package. Another approach was recently presented by Lawonn et al. [273] who create reports for blood vessels with (multiple) aneurysms and certain morphological key features, such as their dimensions. In contrast to the work of Birr et al. [55, 54], the reports created by Lawonn et al. [273] do not employ interactive elements. However, by employing the viewpoint selection method introduced by Neugebauer et al. [358], the authors create various *good*

thus, stations may be abbreviated via 2D or 10S, for example.

viewpoints that *highlight* certain morphological features. Similarly, Rössling et al. [416] presented their "*Tumor Therapy Manager*" application which creates annotation-enhanced reports consisting of endoscopic photographies, stylized presentations, original images and 3D IVR screenshots (see Fig. 7.2).

These approaches mostly employ illustrative depictions of morphological (monomodal) key features, but at varying degrees of abstraction [501]. For example, Birr et al. [55] approximate lung nodules as color-coded circles. Thus, nodule-related disease patterns can be assessed *at a glance*, for example w. r. t. which lung lobes are affected more or less, although the degrees of geometric and photometric abstraction are both rather high. In contrast, for the "*Tumor Therapy Manager*", lower degrees of abstraction were employed, i. e. by depicting anatomy via shaded and stippled surfaces that overall show more anatomic details [416]. Interaction-wise, this application enables *freehand drawing* on images for documentation and therapy planning purposes, e. g. to highlight local tissue abnormalities that surgeons may have to look further into during operations (image-occult tumor infiltration). For both applications, users have the opportunity to alter the *degree of documentation*, e. g. which and how many images will be included into the final report. The resulting digital and on-paper reports are quasi-standardized, i. e. they have a concise and regular layout and/or were heavily influenced by already employed report layouts. These aspects influenced the development of our report generation pipeline, e. g. by offering staging suggestions and by employing original images *next to* pipeline-generated information (cf. Figs. 7.6 and 7.7).

There also exist methods that employ photographies of patients and/or their ailments. For example, Haak et al. [161] presented a mobile application to document the wound healing processes of patients after vascular surgeries. To make them interpretable and comparable,

See [55, Fig. 1].

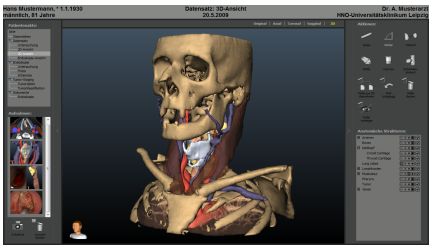

(a) **(b)**

Figure 7.2: Screenshots from the 3D PDF application from Birr et al. [55] **(a)** and the "*Tumor Therapy Manager*" from Rössling et al. [416] **(b)**. On the left, an illustrative presentation of the lungs and airways encompasses approximated (abstracted) representations of various lung nodules. On the right, a DVR depicts various anatomical structures in the head-neck-ear area. In small viewers next to these overview-providing visualizations, the original images are presented.

the authors place color reference cards near the wounds. Certain clinical disciplines that employ photographies, such as ophthalmology, histopathology and dermatology, require standardized color palettes, since *color variations* can result in different (potentially false) assessments [22, 37]. Another approach was presented by Krupinski et al. [257] who measured the influence of patient photography-enhanced chest radiographies.

IMPLICATIONS FOR THIS THESIS. The main aims for the proposed visualization approaches and methods presented in this chapter are

- to simplify the process of clinical reporting and/or report generation in general and
- to support the interdisciplinary communication between clinical experts, e. g. between nuclear medicine physicians and thoracic surgeons, to
  - make diagnoses (specifically w. r. t. the N staging category) and
  - to plan parenchymal and/or LN resections.

These visualization methods depict multimodal PET/CT images at varying degrees of abstraction, e. g. by depicting infiltrated LNSs via airway morphology or map-like images. Some of these approaches were evaluated by two nuclear medicine physicians and were "*deemed to be highly useful from a clinical perspective*" [322], although high degrees of geometric (anatomical) abstraction were employed [501].

7.4 PROCESSING PIPELINE FOR VISUALIZATION-ENHANCED REPORTS

Here, we present a processing pipeline to create visualization-enhanced reports. Although this pipeline is tailored to depict metastatic disease patterns for thoracic LNs, its core can be applied to virtually any other anatomical region and staging category (cf. [72]).

7.4.1 CLINICAL WORKFLOW PERSPECTIVE

In this section, the clinical workflow is briefly presented, whereas the processing pipeline will be discussed over the course of the following sections.

INPUT – PATIENT DATABASE. Generally speaking, the patient database is a Picture Archiving and Communication System (PACS) that stores and manages all acquired images. Here, our *PACS* was a Comma-Separated Values (CSV) file that holds LNS-specific diagnoses for several patients, which was provided by our clinical colleagues. In other words, the table-like file contains patients (rows), LNSs (columns), and individual LNS diagnoses w. r. t. three diagnostic categories (cells), namely benign, inconclusive or malign. Thus, when users use the GUI to assess *another* patient, the respective row is parsed and its contents alter the color-coding of the proposed support visualizations (cf. Fig. 7.7).

IMAGE ACQUISITION AND DIAGNOSIS. In Figure 7.3, a rough diagnostic- and treatment-oriented clinical workflow is depicted and how the proposed methods are intended to be used w. r. t. it. As described in the Chapters 2 and 6, CT and PET images are acquired to assess physiological and morphological abnormalities and their relationships to each other. The images are typically assessed individually and simultaneously, e. g. via color-coded superimpositions (cf Figs 2.14b and 6.6b). During diagnoses, physicians derive key

features, such as tumor dimensions, to assess and stage the patients' diseases [72, 119, 364]. Note that these tasks and/or goals vary w. r. t. the examined patients. For example, in *new* patients, the main goal is to get a first overview about their condition, whereas known patients, e. g. who may have already been treated somehow, are typically examined w. r. t. treatment responses and their eventually improved or worsened disease pattern(s) and condition. Thus, other imaging modalities, such as MRI, can also be employed when physicians want to examine *risk organs*, such as the brain or liver, to search for distant metastases (M-category).

INTERDISCIPLINARY CASE DISCUSSION. Patients are typically discussed in so-called tumor boards which are meetings and discussions between various clinical experts from different disciplines, such as nuclear medicine physicians and physicists, radiologists, radiation oncologists and (thoracic) surgeons. Prior to these meetings, some clinicians often already had some sort of correspondence with each other to discuss patients. Thus, the main goal of tumor boards is to assess (follow-up) treatment options with the help of a broader expert audience. Additionally, the general condition of patients, e. g. how hey present themselves and if they do (not) comply with further and/or certain treatments, is also included in treatment decisions.

TREATMENT. Common treatment options for patients with lung cancer include surgical resections, radiotherapies, chemotherapies, (radiofrequency) ablations, drugs (e. g. kinase inhibitors), SIRTs and combinations of them [103, 201, 215, 282, 398]. Actually feasible treatment options, however, depend on the disease progression (staging) and cancer type

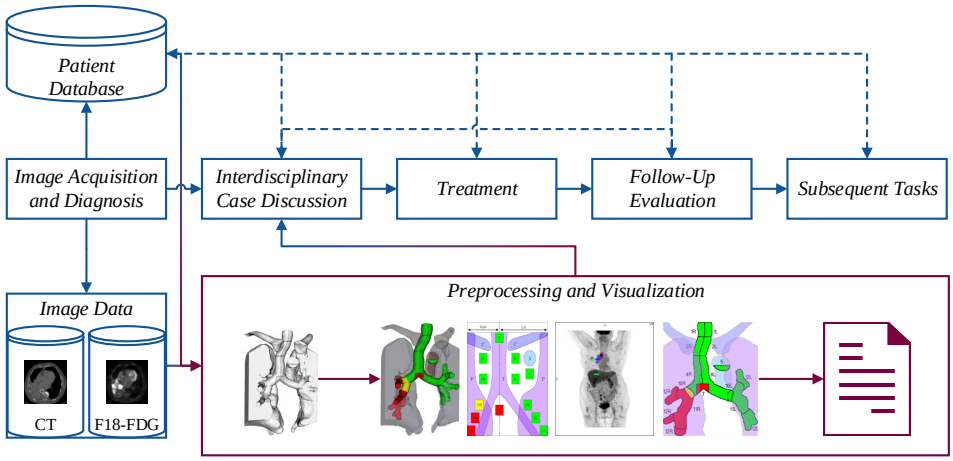

Figure 7.3: A simplified clinical workflow w. r. t. the proposed report generation processing pipeline for PET/CT images. First, the image sources are preprocessed to extract visualization-related key features and anatomical landmarks, i. e. the trachea and main bronchi, the parenchyma, the claviculae and the upper part of the aorta (cf. Fig. 7.4). Subsequently, these structures and landmarks are used to convey thoracic LN disease patterns which are then used to create PDF reports. For simplification purposes, not all relationships are depicted (arrows), since reports could also be created with modalities acquired for follow-up evaluation purposes.

[201, 215]. For example, independent from the actual type of cancer, stage I lung cancers are typically treated via resections to minimize the risk of (distant) metastases. Additionally, in patients with metastatic LNs, surgeons also aim to resect such (suspicious) LNs to limit disease progression [30, 282].

FOLLOW-UP EVALUATION. Treatments are typically evaluated w. r. t. the patient's condition and (quantitative) treatment response, e. g. if a lung nodule decreased in size and/or is less *active* from a physiological perspective [119, 364]. Such assessments can be image-based, which makes additional (multimodal) imaging necessary (cf. Fig. 6.10).

SUBSEQUENT TASKS. This step was intentionally formulated very general, since it can virtually encompass any (combination of) subsequent clinical tasks. With respect to the treatment response, e. g., patients could be discussed again in a tumor board to conclude about further treatment. In contrast and given that the treatment was successful, patients can also be released and invited for regular follow-up examinations, e. g. at a yearly rate.

7.4.2 INTERMISSION – CALCULATING SUVS FROM PET IMAGES

An important key feature to assess metabolic cancer activity is the translation of PET image intensities into so-called SUVs. In contrast to CT image intensities which are quasi-standardized, PET image intensities depend on various factors that make their *direct* interpretation very challenging. For example, PET image intensities depend on the amount and type of administered radiotracer, the waiting time between administration and

Algorithm 7.1: Algorithm to compute $SUVs_{BW}$ from PET image intensities.

```
Input: PETdataSet, x, y, z

# Get PET Image Intensity for a Specific Coordinate
PETimageValue = PETdataSet.getVoxelValue(x, y, z)

# Get DICOM Tags (expected units are shown in square brackets, e.g. [s] for seconds)
radioStartTime = PETdataSet.getTagValue([0x0018, 0x1072]) # [hhmmss]
radioTotalDose = PETdataSet.getTagValue([0x0018, 0x1074]) # [Bq]
radioHalfLife = PETdataSet.getTagValue([0x0018, 0x1075]) # [s]
seriesDate = PETdataSet.getTagValue([0x0008, 0x0021]) # [yyyymmdd]
seriesTime = PETdataSet.getTagValue([0x0008, 0x0031]) # [hhmmss]
patientWeight = PETdataSet.getTagValue([0x0010, 0x1030]) # [Kg]
rescaleIntercept = PETdataSet.getTagValue([0x0028, 0x1052]) # [scalar]
rescaleSlope = PETdataSet.getTagValue([0x0028, 0x1053]) # [scalar]

# Compute SUV w.r.t. Patient Body Weight
administrationDateTime = seriesDate + "." + radioStartTime # [yyyymmdd.hhmmss]
seriesDateTime = seriesDate + "." + seriesTime # [yyyymmdd.hhmmss]
radioDecayTime = seriesDateTime - administrationDateTime # [s]
radioDecayDose = radioTotalDose * exp(-radioDecayTime * (log(2)/radioHalfLife)) #[Bq]
BWscaleFactor = (patientWeight * 1000) / radioDecayDose # [g/Bq]
SUVbw = (PETimageValue + rescaleIntercept) * rescaleSlope * BWscaleFactor

Output: SUVbw
```

Originally published in the proceedings of the German Society of Computer- and Robot-Assisted Surgery [321].

Table 7.2: Exemplaric DICOM tag values to compute $SUVs_{max/BW}$ from PET image intensities (cf. Alg. 7.1). Note that these key values were taken from an actual case that was made available by our clinical colleagues. The corresponding report can be found in Figure 7.8.

radioStartTime	radioTotalDose	radioHalfLife	seriesDate
102 300	224 410 000	6586.2	20 170 802

seriesTime	patientWeight	rescaleIntercept	rescaleSlope
111 802	72	0	1.44

administrationDateTime	seriesDateTime	radioDecayTime	radioDecayDose	BWscaleFactor
20 170 802.102 300	20 170 802.111 802	3302	$\approx 1.585 \times 10^{8}$	$\approx 4.542 \times 10^{-4}$

PET Image Intensity	$SUV_{max/BW}$
5778	3.79

These parameters were taken from images provided and used with permission by Philipp Genseke.

image acquisition (*radioactive decay*) and the *composition* of patients, for example w. r. t. their blood glucose concentration, since ^{18}F-FDG has to compete with other glucose-like substances for GLUT receptors [313, 364] (cf. Sec. 2.1.3). Note two things:

- There exist various types of SUVs. Essentially, from each PET image intensity, a SUV can be calculated. In other words, PET image stacks can be *translated* into SUV image stacks with identical dimensions. However, SUVs can also be *compiled*, e. g. by only denoting the maximum value for a ROI segmentation (SUV_{max}). Moreover, SUVs are always *normalized* w. r. t. patient-specific features, such as with their *raw* bodyweight (SUV_{BW}). With respect to patient height and weight, estimations of the lean body mass (SUV_{LBM}), i. e. *our* weight without stored fat, or of the body surface area (SUV_{BSA}) can also be used [231].
  The code guide presented below computes SUVs w. r. t. the patients' bodyweights (see Alg. 7.1). Note that in clinical practice $SUVs_{max/BW}$ are typically used for diagnostic- and staging-related purposes. The code snippet below, however, is *only* a simplified version to compute $SUVs_{BW}$ and would have to be extended, e. g., to compute ROI-specific $SUVs_{max/BW}$ (cf. Figs. 7.8 and 7.9).
- There already exist different *guides* to compute SUVs, i. e. we did not come up with the theoretical groundwork. However, these guides often *only* provide single formulas with sparse further explanations (cf. [136, 231, 241]). In addition to missing *reference tables*, i. e. tables with matching pairs of input and output values to evaluate implementations, this makes it challenging to (re-)produce results (cf. Tab. 7.2).
  The proposed GUI enables users to *draw* ROI segmentations on slices for which said $SUVs_{max/BW}$ are calculated. This functionality is mimicked from commercial diagnostic software, e. g. from the *Siemens Syngo VG51C* toolbox (cf. Fig. 2.14c). To evaluate the correctness of our $SUVs_{max/BW}$, we manually reconstructed ROIs

from screenshots of said toolbox. When comparing the respective $SUVs_{max/BW}$, our results sometimes showed computational inaccuracies of ±0.01 SUV units. For comparison purposes, in their "*practical PERCIST guide*", O et al. [364] defined a "*partial metabolic response [as] a decrease of greater than 30% and of at least 0.8 SUL units*". Thus, said inaccuracies are negligible. Note that the authors employ $SUVs_{LBM}$ instead of $SUVs_{BW}$, hence the name "*standardized uptake value corrected for lean body mass (SUL)*" [364].

From a clinical perspective, these SUVs can be used, e. g., to quantify treatment responses w. r. t. physiological information or to compare several patients. However, to actually *have* comparable SUVs, PET images have to be acquired and assessed in a similar and controlled manner [364]. The imaging protocols in patients with diabetes, for example, can encompass controlled fasting, eating and insulin intake scheduling prior to imaging.

7.4.3 PROCESSING PIPELINE PERSPECTIVE

In this section, the report-creating processing pipeline will be presented (see Fig. 7.4).

STRUCTURE SEGMENTATION. This chapter's content is based on two publications which build up on each other. In the first publication [322], the aforementioned LNSs were geometrically encoded via airway anatomy. With respect to the landmark descriptions from Table 7.1, segmentations were primarily carried out using MeVisLab [406]. Note that the same applies to the anatomical landmarks, namely the aorta, the claviculae and

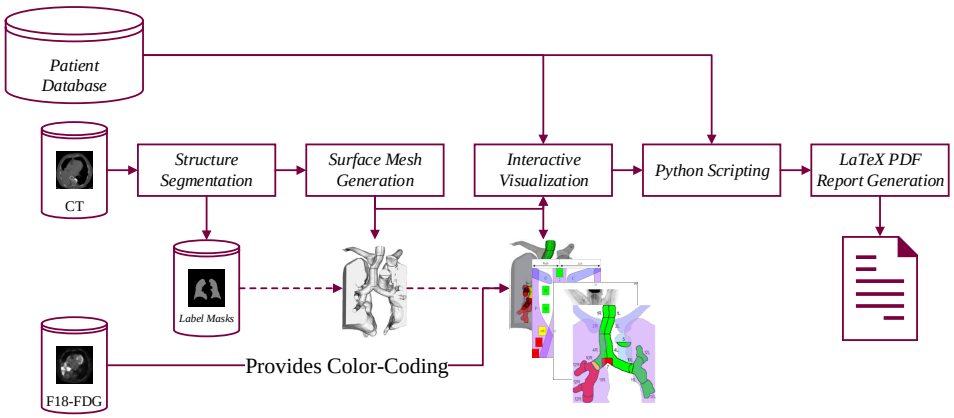

Figure 7.4: The more detailed *Preprocessing and Visualization* step from Figure 7.3. First, segmentations of the aforementioned key structures and anatomical landmarks are carried out which are subsequently translated into surface meshes [25]. Then, an interactive GUI can be used to assess interactive visualizations and to create reports via Python scripting (cf. Fig. 7.7). Note that for presentation purposes certain relationships are omitted. For example, the CT and PET images are also used in the interactive GUI, e. g. to enable users to define ROIs in color-coded superimposition presentations (cf. Fig 7.9). Moreover, the Python script also computes ROI-specific SUVs that are also included into the final report.

[2]This red-brown-blue color-coding was refined later (cf. Sec. 7.6).

the parenchyma.[2] In simplified terms, manually seeded and thresholded region growing was used to acquire first rough segmentation masks which were then separated to create multiple LNSs (see. Fig. 7.5b). Two airway sections had to be treated in a special way: First, due to the slightly *skewed* orientation of the trachea, the upper LNSs (1L/R, 2L/R, 4L/R) could not just be divided vertically without creating too large and/or too small LNSs. Thus, a small Python script was employed to divide the airway segmentation masks in a slice-based manner by computing AABBs and using a quasi-*half space* cutting plane at $\frac{x}{2}$ to create the respective L and R stations. The same was done for the parenchyma-related LNSs, i. e. for 10L/R and beyond. However, these LNSs were separated w. r. t. the number of bronchial branchings. To do so, the *DtfSkeletonization* module was employed to translate the airway segmentation mask into a graph with nodes denoting branching points and edges denoting intermediate bronchi (cf. Fig. 4.1). By traversing the airway graph *downwards* and counting branching nodes, the intermediate bronchi were labeled accordingly, e. g. 10L/R for the edges between the second and third branchings (primary

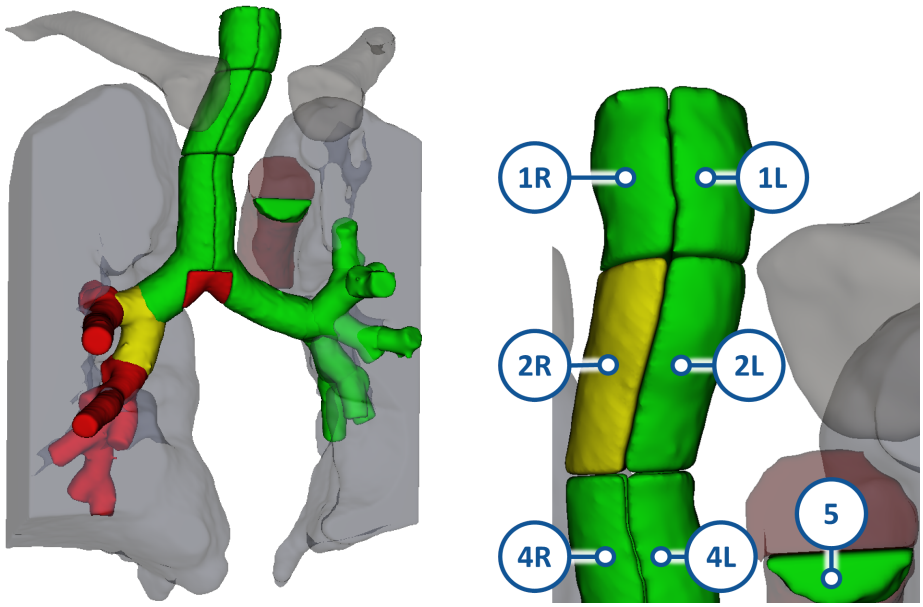

(a) **(b)**

Figure 7.5: A 3D approach to encode LNSs via airway anatomy **(a)**. Here, certain anatomical landmarks, namely the aorta, the claviculae and the lung parenchyma, are used to offer exploration support. Subfigure **(b)** depicts the LNSs 1L/R, 2L/R, 4L/R and 5 in greater detail. The color-coded LNSs encode the expert diagnoses with red denoting an infiltrated (malignant) LNSs, yellow denoting an inconclusive diagnosis and green denoting that no malignant LNs were found in this station.

bronchi → secondary bronchi) and so on. During the visualization, the resulting LNSs are color-coded w. r. t. the aforementioned three diagnostic categories.

SURFACE MESH GENERATION. The *WEMIsoSurface* module was employed to translate segmentation masks into surface meshes [25]. Subsequently, these meshes were smoothed by applying a Laplacian smoothing from the *WEMSmooth* module with a smoothing factor of 1 ($\in [0, 1]$) for four iterations. Thus, surfaces became more round while gaps between LNSs were enhanced, which increased their respective distinguishability (cf. Fig. 7.5b). In contrast, to render the LNSs 10L/R and beyond, not the original but an automatically created surface model was used (cf. Fig. 7.5a). This was done via the *SoVascularSystem* MeVisLab module (cf. [164]). Additionally to the aforementioned edges and nodes, the *DtfSkeletonization* module also creates intermediate sample points with respective radii. These radii are then used by the *SoVascularSystem* module to create round and smooth surface meshes. Here, these radii were set to a fixed value to match the radius of the primary bronchi. Although this further increased the geometrical (anatomical) degree of abstraction, this was done since especially small airways were challenging to visualize due to their limited visibility in the employed low-dose CT images. Moreover, this also resulted in smooth surfaces *out of the box*, but gaps could not be employed for visual separation.

INTERACTIVE VISUALIZATION. A GUI was implemented which enables users to import and assess PET/CT images in an interactive manner. In the first *Import and VOIs* tab, users can import image data and define ROIs (see Fig. 7.6). Here, a four-field viewer

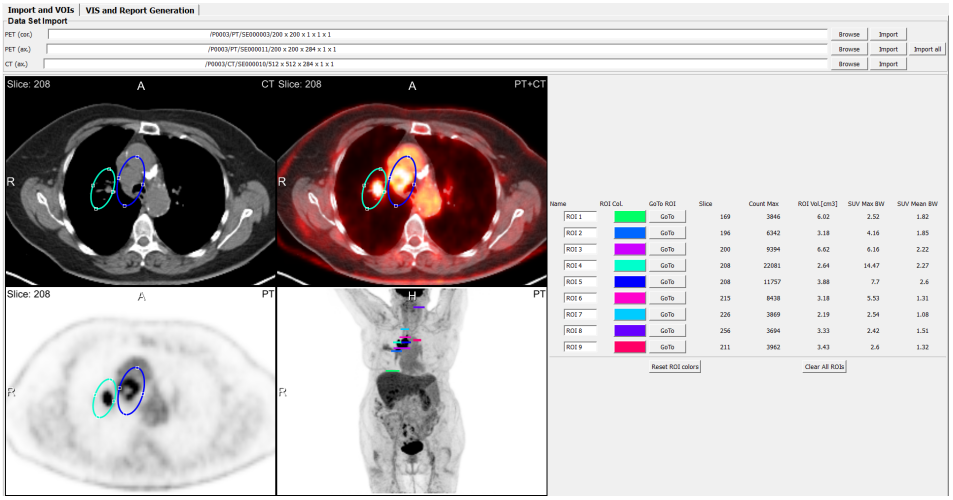

Figure 7.6: In the *Import and VOIs* tab, users can import PET/CT images and assess them interactively, i. e. by defining ROIs around morphological or physiological abnormalities. For each ROI, various key values are listed in a table, such as the encompassed volume and $SUV_{max/BW}$. Note that the depicted ROIs were defined directly after each other and that they are well-distinguishable (read below).

The original medical images were provided and used here with permission by Philipp Genseke.

layout is used which is similar to the *Siemens Syngo VG51C* toolbox our clinical colleagues typically employ for diagnostic purposes. The ROIs creation process is *linked*, i. e. if a ROI is created in one viewer, it is automatically *pushed* to all other viewers. As mentioned before, for all ROIs, certain key values are derived, such as the respective ROIs' volumes and $SUV_{max/BW}$. Note that the depicted color-coding will be discussed in Section 7.6.

After users labeled suspicious image regions, they can further assess *this* patient – and any other patient that is cataloged in the patient database for that matter – via the *VIS and Report Generation* tab (see Fig. 7.7). The patient database can be *browsed* in a slider-based manner.[3] After database import, the anatomical visualizations on the left (cf. Fig. 7.5a) and the right (cf. Sec. 7.5) are color-coded w. r. t. the expert's LNSs' diagnoses. More in-depth information about all LNS diagnoses are provided in a table and a Python script *in the background* automatically derives a staging suggestion w. r. t. the N staging category (cf. Sec. 7.2). If necessary, users can correct or extend this suggestion which will also be included into the final report (cf. Fig. 7.8). Below, the color-coding can be altered and a GUI widget presents the *irregular color hexagon* w. r. t. HSV color wheel (cf. Sec. 7.6). On the bottom, screenshots from the 3D viewer and reports can be exported.

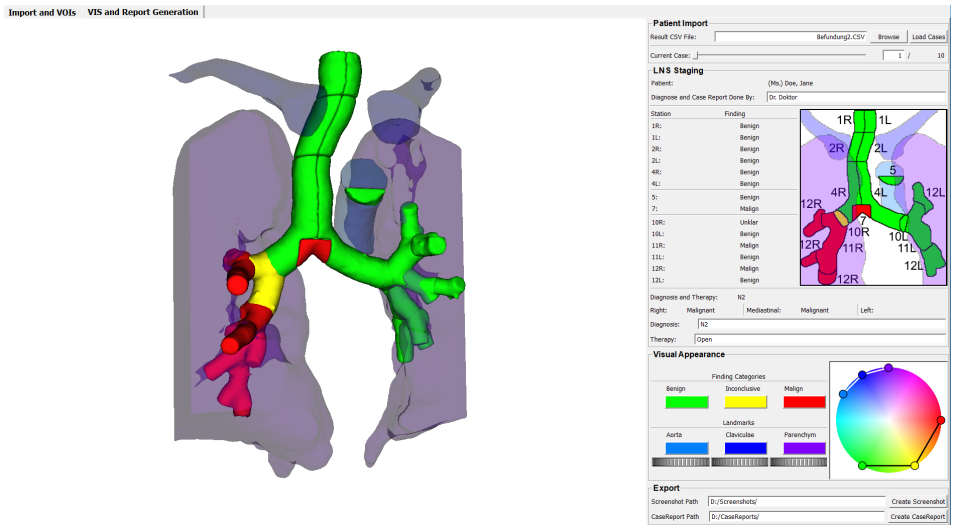

Figure 7.7: In the *VIS and Report Generation* tab, users can assess patient-specific LN disease patterns in more detail. This process is assisted by abstracted 2D and 3D presentations and a detailed itemization about all LNSs (cf. Sec. 7.5). Anatomical landmarks are visualized in non-attention-drawing colors while their visibility can be further decreased by lowering their specific opacities. Note that the illustrative visualization technique from Chapter 6 was employed here, too.

The original medical images were provided and used here with permission by Philipp Genseke.

[3] Note that this application was intended to support the visual exploration of small patient databases, i. e. with $\lesssim 50$ patients, for example in the context of small studies. For larger databases, a (horizontal) slider-based approach would rather not be feasible.

PYTHON SCRIPTING. Prior to triggering the actual report generation, *gaps* in a LaTeX source code cloze (dt. *Lückentext*) are filled. For example, the application creates a screenshot by triggering the VTK rendering pipeline (`vtkPNGWriter`) of the 3D viewer. Subsequently, a certain file name is assigned to this screenshot which is also written into the according `\includegraphics[...]{fileName}` command in the LaTeX cloze.

LATEX PDF REPORT GENERATION. Once the LaTeX source code is complete, it is written into a `.tex` file on the hard drive. Subsequently, a LaTeX command is triggered to create the PDF report, e. g. via `pdflatex`.

RESULTING REPORTS. After generation, users can assess the resulting reports. Basically, these reports consist of two types of pages. On the first page, various key values are compiled (see Fig. 7.8), namely

- clinic-related information, e. g. including the name of the hospital and the name of the responsible physician,
- a map-like presentation of the patient-specific metastatic LN disease, including some information about the patient, a suggested or user-defined staging and treatment decisions, and a color legend for the `TikZ`-based map visualization,[4]
- a table that presents all user-defined ROIs with certain ROI-specific key features, such as their encompassed volumes and $SUVs_{max/BW}$, and
- SUV computation-related key features, such as the amount and type of administered radiotracer and the waiting time between administration and image acquisition.

On the second and all further pages, each ROI is presented in more detail, i. e. by presenting the multimodal image sources next to derived key features (see. Fig. 7.9). With respect to the amount of user-defined ROIs, the actual report can have multiple pages.

When comparing Figure 7.3, i. e. where it appears that various visualization approaches are included into the final report, and Figure 7.8, i. e. where *only* the map-like approach was used, note that any other disease pattern-depicting presentation could have been used instead. In other words, the latest publication this chapter is based on was intentionally designed and written to provide diagnostic evaluation support via stylized map-like presentations [321], and thus, maps with certain LNSs and anatomical landmarks were specifically used for the final reports (cf. Ch. 4 and [326]). However, the actually included visualization can easily be changed by altering the respective source code line in the aforementioned LaTeX cloze, i. e. the final reports can be somewhat tailored to the users' needs and preferences.

EVALUATION. This approach was informally evaluated with our clinical colleagues, who both co-authored the respective publication. On the one hand, this approach was reported to introduce a high degree of anatomical (*geometrical*) abstraction, since LNs are distinct anatomical structures and do not belong to *our* airway anatomy [501]. However, this way of encoding LNS-specific diagnoses was evaluated to be easy to understand. Note that

[4] `https://www.ctan.org/pkg/pgf`, last accessed November 23, 2019

Case Report – (Mrs.) Doe, Jane

A

Date	22. November 2019
Referring Physician	Dr. Doktor
Diagnosis By	Dr. Doktor
Institution	University Clinic X
	Full Address

Patient Information

Name	Doe, Jane
Day of Birth	01.01.9999
Age	078Y
Sex	F

Diagnosis and Therapy

Staging	N2
Therapy	TBA

Visualization Legend

Benign
Inconclusive
Malign
Claviculae
Aorta
Parenchym

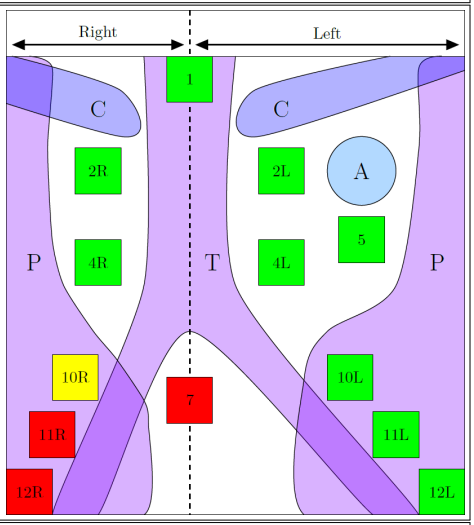

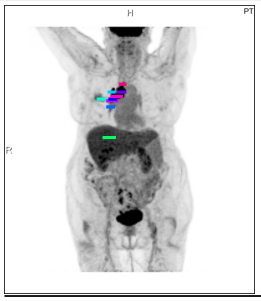

LNS	ROI Col.	ROI Sl.	ROI Vol. [cm3]	PET Quantification $Count_{max}$	PET Quantification $SUV_{max;BW}$	PET Quantification $SUV_{\mu;BW}$
Liver Baseline		155	2.94	5778	3.79	3.01
10R-1		190	2.69	4303	2.82	1.35
10R-2		197	3.38	9559	6.26	2.48
11R		199	2.34	5101	3.34	2.42
10R-3		199	1.99	10224	6.7	3.17
10R-4		202	2.49	12269	8.04	4.25
10R-5		207	1.99	23225	15.22	3.36
10R-6		207	2.89	11618	7.61	2.94
2		216	1.0	8449	5.54	2.25

Radiopharmaceutical Information

Radionuclide	Fluorodeoxyglucose
Administration Time	10:23:00
Total Dose	224.41 MBq
Half Life	6586.2 s

Patient Information

Patient Weight	72.0 Kg

Acquisition Information

Acquisition Date	2017.08.02
Acquisition Time	11:18:02
Decay Time	00:55:02
Rescale Slope	1.443
Manufacturer	SIEMENS

Figure 7.8: A report that was created via the proposed processing pipeline (cf. Fig. 7.4). On top, clinic- and physician-related information are listed. Below, patient-, staging- and therapy-related information are shown. On the right, a stylized map-like visualization depicts the LNSs-related metastatic disease pattern. The corresponding color legend is depicted on the left. In the third part, a coronal PET MIP image with color-coded ROIs is shown. Next to it, ROI-specific key features, such as $SUVs_{max/BW}$, are listed. Note that this table is a compilation and that all ROIs are presented in more detail over the next report pages (see Fig. 7.9). In the last part, SUV computation-related key values are listed.

A similar image was originally published in the proceedings of the German Society of Computer- and Robot-Assisted Surgery [321, Fig. 3]. The original PET image was provided and used here with permission by Philipp Genseke.

the aforementioned segmentations were carried out once for one CT image stack, i. e. all reports show the same *anatomy* and only the color-coding would change between patients. This patient-unspecific approach was chosen since it would increase familiarity with the proposed reports over time and, if repeated for each new case, manually carrying out segmentations in the previously described manner would be too time-consuming.

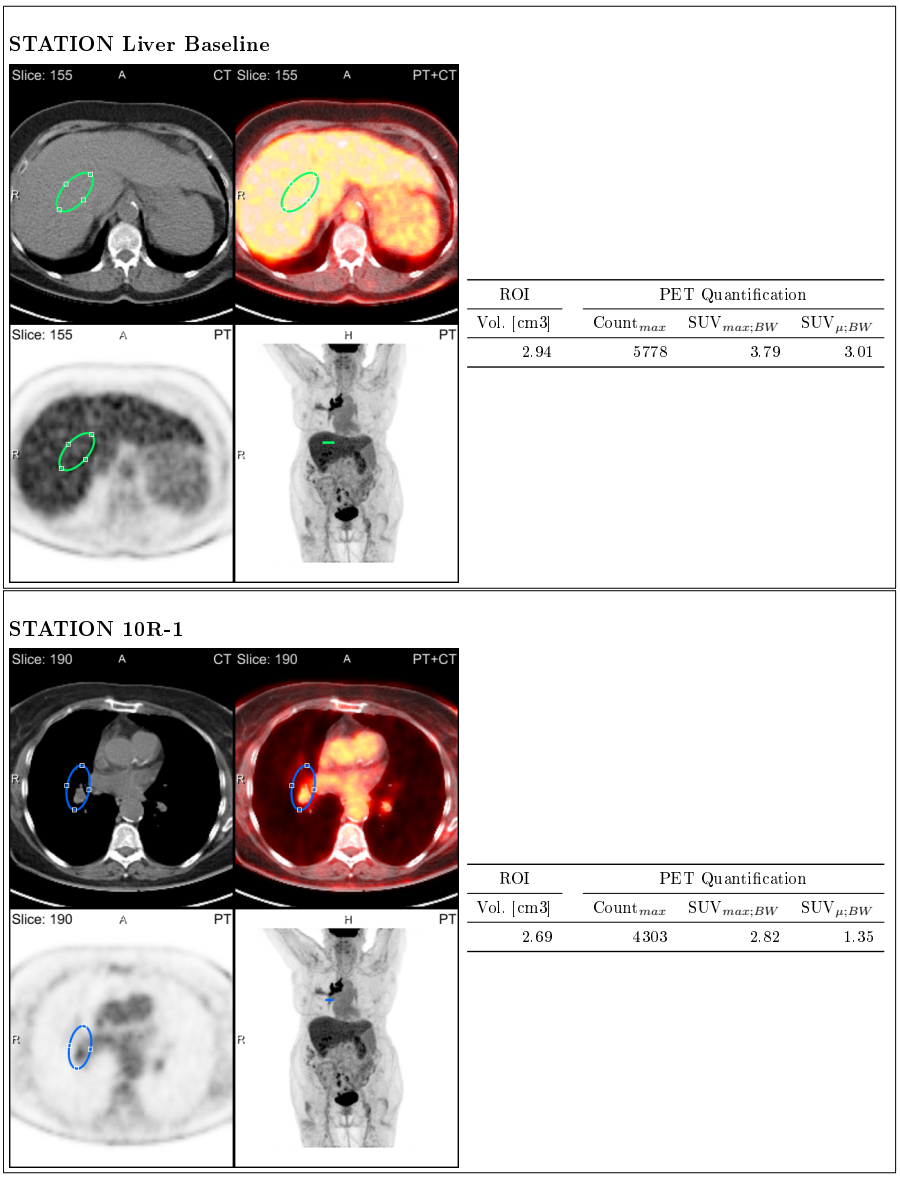

ROI	PET Quantification		
Vol. [cm3]	Count_{max}	$\text{SUV}_{max;BW}$	$\text{SUV}_{\mu;BW}$
2.94	5778	3.79	3.01

ROI	PET Quantification		
Vol. [cm3]	Count_{max}	$\text{SUV}_{max;BW}$	$\text{SUV}_{\mu;BW}$
2.69	4303	2.82	1.35

Figure 7.9: In addition to the compiled presentation from Figure 7.8, for each ROI, a more detailed presentation is provided. For example, all ROIs are depicted w. r. t. the original images (slices) they are embedded in. Note two things: First, this four-field *viewer* setup is mimicking the software toolbox for our clinical colleagues use (cf. Fig 2.14c). Secondly, the values employed for the first detailed ROI presentation on top were taken from the aforementioned *Jane Doe* case from Table 7.2.

The original medical images were provided and used here with permission by Philipp Genseke.

7.5 ABSTRACTED THORACIC LYMPH NODE STATIONS

In this section, the two aforementioned *extensions* of the first approach are discussed in more detail (cf. Fig. 7.10). Originally, LNSs were encoded via airway geometry which resulted in a strong anatomical (≈ geometrical) abstraction [501] (cf. Fig. 7.5). The degree of photometric abstraction was also rather high, since *only* diffuse shading was used, which, however, emphasizes gaps between LNSs (cf. Fig. 7.5b). Since no 4D image data was used, there was no temporal abstraction and scale-wise, rather gross anatomy is visualized.

FROM 3D MESHES TO 2D PROJECTIONS. The upper LNSs are represented by dividing the tracheal surface mesh, whereas *lower* LNSs, i. e. 10L/R and beyond, are abstracted by tubes with fixed radii. Thus, it is challenging to see and/or create gaps between adjacent LNSs, which can affect the *reading* experience negatively. Similar to the map-based approach to visualize transpedicular instrument pathways for RFA interventions (cf. Fig. 5.10a), we translated the previously obtained meshes into a coronal projection-based representation (see Fig. 7.10). This was done with a MIP and subsequent manual corrections to create clear boundaries around LNSs. On the one hand, this resulted in *map-like* presentations with no occlusion artifacts and well-distinguishable LNSs. On the other hand, due to the MIP-based approach, certain LNSs, such as 10R, do not align with

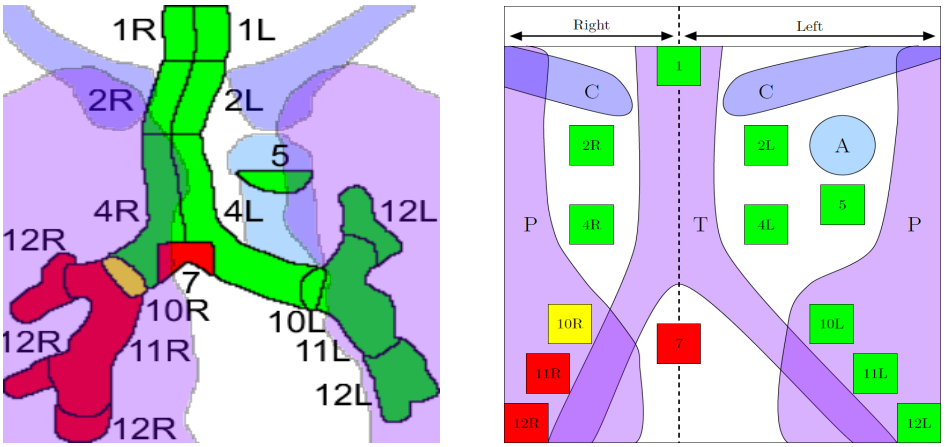

(a) **(b)**

Figure 7.10: In addition to employ meshes to visualize LNS-specific diagnoses (cf. Fig. 7.5), two other approaches were developed. The projection-based approach depicted in Subfigure **(a)** was aimed to simplify said mesh-based approach, e. g. by addressing eventual occlusion artifacts in 3D. This approach was refined by *translating* it into a further simplified `TikZ`-based presentation. Here, LNSs are no longer encoded via airway anatomy and the spatial arrangement between LNSs and orientation-supporting anatomical landmarks, namely the **A**orta, the **C**laviculae, the **P**arenchyma and **T**rachea, is more regular **(b)**. Moreover, the LNSs 1L/R were merged to simplify the presentation of supraclavicular metastases.

Image **(b)** was originally published in the proceedings of the German Society of Computer- and Robot-Assisted Surgery [321, Fig. 1 (left)].

their true anatomical position (cf. Tab. 7.1). Since the presentation is static, this issue was somewhat addressed by *hard-coding* an LNS legend into the image.

From an abstraction perspective, this approach increases the degrees of geometric and photometric abstraction, since less anatomical details are preserved and only a flat-shaded color-coding is employed. However, LNSs are still encoded via airways.

FROM 2D PROJECTIONS TO 2D MAPS. The major downside of the projection-based approach was the large amount of manual processing required to create and separate LNSs. To address this issue and to further streamline the previously presented LaTeX report generation pipeline, we designed a `TikZ`-based map layout. Moreover, this gave us more *control* about the color-coding process (read below). A map-like layout was chosen to exploit the previously described cognition-supporting capabilities of maps, e. g. to provide spatial orientation in complex environments at a glance (cf. Sec. 4.3). However and in contrast to the aforementioned statements to enable users to tailor the GUI and reports, it would be challenging to include these `TikZ`-based maps in the GUI, since they would have to be created before they can be presented. In other words, for all other presentations, the patient-specific LNS color-coding can be adapted interactively, whereas the `TikZ` map would have to be created first, which would result in waiting times and would hinder the interactive nature of the proposed application. If this would be deemed feasible, however, the resulting image could be imported in MeVisLab and included into the GUI.

Compared to the previously presented approaches, such maps both increase and decrease the degree of geometric abstraction. On the one hand, instead of representing LNSs via airway anatomy, LNS diagnoses are now encoded via color-coded boxes which spatially correspond to the "*regional lymph node classification*" introduced by Mountain and Dresler [344] (cf. Fig. 7.1). On the other hand, the resulting maps only roughly preserve anatomical (≈ geometric) details and the presentations appear slightly less *organic*. To address this, the overall layout was modeled slightly asymmetrical with the left side being slightly wider than the right one. This reflects the asymmetry between the main bronchi with the left one ($\approx 5\,cm$) typically being longer than the right one ($\approx 2\,cm$ to $3\,cm$) [424] (cf. Sec. 6.1). Moreover, the LNSs 1L/R were merged, since it is more important to convey *that* there exist supraclavicular cancer infiltrations instead of exactly *where*. This piece of information becomes more important during the actual intervention planning, e. g. for thoracic and/or ear-nose-throat surgeons.

7.6 COLOR-CODING FOR LYMPH NODE STATIONS AND PET/CT IMAGES

Our clinical colleagues inspired us to employ a traffic light-like color-coding to convey LN disease patterns. This color scheme is easy to interpret and supports the process of making distinct and clear decisions, for example w. r. t. diagnoses (cf. Sec. 5.3.4). Still, to provide spatial orientation and interpretation support, anatomical landmarks have to be employed, too. In our first approach and similar to the color-codings for the floor maps from Chapter 4, these landmarks were color-coded more *realistically*, e. g. by assigning a brownish color to the claviculae and a *rich* red color to the aorta (cf. [485] and Fig. 7.5a).

Although this results in an organic appeal, it also results in a color *overlap* w. r. t. malignant LNSs (red vs. red). The risk to mistake LNSs and the aorta is rather small, but since

- colors can be changed interactively, i. e. more *color overlaps* can be introduced and
- some LNSs have strong spatial connections with said landmarks, e. g. LNS 5 with the aorta and LNSs 10L/R with the lungs' hila,

this risk cannot be ruled out. To address this, a color-coding approach to automatically alter all structures' colors if one is changed was developed. Moreover, ROI color scales in diagnostic toolboxes are hard-coded and employ colors that are similar to color scales for, e. g., PET/CT superimpositions (cf. Fig. 7.6). Thus, we also developed a color-coding method with various features, such as defining color schemes that do not introduce *color overlaps* between combined PET/CT images and ROIs while also introducing *large* color differences between subsequently defined ROIs (cf. Fig. 7.6). For usability reasons, the HSV color model was employed (cf. Fig. 7.7), which will be discussed in Section 7.7.

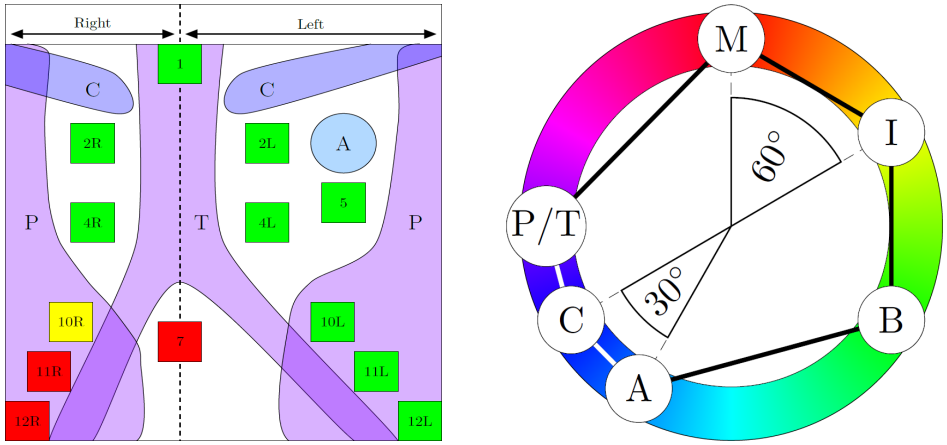

(a) **(b)**

Figure 7.11: The aforementioned map-based visualization approach to depict thoracic LN diseases w. r. t. the proposed color-coding of LNS diagnoses and anatomical landmarks **(a)**. The key hues in the color wheel represent the colors for the LNSs diagnoses, namely **M**alignant, **I**nconclusive and **B**enign, and the aforementioned anatomical landmarks. These *groups* are color-coded in a complementary manner. Thus, when a traffic light-like color scheme for LNS diagnoses is employed, the landmarks are presented in non-attention-drawing blueish shades. If one color is changed, the implied color hexagon on the right is *rotated* while preserving the denoted hue differences of 30° and 60° (cf. Fig. 7.7), respectively **(b)**.

Images were originally published in the proceedings of the German Society of Computer- and Robot-Assisted Surgery [321, Fig. 1].

7.6.1 LYMPH NODE STATIONS AND ANATOMICAL LANDMARKS

To color-code LNSs in the previously presented visualization approaches, a traffic light-like – and also somewhat risk-like – color scheme was used. Since the traffic light colors were inspired by our clinical colleagues, they were treated as key features. In other words, they were treated as being unchangeable, and thus, the proposed method was primarily developed to derive landmark-related color scales w. r. t. LNS color scales. With respect to the aforementioned HSV color model, this results in hue differences of 60° for the LNSs. Inspired by the *Y-shaped* harmonic color "*triad*" described by Itten [209, p. 73], the colors of the anatomical landmarks were defined in a complementary manner. Here, hue differences were decreased to 30°, which results in all landmarks being shaded in blueish colors that are non-attention-drawing but still distinguishable. Note that the colors of the parenchyma and trachea are identical

- to highlight that they (somewhat) belong to the same anatomical structure and
- to minimize the overall number of colors in areas where the lung parenchyma and primary bronchi overlap (cf. Fig. 7.11a).

In combination, these key hues result in an irregular hexagon (cf. Fig. 7.11b).

As mentioned before, all colors can be changed interactively. However, we assumed the aforementioned hue differences to be adaptable but generally fixed. Thus, to preserve its shape, the whole hexagon *changes* if one color is changed. With respect to the HSV color model, three components of a color can be changed and each component-related change is propagated to all other colors (key hues) as follows:

- If the hue is changed, the hexagon is rotated.
- If the saturation is changed, the hexagon is scaled, i. e. the distances between the hexagon's vertices (key hues) and HSV cylinder's middle (value) axis are changed.
- If the *value* (*lightness*) is changed, the hexagon is translated up and/or down along the HSV cylinder's value axis.

Moreover, the anatomical landmarks' opacities can be altered independently via GUI *thumbwheels* (cf. Fig. 7.7).

7.6.2 PET/CT SUPERIMPOSITIONS AND REGIONS OF INTEREST

Our clinical colleagues provided us with an LNS-specific (diagnostic) patient database and according PET/CT images. Additionally, these images also included screenshots from the employed *Siemens Syngo VG51C* toolbox which depicted manually defined ROIs and therefrom derived key values (cf. Fig. 7.9). Upon analyzing these ROIs, we found that the employed color scheme heavily employs certain hue ranges which *overlap* with the black-red-yellow-white color scale of PET/CT superimpositions (see Fig. 7.12). This can result in ambiguous color impressions, which can prolong the search for ROIs on screen and paper. Moreover, this also hinders or even prevents an accurate reconstruction of ROIs, which, e. g., is crucial to reproduce and assess SUVs and their computation. Said toolbox addresses this problem by additionally presenting color-coded ROIs on grayscale PET

images (cf. Fig. 7.9). However, we aimed to develop a color-coding method that makes ROIs well visible on color-coded PET images while no *color overlaps* are introduced.

For simplification purposes, it is assumed that the saturation and value of the resulting ROI colors are equal to 1. However, w. r. t. the aforementioned color-coding hexagon, the resulting colors could be adapted accordingly. Basically, the proposed method can be expressed by two equations that depend on various key parameters, namely

- N, which is the number of ROIs users define,
- $t(N)$, which is the *type* of N that denotes if N is
  - even (e),
  - odd (o),
  - a prime with an even rest for $N-1$ (e. g. 5; pe) or
  - a prime with an odd rest for $N-1$ (e. g. 7; po),
- B_H and M_H, which are the hues of the benign and malignant color-codings, and
- R_H with $R_H = 360 - min(\overline{B_H M_H})$, which is the maximum distance between the benign and malignant color-coding, but also the hue range in which the resulting ROI colors will be defined in.

#	Name	H	S	V
1	Green	120	1	1
2	Cyan	180	1	1
3	Magenta	300	1	1
4	Yellow	60	1	1
5	Dark Red	0	1	0.5
6	Brown	30	1	0.5
7	Dark Magenta	300	1	0.5
8	Orange	30	1	1
9	Pink	330	1	1
10	Purple	270	1	1
11	Light Magenta	300	0.5	1
12	Teal	180	0.5	0.5
13	Gray	240	0.2	0.75

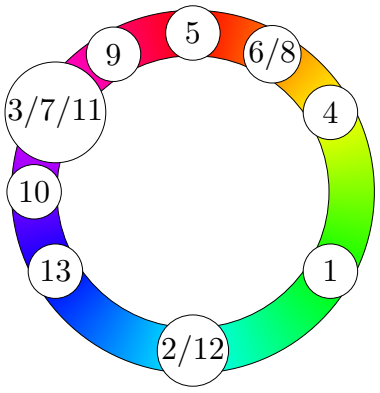

Figure 7.12: The first thirteen HSV colors that the *Siemens Syngo VG51C* employs to color-code ROIs. The table lists the manually reconstructed HSV-encoded ROI colors, whereas the color wheel depicts how often certain hue ranges are (not) employed. With respect to the typical black-red-yellow-white PET/CT in Siemens toolboxes, roughly one third of these ROI colors *overlap* with the PET images.

Table and Image were originally published in the proceedings of the German Society of Computer- and Robot-Assisted Surgery [321, Fig. 2 (middle & right)].

Moreover, note that we assume that red is defined at the 12 o'clock position with $M_H = 0°$ and that the hue *increases* in clockwise direction. With these key values, for a certain region of interest segmentation ROI_i, its hue color $(ROI\boldsymbol{C}_i)_H$ is defined by

$$(ROI\boldsymbol{C}_i)_H = B_H + \left(\frac{R_H}{(N+1)} \times step_{t(N)}(\boldsymbol{C}_i) \right) \tag{7.1}$$

with $i \in [1, N]$. Note two things: First, the $\times$-operator does not denote a scalar multiplication (read below). Secondly, the $step$ function at the end, which is the second of the two aforementioned functions, depends on $t(N)$. Thus, there exist four different $step$ functions:

$$step_e(\boldsymbol{C}_i) = \left(1 + \sum_{j=1}^{i-1} \begin{cases} 4 & , \text{if } j = \frac{N}{2} \\ 2 & , \text{otherwise} \end{cases} \right) \bmod (N+1) \tag{7.2}$$

$$step_o(\boldsymbol{C}_i) = \left(1 + \sum_{j=1}^{i-1} \begin{cases} maxPF(N)+2 & , j \bmod \left(\frac{N}{maxPF(N)} \right) = 0 \\ maxPF(N) & , \text{otherwise} \end{cases} \right) \bmod (N+1) \tag{7.3}$$

$$step_{pe}(\boldsymbol{C}_i) = \left(1 + \sum_{j=1}^{i-1} \begin{cases} \frac{N+1}{2}+2 & , \text{if } isEven(j) \wedge j < \frac{N-1}{2} \\ \frac{N-1}{4}+1 & , \text{if } j = \frac{N-1}{2} \\ \frac{N-1}{4}+2 & , \text{if } j = \frac{N+1}{2} \\ \frac{N+1}{2}+2 & , \text{if } isOdd(j) \wedge j > \frac{N+1}{2} \\ \frac{N-1}{2}+2 & , \text{otherwise} \end{cases} \right) \bmod (N+1) \tag{7.4}$$

$$step_{po}(\boldsymbol{C}_i) = \left(1 + \sum_{j=1}^{i-1} \begin{cases} \frac{N+1}{2}+2 & , \text{if } isEven(j) \wedge j < \frac{N-1}{2} \\ \frac{3N-1}{4} & , \text{if } j = \frac{N-1}{2} \\ \frac{3(N+1)}{4} & , \text{if } j = \frac{N+1}{2} \\ \frac{N+1}{2}+2 & , \text{if } isOdd(j) \wedge j > \frac{N+1}{2} \\ \frac{N-1}{2}+2 & , \text{otherwise} \end{cases} \right) \bmod (N+1) \tag{7.5}$$

Note that the $maxPF(N)$ function in $step_o(\boldsymbol{C}_i)$ is a supporting function that returns the **max**imum value for N's **P**rime **F**actorization, e. g. 7 for 21. For demonstration purposes, in Figure 7.13, the resulting hues for $step_{t(6)}(\boldsymbol{C}_i)$ are listed. A larger compilation for various Ns can be found in Figure 7.14 and a direct comparison between the reference (Siemens toolbox) and our ROI color scales can be seen in Figure 7.15.

To explain the proposed ROI color-coding approach and its results, an important assumption has to be made: It is known *beforehand* how many ROIs a user will define before a report is generated. Of course, during PET/CT image assessment, this is challenging if not impossible. However, given that *we* knew that, e. g. a user defined 6 ROIs, the results of the $step_{t(N)}(\boldsymbol{C}_i)$ functions can be interpreted as follows:[5] $step_6(1)$ would be evaluated to

$$step_6(1) = \left(1 + \sum_{j=1}^{0} \right) \bmod 7 = 1 \bmod 7 = 1$$

[5]For simplification purposes, we rewrite $step_{t(N)} = step_e$ for $N = 6$ to be $step_6$.

Thus, the first ROI's hue would be defined on the first key hue position. In contrast, $step_6(4)$ would be evaluated to

$$step_6(4) = \left(1 + \sum_{j=1}^{3}\right) \bmod 7 = (1+2+2+4) \bmod 7 = 2$$

When reading the equation from left to right ($4 \rightarrow 2$), this result can be interpreted as "*the 4-th key hue (position) is assigned to the 2nd ROI (hue)*". In contrast, when reading from right to left ($2 \rightarrow 4$), the result states that "*the hue of the 2nd ROI is defined on the 4-th key hue position*". This also highlights why the $\times$-operator from Equation 7.1 is not a standard multiplication. From an implementation point of view, prior to color assignment, Equation 7.1 should be evaluated for all ROIs. Subsequently, a `find`-like function is used to ascertain the key hue positions for all ROI hues.

In the application's current version, we address the issue with not being able to know the number of ROIs beforehand by setting a default number of ROIs beforehand, i. e. nine (cf. Fig. 7.6). If more or less ROIs are created, the color-coding is adapted interactively. Nine was chosen since our clinical colleagues most often defined around five to six ROIs in the

		Hue for i-th $(ROIC_i)_H$					
B_H	R_H	1	2	3	4	5	6
120	240	154	257	189	291	223	326

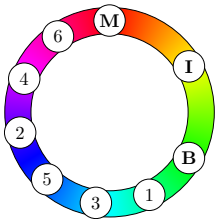

Figure 7.13: Resulting hues for $(ROIC_i)_H$ by applying $step_{t(6)}(C_i)$. To interpret the color wheel, note that the $step_{t(N)}$ functions return the key hue position for the i-th HSV color wheel position. For example, given that a user defined 6 ROIs prior to report generation: "*Which ROI is defined on the 3-th key hue position? The 5th.*".

Table and Image were originally published in the proceedings of the German Society of Computer- and Robot-Assisted Surgery [321, Tab. 1 & Fig. 3 (right)].

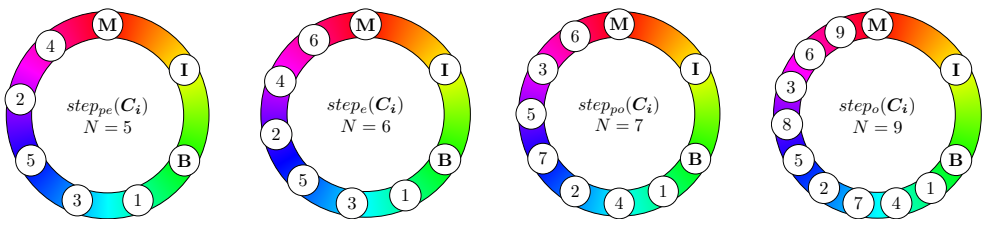

Figure 7.14: Results for various Ns using the proposed ROI color-coding method.

Images were originally published in the proceedings of the German Society of Computer- and Robot-Assisted Surgery [321, Fig. 3 (right)].

provided image data. Due to the straightforward GUI scripting capabilities of MeVisLab, the presented GUI could easily be extended to handle more ROIs [406].

7.7 DISCUSSION

In this section, the approaches and results from this chapter will be discussed.

COLOR-CODED ROIS. One could argue that the proposed $step_{t(N)}$ equations are very complex and that the HSV color wheel could *just* be sampled in a linear and equidistant manner. This would be possible, but the proposed equations have certain features: For example, for subsequently user-defined ROIs, e. g. for the 4th and 5th, there is some *color difference* (see Fig. 7.6). For demonstration purposes, see this color progression for $N = 9$

with the numbers denoting the n-th ROI that the respective key hue was assigned to (cf. Figs 7.8 and 7.14). Note how the color progression has a rough green-blue-red pattern which repeats itself. Thus, subsequently defined ROIs are well-distinguishable. In contrast, for the first nine reference ROI colors, the analyzed toolbox creates this color progression

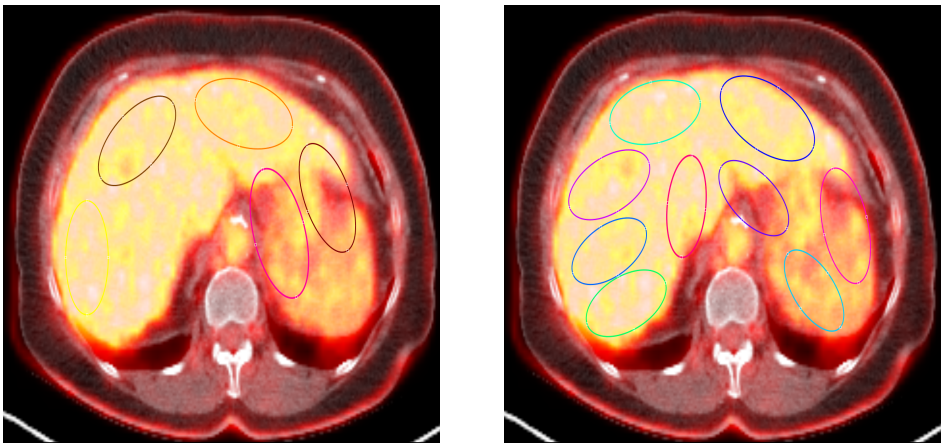

(a) **(b)**

Figure 7.15: A comparison between certain original ROI colors from the *Siemens Syngo VG51C* toolbox **(a)** and the proposed ROI color-coding **(b)**. For our approach, N was set to 9 and all ROIs are well visible. For the reference screenshot, five ROIs were drawn that *overlap* with the PET image color scale. The yellowish ROI in the left part of the liver is virtually invisible. The dark reference ROIs are well visible due to the *homogeneous metabolism* of the liver, but if they would encompass small solitary hotspots, their visibility would be heavily comprised, too.

The original images were provided and used with permission by Philipp Genseke.

which is a categorical color scale with a relatively homogeneous color progression in the mid and end parts (cf. [67]). This design choice was introduced since lung cancer is often found in an already progressed state, which can result in the necessity to define multiple ROIs in a relatively small anatomical region (cf. Fig. 7.8). Moreover, we assumed that during diagnoses physicians would *only* assess image regions in greater detail, e. g. to derive SUVs, that would subsequently be diagnosed as *inconclusive* or *malign*. Due to the black-red-yellow-white color-coding for PET images from the Siemens toolbox, which includes M_H, reddish colors are only assigned to *late* ROIs. For a similar reason, B_H is included into the ROI color-coding method, since we aimed to minimize the risk of introducing interpretation errors by reusing the previously used colorization of benign with at least inconclusive diagnosed LNs and/or LNSs now.

Overall, the $step_{t(N)}$ functions color-code ROIs in a manner that they do not *overlap* with color-coded modalities while minimizing the risk of introducing interpretation mistakes w. r. t. other color scales (cf. Fig. 7.15). Coincidentally, the Siemens toolbox's and the traffic light color-codings overlap, but the methods can be tailored to other modalities and toolboxes, e. g. to the black-blue-yellow-white color scales from GE Healthcare toolboxes. However, with decreasing similarity between the LNS diagnoses' and modalities' color scales, R_H becomes smaller, and thus, ROI colors become more similar. Similarly, with an increasing number of ROIs, ROI colors become more similar w. r. t. each other and the malign and benign color-coding. If necessary, *hue safety margins* can be employed to bring R_H *further away* from M_H and B_H.

COLOR-RELATED EXTENSION IDEAS. There exist various color-related limitations and extension ideas, and thus, they are compiled here:

- The HSV color model was chosen for perceptual reasons, since the respective color wheel (*cylinder*) can be intuitively used. In contrast to certain other color models, such as CIELAB, the HSV color model is not perceptually uniform, i. e. identical distances between color pairs are not perceived as identical distances. Employing such color models could potentially enhance the proposed methods, for example w. r. t. the *lightness* of colors (≈ S and V for HSV), but a simple color wheel is easier to use than a *shoe sole* (CIE), for example (cf. [124, 290]).
- Clinical toolboxes enhance color-coded images by various ROI-specific key values, such as the encompassed volume or derived SUVs, in the viewers themselves. Thus and w. r. t. the black and white viewer backgrounds, these key values are often hard to read in at least one viewer. It would be interesting to extend the proposed methods by limiting R_H to colors that would not only fulfill the aforementioned features, but also result in color schemes that are well-readable on *any* background color.
- Colors are very strong visual cues. With respect to color-coded LNSs, landmarks could just be rendered in grayscale or outlines to omit any attention-drawing potential. Although this is an option, the basic idea of the proposed technique can be applied to virtually any other anatomical region. In other words, by combining the traffic light metaphor with the triad color harmony approach from Itten [209],

  - the risk of employing attention-drawing colors for anatomical landmarks is limited, since they are encoded in the blueish hue range and
  - due to the 30° hue differences between landmarks, they are still distinguishable from each other.

  However, with more landmarks, this feature becomes harder to maintain.

- Disregarding which color-coding approach and/or method would actually be employed to colorize LNSs and/or ROIs, color vision deficiencies should be addressed [206, 253]. The currently implemented methods, however, do not do so.

ANATOMICAL ABSTRACTION. The individual degrees of geometric abstraction of the proposed presentation approaches were already compared and discussed (cf. Sec. 7.5). However, the proposed techniques have a certain limitation w. r. t. anatomical abstraction: On the one hand, all of the presented techniques encode parenchyma-related metastatic infiltrations in LNSs, i. e. for the stations 10L/R and above. However, they do not encode the corresponding lung lobe which an abnormality was found in, which is

- already included in established clinical (case) reports and
- is an important key feature that influences, e. g., treatment decisions.

This could be addressed by employing nodule and lung lobe segmentation methods, e. g. from Kuhnigk et al. [262, 263] and Liu et al. [295]. For example, the LNSs' tokens could be extended, e. g. by denoting infiltrations in the **U**pper lung lobe via 12L/U (cf. Tab. 7.1). Similarly, the proposed application could be extended towards the T and M staging categories. As depicted in Figure 7.7, this was already done implicitly, i. e. by offering users a text-based interface to alter the proposed N staging. However, since this field's contents are directly included into resulting reports (cf. Fig. 7.8), users can manually add further information about the other categories. Overall, this step could be *automated* somehow, but many detection, segmentation and assessment algorithms would have to be combined, e. g. to provide an automated staging and treatment decision support (cf. [145]).

GENERAL APPLICABILITY. The presented approaches and methods within this chapter were discussed w. r. t. PET/CT images. Their basic ideas and principles, however, can be applied to virtually any combination of color-coded modalities as long as segmentations can be carried out and/or segmentation-like representations of *focus and context* structures can be created. The color-coding methods are not applicable to monochrome (grayscale) monitors, but since color-coded multimodal images are typically used in nuclear medicine diagnostics, this is not an issue.

CLINICAL APPLICABILITY. For the two key publications which this chapter is based on [321, 322], we closely worked with the local university clinic for nuclear medicine. The approaches from the *first* publication were evaluated by the two co-authoring nuclear medicine physicians who stated that the presented ideas would "*be highly useful from a clinical perspective*" [322]. However, their extensions, i. e. the map-like 2D visualizations and the color-coding methods, were not yet evaluated.

For simplification purposes, the proposed color-coding methods were limited to fully saturated and *high value* colors, i. e. they are *vibrant*. This can be problematic in certain situations, such as in *dark theme* GUIs or darkened rooms, which are often used for tumor board meetings. As discussed before, in our approach, users can address this by lowering the S and V channels for visualized entities. Another important aspect is that *we* often purposefully employ color cues to enhance certain *messages*, such as feelings and emotions. From a diagnosis-supporting perspective, encoding infiltrated LNSs via **reddish** colors makes sense, since thoracic and/or mediastinal LN diseases should be conveyed and perceived *at a glance*. However, in more *emotional* situations, such as doctor-patient consultations (cf. [193]), very vibrant colors and/or colors that naturally can carry strong messages ("***red means bad***"), should be avoided

- to prevent misconceptions, even if the underlying clinical message may be true, and
- to prevent mental blockades in patients, which can negatively affect their understanding process and/or compliance for further treatment.

A (visualization-enhanced) presentation in grayscale might be beneficial.

7.8 SUMMARY

In this chapter, we introduced the following concepts:

- A processing pipeline to create visualization-enhanced clinical (case) reports,
- various 2D and 3D abstraction approaches, i. e. via
  - 3D airway anatomy and/or geometry in IVRs,
  - planar projections, e. g. on the coronal image plane, and
  - 2D stylized map-like presentations,

  to convey lung cancer-related mediastinal LN disease patterns and
- two color-coding methods that
  - emphasize these disease patterns w. r. t. color-coded and exploration-support providing anatomical landmarks and
  - that create color schemes for ROIs that do not *overlap* color-wise with superimpositions of multimodal medical images.

These approaches were developed to enhance typical text- and table-only clinical reports. Such reports represent patients and their ailments objectively, but they do not reflect the inherent visual nature of certain clinical disciplines, such as nuclear medicine and radiology, and do not exploit *our* visual capabilities [394, 488]. Certain parts of the proposed methods were evaluated and "*deemed to be highly useful from a clinical perspective*" [322], e. g. to simplify (case) report generation in general and to enhance interdisciplinary communication between experts from various clinical disciplines. Limitations and extensions, for example w. r. t. the employed color scales and the automatic detection and/or pre-segmentation of physiological abnormalities (cf. [136]), were discussed. If they would

be addressed, the proposed application could be evaluated in a *real* clinical setting, e. g. to support the reporting for a small clinical case study. With respect to this thesis title, all methods were inspired and developed around color-coded superimpositions of PET/CT images in the anatomical context of the lung. However, this is not a limitation, since the basic ideas can be tailored to virtually any other combination of modalities, color scales from various toolboxes and anatomical regions.

In the next chapter, the contents of this thesis are summarized, while contributions, limitations and extension ideas are highlighted.

8 CONCLUSION

With this chapter, this thesis is concluded. Here, visualization techniques and approaches for multimodal medical images that offer exploration and assessment support for several clinical domains, namely anatomy education, interventional radiology, and the documentation of, e. g. findings and diagnoses, were presented.

In Chapter 2, a background on multimodal medical imaging was provided. Here, the physical phenomena of electromagnetic radiation and magnetism were explained and how they are utilized to acquire images of our bodies and inlying processes. First, mono-modality imaging devices, e. g. CT, PET and MRI scanners, were introduced, while subsequently the advantages of combined scanning units that, for example, typically improve the overall acquisition times were highlighted. Each modality was introduced with a short historical description, while the future of multimodal medical imaging, i. e. tri-modal imaging units, was briefly presented, too.

Subsequently, visualization techniques for such image sources were presented in Chapter 3. Following the categorization from Lawonn et al. [274], a wide range of techniques was described. Here, especially *Visibility-Driven X of Interest* techniques were discussed in more detail. It was highlighted that a distinct categorization is challenging, since many techniques are often combinations of various approaches. For example, *Smart Visibility* and *Focus and Context* are sometimes hard to distinguish. With respect to further research, we refer to the works of Jönsson, Jung, Ljung, and Sunden et al. [221, 226, 297, 464].

8.1 MAPS FOR GROSS ANATOMY

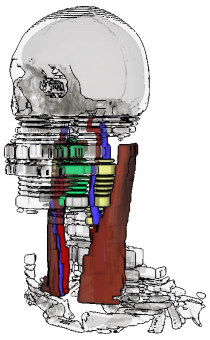

In Chapter 4, a novel visualization technique was presented that transforms pre-labeled medical image stacks into a 3D map layout, namely floor maps. Related visualization methods, for example for digital multi-story maps, were presented. Other aspects, such as *our* cognition of maps and color schemes for medical image and map visualizations, were also briefly discussed. Although there already exist techniques that employ maps or map-like depictions to convey information, the main novelty of our approach is that building-like representations can be created. The method was evaluated by three trained anatomy experts who revealed the potential of floor maps w. r. t. various clinical disciplines, such as anatomy teaching, but also limitations, for example w. r. t. visual clutter. This could be addressed by re-merging *floors* and/or rooms in regions with comparatively low degrees of

anatomical variability. Moreover, it was also presented how physiological hotspots could be used in a so-called *lights out* mode to potentially draw user attention at a glance.

8.2 RISK VISUALIZATIONS FOR RFAS IN THE SPINE

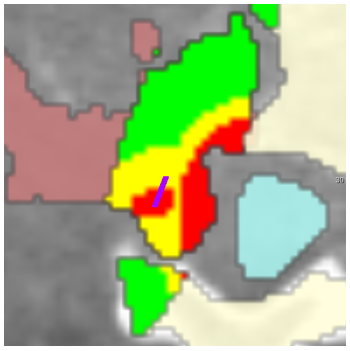

Subsequently, in Chapter 5,

- a requirement analysis and prototypical implementation for computer- and robot-assisted RFAs and
- a two-step risk assessment method for pathway definitions and creations

were presented. The main goal of Step 1 of this method is to offer cognitive support to find *good*, i. e. clinically feasible, instrument pathways by enhancing 2D and 3D visualizations by certain *risk aspects*. Two neuroradiologists acknowledged the potential of the presented techniques, but they also argued that these techniques would have to be evaluated in a real clinical setting. The findings related to Step 2 are primarily aimed to offer physical assistance during robot-assisted drill insertion. Currently, only little to no physical assistance is offered to physicians (cf. [40]), and thus, robotic assistance would offer promising prospects, such as tremor-free and constrained motions [173, 444]. A so-called stiffness criterion ρ was introduced to derive drilling force changes from image intensity changes. During interventions, this could be utilized as a key feature, e. g., to validate drill positions w. r. t. pre-interventionally estimated drilling forces. However, these findings are results of observations alone and a more in-depth evaluation is necessary to deepen the understanding about the relationship of X-ray-based image intensities and drilling forces. Note that although the chapter is focused on robotic assistance, the presented findings could already provide assistance in manually conducted needle-based interventions, e. g. by enhancing 2D images via 3D color-coded safety margins to risk structures.

8.3 ILLUSTRATIVE VISUALIZATIONS FOR SIRTS IN THE LUNG

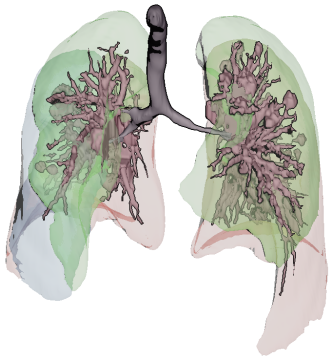

In Chapter 6,

- an illustrative visualization technique which combines OITs, boundary enhancements and silhouettes, and
- the LANCELOT method which enhances lung blood vessels in low-dose CT images

to assist the intervention planning and assessment of SIRTs in the lung were presented. Similar to RFAs, intervention planning for SIRTs is primarily based on the physician's experience to assess multimodal images, for example w. r. t. various target organ compartments and potential (catheter) pathways. Therefore, we aimed to enhance standard 2D PET/CT color superimpositions by illustrative 3D visualizations to cognitively support physicians

- to perceive PET hotspots in their morphological context and

- to examine *radiation patterns* during intervention assessment to evaluate if the employment of radio-labeled embolization media was successful.

Overall, the proposed technique was evaluated to be feasible for these tasks by nine clinical and visualization domain experts. Note that although the individual parts of the visualization technique were not novel themselves [33, 130], their combination and evaluation in the context of interventional radiology were.

Furthermore, the so-called LANCELOT method was introduced which enhances pulmonary blood vessels in low-dose CT images that are often compromised by image noise. This was done to enhance the diagnostic and intervention planning capabilities of said modality w. r. t. catheter-based interventions, such as SIRTs. The method was evaluated by two clinical experts who revealed the method's potentials, e. g. its capability to especially enhance small vessels and branchings, but also conceptional limitations that could be addressed, e. g., by employing 3D instead of 2D *sticks* to also enhance vessels that progress in inferior/superior direction.

8.4 REPORT GENERATION FOR LYMPH NODE METASTASES

In Chapter 7,

- a processing pipeline to create visualization-enhanced clinical (case) reports,
- various 2D and 3D abstraction approaches to convey mediastinal LN disease patterns and
- color-coding methods for these disease patterns, anatomical landmarks and ROIs in color-coded multimodal superimpositions

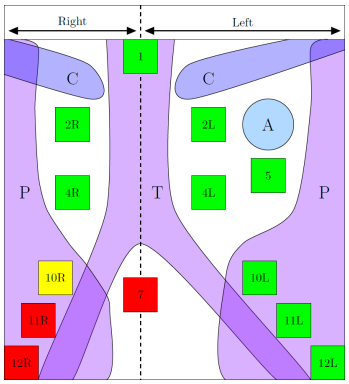

were presented. These approaches were developed to enhance typical text- and table-only clinical reports. Such reports represent patients and their ailments objectively, but they do not reflect the inherent visual nature of certain clinical disciplines, such as nuclear medicine and radiology, and do not exploit *our* visual capabilities [394, 488]. Certain parts of the proposed methods were evaluated by two nuclear medicine physicians and were "*deemed to be highly useful from a clinical perspective*" [322], e. g. to simplify (case) report generation in general and to enhance interdisciplinary communication between experts from various clinical disciplines. Especially color-related limitations were discussed, e. g. employing the perceptually uniform CIELAB instead of the HSV color model, which, if addressed, could further enhance the proposed methods. These methods were also presented w. r. t. combined PET/CT images, but they can virtually be applied to any other combination of modalities and/or color scheme for color-coded superimpositions.

8.5 VISUALIZATION-BASED COGNITIVE SUPPORT

All findings and results presented and discussed in this thesis have a *common denominator*: They do not aim to replace established visualization and/or assessment facilities in clinical practice, i. e. they are intended to enhance them in certain ways. For example, it was

shown that floor maps and volume-based distance fields can be used to enhance 2D image assessment. Nearly all concepts, approaches and techniques presented within this thesis were evaluated by physicians and/or clinical experts.[1] Although the general feedback was almost always positive, virtually all interviews were conducted in a qualitative and informal manner, e. g. in think-aloud settings or (interactive) questionnaires. On the one hand, this revealed the potentialities and limitations of the respective findings. On the other hand, however, it would be interesting to *look beyond* these potentialities by (quantitatively) evaluating the proposed methods in real clinical settings and/or workflows. This could reveal how they really affect – and are affected by – clinical practice and reality. Even, if not especially, in surprising ways.

[1] Note that less than half of all interviewees co-authored the resulting publications (cf. [382]).

REFERENCES

[1] Abellán, P., Tost, D., Grau, S., and Puig, A. "Regions-Based Illustrative Visualization of Multimodal Datasets." In: *Computerized Medical Imaging and Graphics* 37 (4) (2013), pp. 263–271 (cit. on pp. 39–43, 50).

[2] Abrams, H. L. "Skeletal Metastases in Carcinoma." In: *Radiology* 55 (4) (1950), pp. 534–538 (cit. on p. 105).

[3] Abrams, H. L., Spiro, R., and Goldstein, N. "Metastases in Carcinoma. Analysis of 1000 Autopsied Cases." In: *Cancer* 3 (1) (1950), pp. 74–85 (cit. on pp. 105, 154, 155).

[4] ACR Committee on Drugs and Contrast Media. *ACR Manual on Contrast Media (V. 10.3)*. American College of Radiology, 2018 (cit. on p. 7).

[5] Aerssens, J., Boonen, S., Lowet, G., and Dequeker, J. "Interspecies Differences in Bone Composition, Density, and Quality: Potential Implications for In Vivo Bone Research." In: *Endocrinology* 139 (2) (1998), pp. 663–670 (cit. on pp. 113, 141).

[6] Ahmed, M., Brace, C. L., Lee Jr, F. T., and Goldberg, S. N. "Principles of and Advances in Percutaneous Ablation." In: *Radiology* 258 (2) (2011), pp. 351–369 (cit. on pp. 107–109, 121, 139).

[7] Alakija, T. A., Ijisan, O., Huthman, I., Olaseinde, O., Adenowo, T., Adefule, A., and Huthman, A. "Kerosene: A Substitute For Acetone In Bone Preparations." In: *Poultry Science* 4 (2) (2010), pp. 1–4 (cit. on p. 106).

[8] Albert, M. K. "Occlusion, Transparency, and Lightness." In: *Vision Research* 47 (2007), pp. 3061–3069 (cit. on pp. 167, 168).

[9] Alpers, J., Hensen, B., Wacker, F. K., Rieder, C., and Hansen, C. "MRI-Guided Liver Tumor Ablations – A Workflow Design Prototype." In: *Proc. of German Society of Computer- and Robot-Assisted Surgery*. 2019, pp. 165–170 (cit. on p. 122).

[10] Alsing, K., Johannesen, H., Hvass Hansen, R, Dirks, M, Olsen, O, and Serup, J. "MR Scanning, Tattoo Inks, and Risk of Thermal Burn: An Experimental Study of Iron Oxide and Organic Pigments: Effect on Temperature and Magnetic Behavior Referenced to Chemical Analysis." In: *Skin Research and Technology* 24 (2) (2018), pp. 278–284 (cit. on pp. 16, 122).

[11] Alvarez, G. A. and Cavanagh, P. "The Capacity of Visual Short-Term Memory Is Set Both by Visual Information Load and by Number of Objects." In: *Psychological Science* 15 (2) (2004), pp. 106–111 (cit. on pp. 72, 97).

[12] Ambrose, J. "Computerized Transverse Axial Scanning (Tomography): Part 2. Clinical Application." In: *The British Journal of Radiology* 46 (552) (1973), pp. 1023–1047 (cit. on p. 5).

[13] Anderson, B. L. and Winawer, J. "Image Segmentation and Lightness Perception." In: *Nature* 434 (2005), pp. 79–83 (cit. on pp. 167, 168).

[14] Andrä, W. and Nowak, H. *Magnetism in Medicine: A Handbook*. John Wiley & Sons, 2007 (cit. on pp. 14, 15).

[15] Anger, H. O. "A Multiple Scintillation Counter In Vivo Scanner." In: *The American Journal of Roentgenology, Radium Therapy, and Nuclear Medicine* 70 (4) (1953), p. 605 (cit. on p. 10).

[16] Anger, H. O. "Scintillation Camera." In: *Review of Scientific Instruments* 29 (1) (1958), pp. 27–33 (cit. on pp. 10, 28).

[17] Annink, E. and Bruinsma, M. *Gerd Arntz – Graphic Designer*. nai010 Publishing, 2013 (cit. on p. 67).

[18] Anzenberger, P., Jedinger, O., and Zarhuber, K. "Design and Development of a Multilingual Multimedia Based Presurgical Information and Clarification System for Tablet Computers." In: *Proc. of the International Association for Development of the Information Society Conference on e-Health*. 2012, pp. 253–256 (cit. on p. 43).

[19] Armato III, S. G., McLennan, G., Bidaut, L., McNitt-Gray, M. F., Meyer, C. R., Reeves, A. P., Zhao, B., Aberle, D. R., Henschke, C. I., Hoffman, E. A., Kazerooni, E., MacMahon, H, Van Beeke, E., Yankelevitz, D, Biancardi, A., Bland, P., Brown, M., Engelmann, R., Laderach, G., Max, D, Pais, R., Qing, D., Roberts, R., Smith, A., Starkey, A, Batrah, P, Caligiuri, P, Farooqi, A, Gladish, G., Jude, C., Munden, R., Petkovska, I, Quint, L., Schwartz, L., Sundaram, B, Dodd, L., Fenimore, C, D, G., Petrick, N, Freymann, J, Kirby, J, Hughes, B, Casteele, A., Gupte, S, Sallamm, M, Heath, M., Kuhn, M., Dharaiya, E, Burns, R, Fryd, D., Salganicoff, M, Anand, V, Shreter, U, Vastagh, S, and Croft, B. "The Lung Image Database Consortium (LIDC) and Image Database Resource Initiative (IDRI): A Completed Reference Database of Lung Nodules on CT Scans." In: *Medical Physics* 38 (2) (2011), pp. 915–931 (cit. on p. 60).

[20] Ashraf, O., Patel, N. V., Hanft, S., and Danish, S. F. "Laser-Induced Thermal Therapy in Neuro-Oncology: A Review." In: *World Neurosurgery* 112 (2018), pp. 166–177 (cit. on p. 109).

[21] Augustin, G., Davila, S., Mihoci, K., Udiljak, T., Vedrina, D. S., and Antabak, A. "Thermal Osteonecrosis and Bone Drilling Parameters Revisited." In: *Archives of Orthopaedic and Trauma Surgery* 128 (1) (2008), pp. 71–77 (cit. on pp. 113, 146).

[22] Badano, A., Revie, C., Casertano, A., Cheng, W.-C., Green, P., Kimpe, T., Krupinski, E., Sisson, C., Skrøvseth, S., Treanor, D., Boynton, P., Clunie, D., Flynn, M. J., Heki, T., Hewitt, S., Homma, H., Masia, A., Matsui, T., Nagy, B., Nishibori, M., Penczek, J., Schopf, T., Yagi, Y., and Yokoi, H. "Consistency and Standardization of Color in Medical Imaging: A Consensus Report." In: *Journal of Digital Imaging* 28 (1) (2015), pp. 41–52 (cit. on pp. 74, 192).

[23] Baddeley, A. "Working Memory." In: *Current Biology* 20 (4) (2010), R136–R140 (cit. on p. 73).

[24] Baddeley, A. D. and Hitch, G. "Working Memory." In: *Psychology of Learning and Motivation* 8 (1974), pp. 47–89 (cit. on pp. 72, 73).

[25] Bade, R., Konrad, O., and Preim, B. "Reducing Artifacts in Surface Meshes Extracted from Binary Volumes." In: *Journal of WSCG* 15 (1–3) (2007), pp. 67–74 (cit. on pp. 91, 96, 134, 163, 169, 196, 198).

[26] Baegert, C., Villard, C., Schreck, P., and Soler, L. "Multi-Criteria Trajectory Planning for Hepatic Radiofrequency Ablation." In: *Proc. of Medical Image Computing and Computer-Assisted Intervention*. 2007, pp. 676–684 (cit. on pp. 114, 115).

[27] Baert, A. L., Knauth, M., and Sartor, K. *MRI of the Lung*. Springer Science & Business Media, 2008 (cit. on pp. 19–21, 59, 155).

[28] Balabanian, J.-P., Viola, I., and Gröller, E. "Interactive Illustrative Visualization of Hierarchical Volume Data." In: *Proc. of Graphics Interface*. 2010, pp. 137–144 (cit. on pp. 84, 97).

[29] Bale, R., Widmann, G., and Haidu, M. "Stereotactic Radiofrequency Ablation." In: *Cardiovascular and Interventional Radiology* 34 (4) (2011), pp. 852–856 (cit. on pp. 128, 129).

[30] Baltayiannis, N., Chandrinos, M., Anagnostopoulos, D., Zarogoulidis, P., Tsakiridis, K., Mpakas, A., Machairiotis, N., Katsikogiannis, N., Kougioumtzi, I., Courcoutsakis, N., and Zarogoulidis, K. "Lung Cancer Surgery: An Up to Date." In: *Journal of Thoracic Disease* 5 (Supplement 4) (2013), pp. 425–439 (cit. on pp. 190, 194).

[31] Barberis, C., Andrea, B., Giovanni, M., and Paolo, M. "Experiencing Indoor Navigation on Mobile Devices." In: *IT Professional* 16 (1) (2013), pp. 50–57 (cit. on pp. 75, 76, 81).

[32] Barr, J. D., Jensen, M. E., Hirsch, J. A., McGraw, J. K., Barr, R. M., Brook, A. L., Meyers, P. M., Munk, P. L., Murhphy, K. J., O'Toole, J. E., Rasmussen, P. A., Ryken, T. C., Danelli, P. C., Schwartzberg, M. C., Seidenwurm, D., Tutton, S. M., Zoarski, G. H., Kuo, M. D., Rose, S. C., and Cardella, J. F. "Position Statement on Percutaneous Vertebral Augmentation: A Consensus Statement Developed by the Society of Interventional Radiology (SIR), American Association of Neurological Surgeons (AANS) and the Congress of Neurological Surgeons (CNS), American College of Radiology (ACR)." In: *Journal of Vascular and Interventional Radiology* 25 (2014), pp. 171–181 (cit. on p. 111).

[33] Barta, P., Kovács, B., Szecsi, L., and Szirmay-Kalos, L. "Order Independent Transparency with Per-Pixel Linked Lists." In: *Proc. of Central European Seminar on Computer Graphics*. 2011, pp. 51–57 (cit. on pp. 64, 93, 166, 170, 177, 186, 217).

[34] Bashir, U., Mallia, A., Stirling, J., Joemon, J., MacKewn, J., Charles-Edwards, G., Goh, V., and Cook, G. "PET/MRI in Oncological Imaging: State of the Art." In: *Diagnostics* 5 (3) (2015), pp. 333–357 (cit. on pp. 25–27).

[35] Bauer, S., Wiest, R., Nolte, L.-P., and Reyes, M. "A Survey of MRI-Based Medical Image Analysis for Brain Tumor Studies." In: *Physics in Medicine & Biology* 58 (13) (2013), R97–R129 (cit. on p. 21).

[36] Becker, B. C., MacLachlan, R. A., Lobes, L. A., Hager, G. D., and Riviere, C. N. "Vision-Based Control of a Handheld Surgical Micromanipulator With Virtual Fixtures." In: *IEEE Transactions on Robotics* 29 (3) (2013), pp. 674–683 (cit. on p. 122).

[37] Bejnordi, B. E., Litjens, G., Timofeeva, N., Otte-Höller, I., Homeyer, A., Karssemeijer, N., and Laak, J. A. van der. "Stain Specific Standardization of Whole-Slide Histopathological Images." In: *IEEE Transactions on Medical Imaging* 35 (2) (2015), pp. 404–415 (cit. on pp. 74, 192).

[38] Beni, M. S., Krstic, D, Nikezic, D, and Yu, K. "Monte Carlo Studies on Photon Interactions in Radiobiological Experiments." In: *PloS One* 13 (3) (2018), e0193575 (cit. on p. 8).

[39] Benjamin, E. J., Muntner, P., Alonso, A., Bittencourt, M. S., Callaway, C. W., Carson, A. P., Chamberlain, A. M., Chang, A. R., Cheng, S., Das, S. R., Delling, F. N., Djousse, L., Elkind, M. S., Ferguson, J. F., Fornage, M., Jordan, L. C., Khan, S. S., Kissela, B. M.,

Knutson, K. L., Kwan, T. W., Lackland, D. T., Lewis, T. T., Lichtman, J. H., Longenecker, C. T., Loop, M. S., Lutsey, P. L., Martin, S. S., Matsushita, K., Moran, A. E., Mussolino, M. E., O'Flaherty, M., Pandey, A., Perak, A. M., Rosamond, W. D., Roth, G. A., Sampson, U. K., Satou, G. M., Schroeder, E. B., Shah, S. H., Spartano, N. L., Stokes, A., Tirschwell, D. L., Tsao, C. W., Turakhia, M. P., VanWagner, L. B., Wilkins, J. T., Wong, S. S., and Virani, S. S. "Heart Disease and Stroke Statistics – 2019 Update: A Report from the American Heart Association." In: *Circulation* 139 (10) (2019), e56–e528 (cit. on pp. 75, 76).

[40] Berenson, J. R., Yellin, O., Blumenstein, B., Bojanower, D., Croopnick, J., Aboulafia, D., Upadhyaya, G., and Spadaccini, C. "Using a Powered Bone Marrow Biopsy System Results in Shorter Procedures, Causes Less Residual Pain to Adult Patients, and Yields Larger Specimens." In: *Diagnostic Pathology* 6 (1) (2011), p. 23 (cit. on pp. 111, 112, 120, 135, 148, 216).

[41] Bergström, M, Eriksson, L, Bohm, C, Blomqvist, G, and Litton, J. "Correction for Scattered Radiation in a Ring Detector Positron Camera by Integral Transformation of the Projections." In: *Journal of Computer Assisted Tomography* 7 (1) (1983), pp. 42–50 (cit. on p. 13).

[42] Berjano, E. J. "Theoretical Modeling for Radiofrequency Ablation: State-of-the-Art and Challenges for the Future." In: *Biomedical Engineering Online* 5 (1) (2006), pp. 24–1–24–17 (cit. on p. 101).

[43] Berker, Y., Franke, J., Salomon, A., Palmowski, M., Donker, H. C., Temur, Y., Mottaghy, F. M., Kuhl, C., Izquierdo-Garcia, D., Fayad, Z. A., Kiessling, F., and Schulz, V. "MRI-Based Attenuation Correction for Hybrid PET/MRI Systems: A 4-Class Tissue Segmentation Technique Using a Combined Ultrashort-Echo-Time/Dixon MRI Sequence." In: *Journal of Nuclear Medicine* 53 (5) (2012), pp. 796–804 (cit. on p. 27).

[44] Bernstein, M. A., King, K. F., and Zhou, X. J. *Handbook of MRI Pulse Sequences*. Elsevier, 2004 (cit. on pp. 21, 22).

[45] Bertin, J. *Semiology of Graphics: Diagrams, Networks, Maps*. University of Wisconsin Press, 1983 (cit. on pp. 68, 73, 74, 81).

[46] Besançon, L., Semmo, A., Biau, D., Frachet, B., Pineau, V., Sariali, E. H., Taouachi, R., Isenberg, T., and Dragicevic, P. "Reducing Affective Responses to Surgical Images Through Color Manipulation and Stylization." In: *Proc. of the Joint Symposium on Computational Aesthetics and Sketch-Based Interfaces and Modeling and Non-Photorealistic Animation and Rendering*. 2018, pp. 11–1–1–13 (cit. on p. 74).

[47] Beyer, J., Hadwiger, M., Wolfsberger, S., and Bühler, K. "High-Quality Multimodal Volume Rendering for Preoperative Planning of Neurosurgical Interventions." In: *IEEE Transactions on Visualization and Computer Graphics* 13 (6) (2007), pp. 1696–1703 (cit. on pp. 59–61, 75, 164).

[48] Beyer, T., Townsend, D. W., Brun, T., Kinahan, P. E., Charron, M., Roddy, R., Jerin, J., Young, J., Byars, L., and Nutt, R. "A Combined PET/CT Scanner for Clinical Oncology." In: *Journal of Nuclear Medicine* 41 (8) (2000), pp. 1369–1379 (cit. on p. 22).

[49] Bhargava, P., Hanif, M., and Nash, C. "Whole-Body F-18 Sodium Fluoride PET-CT in a Patient with Renal Cell Carcinoma." In: *Clinical Nuclear Medicine* 33 (12) (2008), pp. 894–895 (cit. on p. 12).

[50] Biczok, G., Martínez, S. D., Jelle, T., and Krogstie, J. "Navigating MazeMap: Indoor Human Mobility, Spatio-Logical Ties and Future Potential." In: *Proc. of IEEE International Conference on Pervasive Computing and Communication Workshops*. 2014, pp. 266–271 (cit. on pp. 79, 80).

[51] Bier, E. A., Stone, M. C., Pier, K., Buxton, W., and DeRose, T. D. "Toolglass and Magic Lenses: The See-Through Interface." In: *Proc. of International Conference on Computer Graphics and Interactive Techniques*. 1993, pp. 73–80 (cit. on pp. 46, 68).

[52] Bilchik, A. J., Wood, T. F., Allegra, D., Tsioulias, G. J., Chung, M., Rose, D. M., Ramming, K. P., and Morton, D. L. "Cryosurgical Ablation and Radiofrequency Ablation for Unresectable Hepatic Malignant Neoplasms: A Proposed Algorithm." In: *Archives of Surgery* 135 (6) (2000), pp. 657–664 (cit. on p. 107).

[53] Birkeland, Å. and Viola, I. "View-Dependent Peel-Away Visualization for Volumetric Data." In: *Proc. of the Spring Conference on Computer Graphics*. 2009, pp. 121–128 (cit. on p. 47).

[54] Birr, S., Dicken, V., Geisler, B., Mühler, K., Preim, B., and Stöcker, C. "Interaktive Reports für die Planung von Lungentumoroperationen." In: *Proc. of Mensch und Computer*. 2011, pp. 131–140 (cit. on p. 190).

[55] Birr, S., Dicken, V., Geisler, B., and Preim, B. "3D-PDF: Ein interaktives Tool für das onkologische Reporting und die Operationsplanung von Lungentumoren." In: *Proc. of German Society of Computer- and Robot-Assisted Surgery*. 2011, pp. 11–16 (cit. on pp. 160, 190, 191).

[56] Bischoff, R., Kurth, J., Schreiber, G., Koeppe, R., Albu-Schäffer, A., Beyer, A., Eiberger, O., Haddadin, S., Stemmer, A., Grunwald, G., and Hirzinger, G. "The KUKA-DLR Lightweight Robot Arm – A New Reference Platform for Robotics Research and Manufacturing." In: *Proc. of International Symposium on Robotics and German Conference on Robotics*. 2010, pp. 1–8 (cit. on pp. 123, 124).

[57] Blackett, P. M. S. "The Ejection of Protons from Nitrogen Nuclei, Photographed by the Wilson Method." In: *Proc. of the Royal Society of London. Series A, Containing Papers of a Mathematical and Physical Character* 107 (742) (1925), pp. 349–360 (cit. on p. 10).

[58] Bloch, F. "Nuclear Induction." In: *Physical Review* 70 (7 & 8) (1946), pp. 460–474 (cit. on p. 16).

[59] Bock, A., Lang, N., Evangelista, G., Lehrke, R., and Ropinski, T. "Guiding Deep Brain Stimulation Interventions by Fusing Multimodal Uncertainty Regions." In: *Proc. of IEEE Pacific Visualization Symposium*. 2013, pp. 97–104 (cit. on pp. 59, 61).

[60] Boguslawski, P., Mahdjoubi, L., Zverovich, V., and Fadli, F. "Automated Construction of Variable Density Navigable Networks in a 3D Indoor Environment for Emergency Response." In: *Automation in Construction* 72 (2016), pp. 115–128 (cit. on pp. 75, 81, 82).

[61] Bønaa, K. H., Mannsverk, J., Wiseth, R., Aaberge, L., Myreng, Y., Nygård, O., Nilsen, D. W., Kløw, N.-E., Uchto, M., Trovik, T., Bendz, B., Stavnes, S., Bjørnerheim, R., Larsen, A.-I., Slette, M., Steigen, T., Jakobsen, O. J., Bleie, Ø., Fossum, E., Hanssen, T. A., Dahl-Erisen, Ø., Njølstad, I., Rasmussen, K., Wilsgaard, T., and Nordrehaug, J. E. "Drug-Eluting or Bare-Metal Stents for Coronary Artery Disease." In: *New England Journal of Medicine* 375 (13) (2016), pp. 1242–1252 (cit. on p. 76).

[62] Borkin, M. A., Vo, A. A., Bylinskii, Z., Isola, P., Sunkavalli, S., Oliva, A., and Pfister, H. "What Makes a Visualization Memorable?" In: *IEEE Transactions on Visualization and Computer Graphics* 19 (12) (2013), pp. 2306–2315 (cit. on p. 73).

[63] Bourquain, H, Schenk, A, Link, F, Preim, B, Prause, G, and Peitgen, H.-O. "HepaVision2 – A Software Assistant for Preoperative Planning in Living-Related Liver Transplantation and Oncologic Liver Surgery." In: *Proc. of Computer-Assisted Radiology and Surgery*. 2002, pp. 341–346 (cit. on p. 87).

[64] Bouziotis, P. and Fiorini, C. "SPECT/MRI: Dreams or Reality?" In: *Clinical and Translational Imaging* 2 (6) (2014), pp. 571–573 (cit. on p. 28).

[65] Brady, T. F. and Alvarez, G. A. "No Evidence for a Fixed Object Limit in Working Memory: Spatial Ensemble Representations Inflate Estimates of Working Memory Capacity for Complex Objects." In: *Journal of Experimental Psychology: Learning, Memory, and Cognition* 41 (3) (2015), pp. 921–929 (cit. on p. 72).

[66] Bresenham, J. E. "Algorithm for Computer Control of a Digital Plotter." In: *IBM Systems Journal* 4 (1) (1965), pp. 25–30 (cit. on pp. 127, 180).

[67] Brewer, C. A. "Color Use Guidelines For Mapping." In: *Visualization in Modern Cartography* 1994 (1994), pp. 123–148 (cit. on pp. 73, 74, 97, 211).

[68] Burns, M., Haidacher, M., Wein, W., Viola, I., and Gröller, E. "Feature Emphasis and Contextual Cutaways for Multimodal Medical Visualization." In: *Proc. of IEEE/ Eurographics Symposium on Visualization*. Vol. 7. 2007, pp. 275–282 (cit. on pp. 45, 46, 49).

[69] Busking, S., Botha, C. P., Ferrarini, L., Milles, J., and Post, F. H. "Image-Based Rendering of Intersecting Surfaces for Dynamic Comparative Visualization." In: *The Visual Computer* 27 (5) (2011), pp. 347–363 (cit. on p. 41).

[70] Byars, A. W., Holland, S. K., Strawsburg, R. H., Bommer, W., Dunn, R. S., Schmithorst, V. J., and Plante, E. "Practical Aspects of Conducting Large-Scale Functional Magnetic Resonance Imaging Studies in Children." In: *Journal of Child Neurology* 17 (12) (2002), pp. 885–889 (cit. on p. 21).

[71] Cai, L, Shen, Z., Zhang, J., Chen, C., and Meng, L. J. "First Imaging Result with an Ultrahigh Resolution Stationary MR Compatible SPECT System." In: *Proc. of Nuclear Science Symposium and Medical Imaging Conference Record*. 2012, pp. 3568–3571 (cit. on p. 28).

[72] Cancer, A. J. C. on. *AJCC Cancer Staging Manual*. 7th ed. Springer-Verlag New York, 2010 (cit. on pp. 158, 159, 168, 187, 189, 190, 192, 193).

[73] Carney, J. P., Townsend, D. W., Rappoport, V., and Bendriem, B. "Method for Transforming CT Images for Attenuation Correction in PET/CT Imaging." In: *Medical Physics* 33 (4) (2006), pp. 976–983 (cit. on pp. 9, 24, 25).

[74] Chai, W. J., Abd Hamid, A. I., and Abdullah, J. M. "Working Memory from the Psychological and Neurosciences Perspectives: A Review." In: *Frontiers in Psychology* 9 (2018), pp. 401–1–401–16 (cit. on p. 73).

[75] Cheirsilp, R., Bascom, R., Allen, T. W., and Higgins, W. E. "Thoracic Cavity Definition for 3D PET/CT Analysis and Visualization." In: *Computers in Biology and Medicine* 62 (2015), pp. 222–238 (cit. on pp. 37, 38, 50, 75, 164).

[76] Chen, L. "Architectural Visualization: An Analysis from Human Visual Cognition Process." In: *http://citeseerx.ist.psu.edu/viewdoc/summary?doi=10.1.1.135.3081* (2004) (cit. on p. 81).

[77] Chen, L.-C., Wu, C.-H., Shen, T.-S., and Chou, C.-C. "The Application of Geometric Network Models and Building Information Models in Geospatial Environments for Fire-Fighting Simulations." In: *Computers, Environment and Urban Systems* 45 (2014), pp. 1–12 (cit. on p. 81).

[78] Chen, P and Truc, N. "Computer-Aided Visual Communication for Way-Finding in Emergency in Indoor Environment." In: *Proc. of International Symposium on Automation and Robotics in Construction*. 2008, pp. 440–446 (cit. on p. 81).

[79] Chen, Y.-R., Deb, S., Pham, L., and Singh, H. "Minimally Invasive Lumbar Pedicle Screw Fixation Using Cortical Bone Trajectory – A Prospective Cohort Study on Postoperative Pain Outcomes." In: *Cureus Journal of Medical Science* 10 (10) (2016), e3462 (cit. on pp. 112, 120).

[80] Cherry, S. R., Jones, T., Karp, J. S., Qi, J., Moses, W. W., and Badawi, R. D. "Total-Body PET: Maximizing Sensitivity to Create New Opportunities for Clinical Research and Patient Care." In: *Journal of Nuclear Medicine* 59 (1) (2018), pp. 3–12 (cit. on p. 10).

[81] Chi, A. and Nguyen, N. P. "4D PET/CT as a Strategy to Reduce Respiratory Motion Artifacts in FDG-PET/CT." In: *Frontiers in Oncology* 4 (2014), pp. 205–1–205–4 (cit. on pp. 25, 62).

[82] Chou, C.-C., Chiang, C.-T., Wu, P.-Y., Chu, C.-P., and Lin, C.-Y. "Spatiotemporal Analysis and Visualization of Power Consumption Data Integrated with Building Information Models for Energy Savings." In: *Resources, Conservation and Recycling* 123 (2017), pp. 219–229 (cit. on pp. 76, 77).

[83] Christensen, N., Hammer, B., Heil, B., and Fetterly, K. "Positron Emission Tomography Within a Magnetic Field Using Photomultiplier Tubes and Lightguides." In: *Physics in Medicine & Biology* 40 (4) (1995), pp. 691–697 (cit. on p. 25).

[84] Christodoulou, A. G., Apostolou, T., Ploumis, A., Terzidis, I., Hantzokos, I., and Pournaras, J. "Pedicle Dimensions of the Thoracic and Lumbar Vertebrae in the Greek Population." In: *Clinical Anatomy* 18 (6) (2005), pp. 404–408 (cit. on p. 112).

[85] Chu, K. F. and Dupuy, D. E. "Thermal Ablation of Tumours: Biological Mechanisms and Advances in Therapy." In: *Nature Reviews Cancer* 14 (3) (2014), pp. 199–208 (cit. on pp. 107–109).

[86] Ciompi, F., Chung, K., Van Riel, S. J., Setio, A. A. A., Gerke, P. K., Jacobs, C., Scholten, E. T., Schaefer-Prokop, C., Wille, M. M., Marchiano, A., Pastorino, U., Prokop, M., and Ginneken, B. van. "Towards Automatic Pulmonary Nodule Management in Lung Cancer Screening with Deep Learning." In: *Scientific Reports* 7 (2017), pp. 46479–1–46479–10 (cit. on p. 160).

[87] Clarke, B. "Normal Bone Anatomy and Physiology." In: *Clinical Journal of the American Society of Nephrology* 3 (Supplement 3) (2008), S131–S139 (cit. on pp. 103, 113).

[88] Coleman, R, Body, J.-J., Aapro, M, Hadji, P, and Herrstedt, J. "Bone Health in Cancer Patients: ESMO Clinical Practice Guidelines." In: *Annals of Oncology* 25 (Supplement 3) (2014), pp. iii124–iii137 (cit. on pp. 101, 111, 131).

[89] Coleman, R. "Metastatic Bone Disease: Clinical Features, Pathophysiology and Treatment Strategies." In: *Cancer Treatment Reviews* 27 (3) (2001), pp. 165–176 (cit. on p. 105).

[90] Coleman, R. E. "Bisphosphonates: Clinical Experience." In: *The Oncologist* 9 (Supplement 4) (2004), pp. 14–27 (cit. on pp. 105, 111).

[91] Compton, A. H. "A Quantum Theory of the Scattering of X-Rays by Light Elements." In: *Physical Review* 21 (5) (1923), pp. 483–502 (cit. on p. 9).

[92] Cooper, D. N. *The Molecular Genetics of Lung Cancer*. Springer-Verlag Berlin Heidelberg, 2005 (cit. on pp. 153, 154).

[93] Correa, C. D. and Ma, K.-L. "Visibility-Driven Transfer Functions." In: *Proc. of IEEE Pacific Visualization Symposium*. 2009, pp. 177–184 (cit. on pp. 51–58, 77).

[94] Cowan, N. "An Embedded-Processes Model of Working Memory." In: *Models of Working Memory: Mechanisms of Active Maintenance and Executive Control*. Vol. 20. 1999, pp. 62–101 (cit. on p. 73).

[95] Cox, J. D., Chang, J. Y., and Komaki, R. *Image-Guided Radiotherapy of Lung Cancer*. Informa Healthcare USA, Inc., 2007 (cit. on p. 164).

[96] Croswell, J. M., Baker, S. G., Marcus, P. M., Clapp, J. D., and Kramer, B. S. "Cumulative Incidence of False-Positive Test Results in Lung Cancer Screening: A Randomized Trial." In: *Annals of Internal Medicine* 152 (8) (2010), pp. 505–512 (cit. on p. 155).

[97] Czerwinski, R. N., Jones, D. L., and O'brien, W. D. "Line and Boundary Detection in Speckle Images." In: *IEEE Transactions on Image Processing* 7 (12) (1998), pp. 1700–1714 (cit. on pp. 150, 163, 179, 180).

[98] Dacic, S. "Pros: The Present Classification of Mucinous Adenocarcinomas of the Lung." In: *Translational Lung Cancer Research* 6 (2) (2017), pp. 230–233 (cit. on p. 19).

[99] Dai, Y. and King, A. "State of the Art MRI in Head and Neck Cancer." In: *Clinical Radiology* 73 (1) (2018), pp. 45–59 (cit. on p. 25).

[100] Damadian, R. "Tumor Detection by Nuclear Magnetic Resonance." In: *Science* 171 (3976) (1971), pp. 1151–1153 (cit. on p. 16).

[101] Datir, S. P. and Mitra, S. R. "Morphometric Study of the Thoracic Vertebral Pedicle in an Indian Population." In: *Spine* 29 (11) (2004), pp. 1174–1181 (cit. on p. 112).

[102] Davies, B., Harris, S., Lin, W., Hibberd, R., Middleton, R, and Cobb, J. "Active Compliance in Robotic Surgery - The Use of Force Control as a Dynamic Constraint." In: *Journal of Engineering in Medicine* 211 (4) (1997), pp. 285–292 (cit. on p. 122).

[103] De Baere, T, Aupérin, A, Deschamps, F, Chevallier, P, Gaubert, Y, Boige, V, Fonck, M, Escudier, B, and Palussiére, J. "Radiofrequency Ablation Is a Valid Treatment Option for Lung Metastases: Experience in 566 Patients With 1037 Metastases." In: *Annals of Oncology* 26 (5) (2015), pp. 987–991 (cit. on pp. 101, 140, 193).

[104] D'Esposito, M. and Postle, B. R. "The Cognitive Neuroscience of Working Memory." In: *Annual Review of Psychology* 66 (2015), pp. 115–142 (cit. on p. 73).

[105] Diepenbrock, S., Prassni, J.-S., Lindemann, F., Bothe, H.-W., and Ropinski, T. "2010 IEEE Visualization Contest Winner: Interactive Planning for Brain Tumor Resections." In: *IEEE Computer Graphics and Applications* 31 (5) (2011), pp. 6–13 (cit. on pp. 59, 61, 64, 84).

[106] Disibio, G. and French, S. W. "Metastatic Patterns of Cancers: Results from a Large Autopsy Study." In: *Archives of Pathology & Laboratory Medicine* 132 (6) (2008), pp. 931–939 (cit. on p. 105).

[107] Doerfler, A, Gölitz, P, Engelhorn, T, Kloska, S, and Struffert, T. "Flat-Panel Computed Tomography (DYNA-CT) in Neuroradiology. From High-Resolution Imaging of Implants to One-Stop-Shopping for Acute Stroke." In: *Clinical Neuroradiology* 25 (2) (2015), pp. 291–297 (cit. on p. 120).

[108] Dornheim, L., Dornheim, J., and Rössling, I. "Complete Fully Automatic Model-Based Segmentation of Normal and Pathological Lymph Nodes in CT Data." In: *International Journal of Computer Assisted Radiology and Surgery* 5 (6) (2010), pp. 565–581 (cit. on pp. 62, 87).

[109] Douglas, D. H. and Peucker, T. K. "Algorithms for the Reduction of the Number of Points Required to Represent a Digitized Line or its Caricature." In: *Cartographica* 10 (2) (1973), pp. 112–122 (cit. on p. 67).

[110] Dresky, C. von, Ballhausen, H., Becker, M., Serowy, S., Skalej, S., and Rieder, C. "Towards the Optimization of Generator Modulation and Applicator Positions for Radiofrequency Ablation of Spine Metastases." In: *Proc. of German Society of Computer- and Robot-Assisted Surgery*. 2018, pp. 208–213 (cit. on p. 108).

[111] Drzezga, A., Souvatzoglou, M., Eiber, M., Beer, A. J., Fürst, S., Martinez-Möller, A., Nekolla, S. G., Ziegler, S., Ganter, C., Rummeny, E. J., and Schwaiger, M. "First Clinical Experience with Integrated Whole-Body PET/MR: Comparison to PET/CT in Patients with Oncologic Diagnoses." In: *Journal of Nuclear Medicine* 53 (6) (2012), pp. 845–855 (cit. on p. 27).

[112] Du, J., Li, W., Lu, K., and Xiao, B. "An Overview of Multi-Modal Medical Image Fusion." In: *Neurocomputing* 215 (2016), pp. 3–20 (cit. on pp. 30, 60).

[113] Dunet, V. and Prior, J. O. "Diagnostic Accuracy of F-18-Fluoroethyltyrosine PET and PET/CT in Patients with Brain Tumor." In: *Clinical and Translational Imaging* 1 (2) (2013), pp. 135–144 (cit. on pp. 12, 157).

[114] Dupuy, D. E., Hong, R., Oliver, B., and Goldberg, S. N. "Radiofrequency Ablation of Spinal Tumors: Temperature Distribution in the Spinal Canal." In: *American Journal of Roentgenology* 175 (5) (2000), pp. 1263–1266 (cit. on pp. 108, 113, 140).

[115] D'Zmura, M., Rinner, O., and Gegenfurtner, K. R. "The Colors Seen Behind Transparent Filters." In: *Perception* 29 (8) (2000), pp. 911–926 (cit. on p. 167).

[116] Edelsbrunner, H., Kirkpatrick, D., and Seidel, R. "On the Shape of a Set of Points in the Plane." In: *IEEE Transactions on Information Theory* 29 (4) (1983), pp. 551–559 (cit. on p. 68).

[117] Ehman, E. C., Johnson, G. B., Villanueva-Meyer, J. E., Cha, S., Leynes, A. P., Larson, P. E. Z., and Hope, T. A. "PET/MRI: Where Might it Replace PET/CT?" In: *Journal of Magnetic Resonance Imaging* 46 (5) (2017), pp. 1247–1262 (cit. on p. 27).

[118] Einstein, A. "Über einen die Erzeugung und Verwandlung des Lichtes betreffenden heuristischen Gesichtspunkt." In: *Annals of Physics* 322 (6) (1905), pp. 132–148 (cit. on pp. 9, 24, 105).

[119] Eisenhauer, E. A., Therasse, P., Bogaerts, J., Schwartz, L. H., Sargent, D, Ford, R., Dancey, J., Arbuck, S, Gwyther, S., Mooney, M., Rubinstein, L., Shankar, L., Dodd, L., Kaplan, R., Lacombe, D., and Verweij, J. "New Response Evaluation Criteria in Solid Tumours: Revised RECIST Guideline (Version 1.1)." In: *European Journal of Cancer* 45 (2) (2009), pp. 228–247 (cit. on pp. 30, 59, 159, 164, 166, 193, 194).

[120] Ellis, L. M., Curley, S. A., and Tanabe, K. K. *Radiofrequency Ablation for Cancer: Current Indications, Techniques, and Outcomes*. Springer Science & Business Media, 2003 (cit. on pp. 107, 108).

[121] Eriksson, A. R., Albrektsson, T., and Albrektsson, B. "Heat Caused by Drilling Cortical Bone: Temperature Measured In Vivo in Patients and Animals." In: *Acta Orthopaedica Scandinavica* 55 (6) (1984), pp. 629–631 (cit. on pp. 113, 146).

[122] Fairchild, M. D. *Color Appearance Models*. 2nd ed. John Wiley & Sons, 2013 (cit. on p. 73).

[123] Fanti, S., Farsad, M., and Mansi, L. *Atlas of SPECT-CT*. Springer-Verlag Berlin Heidelberg, 2011 (cit. on pp. 28, 110).

[124] Faridul, H. S., Pouli, T., Chamaret, C., Stauder, J., Trémeau, A., and Reinhard, E. "A Survey of Color Mapping and its Applications." In: *Proc. of Eurographics – State of the Art Reports*. 2014 (cit. on pp. 73, 211).

[125] Fernandes, M. G. A., Fonseca, E. M. M., Natal, R., Manzanares, M. C., and Azevedo, L. "Effect of Drill Speed During Drilling of Human Cadaveric Tibiae." In: *Proc. of Congresso Nacional de Biomecânica*. 2017 (cit. on p. 113).

[126] Fernandes, M. G. A., Fonseca, E., and Natal, R. "Effect of Different Feed-Rate in Bone Drilling: Experimental and Numerical Study." In: *Proc. of Congresso Nacional de Mecânica Experimental*. 2016 (cit. on p. 113).

[127] Ferreiro, C. and Alcamo, I. E. *Deadly Diseases and Epidemics – Lung Cancer*. Infobase Publishing, 2007 (cit. on pp. 153, 154, 158, 164).

[128] Filippi, M. and Filippi. *fMRI Techniques and Protocols*. 2nd ed. Humana Press, New York, 2016 (cit. on p. 41).

[129] Filippiadis, D. K., Tutton, S., and Kelekis, A. "Percutaneous Bone Lesion Ablation." In: *La Radiologia Medica* 119 (7) (2014), pp. 462–469 (cit. on pp. 101, 109).

[130] Fischer, J., Bartz, D., and Straßer, W. "Illustrative Display of Hidden Iso-Surface Structures." In: *Proc. of IEEE Visualization*. 2005, pp. 663–670 (cit. on pp. 166, 170, 177, 178, 186, 217).

[131] Fishman, E. K., Ney, D. R., Heath, D. G., Corl, F. M., Horton, K. M., and Johnson, P. T. "Volume Rendering Versus Maximum Intensity Projection in CT Angiography: What Works Best, When, and Why." In: *Radiographics* 26 (3) (2006), pp. 905–922 (cit. on p. 38).

[132] Flohr, T. "CT systems." In: *Current Radiology Reports* 1 (1) (2013), pp. 52–63 (cit. on p. 6).

[133] Florencio-Silva, R., Sasso, G. R. d. S., Sasso-Cerri, E., Simões, M. J., and Cerri, P. S. "Biology of Bone Tissue: Structure, Function, and Factors that Influence Bone Cells." In: *BioMed Research International* 2015 (2015), pp. 1–17 (cit. on p. 105).

[134] Ford, S. T., Viola, I., Bruckner, S., Torp, H., and Kiss, G. "HeartPad: Real-Time Visual Guidance for Cardiac Ultrasound." In: *Proc. of the Workshop at SIGGRAPH Asia*. 2012, pp. 169–176 (cit. on pp. 42, 43).

[135] Forseen, S. E. and Borden, N. M. *Imaging Anatomy of the Human Spine: A Comprehensive Atlas Including Adjacent Structures*. Demos Medical - Springer Publishing, 2015 (cit. on p. 103).

[136] Foster, B., Bagci, U., Mansoor, A., Xu, Z., and Mollura, D. J. "A Review on Segmentation of Positron Emission Tomography Images." In: *Computers in Biology and Medicine* 50 (2014), pp. 76–96 (cit. on pp. 50, 51, 159, 160, 169, 174, 175, 195, 213).

[137] Frangi, A. F., Niessen, W. J., Vincken, K, and Viergever, M. A. "Multiscale vessel enhancement filtering." In: *Proc. of Medical Image Computing and Computer-Assisted Intervention*. 1998, pp. 130–137 (cit. on pp. 150, 162, 163, 179, 180, 182, 183, 185).

[138] Frericks, B. B., Ritz, J. P., Roggan, A., Wolf, K.-J., and Albrecht, T. "Multipolar Radiofrequency Ablation of Hepatic Tumors: Initial Experience." In: *Radiology* 237 (3) (2005), pp. 1056–1062 (cit. on p. 108).

[139] Fürweger, C., Drexler, C. G., Kufeld, M., and Wowra, B. "Feasibility of Fiducial-Free Prone-Position Treatments with CyberKnife for Lower Lumbosacral Spine Lesions." In: *Cureus Journal of Medical Science* 3 (1) (2011), e21 (cit. on p. 129).

[140] Gaemperli, O., Schepis, T., Kalff, V., Namdar, M., Valenta, I., Stefani, L., Desbiolles, L., Leschka, S., Husmann, L., Alkadhi, H., and Kaufmann, P. A. "Validation of a New Cardiac Image Fusion Software for Three-Dimensional Integration of Myocardial Perfusion SPECT and Stand-Alone 64-Slice CT Angiography." In: *European Journal of Nuclear Medicine and Molecular Imaging* 34 (7) (2007), pp. 1097–1106 (cit. on pp. 43–45, 76).

[141] Gai, M. and Wang, G. "Indoor3D: A WebGL Based Open Source Framework for 3D Indoor Maps Visualization." In: *Proc. of the International Conference on 3D Web Technology*. 2015, pp. 181–187 (cit. on pp. 50, 77, 81, 82).

[142] Gammon, S. T., Foje, N., Brewer, E. M., Owers, E., Downs, C. A., Budde, M. D., Leevy, W. M., and Helms, M. N. "Preclinical Anatomical, Molecular, and Functional Imaging of the Lung with Multiple Modalities." In: *American Journal of Physiology–Lung Cellular and Molecular Physiology* 306 (10) (2014), pp. L897–L914 (cit. on p. 28).

[143] Gasteiger, R., Neugebauer, M., Beuing, O., and Preim, B. "The FlowLens: A Focus-and-Context Visualization Approach for Exploration of Blood Flow in Cerebral Aneurysms." In: *IEEE Transactions on Visualization and Computer Graphics* 17 (12) (2011), pp. 2183–2192 (cit. on pp. 49, 51, 80).

[144] Gazis, A. N., Beuing, O., Franke, J., Jöllenbeck, B., and Skalej, M. "Bipolar Radiofrequency Ablation of Spinal Tumors: Predictability, Safety and Outcome." In: *The Spine Journal* 14 (4) (2014), pp. 604–608 (cit. on pp. 101, 107, 108, 122).

[145] Genseke, P., Wielenberg, C., Schreiber, J., Walles, T., and Kreissl, M. "Quantitative F-18-FDG-PET/CT in Preoperative Staging of Lung Cancer as a Potential Target for Machine Learning – A Prospective Study." In: *Journal of Nuclear Medicine* 60 (Supplement 1) (2019), pp. 1341–1341 (cit. on p. 212).

[146] Ghanem, N, Uhl, M, Brink, I, Schäfer, O, Kelly, T, Moser, E, and Langer, M. "Diagnostic Value of MRI in Comparison to Scintigraphy, PET, MS-CT and PET/CT for the Detection

of Metastases of Bone." In: *European Journal of Radiology* 55 (1) (2005), pp. 41–55 (cit. on pp. 21, 28, 110).

[147] Gillies, R. J., Kinahan, P. E., and Hricak, H. "Radiomics: Images Are More Than Pictures, They Are Data." In: *Radiology* 278 (2) (2015), pp. 563–577 (cit. on p. 34).

[148] Giordano, A., Calcagni, M. L., Meduri, G., Valente, S., and Galli, G. "Perfusion Lung Scintigraphy for the Prediction of Postlobectomy Residual Pulmonary Function." In: *Chest* 111 (6) (1997), pp. 1542–1547 (cit. on p. 149).

[149] Giraud, P. and Houle, A. "Respiratory Gating for Radiotherapy: Main Technical Aspects and Clinical Benefits." In: *International Scholarly Research Notes – Pulmonology* 2013 (519602 2013), pp. 1–13 (cit. on pp. 62, 122, 129).

[150] Glaßer, S., Lawonn, K., Hoffmann, T., Skalej, M., and Preim, B. "Combined Visualization of Wall Thickness and Wall Shear Stress for the Evaluation of Aneurysms." In: *IEEE Transactions on Visualization and Computer Graphics* 20 (12) (2014), pp. 2506–2515 (cit. on pp. 47, 48).

[151] Glaßer, S., Saalfeld, P., Berg, P., **Merten, N.**, and Preim, B. "How to Evaluate Medical Visualizations on the Example of 3D Aneurysm Surfaces." In: *Proc. of Eurographics Workshop on Visual Computing in Biology and Medicine*. 2016, pp. 153–162 (cit. on pp. 41, 97, 260).

[152] Goetz, M. "Using Crowdsourced Indoor Geodata for the Creation of a Three-Dimensional Indoor Routing Web Application." In: *Future Internet* 4 (2) (2012), pp. 575–591 (cit. on pp. 75, 81).

[153] Goetz, M. and Zipf, A. "Extending OpenStreetMap to Indoor Environments: Bringing Volunteered Geographic Information to the Next Level." In: vol. 2011. 2011, pp. 47–58 (cit. on p. 81).

[154] Gould, P. and White, R. *Mental Maps*. 1st ed. Penguin Books, 1974 (cit. on p. 72).

[155] Graaf, F. R. de, Schuijf, J. D., Velzen, J. E. van, Kroft, L. J., Roos, A. de, Reiber, J. H., Boersma, E., Schalij, M. J., Spanó, F., Jukema, J. W., Wall, E. E. van der, and Box, J. J. "Diagnostic Accuracy of 320-Row Multidetector Computed Tomography Coronary Angiography in the Non-Invasive Evaluation of Significant Coronary Artery Disease." In: *European Heart Journal* 31 (15) (2010), pp. 1908–1915 (cit. on p. 7).

[156] Gramazio, C. C., Laidlaw, D. H., and Schloss, K. B. "Colorgorical: Creating Discriminable and Preferable Color Palettes for Information Visualization." In: *IEEE Transactions on Visualization and Computer Graphics* 23 (1) (2016), pp. 521–530 (cit. on p. 73).

[157] Großer, O. S., Amthauer, H., and Ricke, J. "General Theory of Predictive Dosimetry for Yttrium-90 Radioembolization to Sites Other Than the Liver: Reply." In: *Cardiovascular and Interventional Radiology* 37 (4) (2014), pp. 1120–1121 (cit. on p. 164).

[158] Guthart, G. S. and Salisbury, J. K. "The Intuitive™ Telesurgery System: Overview and Application." In: *Proc. of IEEE International Conference on Robotics and Automation.* 2000, pp. 618–621 (cit. on p. 122).

[159] Ha, J. F. and Longnecker, N. "Doctor-Patient Communication: A Review." In: *Ochsner Journal* 10 (1) (2010), pp. 38–43 (cit. on pp. 43, 81, 97).

[160] Haak, D., Simon, H., Yu, J., Harmsen, M., and Deserno, T. M. "Bone Age Assessment Using Support Vector Machine Regression." In: *Proc. of Bildverarbeitung für die Medizin*. 2013, pp. 164–169 (cit. on p. 112).

[161] Haak, D., Simon, H., Yu, J., Harmsen, M., and Deserno, T. M. "Photographic Documentation by Mobile Devices Integrated into Case Report Forms of Clinical Trials." In: *Proc. of Bildverarbeitung für die Medizin*. 2016, pp. 254–259 (cit. on p. 191).

[162] Hafting, T., Fyhn, M., Molden, S., Moser, M.-B., and Moser, E. I. "Microstructure of a Spatial Map in the Entorhinal Cortex." In: *Nature* 436 (7052) (2005), pp. 801–806 (cit. on pp. 65, 72, 73).

[163] Hagedorn, B., Trapp, M., Glander, T., and Döllner, J. "Towards an Indoor Level-of-Detail Model for Route Visualization." In: *Proc. of International Conference on Mobile Data Management: Systems, Services and Middleware*. 2009, pp. 692–697 (cit. on pp. 70, 78, 79).

[164] Hahn, H. K., Preim, B., Selle, D., and Peitgen, H.-O. "Visualization and Interaction Techniques for the Exploration of Vascular Structures." In: *Proc. of IEEE Visualization*. 2001, pp. 395–578 (cit. on p. 198).

[165] Hahn, H. K. and Peitgen, H.-O. "IWT-Interactive Watershed Transform: A Hierarchical Method for Efficient Interactive and Automated Segmentation of Multidimensional Grayscale Images." In: *Proc. of SPIE Medical Imaging – Image Processing*. 2003, pp. 643–653 (cit. on p. 161).

[166] Halvorson, K. G., Sevcik, M. A., Ghilardi, J. R., Rosol, T. J., and Mantyh, P. W. "Similarities and Differences in Tumor Growth, Skeletal Remodeling and Pain in an Osteolytic and Osteoblastic Model of Bone Cancer." In: *The Clinical Journal of Pain* 22 (7) (2006), pp. 587–600 (cit. on pp. 106, 111).

[167] Hamamura, M. J., Ha, S., Roeck, W. W., Muftuler, L. T., Wagenaar, D. J., Meier, D., Patt, B. E., and Nalcioglu, O. "Development of an MR-Compatible SPECT System (MRSPECT) for Simultaneous Data Acquisition." In: *Physics in Medicine & Biology* 55 (6) (2010), pp. 1563–1575 (cit. on p. 28).

[168] Han, S., Son, J. P., Cho, H., Park, J.-Y., and Kim, S.-G. "Gradient-Echo and Spin-Echo Blood Oxygenation Level–Dependent Functional MRI at Ultrahigh Fields of 9.4 and 15.2 Tesla." In: *Magnetic Resonance in Medicine* 81 (2) (2018), pp. 1237–1246 (cit. on p. 16).

[169] Handels, H., Werner, R., Schmidt, R., Frenzel, T., Lu, W., Low, D., and Ehrhardt, J. "4D Medical Image Computing and Visualization of Lung Tumor Mobility in Spatio-Temporal CT Image Data." In: *International Journal of Medical Informatics* 76 (2007), S433–S439 (cit. on pp. 62, 63, 129, 159).

[170] Hansen, C., Wieferich, J., Ritter, F., Rieder, C., and Peitgen, H.-O. "Illustrative Visualization of 3D Planning Models for Augmented Reality in Liver Surgery." In: *International Journal of Computer Assisted Radiology and Surgery* 5 (2) (2010), pp. 133–141 (cit. on p. 121).

[171] Hansen, C., Zidowitz, S., Preim, B., Stavrou, G., Oldhafer, K. J., and Hahn, H. K. "Impact of Model-Based Risk Analysis for Liver Surgery Planning." In: *International Journal of Computer Assisted Radiology and Surgery* 9 (3) (2014), pp. 473–480 (cit. on pp. 117, 147).

[172] Hansen, C., Zidowitz, S., Ritter, F., Lange, C., Oldhafer, K., and Hahn, H. K. "Risk Maps for Liver Surgery." In: *International Journal of Computer Assisted Radiology and Surgery* 8 (3) (2013), pp. 419–428 (cit. on pp. 80, 81, 117).

[173] Hanses, M., Adler, S., Wolff, S., Skalej, M., and Elkmann, N. "Robotic Assistance for Spine Interventions." In: *Proc. of German Society of Computer- and Robot-Assisted Surgery*. 2016, pp. 231–236 (cit. on pp. 124, 125, 129, 148, 216).

[174] Haraikawa, M., Suzuki, M., Inoue, K., Kozawa, E., Tanaka, J., and Niitsu, M. "Simultaneous Multi-Slice MR Imaging of the Hip at 3 T to Reduce Acquisition Times and Maintain Image Quality." In: *BMC Musculoskeletal Disorders* 19 (1) (2018), pp. 440–1–440–8 (cit. on p. 20).

[175] Harley, J. B. and Woodward, D. *Cartography in Prehistoric, Ancient, and Medieval Europe and the Mediterranean*. University of Chicago Press, 1987 (cit. on p. 66).

[176] Harley, J. B. and Woodward, D. *Cartography in the Traditional East and Southeast Asian Societies*. University of Chicago Press, 1994 (cit. on p. 66).

[177] Harley, J. B. and Woodward, D. *Cartography in the Traditional Islamic and South Asian Societies*. University of Chicago Press, 1992 (cit. on p. 66).

[178] Harrower, M. and Brewer, C. A. "ColorBrewer.org: An Online Tool for Selecting Colour Schemes for Maps." In: *The Cartographic Journal* 40 (1) (2003), pp. 27–37 (cit. on p. 56).

[179] Hasegawa, B. H., Gingold, E. L., Reilly, S. M., Liew, S.-C., and Cann, C. E. "Description of a Simultaneous Emission-Transmission CT System." In: *Proc. of Medical Imaging IV: Image Formation*. Vol. 1231. 1990, pp. 50–60 (cit. on p. 28).

[180] Hashimoto, M., Miyauchi, T., Heianna, J., Sugawara, M., Ishiyama, K., Watarai, J., and Nanjo, H. "Accurate Diagnosis of Peripheral Small Cell Lung Cancer with Computed Tomography." In: *The Tohoku Journal of Experimental Medicine* 217 (3) (2009), pp. 217–221 (cit. on p. 157).

[181] Haskins, G., Kruger, U., and Yan, P. "Deep Learning in Medical Image Registration: A Survey." In: *arXiv preprint arXiv:1903.02026* (2019) (cit. on p. 35).

[182] Hata, A., Yanagawa, M., Honda, O., Kikuchi, N., Miyata, T., Tsukagoshi, S., Uranishi, A., and Tomiyama, N. "Effect of Matrix Size on the Image Quality of Ultra-high-resolution CT of the Lung: Comparison of 512× 512, 1024× 1024, and 2048× 2048." In: *Academic Radiology* 25 (7) (2018), pp. 869–876 (cit. on p. 6).

[183] Heiken, J. P., Brink, J. A., and Vannier, M. W. "Spiral (Helical) CT." In: *Radiology* 189 (3) (1993), pp. 647–656 (cit. on p. 6).

[184] Heindel, W., Gübitz, R., Vieth, V., Weckesser, M., Schober, O., and Schäfers, M. "The Diagnostic Imaging of Bone Metastases." In: *Deutsches Ärzteblatt International* 111 (44) (2014), pp. 741–747 (cit. on p. 110).

[185] Heinrich, F., Joeres, F., Lawonn, K., and Hansen, C. "Comparison of Projective Augmented Reality Concepts to Support Medical Needle Insertion." In: *IEEE Transactions on Visualization and Computer Graphics* 25 (6) (2019), pp. 2157–2167 (cit. on pp. 40, 118, 121).

[186] Henschke, C. I., Yankelevitz, D. F., Mirtcheva, R., McGuinness, G., McCauley, D., and Miettinen, O. S. "CT Screening for Lung Cancer: Frequency and Significance of Part-

Solid and Nonsolid Nodules." In: *American Journal of Roentgenology* 178 (5) (2002), pp. 1053–1057 (cit. on p. 156).

[187] Herghelegiu, P.-C., Manta, V., Perin, R., Bruckner, S., and Gröller, E. "Biopsy Planner – Visual Analysis for Needle Pathway Planning in Deep Seated Brain Tumor Biopsy." In: 31 (3pt2) (2012), pp. 1085–1094 (cit. on pp. 2, 54, 61, 114, 116–119, 147).

[188] Hernandez, R. K., Wade, S. W., Reich, A., Pirolli, M., Liede, A., and Lyman, G. H. "Incidence of Bone Metastases in Patients with Solid Tumors: Analysis of Oncology Electronic Medical Records in the United States." In: *BMC Cancer* 18 (2018), pp. 44–1–44–11 (cit. on pp. 105, 106).

[189] Herschel, W. "XIV. Experiments on the Refrangibility of the Invisible Rays of the Sun." In: *Philosophical Transactions of the Royal Society of London* (90) (1800), pp. 284–292 (cit. on p. 5).

[190] Hertz, H. R. "Überber einen Einfluss des ultravioletten Lichtes auf die electrische Entladung." In: *Annals of Physics* 267 (8) (1887), 983–1000 (cit. on p. 5).

[191] Heverhagen, J. T., Bourekas, E., Sammet, S., Knopp, M. V., and Schmalbrock, P. "Time-of-Flight Magnetic Resonance Angiography at 7 Tesla." In: *Investigative Radiology* 43 (8) (2008), pp. 568–573 (cit. on p. 21).

[192] Hille, G., Dünnwald, M., Becker, M., Steffen, J., Saalfeld, S., and Tönnies, K. "Segmentation of Vertebral Metastases in MRI Using an U-Net like Convolutional Neural Network." In: *Proc. of Bildverarbeitung für die Medizin*. 2019, pp. 31–36 (cit. on p. 145).

[193] Hille, G., **Merten, N.**, Serowy, S., Glaßer, S., Tönnies, K., and Preim, B. "Assessing the Benefits of Interactive Patient-Specific Visualisations for Patient Information." In: *Proc. of Bildverarbeitung für die Medizin*. 2017, pp. 224–229 (cit. on pp. 213, 260).

[194] Hoffmann, K., Hinz, U., Stravodimos, C., Knoblich, T., Schön, M. R., Büchler, M. W., and Mehrabi, A. "Risk Assessment for Liver Resection." In: *Surgery* 164 (5) (2018), pp. 998–1005 (cit. on p. 117).

[195] Hofman, M. S. and Hicks, R. J. "How We Read Oncologic FDG PET/CT." In: *Cancer Imaging* 16 (1) (2016), pp. 35–1–35–14 (cit. on p. 30).

[196] Höhne, K. H., Pommert, A., Riemer, M., Schiemann, T., Schubert, R., Tiede, U., and Lierse, W. "Anatomical Atlases Based on Volume Visualization." In: *Proc. of Visualization*. 1992, pp. 115–122 (cit. on pp. 2, 66).

[197] Hoogeman, M. S., Nuyttens, J. J., Levendag, P. C., and Heijmen, B. J. "Time Dependence of Intrafraction Patient Motion Assessed by Repeat Stereoscopic Imaging." In: *International Journal of Radiation Oncology*Biology*Physics* 70 (2) (2008), pp. 609–618 (cit. on p. 129).

[198] Horsfield, K. "Morphometry of the Small Pulmonary Arteries in Man." In: *Circulation Research* 42 (5) (1978), pp. 593–597 (cit. on p. 163).

[199] Hosokawa, K., Abe, K., Kashihara, S., and Tsutsui, H. "3-Dimensional SPECT/CT Fusion Imaging-Guided Balloon Pulmonary Angioplasty for Chronic Thromboembolic Pulmonary Hypertension." In: *JACC: Cardiovascular Interventions* 10 (20) (2017), e193–e194 (cit. on pp. 43, 44).

[200] Hounsfield, G. N. "Computerized Transverse Axial Scanning (Tomography): Part 1. Description of System." In: *The British Journal of Radiology* 46 (552) (1973), pp. 1016–1022 (cit. on p. 5).

[201] Howington, J. A., Blum, M. G., Chang, A. C., Balekian, A. A., and Murthy, S. C. "Treatment of Stage I and II Non-Small Cell Lung Cancer: Diagnosis and Management of Lung Cancer: American College of Chest Physicians Evidence-Based Clinical Practice Guidelines." In: *Chest* 143 (5) (2013), e278S–e313S (cit. on pp. 34, 140, 193, 194).

[202] Hsieh, J. *Computed Tomography: Principles, Design, Artifacts, and Recent Advances*. 2nd ed. SPIE Washington and John Wiley & Sons New Jersey, 2009 (cit. on p. 6).

[203] Hu, S., Hoffman, E. A., and Reinhardt, J. M. "Automatic Lung Segmentation for Accurate Quantitation of Volumetric X-ray CT Images." In: *IEEE Transactions on Medical Imaging* 20 (6) (2001), pp. 490–498 (cit. on pp. 97, 161).

[204] Hu, Y., Jin, H., Zhang, L., Zhang, P., and Zhang, J. "State Recognition of Pedicle Drilling with Force Sensing in a Robotic Spinal Surgical System." In: *IEEE/ASME Transactions on Mechatronics* 19 (1) (2013), pp. 357–365 (cit. on p. 121).

[205] Hua, K.-L., Hsu, C.-H., Hidayati, S. C., Cheng, W.-H., and Chen, Y.-J. "Computer-aided classification of lung nodules on computed tomography images via deep learning technique." In: *OncoTargets and Therapy* 8 (2015), pp. 2015–2022 (cit. on p. 160).

[206] Huang, J.-B., Chen, C.-S., Jen, T.-C., and Wang, S.-J. "Image Recolorization for the Colorblind." In: *Proc. of IEEE International Conference on Acoustics, Speech and Signal Processing*. 2009, pp. 1161–1164 (cit. on pp. 74, 98, 212).

[207] Iñarrairaegui, M, Pardo, F, Bilbao, J., Rotellar, F, Benito, A, D'Avola, D, Herrero, J., Rodriguez, M, Martí, P, Zozaya, G, Dominguez, I., Quiroga, J., and Sangro, B. "Response to Radioembolization with Yttrium-90 Resin Microspheres May Allow Surgical Treatment with Curative Intent and Prolonged Survival in Previously Unresectable Hepatocellular Carcinoma." In: *European Journal of Surgical Oncology* 38 (7) (2012), pp. 594–601 (cit. on p. 149).

[208] Isenberg, T. "Visual Abstraction and Stylisation of Maps." In: *The Cartographic Journal* 50 (1) (2013), pp. 8–18 (cit. on p. 67).

[209] Itten, J. *The Elements of Color*. John Wiley & Sons, 1970 (cit. on pp. 73, 206, 211).

[210] Jain, V. V., Gupta, O., and Jain, J. "A Rare Case of Situs Inversus with Dextrocardia, Lutembacher Syndrome, and Pericardial Effusion." In: *Heart Views* 12 (3) (2011), pp. 107–111 (cit. on p. 152).

[211] Jainek, W. M., Born, S., Bartz, D., Straßer, W., and Fischer, J. "Illustrative Hybrid Visualization and Exploration of Anatomical and Functional Brain Data." In: *Computer Graphics Forum* 27 (3) (2008), pp. 855–862 (cit. on pp. 39–41).

[212] James, A. P. and Dasarathy, B. V. "Medical Image Fusion: A Survey of the State of the Art." In: *Information Fusion* 19 (2014), pp. 4–19 (cit. on pp. 30, 60).

[213] Jandial, R. *Metastatic Cancer: Clinical and Biological Perspectives*. 1st ed. CRC Press, 2013 (cit. on p. 152).

[214] Jansen, W. "Neurath, Arntz and ISOTYPE: The Legacy in Art, Design and Statistics." In: *Journal of Design History* 22 (3) (2009), pp. 227–242 (cit. on p. 67).

[215] Jett, J. R., Schild, S. E., Kesler, K. A., and Kalemkerian, G. P. "Treatment of Small Cell Lung Cancer: Diagnosis and Management of Lung Cancer: American College of Chest Physicians Evidence-Based Clinical Practice Guidelines." In: *Chest* 143 (5) (2013), e400S–e419S (cit. on pp. 140, 193, 194).

[216] Jiang, H., Ma, H., Qian, W., Gao, M., and Li, Y. "An Automatic Detection System of Lung Nodule Based on Multigroup Patch-Based Deep Learning Network." In: *IEEE Journal of Biomedical and Health Informatics* 22 (4) (2017), pp. 1227–1237 (cit. on p. 160).

[217] Jin, J. J., Yajun, Z. Z., Plocher, T. A., Zhang, R., and Chen, E. "Method and System for Distinctively Displaying Selected Floor With Sufficient Details in a Three-Dimensional Building Model." In: *US Patent 8,233,008* (2012) (cit. on pp. 82, 98).

[218] Jones, K. C., Redler, G., Templeton, A., Bernard, D., Turian, J. V., and Chu, J. C. "Characterization of Compton-Scatter Imaging with an Analytical Simulation Method." In: *Physics in Medicine & Biology* 63 (2) (2018), p. 025016 (cit. on p. 9).

[219] Jones, T. and Townsend, D. W. "History and Future Technical Innovation in Positron Emission Tomography." In: *Journal of Medical Imaging* 4 (1) (2017), pp. 011013–1–011013–17 (cit. on pp. 8, 10, 11, 22, 23).

[220] Joniau, S., Tailly, T., Goeman, L., Blyweert, W., Gontero, P., and Joyce, A. "Kidney Radiofrequency Ablation for Small Renal Tumors: Oncologic Efficacy." In: *Journal of Endourology* 24 (5) (2010), pp. 721–728 (cit. on p. 101).

[221] Jönsson, D., Sundén, E., Ynnerman, A., and Ropinski, T. "A Survey of Volumetric Illumination Techniques for Interactive Volume Rendering." In: *Computer Graphics Forum* 33 (1) (2014), pp. 27–51 (cit. on pp. 49, 215).

[222] Jung, Y., Kim, J., Eberl, S., Fulham, M., and Feng, D. D. "Visibility-Driven PET-CT Visualisation with Region of Interest (ROI) Segmentation." In: *The Visual Computer* 29 (6–8) (2013), pp. 805–815 (cit. on pp. 51, 55–58).

[223] Jung, Y., Kim, J., Feng, D., and Fulham, M. "Occlusion and Slice-Based Volume Rendering Augmentation for PET-CT." In: *IEEE Journal of Biomedical and Health Informatics* 21 (4) (2016), pp. 1005–1014 (cit. on p. 55).

[224] Jung, Y., Kim, J., and Feng, D. D. "Dual-Modal Visibility Metrics for Interactive PET-CT Visualization." In: *Proc. of International Conference of the IEEE Engineering in Medicine and Biology Society*. 2012, pp. 2696–2699 (cit. on p. 57).

[225] Jung, Y., Kim, J., Fulham, M., and Feng, D. D. "Opacity-Driven Volume Clipping for Slice of Interest (SOI) Visualisation of Multi-Modality PET-CT Volumes." In: *Proc. of International Conference of the IEEE Engineering in Medicine and Biology Society*. 2014, pp. 6714–6717 (cit. on pp. 54, 55).

[226] Jung, Y., Kim, J., Kumar, A., Feng, D. D., and Fulham, M. "Feature of Interest-Based Direct Volume Rendering Using Contextual Saliency-Driven Ray Profile Analysis." In: *Computer Graphics Forum* 37 (6) (2018), pp. 5–19 (cit. on pp. 55, 56, 215).

[227] Juntu, J., Sijbers, J., Van Dyck, D., and Gielen, J. "Bias Field Correction for MRI Images." In: *Proc. of Computer Recognition Systems*. 2005, pp. 543–551 (cit. on p. 21).

[228] Kägebein, U., Godenschweger, F., Armstrong, B. S., Rose, G., Wacker, F. K., Speck, O., and Hensen, B. "Percutaneous MR-Guided Interventions Using an Optical Moiré Phase

Tracking System: Initial Results." In: *PloS One* 13 (10) (2018), e0205394 (cit. on pp. 121, 122).

[229] Kaptanoglu, E., Cemil, B., Gurcay, A. G., Tun, K., and Cevirgen, B. "Morphometric Characteristics of the Inner and Outer Diameter of Lumbar Pedicles on Computed Tomography." In: *Neurologia i Neurochirurgia Polska* 43 (43) (), pp. 533–537 (cit. on p. 112).

[230] Kath, N., Handels, H., and Mastmeyer, A. "Simulation von Radiofrequenzablationen für die Leberpunktion in 4D-VR-Simulationen." In: *Proc. of Bildverarbeitung für die Medizin*. 2019, pp. 289–294 (cit. on p. 108).

[231] Kelly, M. "SUV: Advancing Comparability and Accuracy." In: *White Paper Siemens* (2009) (cit. on p. 195).

[232] Kennedy, A., Nag, S., Salem, R., Murthy, R., McEwan, A. J., Nutting, C., Espat, J., Bilbao, J. I., Sharma, R. A., Thomas, J. P., and coldwell, D. "Recommendations for Radioembolization of Hepatic Malignancies Using Yttrium-90 Microsphere Brachytherapy: A Consensus Panel Report from the Radioembolization Brachytherapy Oncology Consortium." In: *International Journal of Radiation Oncology*Biology*Physics* 68 (1) (2007), pp. 13–23 (cit. on p. 149).

[233] Khairy, P., Chauvet, P., Lehmann, J., Lambert, J., Macle, L., Tanguay, J.-F., Sirois, M. G., Santoianni, D., and Dubuc, M. "Lower Incidence of Thrombus Formation with Cryoenergy Versus Radiofrequency Catheter Ablation." In: *Circulation* 107 (15) (2003), pp. 2045–2050 (cit. on p. 107).

[234] Khan, A. N., Al-Jahdali, H. H., Allen, C. M., Irion, K. L., Al Ghanem, S., and Koteyar, S. S. "The Calcified Lung Nodule: What Does it Mean?" In: *Annals of Thoracic Medicine* 5 (2) (2010), pp. 67–79 (cit. on p. 157).

[235] Kim, J., Eberl, S., and Feng, D. "Visualizing Dual-Modality Rendered Volumes Using a Dual-Lookup Table Transfer Function." In: *Computing in Science & Engineering* 9 (1) (2007), pp. 20–25 (cit. on pp. 42, 43).

[236] Kim, J., Kumar, A., Eberl, S., Fulham, M., and Feng, D. "Interactive Point-of-Interest Volume Rendering Visualization of PET-CT Data." In: *Proc. of IEEE Nuclear Science Symposium Conference Record*. 2008, pp. 4384–4387 (cit. on pp. 52, 53).

[237] Kim, T. T., Johnson, J. P., Pashman, R., and Drazin, D. "Minimally Invasive Spinal Surgery with Intraoperative Image-Guided Navigation." In: *BioMed Research International* 2016 (2016), pp. 1–7 (cit. on p. 121).

[238] Kim, W., Donalson, L., Herrera, P, Woodward, C., Kubena, L., Nisbet, D., and Ricke, S. "Research Note: Effects of Different Bone Preparation Methods (Fresh, Dry, and Fat-Free Dry) on Bone Parameters and The Correlations Between Bone Breaking Strength and the Other Bone Parameters." In: *Poultry Science* 83 (10) (2004), pp. 1663–1666 (cit. on pp. 106, 141).

[239] Kim, Y.-H., Choi, M., and Kim, J.-W. "Are Titanium Implants Actually Safe for Magnetic Resonance Imaging Examinations?" In: *Archives of Plastic Surgery* 46 (1) (2019), p. 96 (cit. on pp. 16, 122).

[240] Kim, Y.-s., Lee, W. J., Rhim, H., Lim, H. K., Choi, D., and Lee, J. Y. "The Minimal Ablative Margin of Radiofrequency Ablation of Hepatocellular Carcinoma (>2 and <5 cm) Needed to Prevent Local Tumor Progression: 3D Quantitative Assessment Using CT

Image Fusion." In: *American Journal of Roentgenology* 195 (3) (2010), pp. 758–765 (cit. on pp. 121, 122).

[241] Kinahan, P. E. and Fletcher, J. W. "Positron Emission Tomography-Computed Tomography Standardized Uptake Values in Clinical Practice and Assessing Response to Therapy." In: *Seminars in Ultrasound, CT and MRI* 31 (6) (2009), pp. 496–505 (cit. on p. 195).

[242] Kinahan, P. E., Townsend, D., Beyer, T, and Sashin, D. "Attenuation Correction for a Combined 3D PET/CT Scanner." In: *Medical Physics* 25 (10) (1998), pp. 2046–2053 (cit. on pp. 9, 24, 105).

[243] Kirişli, H. A., Gupta, V., Shahzad, R., Al Younis, I., Dharampal, A., Geuns, R.-J. van, Scholte, A. J., Graaf, M. A. de, Joemai, R. M., Nieman, K., Vliet, L. van, Walsum, T. van, Lelieveldt, B., and Niessen, W. J. "Additional Diagnostic Value of Integrated Analysis of Cardiac CTA and SPECT MPI Using the SMARTVis System in Patients with Suspected Coronary Artery Disease." In: *Journal of Nuclear Medicine* 55 (1) (2014), pp. 50–57 (cit. on pp. 75, 76).

[244] Kirmizibayrak, C., Yim, Y., Wakid, M., and Hahn, J. "Interactive Visualization and Analysis of Multimodal Datasets for Surgical Applications." In: *Journal of Digital Imaging* 25 (6) (2012), pp. 792–801 (cit. on pp. 46, 49, 60).

[245] Kitchin, R. M. "Cognitive Maps: What Are They and Why Study Them?" In: *Journal of Environmental Psychology* 14 (1) (1994), pp. 1–19 (cit. on p. 72).

[246] Klemm, P., Lawonn, K., Rak, M., Preim, B., Tönnies, K. D., Hegenscheid, K., Völzke, H., and Oeltze, S. "Visualization and Analysis of Lumbar Spine Canal Variability in Cohort Study Data." In: *Proc. of Symposium on Vision, Modeling, and Visualization*. 2013, pp. 121–128 (cit. on p. 79).

[247] Köhler, B. "Guided Qualitative and Quantitative Analysis of Cardiac 4D PC-MRI Blood Flow Data." PhD thesis. Otto-von-Guericke-University, 2016 (cit. on pp. 16–18, 20–22, 47, 122).

[248] Konate, S., Pretorius, P. H., Gifford, H. C., O'Connor, J. M., Konik, A., Shazeeb, M. S., and King, M. A. "Combined Collimator/ Reconstruction Optimization for Myocardial Perfusion SPECT Imaging Using Polar Map-Based LROC Numerical Observer." In: *Proc. of SPIE Image Perception, Observer Performance, and Technology Assessment*. Vol. 8318. 2012, p. 83181L (cit. on p. 45).

[249] Konno, S., Olmarker, K., Byröd, G., Nordborg, C., Strömqvist, B., and Rydevik, B. "Acute Thermal Nerve Root Jnjury." In: *European Spine Journal* 3 (6) (1994), pp. 299–302 (cit. on p. 113).

[250] Kothe, R., Strauss, J. M., Deuretzbacher, G., Hemmi, T., Lorenzen, M., and Wiesner, L. "Computer Navigation of Parapedicular Screw Fixation in the Thoracic Spine: A Cadaver Study." In: *Spine* 26 (21) (2001), E496–E501 (cit. on p. 112).

[251] Kovacević-Kuśmierek, K., Kozak, J., Pryt, Ł., Bieńkiewicz, M., Cichocki, P., Kuśmierek, J., and Płachcińska, A. "Perfusion Lung Scintigraphy for the Prediction of Postoperative Residual Pulmonary Function in Patients with Lung Cancer." In: *Nuclear Medicine Review* 18 (2) (2015), pp. 70–77 (cit. on p. 28).

[252] Kraak, M.-J. and Ormeling, F. J. *Cartography: Visualization of Spatial Data*. 3rd ed. Guilford Press, 2013 (cit. on pp. 66, 67).

[253] Kremers, J., Baraas, R. C., and Marshall, N. J. *Human Color Vision*. Vol. 5. 2016 (cit. on pp. 73, 98, 212).

[254] Krüger, A. "Automatic Graphical Abstraction in Intent-Based 3D-Illustrations." In: *Proceedings of the working conference on Advanced visual interfaces*. 1998, pp. 47–56 (cit. on pp. 69–71).

[255] Krüger, J., Schneider, J., and Westermann, R. "Clearview: An Interactive Context Preserving Hotspot Visualization Technique." In: *IEEE Transactions on Visualization and Computer Graphics* 12 (5) (2006), pp. 941–948 (cit. on pp. 47, 48).

[256] Krupinski, E. A. "Current Perspectives in Medical Image Perception." In: *Attention, Perception, & Psychophysics* 72 (5) (2010), pp. 1205–1217 (cit. on pp. 29, 97).

[257] Krupinski, E. A., Chung, A., Applegate, K., DeSimone, A. K., and Tridandapani, S. "Impact of Patient Photographs on Radiologists' Visual Search of Chest Radiographs." In: *Academic Radiology* 23 (8) (2016), pp. 953–960 (cit. on p. 192).

[258] Kubiessa, K, Purz, S, Gawlitza, M, Kühn, A, Fuchs, J, Steinhoff, K., Boehm, A, Sabri, O, Kluge, R, Kahn, T, and Stumpp, P. "Initial Clinical Results of Simultaneous 18 F-FDG PET/MRI in comparison to 18 F-FDG PET/CT in Patients with Head and Neck Cancer." In: *European Journal of Nuclear Medicine and Molecular Imaging* 41 (4) (2014), pp. 639–648 (cit. on p. 60).

[259] Kuhl, D. E. "Rotational Scanning of the Liver." In: *Radiology* 71 (6) (1958), pp. 875–876 (cit. on p. 10).

[260] Kuhl, D. E., Chamberlain, R. H., Hale, J., and Gorson, R. O. "A High-Contrast Photographic Recorder for Scintillation Counter Scanning." In: *Radiology* 66 (5) (1956), pp. 730–739 (cit. on pp. 10, 29).

[261] Kuhl, D. E., Hale, J., and Eaton, W. L. "Transmission Scanning: A Useful Adjunct to Conventional Emission Scanning for Accurately Keying Isotope Deposition to Radiographic Anatomy." In: *Radiology* 87 (2) (1966), pp. 278–284 (cit. on pp. 28, 29).

[262] Kuhnigk, J.-M., Dicken, V., Bornemann, L., Bakai, A., Wormanns, D., Krass, S., and Peitgen, H.-O. "Morphological Segmentation and Partial Volume Analysis for Volumetry of Solid Pulmonary Lesions in Thoracic CT Scans." In: *IEEE Transactions on Medical Imaging* 25 (4) (2006), pp. 417–434 (cit. on pp. 159, 160, 185, 212).

[263] Kuhnigk, J.-M., Dicken, V., Zidowitz, S., Bornemann, L., Kuemmerlen, B., Krass, S., Peitgen, H.-O., Yuval, S., Jend, H.-H., Rau, W. S., and Aschenbach, T. "New Tools for Computer Assistance in Thoracic CT. Part 1. Functional Analysis of Lungs, Lung Lobes, and Bronchopulmonary Segments." In: *Radiographics* 25 (2) (2005), pp. 525–536 (cit. on pp. 131, 141, 160–162, 169, 178, 212, 260).

[264] Kuhnigk, J.-M., Hahn, H., Hindennach, M., Dicken, V., Krass, S., and Peitgen, H.-O. "Lung Lobe Segmentation by Anatomy-Guided 3D Watershed Transform." In: *Proc. of SPIE Medical Imaging – Image Processing*. 2003, pp. 1482–1490 (cit. on pp. 161, 163).

[265] Kurumi, Y., Tani, T., Naka, S., Shiomi, H., Shimizu, T., Abe, H., Endo, Y., and Morikawa, S. "MR-Guided Microwave Ablation for Malignancies." In: *International Journal of Clinical Oncology* 12 (2) (2007), pp. 85–93 (cit. on p. 121).

[266] Lang, T., Hasegawa, B., Liew, S., Brown, J., Blankespoor, S, Reilly, S., Gingold, E., and Cann, C. "A Prototype Emission-Transmission Imaging System." In: *Proc. of the 1991 IEEE Nuclear Science Symposium and Medical Imaging Conference*. 1991, pp. 1902–1906 (cit. on p. 22).

[267] Larmor, J. "The Influence of a Magnetic Field on Radiation Frequency." In: *Proc. of the Royal Society* 60 (1897), pp. 514–515 (cit. on p. 16).

[268] Lassen, B., Kuhnigk, J.-M., Schmidt, M., Krass, S., and Peitgen, H.-O. "Lung and Lung Lobe Segmentation Methods at Fraunhofer MEVIS." In: *Proc. of International Workshop on Pulmonary Image Analysis*. 2011, pp. 185–199 (cit. on pp. 160, 162).

[269] Lassen, B., Rikxoort, E. M. van, Schmidt, M., Kerkstra, S., Ginneken, B. van, and Kuhnigk, J.-M. "Automatic Segmentation of the Pulmonary Lobes from Chest CT Scans Based on Fissures, Vessels, and Bronchi." In: *IEEE Transactions on Medical Imaging* 32 (2) (2013), pp. 210–222 (cit. on pp. 160, 161, 169, 178, 260).

[270] Laurentini, A. "The Visual Hull Concept for Silhouette-Based Image Understanding." In: *IEEE Transactions on Pattern Analysis and Machine Intelligence* 16 (2) (1994), pp. 150–162 (cit. on p. 68).

[271] Lauterbur, P. C. "Image Formation by Induced Local Interactions: Examples Employing Nuclear Magnetic Resonance." In: *Nature* 242 (5394) (1973), pp. 190–191 (cit. on p. 16).

[272] Lawonn, K., Glaßer, S., Vilanova, A., Preim, B., and Isenberg, T. "Occlusion-Free Blood Flow Animation with Wall Thickness Visualization." In: *IEEE Transactions on Visualization and Computer Graphics* 22 (1) (2016), pp. 728–737 (cit. on pp. 46, 47, 49).

[273] Lawonn, K., Meuschke, M., Wickenhöfer, R., Preim, B., and Hildebrandt, K. "A Geometric Optimization Approach for the Detection and Segmentation of Multiple Aneurysms." In: *Computer Graphics Forum* 38 (3) (2019), pp. 413–425 (cit. on p. 190).

[274] Lawonn, K., Smit, N. N., Bühler, K., and Preim, B. "A Survey on Multimodal Medical Data Visualization." In: *Computer Graphics Forum* 37 (1) (2018), pp. 413–438 (cit. on pp. 33, 34, 49, 52, 215).

[275] Lawonn, K., Smit, N. N., Preim, B., and Vilanova, A. "Illustrative Multi-Volume Rendering for PET/CT Scans." In: *Proc. of Eurographics Workshop on Visual Computing in Biology and Medicine*. 2015, pp. 103–112 (cit. on pp. 33, 34, 49, 50, 76).

[276] Lawonn, K., Viola, I., Preim, B., and Isenberg, T. "A Survey of Surface-Based Illustrative Rendering for Visualization." In: *Computer Graphics Forum* 37 (6) (2018), pp. 205–234 (cit. on p. 178).

[277] Le Bihan, D., Mangin, J.-F., Poupon, C., Clark, C. A., Pappata, S., Molko, N., and Chabriat, H. "Diffusion Tensor Imaging: Concepts and Applications." In: *Journal of Magnetic Resonance Imaging* 13 (4) (2001), pp. 534–546 (cit. on p. 21).

[278] Lecoq, P. "Pushing The Limits in Time-of-Flight PET Imaging." In: *IEEE Transactions on Radiation and Plasma Medical Sciences* 1 (6) (2017), pp. 473–485 (cit. on p. 14).

[279] Lecouvet, F., Talbot, J. N., Messiou, C., Bourguet, P., Liu, Y., Souza, N. M. de, and Group, E. I. "Monitoring the Response of Bone Metastases to Treatment with Magnetic Resonance Imaging and Nuclear Medicine Techniques: A Review and Position Statement by the European Organisation for Research and Treatment of Cancer Imaging Group." In: *European Journal of Cancer* 50 (15) (2014), pp. 2519–2531 (cit. on p. 111).

[280] Lee, W.-Y., Shih, C.-L., and Lee, S.-T. "Force Control and Breakthrough Detection of a Bone-Drilling System." In: *IEEE/ASME Transactions on Mechatronics* 9 (1) (2004), pp. 20–29 (cit. on p. 121).

[281] Leggett, L. E., Soril, L. J., Lorenzetti, D. L., Noseworthy, T., Steadman, R., Tiwana, S., and Clement, F. "Radiofrequency Ablation for Chronic Low Back Pain: A Systematic Review of Randomized Controlled Trials." In: *Pain Research and Management* 19 (5) (2014), e146–e153 (cit. on pp. 107, 111, 131).

[282] Lemjabbar-Alaoui, H., Hassan, O. U., Yang, Y.-W., and Buchanan, P. "Lung Cancer: Biology and Treatment Options." In: *Biochimica et Biophysica Acta – Reviews on Cancer* 1856 (2) (2015), pp. 189–210 (cit. on pp. 25, 34, 59, 140, 190, 193, 194).

[283] Li, H. and Mould, D. "Contrast-Enhanced Black and White Images." In: *Computer Graphics Forum* 34 (7) (2015), pp. 319–328 (cit. on pp. 150, 163, 179, 180).

[284] Li, R. and Chen, J. "Toward A Deep Understanding of What Makes a Scientific Visualization Memorable." In: *arXiv preprint arXiv:1808.00607* (2018) (cit. on pp. 71, 73).

[285] Li, Z., Gupte, A. A., Zhang, A., and Hamilton, D. J. "PET Imaging and its Application in Cardiovascular Diseases." In: *Methodist DeBakey Cardiovascular Journal* 13 (1) (2017), pp. 29–33 (cit. on p. 79).

[286] Lide, D. R. *CRC Handbook of Chemistry and Physics*. 85th ed. CRC Press, 2004 (cit. on p. 16).

[287] Lieberman, I. H., Togawa, D., Kayanja, M. M., Reinhardt, M. K., Friedlander, A., Knoller, N., and Benzel, E. C. "Bone-Mounted Miniature Robotic Guidance for Pedicle Screw and Translaminar Facet Screw Placement: Part I – Technical Development and a Test Case Result." In: *Neurosurgery* 59 (3) (2006), pp. 641–650 (cit. on p. 120).

[288] Liljenqvist, U. R., Link, T. M., and Halm, H. F. "Morphometric Analysis of Thoracic and Lumbar Vertebrae in Idiopathic Scoliosis." In: *Spine* 25 (10) (2000), pp. 1247–1253 (cit. on p. 112).

[289] Lin, A. E., Ticho, B. S., Houde, K., Westgate, M.-N., and Holmes, L. B. "Heterotaxy: Associated Conditions and Hospital-Based Prevalence in Newborns." In: *Genetics in Medicine* 2 (3) (2000), pp. 157–172 (cit. on p. 152).

[290] Lin, S., Ritchie, D., Fisher, M., and Hanrahan, P. "Probabilistic Color-By-Numbers: Suggesting Pattern Colorizations Using Factor Graphs." In: *ACM Transactions on Graphics* 32 (4) (2013), pp. 37–1–37–12 (cit. on p. 211).

[291] Linden, P. A., Bueno, R., Colson, Y. L., Jaklitsch, M. T., Lukanich, J., Mentzer, S., and Sugarbaker, D. J. "Lung Resection in Patients with Preoperative FEV1 Less Than 35 Percent Predicted." In: *Chest* 127 (6) (2005), pp. 1984–1990 (cit. on pp. 140, 167).

[292] Lipton, A. "Future Treatment of Bone Metastases." In: *Clinical Cancer Research* 12 (20) (2006), 6305s–6308s (cit. on p. 111).

[293] Listemann, M., Trapp, M., and Döllner, J. "Lens-Based Focus+Context Visualization Techniques for Interactive Exploration of Web-based Reachability Maps." In: *Journal of WSCG* 27 (2) (2019), pp. 83–92 (cit. on p. 80).

[294] Littmann, A., Schenk, A., Preim, B., Prause, G, Lehmann, K., Roggan, A., and Peitgen, H.-O. "Planning of Anatomical Resections and In Situ Ablations in Oncologic Liver Surgery." In: *International Congress Series* 1256 (2003), pp. 684–689 (cit. on p. 109).

[295] Liu, J., Hoffman, J., Zhao, J., Yao, J., Lu, L., Kim, L., Turkbey, E. B., and Summers, R. M. "Mediastinal Lymph Node Detection and Station Mapping on Chest CT Using Spatial Priors and Random Forest." In: *Medical Physics* 43 (7) (2016), pp. 4362–4374 (cit. on p. 212).

[296] Liu, J., Napolitano, J. T., and Ebraheim, N. A. "Systematic Review of Cervical Pedicle Dimensions and Projections." In: *Spine* 35 (24) (2010), E1373–E1380 (cit. on p. 112).

[297] Ljung, P., Krüger, J., Gröller, E., Hadwiger, M., Hansen, C. D., and Ynnerman, A. "State of the Art in Transfer Functions for Direct Volume Rendering." In: *Computer Graphics Forum* 35 (3) (2016), pp. 669–691 (cit. on pp. 21, 215).

[298] Lodge, M. A., Lucas, J. D., Marsden, P. K., Cronin, B. F., O'Doherty, M. J., and Smith, M. A. "A PET Study of 18FDG Uptake in Soft Tissue Masses." In: *European Journal of Nuclear Medicine* 26 (1) (1999), pp. 22–30 (cit. on p. 11).

[299] Lorensen, W. E. and Cline, H. E. "Marching Cubes: A High Resolution 3D Surface Construction Algorithm." In: *ACM Siggraph Computer Graphics* 21 (4) (1987), pp. 163–169 (cit. on pp. 62, 91, 96, 134, 163).

[300] Loth, F., Yardimci, M. A., and Alperin, N. "Hydrodynamic Modeling of Cerebrospinal Fluid Motion Within the Spinal Cavity." In: *Journal of Biomechanical Engineering* 123 (1) (2001), pp. 71–79 (cit. on p. 104).

[301] Lott, B., Reece, F., and Drott, J. "Effect of Preconditioning on Bone Breaking Strength." In: *Poultry Science* 59 (4) (1979), pp. 724–725 (cit. on pp. 106, 141).

[302] Lu, F.-M. and Yuan, Z. "PET/SPECT Molecular Imaging in Clinical Neuroscience: Recent Advances in the Investigation of CNS Diseases." In: *Quantitative Imaging in Medicine and Surgery* 5 (3) (2015), pp. 433–447 (cit. on p. 12).

[303] Lu, S., Xu, Y. Q., Zhang, Y. Z., Li, Y. B., Xie, L., Shi, J. H., Guo, H., Chen, G. P., and Chen, Y. B. "A Novel Computer-Assisted Drill Guide Template for Lumbar Pedicle Screw Placement: A Cadaveric and Clinical Study." In: *The International Journal of Medical Robotics and Computer Assisted Surgery* 5 (2) (2009), pp. 184–191 (cit. on p. 120).

[304] Lu, S., Xu, Y. Q., Zhang, Y. Z., Xie, L., Guo, H., and Li, D. P. "A Novel Computer-Assisted Drill Guide Template for Placement of C2 Laminar Screws." In: *European Spine Journal* 18 (9) (2009), 1379—1385 (cit. on pp. 112, 120).

[305] Luce, M. F. and Kahn, B. E. "Avoidance or Vigilance? The Psychology of False-Positive Test Results." In: *Journal of Consumer Research* 26 (3) (1999), pp. 242–259 (cit. on pp. 155, 156).

[306] Luft, T., Colditz, C., and Deussen, O. "Image Enhancement by Unsharp Masking the Depth Buffer." In: *ACM Siggraph Computer Graphics* 25 (3) (2006), pp. 1206–1213 (cit. on p. 61).

[307] Lutz, S., Berk, L., Chang, E., Chow, E., Hahn, C., Hoskin, P., Howell, D., Konski, A., Kachnic, L., Lo, S., Sahgal, A., Silverman, L., Gunten, C. von, Mendel, E., Vassil, A., Bruner, D. W., and Hartsell, W. "Palliative Radiotherapy for Bone Metastases: An ASTRO Evidence-Based Guideline." In: *International Journal of Radiation Oncology*Biology*Physics* 79 (4) (2011), pp. 965–976 (cit. on p. 111).

[308] Maier-Hein, L., Müller, S. A., Pianka, F., Wörz, S., Müller-Stich, B. P., Seitel, A., Rohr, K., Meinzer, H.-P., Schmied, B. M., and Wolf, I. "Respiratory Motion Compensation for CT-Guided Interventions in the Liver." In: *Computer Aided Surgery* 13 (3) (2008), pp. 125–138 (cit. on pp. 62, 122, 129).

[309] Maintz, J. A. and Viergever, M. A. "A survey of Medical Image Registration." In: *Medical Image Analysis* 2 (1) (1998), pp. 1–36 (cit. on pp. 35, 36).

[310] Mairinger, S., Erker, T., Muller, M., and Langer, O. "PET and SPECT Radiotracers to Assess Function and Expression of ABC Transporters In Vivo." In: *Current Drug Metabolism* 12 (8) (2011), pp. 774–792 (cit. on p. 12).

[311] Mansfield, P. and Grannell, P. K. "NMR 'diffraction' in Solids?" In: *Journal of Physics C: Solid State Physics* 6 (22) (1973), pp. L422–L426 (cit. on p. 16).

[312] Marten, K, Dicken, V, Kneitz, C, Hoehmann, M, Kenn, W, Hahn, D, and Engelke, C. "Computer-Assisted Quantification of Interstitial Lung Disease Associated with Rheumatoid Arthritis: Preliminary Technical Validation." In: *European Journal of Radiology* 72 (2) (2009), pp. 278–283 (cit. on p. 155).

[313] Martin, J. and Saleem, N. "18F-FDG PET-CT Scanning and Diabetic Patients: What To Do?" In: *Nuclear Medicine Communications* 35 (12) (2014), pp. 1197–1203 (cit. on pp. 12, 152, 195).

[314] Martini, F. H., Timmons, M. J., and Tallitsch, R. B. *Human Anatomy*. 7th ed. Pearson Education, 2011 (cit. on pp. 66, 151, 152, 163).

[315] Martini, N., Flehinger, B. J., Zaman, M. B., and Beattie Jr, E. J. "Results of Resection in Non-Oat Cell Carcinoma of the Lung with Mediastinal Lymph Node Metastases." In: *Annals of Surgery* 198 (3) (1983), pp. 386–396 (cit. on pp. 152, 188).

[316] Matschek, J., Bullinger, E., Haeseler, F. von, Skalej, M., and Findeisen, R. "Mathematical 3D Modelling and Sensitivity Analysis of Multipolar Radiofrequency Ablation in the Spine." In: *Mathematical biosciences* 284 (2017), pp. 51–60 (cit. on p. 108).

[317] Mattern, H., Sciarra, A., Godenschweger, F., Stucht, D., Lüsebrink, F., Rose, G., and Speck, O. "Prospective Motion Correction Enables Highest Resolution Time-of-Flight Angiography at 7T." In: *Magnetic Resonance in Medicine* 80 (1) (2018), pp. 248–258 (cit. on p. 21).

[318] Meier, D, Wagenaar, D., Chen, S, Xu, J., Yu, J, and Tsui, B. "A SPECT Camera for Combined MRI and SPECT for Small Animals." In: *Nuclear Instruments and Methods in Physics Research Section A: Accelerators, Spectrometers, Detectors and Associated Equipment* 652 (1) (2011), pp. 731–734 (cit. on p. 28).

[319] **Merten, N.**, Adler, S., Georg, H., Hanses, M., Becker, M., Saalfeld, S., and Preim, B. "A Two-Step Risk Assessment Method for Radiofrequency Ablations of Spine Metastases." In: *Computers in Biology and Medicine* 108 (2019), pp. 174–181 (cit. on pp. 102, 109, 114, 118, 127, 130, 132, 133, 135–137, 139, 142–144, 259, 260).

[320] **Merten, N.**, Adler, S., Hanses, M., Saalfeld, S., Becker, M., and Preim, B. "Two-Step Trajectory Visualization for Robot-Assisted Spine Radiofrequency Ablations." In: *Proc. of Bildverarbeitung für die Medizin*. 2018, pp. 55–60 (cit. on pp. 65, 102, 118–120, 130, 131, 135, 141, 259, 260).

[321] **Merten, N.**, Genseke, P., Preim, B., Kreißl, M. C., and Saalfeld, S. "Maps, Colors, and SUVs for Standardized Clinical Reports." In: *Proc. of German Society of Computer- and Robot-Assisted Surgery*. 2019, pp. 292–297 (cit. on pp. 65, 188, 194, 200, 201, 203, 205, 207, 209, 212, 259).

[322] **Merten, N.**, Genseke, P., Preim, B., Kreißl, M. C., and Saalfeld, S. "Towards Automated Reporting and Visualization of Lymph Node Metastases of Lung Cancer." In: *Proc. of Bildverarbeitung für die Medizin*. 2019, pp. 185–190 (cit. on pp. 65, 188, 192, 196, 197, 212, 213, 217, 259).

[323] **Merten, N.**, Glaßer, S., Lassen-Schmidt, B., Großer, O. S., Ricke, J., Amthauer, H., and Preim, B. "Illustrative PET/CT Visualisation of SIRT-Treated Lung Metasteses." In: *Proc. of Eurographics Workshop on Visual Computing in Biology and Medicine*. 2016, pp. 99–104 (cit. on pp. 151, 155, 166, 169–172, 174, 175, 178, 259, 260).

[324] **Merten, N.**, Lawonn, K., Genseke, P., Großer, O. S., and Preim, B. "Lung Vessel Enhancement in Low-Dose CT Scans – The LANCELOT Method." In: *Proc. of Bildverarbeitung für die Medizin*. 2018, pp. 347–352 (cit. on pp. 151, 163, 181–183, 259).

[325] **Merten, N.**, Saalfeld, S., Hanses, M., Becker, M., Adler, S., and Preim, B. "A Software Prototype for Treatment Planning and Intervention Support of Robot-Assisted Radiofrequency Ablations of Vertebral Metastases." In: *Proc. of German Society of Computer- and Robot-Assisted Surgery*. 2017, pp. 89–94 (cit. on pp. 102, 124–126, 128, 129, 260).

[326] **Merten, N.**, Saalfeld, S., and Preim, B. "Floor Map Visualizations of Medical Volume Data." In: *Journal of WSCG* 27 (1) (2019), pp. 49–58 (cit. on pp. 65, 66, 84–95, 200, 259).

[327] Meuschke, M., Engelke, W., Beuing, O., Preim, B., and Lawonn, K. "Automatic Viewpoint Selection for Exploration of Time-dependent Cerebral Aneurysm Data." In: *Proc. of Bildverarbeitung für die Medizin*. 2017, pp. 352–357 (cit. on pp. 50, 77).

[328] Meuschke, M., Oeltze-Jafra, S., Beuing, O., Preim, B., and Lawonn, K. "Classification of Blood Flow Patterns in Cerebral Aneurysms." In: *IEEE Transactions on Visualization and Computer Graphics* 14 (8) (2018) (cit. on pp. 70, 78, 79).

[329] Meuschke, M., Voss, S., Beuing, O., Preim, B., and Lawonn, K. "Combined Visualization of Vessel Deformation and Hemodynamics in Cerebral Aneurysms." In: *IEEE Transactions on Visualization and Computer Graphics* 23 (1) (2016), pp. 761–770 (cit. on pp. 80, 81).

[330] Mewes, A., Heinrich, F., Kägebein, U., Hensen, B., Wacker, F., and Hansen, C. "Projector-Vased Augmented Reality System for Interventional Visualization Inside MRI Scanners." In: *The International Journal of Medical Robotics and Computer Assisted Surgery* 15 (1) (2019), e1950 (cit. on p. 121).

[331] Michel, M., Ritter, M, Schönberg, S, Häcker, A, and Weisser, G. "Das urologische Dyna-CT." In: *Der Urologe* 51 (6) (2012), pp. 857–861 (cit. on p. 121).

[332] Mikell, J. K., Kaza, R. K., Roberson, P. L., Younge, K. C., Srinivasa, R. N., Majdalany, B. S., Cuneo, K. C., Owen, D., Devasia, T., Schipper, M. J., and Dewaraja, Y. K. "Impact of 90 Y PET Gradient-Based Tumor Segmentation on Voxel-Level Dosimetry in Liver Radioembolization." In: *European Journal of Nuclear Medicine and Molecular Imaging Physics* 5 (1) (2018), pp. 31–1–31–17 (cit. on p. 174).

[333] Miles, B., Ayed, I. B., Law, M. W., Garvin, G., Fenster, A., and Li, S. "Spine Image Fusion via Graph Cuts." In: *IEEE Transactions on Biomedical Engineering* 60 (7) (2013), pp. 1841–1850 (cit. on pp. 43, 44).

[334] Miller, G. A., Galanter, E., and Pribram, K. H. *Plans and the Structure of Behavior*. Henry Holt and Co, 1960 (cit. on p. 72).

[335] Miller, G. A. "The Magical Number Seven, Plus or Minus Two: Some Limits on our Capacity for Processing Information." In: *Psychological Review* 63 (2) (1956), p. 81 (cit. on pp. 72, 73).

[336] Milovanovic, I. S., Stjepanovic, M., and Mitrovic, D. "Distribution Patterns of the Metastases of the Lung Carcinoma in Relation to Histological Type of the Primary Tumor: An Autopsy Study." In: *Annals of Thoracic Medicine* 12 (3) (2017), pp. 191–198 (cit. on pp. 152–154, 189).

[337] Minami, Y. and Kudo, M. "Radiofrequency Ablation of Hepatocellular Carcinoma: Current Status." In: *World Journal of Radiology* 2 (11) (2010), pp. 417–424 (cit. on p. 101).

[338] Mindek, P., Mistelbauer, G., Gröller, E., and Bruckner, S. "Data-Sensitive Visual Navigation." In: *Computers & Graphics*. 2017, pp. 77–85 (cit. on pp. 85, 88, 97).

[339] Moccia, S., De Momi, E., El Hadji, S., and Mattos, L. S. "Blood Vessel Segmentation Algorithms -— Review of Methods, Datasets and Evaluation Metrics." In: *Computer Methods and Programs in Biomedicine* 158 (2018), pp. 71–91 (cit. on pp. 150, 163, 179).

[340] Modaressi, K., Bode-Lesniewska, B., Studer, G., Hofer, S., and Fuchs, B. "Knochenmetastasen – Abklärung und Therapie." In: *Swiss Medical Forum* 13 (29–30) (2013), pp. 571–579 (cit. on p. 111).

[341] Mönch, T., Adler, S., Hahn, P., Rössling, I., and Preim, B. "Distance-Aware Smoothing of Surface Meshes for Surgical Planning." In: *Proc. of International Workshop on Digital Engineering*. 2010, pp. 45–51 (cit. on p. 177).

[342] Monmonier, M. *How to Lie with Maps*. University of Chicago Press, 1996 (cit. on pp. 66, 67).

[343] Moses, W. W. "Fundamental Limits of Spatial Resolution in PET." In: *Nuclear Instruments and Methods in Physics Research Section A: Accelerators, Spectrometers, Detectors and Associated Equipment* 648 (2011), S236–S240 (cit. on p. 14).

[344] Mountain, C. F. and Dresler, C. M. "Regional Lymph Node Classification for Lung Cancer Staging." In: *Chest* 111 (6) (1997), pp. 1718–1723 (cit. on pp. 188, 189, 204).

[345] Mourino, M. R. "From Thales to Lauterbur, or from the Lodestone to MR Imaging: Magnetism and Medicine." In: *Radiology* 180 (3) (1991), pp. 593–612 (cit. on pp. 14, 16).

[346] Mühler, K., Neugebauer, M., Tietjen, C., and Preim, B. "Viewpoint Selection for Intervention Planning." In: *Proc. of IEEE/Eurographics Symposium on Visualization*. 2007, pp. 267–274 (cit. on p. 77).

[347] Mühler, K., Tietjen, C., Ritter, F., and Preim, B. "The Medical Exploration Toolkit: An Efficient Support for Visual Computing in Surgical Planning and Training." In: *IEEE Transactions on Visualization and Computer Graphics* 16 (1) (2009), pp. 133–146 (cit. on p. 62).

[348] Muller, L., Saeed, M., Wilson, M. W., and Hetts, S. W. "Remote Control Catheter Navigation: Options for Guidance under MRI." In: *Journal of Cardiovascular Magnetic Resonance* 14 (1) (2012), pp. 33–1–33–9 (cit. on p. 165).

[349] Mundy, G. R. "Metastasis to Bone: Causes, Consequences and Therapeutic Opportunities." In: *Nature Reviews Cancer* 2 (8) (2002), pp. 584–593 (cit. on pp. 105, 106, 110, 111).

[350] Muzic Jr, R. F. and DiFilippo, F. P. "PET/MRI–Technical Review." In: *Seminars in Roentgenology*. Vol. 49. 3. 2014, pp. 242–254 (cit. on p. 26).

[351] Myocardial Segmentation, A. H. A. W. G. on, Cardiac Imaging: R. for, Cerqueira, M. D., Weissman, N. J., Dilsizian, V., Jacobs, A. K., Kaul, S., Laskey, W. K., Pennell, D. J., Rumberger, J. A., Ryan, T., and Verani, M. S. "Standardized Mmyocardial Segmentation and Nomenclature for Tomographic Imaging of the Heart: A Statement for Healthcare Professionals from the Cardiac Imaging Committee of the Council on Clinical Cardiology of the American Heart Association." In: *Circulation* 105 (4) (2002), pp. 539–542 (cit. on p. 45).

[352] Nagata, H., Murayama, K., Suzuki, S., Watanabe, A., Hayakawa, M., Saito, Y., Katada, K., and Toyama, H. "Initial Clinical Experience of a Prototype Ultra-High-Resolution CT for Assessment of Small Intracranial Arteries." In: *Japanese Journal of Radiology* 37 (4) (2019), pp. 283–291 (cit. on p. 6).

[353] Nageotte, F., Zanne, P., Doignon, C., and De Mathelin, M. "Stitching Planning in Laparoscopic Surgery: Towards Robot-Assisted Suturing." In: *The International Journal of Robotics Research* 28 (10) (2009), pp. 1303–1321 (cit. on p. 121).

[354] Naidich, D. P., Rusinek, H., McGuinness, G., Leitman, B., McCauley, D. I., and Henschke, C. I. "Variables Affecting Pulmonary Nodule Detection with Computed Tomography: Evaluation with Three-Dimensional Computer Simulation." In: *Journal of Thoracic Imaging* 8 (4) (1993), pp. 291–299 (cit. on p. 157).

[355] Nakahara, K., Ohno, K., Hashimoto, J., Miyoshi, S., Maeda, H., Matsumura, A., Mizuta, T., Akashi, A., Nakagawa, K., and Kawashima, Y. "Prediction of Postoperative Respiratory Failure in Patients Undergoing Lung Resection for Lung Cancer." In: *The Annals of Thoracic Surgery* 46 (5) (1988), pp. 549–552 (cit. on p. 167).

[356] Navkar, N. V., Tsekos, N. V., Stafford, J. R., Weinberg, J. S., and Deng, Z. "Visualization and planning of neurosurgical interventions with straight access." In: *Proc. of Information Processing in Computer-Assisted Interventions*. 2010, pp. 1–11 (cit. on pp. 114–117).

[357] Neeman, Z. and Wood, B. J. "Radiofrequency Ablation Beyond the Liver." In: *Techniques in Vascular and Interventional Radiology* 5 (3) (2002), pp. 156–163 (cit. on p. 111).

[358] Neugebauer, M., Lawonn, K., Beuing, O., and Preim, B. "Automatic Generation of Anatomic Characteristics from Cerebral Aneurysm Surface Models." In: *International Journal of Computer Assisted Radiology and Surgery* 8 (2) (2013), pp. 279–289 (cit. on pp. 77, 190).

[359] Neurath, O. *International Picture Language: The First Rules of Isotype*. Kegan Paul Trench Trubner & Co. Ltd, 1936 (cit. on p. 67).

[360] Nguyen, T. K., Ohlsson, H., Eklund, A., Hernell, F., Ljung, P., Forsell, C., Andersson, M., Knutsson, H., and Ynnerman, A. "Concurrent Volume Visualization of Real-Time fMRI." In: *Proc. of IEEE/Eurographics Symposium on Volume Graphics*. 2010, pp. 53–60 (cit. on pp. 39–41, 77, 98).

[361] Nguyen, T., Hattery, E., and Khatri, V. P. "Radiofrequency Ablation and Breast Cancer: A Review." In: *Gland Surgery* 3 (2) (2014), pp. 128–135 (cit. on p. 101).

[362] Nievelstein, R., Ufford, H. Q. van, Kwee, T., Bierings, M., Ludwig, I, Beek, F., Klerk, J. de, Mali, W. T. M., Bruin, P. de, and Geleijns, J. "Radiation Exposure and Mortality Risk from CT and PET Imaging of Patients with Malignant Lymphoma." In: *European Radiology* 22 (9) (2012), pp. 1946–1954 (cit. on p. 10).

[363] Norouzi, N., Shabak, M., Rashid Bin Embi, M, and Hayat Khan, T. "Participation Problems and Communication Difficulties in Architectural Design Practice." In: *Life Sciences* 11 (9) (2014), pp. 984–990 (cit. on pp. 71, 81).

[364] O, J. H., Lodge, M. A., and Wahl, R. L. "Practical PERCIST: A Simplified Guide to PET Response Criteria in Solid Tumors 1.0." In: *Radiology* 280 (2) (2016), pp. 576–584 (cit. on pp. 30, 59, 159, 166, 176, 193–196).

[365] Oeltze-Jafra, S., Meuschke, M., Neugebauer, M., Saalfeld, S., Lawonn, K., Janiga, G., Hege, H.-C., Zachow, S., and Preim, B. "Generation and Visual Exploration of Medical Flow Data: Survey, Research Trends and Future Challenges." In: *Computer Graphics Forum* 38 (1) (2019), pp. 87–125 (cit. on pp. 46, 70).

[366] Pandey, R. K. and Panda, S. S. "Drilling of Bone: A Comprehensive Review." In: *Journal of Clinical Orthopaedics and Trauma* 4 (1) (2013), pp. 15–30 (cit. on p. 113).

[367] Parent, S., Labelle, H., Skalli, W., and Guise, J. de. "Thoracic Pedicle Morphometry in Vertebrae from Scoliotic Spines." In: *Spine* 29 (3) (2004), pp. 239–248 (cit. on p. 112).

[368] Park, J. K., Kim, S. K., Cho, I. H., and Kong, E. J. "Measurement of SUVs-Maximum for Normal Region Using VOI in PET/MRI and PET/CT." In: *The Scientific World Journal* 2014 (2014), pp. 194925–1–194925–10 (cit. on p. 25).

[369] Patel, D., Al Hossain, M. S., Qiu, W., Jie, H., Yamauchi, Y., Maeda, M., Tomsic, M., Choi, S., and Kim, J. H. "Solid Cryogen: A Cooling System for future MgB2 MRI Magnet." In: *Scientific Reports* 7 (2017), pp. 43444–1–43444–8 (cit. on p. 21).

[370] Pawsey, J. L. and Bracewell, R. N. "Radio Astronomy." In: *Oxford, Clarendon Press, 1955.* (1955) (cit. on p. 6).

[371] Peitgen, H.-O., Preim, B., Selle, D., Böhm, D., Schenk, A., and Spindler, W. "Risk Analysis for Liver Surgery." In: *Mathematics and Culture* 1 (2003) (cit. on p. 117).

[372] Peterhans, M., Anderegg, S., Gaillard, P., Oliveira-Santos, T., and Weber, S. "A Fully Automatic Calibration Framework for Navigated Ultrasound Imaging." In: *Proc. of International Conference of the IEEE Engineering in Medicine and Biology Society*. 2010, pp. 1242–1245 (cit. on pp. 120, 121, 125).

[373] Pilge, H, Holzapfel, B., Prodinger, P., Hadjamu, M, Gollwitzer, H, and Rechl, H. "Diagnostik und Therapie von Wirbelsäulenmetastasen." In: *Der Orthopäde* 40 (2) (2011), pp. 185–196 (cit. on pp. 106, 110, 111).

[374] Pluim, J. P., Maintz, J. A., and Viergever, M. A. "Mutual-Information-Based Registration of Medical Images: A Survey." In: *IEEE Transactions on Medical Imaging* 22 (8) (2003), pp. 986–1004 (cit. on pp. 36, 37).

[375] Poffo, R., Toschi, A. P., Pope, R. B., Celullare, A. L., Benício, A., Fischer, C. H., Vieira, M. L. C., Teruya, A., Hatanaka, D. M., Rusca, G. F., and Makdisse, M. "Robotic Surgery

in Cariology: A Safe and Effective Procedure." In: *Einstein (Sao Paulo)* 11 (3) (2013), pp. 296–302 (cit. on p. 123).

[376] Pöpperl, G., Helmberger, T., Münzing, W., Schmid, R., Jacobs, T. F., and Tatsch, K. "Selective Internal Radiation Therapy with SIR-Spheres® in Patients with Nonresectable Liver Tumors." In: *Cancer Biotherapy & Radiopharmaceuticals* 20 (2) (2005), pp. 200–208 (cit. on pp. 149, 164, 185).

[377] Posner, M. I. "Orienting of Attention." In: *Quarterly Journal of Experimental Psychology* 32 (1) (1980), pp. 3–25 (cit. on p. 68).

[378] Posteraro, A., Dupuy, D., and Mayo-Smith, W. "Radiofrequency Ablation of Bony Metastatic Disease." In: *Clinical Radiology* 59 (9) (2004), pp. 803–811 (cit. on p. 111).

[379] Preim, B and Meuschke, M. "Medical Animations: A Survey and a Research Agenda." In: *Proc. of Eurographics Workshop on Visual Computing in Biology and Medicine*. 2019, in print (cit. on pp. 70, 72).

[380] Preim, B., Baer, A., Cunningham, D., Isenberg, T., and Ropinski, T. "A Survey of Perceptually Motivated 3D Visualization of Medical Image Data." In: *Computer Graphics Forum* 35 (3) (2016), pp. 501–525 (cit. on p. 50).

[381] Preim, B. and Botha, C. P. *Visual Computing for Medicine: Theory, Algorithms, and Applications*. Newnes, 2014 (cit. on pp. 30, 35, 36, 45, 74, 75, 121, 164).

[382] Preim, B., Ropinski, T., and Isenberg, P. "A Critical Analysis of the Evaluation Practice in Medical Visualization." In: *Proc. of Eurographics Workshop on Visual Computing in Biology and Medicine*. 2018, pp. 45–56 (cit. on pp. 97, 218).

[383] Preim, B. and Saalfeld, P. "A Survey of Virtual Human Anatomy Education Systems." In: *Computers & Graphics* 71 (2018), pp. 132–153 (cit. on pp. 2, 66).

[384] Puerta, A. M. "The Power of Shadows: Shadow Stereopsis." In: *Journal of the Optical Society of America A* 6 (2) (1989), pp. 309–311 (cit. on p. 176).

[385] Purcell, E. M., Torrey, H. C., and Pound, R. V. "Resonance Absorption by Nuclear Magnetic Moments in a Solid." In: *Physical Review* 69 (1 & 2) (1946), p. 37 (cit. on p. 16).

[386] Rabi, I. I., Zacharias, J. R., Millman, S., and Kusch, P. "A New Method of Measuring Nuclear Magnetic Moment." In: *Physical Review* 53 (4) (1938), p. 318 (cit. on p. 15).

[387] Radon, J. "Über die Bestimmung von Funktionen durch ihre Integralwerte längs gewisser Mannigfaltigkeiten." In: *Berichte über die Verhandlungen der Königlich-Sächsischen Akademie der Wissenschaften zu Leipzig, Mathematisch-Physische Klasse* 69 (1917), 262–277 (cit. on p. 6).

[388] Rak, M. and Tönnies, K.-D. "On Computerized Methods for Spine Analysis in MRI: A Systematic Review." In: *International Journal of Computer Assisted Radiology and Surgery* 11 (8) (2016), pp. 1445–1465 (cit. on p. 145).

[389] Ramer, U. "An Iterative Procedure for the Polygonal Approximation of Plane Curves." In: *Computer Graphics and Image Processing* 1 (3) (1972), pp. 244–256 (cit. on p. 67).

[390] Rami-Porta, R., Crowley, J. J., and Goldstraw, P. "Review – The Revised TNM Staging System for Lung Cancer." In: *Annals of Thoracic and Cardiovascular Surgery* 15 (1) (2009), pp. 4–9 (cit. on p. 64).

[391] Rampinelli, C., Origgi, D., and Bellomi, M. "Low-Dose CT: Technique, Reading Methods and Image Interpretation." In: *Cancer Imaging* 12 (3) (2012), pp. 548–556 (cit. on pp. 156, 157).

[392] Rangacharyulu, C. and Roh, C. K. "Isotopes for Combined PET/SPECT Imaging." In: *Journal of Radioanalytical and Nuclear Chemistry* 305 (1) (2015), pp. 87–92 (cit. on p. 29).

[393] Reilly, D., Ensslin, N., Smith Jr, H., and Kreiner, S. *Passive Nondestructive Assay of Nuclear Materials*. Tech. rep. Nuclear Regulatory Commission, 1991 (cit. on p. 10).

[394] Reiner, B. and Siegel, E. "Radiology Reporting: Returning to Our Image-Centric Roots." In: *American Journal of Roentgenology* 187 (5) (2006), pp. 1151–1155 (cit. on pp. 2, 187, 213, 217).

[395] Ren, H., Campos-Nanez, E., Yaniv, Z., Banovac, F., Abeledo, H., Hata, N., and Cleary, K. "Treatment Planning and Image Guidance for Radiofrequency Ablation of Large Tumors." In: *IEEE Journal of Biomedical and Health Informatics* 18 (3) (2013), pp. 920–928 (cit. on p. 107).

[396] Reuter, S., Gupta, S. C., Chaturvedi, M. M., and Aggarwal, B. B. "Oxidative Stress, Inflammation, and Cancer: How Are They Linked?" In: *Free radical biology and medicine* 49 (11) (2010), pp. 1603–1616 (cit. on pp. 7, 9).

[397] Rhyne, T.-M. "Applying Color Theory to Digital Media and Visualization." In: *Proc. of ACM SIGGRAPH Courses*. 2012, pp. 1–1–1–82 (cit. on p. 73).

[398] Ricke, J., Großer, O., and Amthauer, H. "Y90-Radioembolization of Lung Metastases via the Bronchial Artery: A Report of 2 Cases." In: *Cardiovascular and Interventional Radiology* 36 (6) (2013), pp. 1664–1669 (cit. on pp. 148, 149, 163–165, 167, 179, 193).

[399] Ricke, J., Wust, P., Wieners, G., Hengst, S., Pech, M., Hänninen, E. L., and Felix, R. "CT-Guided Interstitial Single-Fraction Brachytherapy of Lung Tumors: Phase I Results of a Novel Technique." In: *Chest* 127 (6) (2005), pp. 2237–2242 (cit. on p. 165).

[400] Rieder, C., Kroeger, T., Schumann, C., and Hahn, H. K. "GPU-Based Real-Time Approximation of the Ablation Zone for Radiofrequency Ablation." In: *IEEE Transactions on Visualization and Computer Graphics* 17 (12) (2011), pp. 1812–1821 (cit. on p. 108).

[401] Rieder, C., Ritter, F., Raspe, M., and Peitgen, H.-O. "Interactive Visualization of Multimodal Volume Data for Neurosurgical Tumor Treatment." In: *Computer Graphics Forum* 27 (3) (2008), pp. 1055–1062 (cit. on pp. 52, 54, 59–61, 64).

[402] Rieder, C., Schwier, M., Hahn, H. K., and Peitgen, H.-O. "High-Quality Multimodal Volume Visualization of Intracerebral Pathological Tissue." In: *Proc. of Eurographics Workshop on Visual Computing in Biology and Medicine*. 2008, pp. 167–176 (cit. on pp. 52–54, 60).

[403] Rieder, C., Weihusen, A., Schumann, C., Zidowitz, S., and Peitgen, H.-O. "Visual Support for Interactive Post-Interventional Assessment of Radiofrequency Ablation Therapy." In: *Computer Graphics Forum* 29 (3) (2010), pp. 1093–1102 (cit. on pp. 2, 80, 81, 114, 116–118, 122, 146).

[404] Rieke, V. and Butts Pauly, K. "MR Thermometry." In: *Journal of Magnetic Resonance Imaging* 27 (2) (2008), pp. 376–390 (cit. on p. 113).

[405] Rincón-Nigro, M., Navkar, N. V., Tsekos, N. V., and Deng, Z. "GPU-Accelerated Interactive Visualization and Planning of Neurosurgical Interventions." In: *IEEE Computer Graphics and Applications* 34 (1) (2014), pp. 22–31 (cit. on pp. 114–116).

[406] Ritter, F., Boskamp, T., Homeyer, A., Laue, H., Schwier, M., Link, F., and Peitgen, H.-O. "Medical Image Analysis." In: *IEEE Pulse* 2 (6) (2011), pp. 60–70 (cit. on pp. 38, 87, 126, 134, 182, 190, 196, 210).

[407] Ritter, J. W. "Ausfindung nicht lichtbarer Sonnenstrahlen ausserhalb des Farbenspectrums, an der Seite des Violetts." In: *Annals of Physics* 7 (1801), pp. 501–528 (cit. on p. 5).

[408] Röntgen, W. C. "On a New Kind of Rays." In: *Science* 3 (59) (1896), pp. 227–231 (cit. on p. 5).

[409] Ropinski, T., Hermann, S., Reich, R., Schafers, M., and Hinrichs, K. "Multimodal Vessel Visualization of Mouse Aorta PET/CT Scans." In: *IEEE Transactions on Visualization and Computer Graphics* 15 (6) (2009), pp. 1515–1522 (cit. on p. 38).

[410] Ropinski, T., Oeltze, S., and Preim, B. "Survey of Glyph-Based Visualization Techniques for Spatial Multivariate Medical Data." In: *Computers & Graphics* 35 (2) (2011), pp. 392–401 (cit. on pp. 79, 80).

[411] Ropinski, T., Specht, M., Meyer-Spradow, J., Hinrichs, K. H., and Preim, B. "Surface Glyphs for Visualizing Multimodal Volume Data." In: *Proc. of Symposium on Vision, Modeling, and Visualization*. 2007, pp. 3–12 (cit. on p. 79).

[412] Rösch, J., Keller, F. S., and Kaufman, J. A. "The Birth, Early Years, and Future of Interventional Radiology." In: *Journal of Vascular and Interventional Radiology* 14 (7) (2003), pp. 841–853 (cit. on p. 2).

[413] Rosenthal, D. and Callstrom, M. R. "Critical Review and State of the Art in Interventional Oncology: Benign and Metastatic Disease Involving Bone." In: *Radiology* 262 (3) (2012), pp. 765–780 (cit. on pp. 111, 131).

[414] Rosset, A., Spadola, L., Pysher, L., and Ratib, O. "Navigating the Fifth Dimension: Innovative Interface for Multidimensional Multimodality Image Navigation." In: *Radiographics* 26 (1) (2006), pp. 299–308 (cit. on pp. 37, 38).

[415] Rössling, I., Cyrus, C., Dornheim, L., Boehm, A., and Preim, B. "Fast and Flexible Distance Measures for Treatment Planning." In: *International Journal of Computer Assisted Radiology and Surgery* 5 (6) (2010), pp. 633–646 (cit. on p. 147).

[416] Rössling, I., Dornheim, J., Dornheim, L., Boehm, A., and Preim, B. "The Tumor Therapy Manager – Design, Refinement and Clinical Use of a Software Product for ENT Surgery Planning and Documentation." In: *Proc. of Information Processing in Computer-Assisted Interventions*. 2011, pp. 1–12 (cit. on p. 191).

[417] Roth, C. G. *Fundamentals of Body MRI*. Saunders, 2011 (cit. on pp. 16, 17, 19–22).

[418] Röttger, D., Engelhardt, S., and Müller, S. "Multimodal Visualizations for Pre-operative Neurosurgical Planning." In: *Proc. of German Informatics Society*. 2011, pp. 438–1–438–13 (cit. on pp. 59, 61, 64).

[419] Ruiz, M., Boada, I., Viola, I., Bruckner, S., Feixas, M., and Sbert, M. "Obscurance-Based Volume Rendering Framework." In: *Proc. of the Eurographics/IEEE Conference on Point-Based Graphics*. 2008, pp. 113–120 (cit. on pp. 47, 48, 55, 56).

[420] Rusch, V. W., Asamura, H., Watanabe, H., Giroux, D. J., Rami-Porta, R., and Goldstraw, P. "The IASLC Lung Cancer Staging Project: A Proposal for a New International Lymph Node Map in the Forthcoming Seventh Edition of the TNM Classification for Lung Cancer." In: *Journal of Thoracic Oncology* 4 (5) (2009), pp. 568–577 (cit. on pp. 188–190).

[421] Saalfeld, P., Mewes, A., Hansen, C., and Preim, B. "Gaze-Based Annotations: Labels on Demand." In: *Proc. of German Society of Computer- and Robot-Assisted Surgery*. 2015, pp. 261–266 (cit. on pp. 80, 97).

[422] Saalfeld, P., Stojnic, A., Preim, B., and Oeltze-Jafra, S. "Semi-Immersive 3D Sketching of Vascular Structures for Medical Education." In: *Proc. of Eurographics Workshop on Visual Computing in Biology and Medicine*. 2016, pp. 123–132 (cit. on p. 68).

[423] Saha, G. B. *Basics of PET Imaging: Physics, Chemistry, and Regulations*. Springer, Cham, 2015 (cit. on p. 12).

[424] Saladin, K. S. *Human Anatomy*. 2nd ed. McGraw-Hill, 2008 (cit. on pp. 66, 151–153, 161, 163, 188, 204).

[425] Sánchez, F, Orero, A, Soriano, A, Correcher, C, Conde, P, González, A, Hernández, L, Moliner, L, Rodríguez-Alvarez, M. J., Vidal, L., Benlloch, J. M., Chapman, S. E., and Leevy, W. M. "ALBIRA: A Small Animal PET/SPECT/CT Imaging System." In: *Medical Physics* 40 (5) (2013), pp. 051906–1–051906–11 (cit. on p. 28).

[426] Sato, Y., Nakajima, S., Atsumi, H., Koller, T., Gerig, G., Yoshida, S., and Kikinis, R. "3D Multi-Scale Line Filter for Segmentation and Visualization of Curvilinear Structures in Medical Images." In: *Proc. of Computer Vision, Virtual Reality and Robotics in Medicine and Medical Robotics and Computer-Assisted Surgery*. 1997, pp. 213–222 (cit. on pp. 150, 162, 179, 180, 182, 183, 185).

[427] Schaefer, O., Lohrmann, C., Markmiller, M., Uhrmeister, P., and Langer, M. "Combined Treatment of a Spinal Metastasis with Radiofrequency Heat Ablation and Vertebroplasty." In: *American Journal of Roentgenology* 180 (4) (2003), pp. 1075–1077 (cit. on pp. 111, 131).

[428] Schlachter, M., Fechter, T., Nestle, U., and Bühler, K. "Visualization of 4D-Pet/CT, Target Volumes and Dose Distribution: Applications in Radiotherapy Planning." In: *Proc. of MICCAI Workshop on Image-Guided Adaptive Radiation Therapy*. 2014 (cit. on p. 63).

[429] Schlachter, M., Raidou, R. G., Muren, L. P., Preim, B., Putora, P. M., and Bühler, K. "State-of-the-Art Report: Visual Computing in Radiation Therapy Planning." In: *Computer Graphics Forum* 38 (3) (2019), pp. 753–779 (cit. on pp. 34, 62, 63, 111, 159).

[430] Schlemmer, H.-P. W., Pichler, B. J., Schmand, M., Burbar, Z., Michel, C., Ladebeck, R., Jattke, K., Townsend, D., Nahmias, C., Jacob, P. K., Heiss, W. D., and Claussen, C. D. "Simultaneous MR/PET Imaging of the Human Brain: Feasibility Study." In: *Radiology* 248 (3) (2008), pp. 1028–1035 (cit. on pp. 25, 26).

[431] Schmidt Júnior, A. F., Rodrigues, O. R., Matheus, R. S., Kim, J. D. U., and Jatene, F. B. "Mediastinal Lymph Node Distribution, Size and Number: Definitions Based on an Anatomical Study." In: *Jornal Brasileiro de Pneumologia* 33 (2) (2007), pp. 134–140 (cit. on p. 189).

[432] Schreiber, J. J., Anderson, P. A., and Hsu, W. K. "Use of Computed Tomography for Assessing Bone Mineral Density." In: *Neurosurgical Focus* 37 (1) (2014), E4–1–E4–8 (cit. on p. 127).

[433] Schreiber, J. J., Anderson, P. A., Rosas, H. G., Buchholz, A. L., and Au, A. G. "Hounsfield Units for Assessing Bone Mineral Density and Strength: A Tool for Osteoporosis Management." In: *The Journal of Bone and Joint Surgery* 93 (11) (2011), pp. 1057–1063 (cit. on p. 127).

[434] Schulz, C. J., Schmitt, M., Böckler, D., and Geisbüsch, P. "Feasibility and Accuracy of Fusion Imaging During Thoracic Endovascular Aortic Repair." In: *Journal of Vascular Surgery* 63 (2) (2016), pp. 314–322 (cit. on p. 42).

[435] Seemann, M. D., Nekolla, S, Ziegler, S, Bengel, F, and Schwaiger, M. "PET/CT: Fundamental Principles." In: *European Journal of Medical Research* 9 (2004), pp. 241–246 (cit. on p. 24).

[436] Seibold, U., Kübler, B., and Hirzinger, G. "Prototype of Instrument for Minimally Invasive Surgery with 6-Axis Force Sensing Capability." In: *Proc. of IEEE International Conference on Robotics and Automation.* 2005, pp. 496–501 (cit. on p. 121).

[437] Selvaggi, G. and Scagliotti, G. V. "Management of Bone Metastases in Cancer: A Review." In: *Critical Reviews in Oncology/Hematology* 56 (3) (2005), pp. 365–378 (cit. on pp. 105, 106).

[438] Semmo, A. and Döllner, J. "Interactive Image Filtering for Level-of-Abstraction Texturing of Virtual 3D Scenes." In: *Computers & Graphics* 52 (2015), pp. 181–198 (cit. on p. 70).

[439] Semonche, A., Eichberg, D., Shah, A., and Ivan, M. E. "Laser Ablation for Gliomas." In: *IntechOpen: 10.5772/intechopen.86829* (2019) (cit. on p. 109).

[440] Shao, Y., Cherry, S. R., Farahani, K., Meadors, K., Siegel, S., Silverman, R. W., and Marsden, P. K. "Simultaneous PET and MR Imaging." In: *Physics in Medicine & Biology* 42 (1997), pp. 1965–1970 (cit. on pp. 25, 26).

[441] Shariat, S. F., Raptidis, G., Masatoschi, M., Bergamaschi, F., and Slawin, K. M. "Pilot Study of Radiofrequency Interstitial Tumor Ablation (RITA) for the Treatment of Radio-Recurrent Prostate Cancer." In: *The Prostate* 65 (3) (2005), pp. 260–267 (cit. on p. 101).

[442] Shea, K. S. and McMaster, R. B. "Cartographic Generalization in a Digital Environment: When and How to Generalize." In: *Proc. of International Research Symposium on Computer-Based Cartography*. 1989, pp. 56–67 (cit. on p. 67).

[443] Shneiderman, B. "The Eyes Have It: A Task by Data Type Taxonomy for Information Visualizations." In: *Proc. of IEEE Symposium on Visual Languages*. 1996, pp. 336–343 (cit. on p. 70).

[444] Siciliano, B. and Khatib, O. *Springer Handbook of Robotics*. Springer, 2016 (cit. on pp. 122, 123, 148, 216).

[445] Siegel, R. L., Miller, K. D., and Jemal, A. "Cancer Statistics, 2019." In: *CA: A Cancer Journal for Clinicians* 69 (1) (2019), pp. 7–34 (cit. on pp. 105, 106, 153–155).

[446] Simons, D. J. and Levin, D. T. "Change Blindness." In: *Trends in Cognitive Sciences* 1 (7) (1997), pp. 261–267 (cit. on p. 72).

[447] Singh, M. and Anderson, B. L. "Toward a Perceptual Theory of Transparency." In: *Psychological Review* 109 (3) (2002), pp. 492–519 (cit. on pp. 41, 168).

[448] Singh, M. and Hoffman, D. D. "Part Boundaries Alter the Perception of Transparency." In: *Psychological Science* 9 (5) (1998), pp. 370–378 (cit. on pp. 167, 168).

[449] Sivesgaard, K., Larsen, L. P., Sørensen, M., Kramer, S., Schlander, S., Amanavicius, N., Bharadwaz, A., Nielsen, D. T., Mortensen, F. V., and Pedersen, E. M. "Diagnostic Accuracy of CE-CT, MRI and FDG PET/CT for Detecting Colorectal Cancer Liver Metastases in Patients Considered Eligible for Hepatic Resection and/or Local Ablation." In: *European Radiology* 28 (11) (2018), pp. 4735–4747 (cit. on p. 60).

[450] Skanes, A. C., Klein, G., Krahn, A., and Yee, R. "Cryoablation: Potentials and Pitfalls." In: *Journal of Cardiovascular Electrophysiology* 15 (2004), S28–S34 (cit. on pp. 107, 185).

[451] Smit, N. and Bruckner, S. "Towards Advanced Interactive Visualization for Virtual Atlases." In: *Biomedical Visualisation*. 2019, pp. 85–96 (cit. on p. 66).

[452] Smyth, J., Sutton, D., and Houston, J. "Evaluation of the Quality of CT-Like Images Obtained Using a Commercial Flat Panel Detector System." In: *Biomedical Imaging and Intervention Journal* 2 (4) (2006) (cit. on p. 128).

[453] Šoltészová, V., Patel, D., and Viola, I. "Chromatic Shadows for Improved Perception." In: *Proc. of the Joint ACM SIGGRAPH/ Eurographics Symposium on Non-Photorealistic Animation and Rendering*. 2011, pp. 105–116 (cit. on p. 176).

[454] Sonnenberg, E. van, McMullen, W., Livraghi, T., and Solbiati, L. *Tumor Ablation: Principles and Practice*. Springer Science & Business Media, 2005 (cit. on pp. 107, 108).

[455] Souza, P. de, Aslan, P., Clark, W., Patel, M., Vass, J., Cade, D., and Silva, S. de. "Phase 1 Study of Selective Internal Radiation Therapy (SIRT) with Yttrium-90 (Y-90) Resin Microspheres in Patients (PTS) with Renal Cell Carcinoma (RCC): RESIRT." In: *Annals of Oncology* 27 (Supplement 6) (2016), pp. vi266–vi295 (cit. on p. 149).

[456] Spaepen, K., Stroobants, S., Dupont, P., Bormans, G., Balzarini, J., Verhoef, G., Mortelmans, L., Vandenberghe, P., and De Wolf-Peeters, C. "[18F]FDG PET Monitoring of Tumour Response to Chemotherapy: Does [18F]FDG Uptake Correlate with the Viable Tumour Cell Fraction?" In: *European Journal of Nuclear Medicine and Molecular Imaging* 30 (5) (2003), pp. 682–688 (cit. on p. 30).

[457] Spector, R., Snodgrass, S. R., and Johanson, C. E. "A Balanced View of the Cerebrospinal Fluid Composition and Functions: Focus on Adult Humans." In: *Experimental Neurology* 273 (2015), pp. 57–68 (cit. on p. 19).

[458] Spick, C., Herrmann, K., and Czernin, J. "18F-FDG PET/CT and PET/MRI Perform Equally Well in Cancer: Evidence from Studies on More Than 2,300 Patients." In: *Journal of Nuclear Medicine* 57 (3) (2016), pp. 420–430 (cit. on p. 60).

[459] Spitzer, V., Ackerman, M. J., Scherzinger, A. L., and Whitlock, D. "The Visible Human Male: A Technical Report." In: *Journal of the American Medical Informatics Association* 3 (2) (1996), pp. 118–130 (cit. on p. 48).

[460] Standring, S. *Gray's Anatomy E-Book: The Anatomical Basis of Clinical Practice*. 41st ed. Elsevier Health Sciences, 2016 (cit. on pp. 24, 66, 103, 105).

[461] Stickel, J. R. and Cherry, S. R. “High-Resolution PET Detector Design: Modelling Components of Intrinsic Spatial Resolution.” In: *Physics in Medicine & Biology* 50 (2) (2004), pp. 179–195 (cit. on p. 14).

[462] Stokking, R., Zuiderveld, K. J., and Viergever, M. A. “Integrated Volume Visualization of Functional Image Data and Anatomical Surfaces Using Normal Fusion.” In: *Human Brain Mapping* 12 (4) (2001), pp. 203–218 (cit. on pp. 39, 40).

[463] Strothotte, T. *Computational Visualization – Graphics, Abstraction and Interactivity*. Springer-Verlag Berlin Heidelberg, 1998 (cit. on pp. 69–71).

[464] Sundén, E., Kottravel, S., and Ropinski, T. “Multimodal Volume Illumination.” In: *Computers & Graphics* 50 (2015), pp. 47–60 (cit. on pp. 49, 62, 215).

[465] Sundén, E. and Ropinski, T. “Efficient Volume Illumination with Multiple Light Sources Through Selective Light Updates.” In: *Proc. of IEEE Pacific Visualization Symposium*. 2015, pp. 231–238 (cit. on p. 62).

[466] Tai, Y.-C., Chatziioannou, A. F., Yang, Y., Silverman, R. W., Meadors, K., Siegel, S., Newport, D. F., Stickel, J. R., and Cherry, S. R. “MicroPET II: Design, Development and Initial Performance of an Improved MicroPET Scanner for Small-Animal Imaging.” In: *Physics in Medicine & Biology* 48 (11) (2003), 2527—2545 (cit. on p. 14).

[467] Tam, A. L., Mohamed, A., Pfister, M., Chinndurai, P., Rohm, E., Hall, A. F., and Wallace, M. J. “C-Arm Cone Beam Computed Tomography Needle Path Overlay for Fluoroscopic Guided Vertebroplasty.” In: *Spine* 35 (10) (2010), pp. 1095–1099 (cit. on p. 122).

[468] Tappenbeck, A., Preim, B., and Dicken, V. “Distance-Based Transfer Function Design: Specification Methods and Applications.” In: *Proc. of the Conference on Simulation and Visualization*. 2006, pp. 259–274 (cit. on p. 133).

[469] Taylor, R., Thomson, H., Sutton, D., and Donkin, C. “Does Working Memory Have a Single Capacity Limit?” In: *Journal of Memory and Language* 93 (2017), pp. 67–81 (cit. on p. 72).

[470] Team, N. L. S. T. R. “The National Lung Screening Trial: Overview and Study Design.” In: *Radiology* 258 (1) (2011), pp. 243–253 (cit. on pp. 150, 156, 180, 182).

[471] Teo, T.-A. and Cho, K.-H. “BIM-Oriented Indoor Network Model for Indoor and Outdoor Combined Route Planning.” In: *Advanced Engineering Informatics* 30 (3) (2016), pp. 268–282 (cit. on pp. 75, 81, 82).

[472] Ter-Pogossian, M. M., Phelps, M. E., Hoffman, E. J., and Mullani, N. A. “A Positron-Emission Transaxial Tomograph for Nuclear Imaging (PETT).” In: *Radiology* 114 (1) (1975), pp. 89–98 (cit. on p. 10).

[473] Tietjen, C., Isenberg, T., and Preim, B. “Combining Silhouettes, Surface, and Volume Rendering for Surgery Education and Planning.” In: *Proc. of IEEE/Eurographics Symposium on Visualization*. 2005, pp. 303–310 (cit. on pp. 49, 50, 54, 71).

[474] Tietjen, C., Meyer, B., Schlechtweg, S., Preim, B., Hertel, I., and Strauss, G. “Enhancing Slice-based Visuaizations of Medical Volume Data.” In: *Proc. of IEEE/Eurographics Symposium on Visualization*. 2006, pp. 123–130 (cit. on pp. 62, 84, 85).

[475] Todoh, M, Tadano, S, and Imari, Y. “Effect of Heat Denaturation of Collagen Matrix on Bone Strength.” In: *Proc. of International Conference on Biomedical Engineering*. 2009, pp. 2034–2037 (cit. on p. 106).

[476] Togawa, D., Kayanja, M. M., Reinhardt, M. K., Shoham, M., Balter, A., Friedlander, A., Knoller, N., Benzel, E. C., and Lieberman, I. H. "Bone-Mounted Miniature Robotic Guidance for Pedicle Screw and Translaminar Facet Screw Placement: Part II – Evaluation of System Accuracy." In: *Operative Neurosurgery* 60 (Supplement 2) (2007), ONS–129–ONS–139 (cit. on p. 120).

[477] Tokuhashi, Y., Matsuzaki, H., Oda, H., Oshima, M., and Ryu, J. "A Revised Scoring System for Preoperative Evaluation of Metastatic Spine Tumor Prognosis." In: *Spine* 30 (19) (2005), pp. 2186–2191 (cit. on p. 111).

[478] Tolman, E. C. "Cognitive Maps in Rats and Men." In: *Psychological Review* 55 (4) (1948), pp. 189–208 (cit. on p. 72).

[479] Tomita, K., Kawahara, N., Kobayashi, T., Yoshida, A., Murakami, H., and Akamaru, T. "Surgical Strategy for Spinal Metastases." In: *Spine* 26 (3) (2001), pp. 298–306 (cit. on p. 111).

[480] Tong, D., Gillick, L., and Hendrickson, F. R. "The Palliation of Symptomatic Osseous Metastases Final Results of the Study by the Radiation Therapy Oncology Group." In: *Cancer* 50 (5) (1982), pp. 893–899 (cit. on p. 111).

[481] Townsend, D. W. "Dual-Modality Imaging: Combining Anatomy and Function." In: *Journal of Nuclear Medicine* 49 (6) (2008), pp. 938–955 (cit. on pp. 22–25).

[482] Townsend, D. W., Wensveen, M., Byars, L. G., Geissbuhler, A., Tochon-Danguy, H. J., Christin, A., Defrise, M., Bailey, D. L., Grootoonk, S., Donath, A., and Nutt, R. "A Rotating PET Scanner using BGO Block Detectors: Design, Performance and Applications." In: *Journal of Nuclear Medicine* 34 (1993), pp. 1367–1376 (cit. on p. 10).

[483] Townsend, D. "Physical Principles and Technology of Clinical PET Imaging." In: *Annals of the Academy of Medicine Singapore* 33 (2) (2004), pp. 133–145 (cit. on pp. 7, 10–14, 23).

[484] Townsley, M. I. "Structure and Composition of Pulmonary Arteries, Capillaries, and Veins." In: *Comprehensive Physiology* 2 (2011), pp. 675–709 (cit. on p. 163).

[485] Tsai, C., Schneider, D., Hermann, J., Mueller, F., Heeb, N., Holler, A., and Simon Tschachtli Gabriela O'Toole Bom Braga, S. W. "Life-Like Rendering of Inner Ear Anatomy." In: *Proc. of German Society of Computer- and Robot-Assisted Surgery*. 2019, pp. 229–233 (cit. on pp. 71, 74, 204).

[486] Tseng, H.-J., Henry, T. S., Veeraraghavan, S., Mittal, P. K., and Little, B. P. "Pulmonary Function Tests for the Radiologist." In: *Radiographics* 37 (4) (2017), pp. 1037–1058 (cit. on p. 149).

[487] Tsunezuka, Y., Oda, M., Ohta, Y., and Watanabe, G. "Congenital Absence of the Right Upper Lobe of the Lung." In: *The Annals of Thoracic Surgery* 74 (2) (2002), pp. 571–573 (cit. on p. 152).

[488] Tufte, E. R. *The Visual Display of Quantitative Information*. Graphics Press Cheshire, Connecticut, 2001 (cit. on pp. 187, 213, 217).

[489] Turk, G. and O'Brien, J. F. "Shape Transformation Using Variational Implicit Functions." In: *Proc. of ACM SIGGRAPH Courses*. 1999, pp. 335–342 (cit. on p. 126).

[490] Turner, P. and Holdsworth, G. "CT Stroke Window Settings: An Unfortunate Misleading Misnomer?" In: *The British Journal of Radiology* 84 (1008) (2011), pp. 1061–1066 (cit. on p. 29).

[491] Udiljak, T., Ciglar, D., and Skoric, S. "Investigation Into Bone Drilling and Thermal Bone Necrosis." In: *Advances in Production Engineering & Management* 2 (3) (2007), pp. 103–112 (cit. on p. 113).

[492] Valente, I. R. S., Cortez, P. C., Neto, E. C., Soares, J. M., Albuquerque, V. H. C. de, and Tavares, J. M. R. "Automatic 3D Pulmonary Nodule Detection in CT Images: A Survey." In: *Computer Methods and Programs in Biomedicine* 124 (2016), pp. 91–107 (cit. on p. 157).

[493] Van De Berg, N. J., De Jong, T. L., Van Gerwen, D. J., Dankelman, J., and Van Den Dobbelsteen, J. J. "The Influence of Tip Shape on Bending Force During Needle Insertion." In: *Scientific Reports* 7 (2017), pp. 40477–1–40477–8 (cit. on p. 121).

[494] Van Rikxoort, E. M., De Hoop, B., Van De Vorst, S., Prokop, M., and Van Ginneken, B. "Automatic Segmentation of Pulmonary Segments from Volumetric Chest CT Scans." In: *IEEE Transactions on Medical Imaging* 28 (4) (2009), pp. 621–630 (cit. on p. 162).

[495] Vander Heiden, M. G., Cantley, L. C., and Thompson, C. B. "Understanding the Warburg Effect: The Metabolic Requirements of Cell Proliferation." In: *Science* 324 (5930) (2009), pp. 1029–1033 (cit. on p. 12).

[496] Vanel, D. "MRI of Bone Metastases: The Choice of the Sequence." In: *Cancer Imaging* 4 (2003), pp. 30–35 (cit. on p. 111).

[497] Varrone, A., Asenbaum, S., Vander Borght, T., Booij, J., Nobili, F., Någren, K., Darcourt, J., Kapucu, Ö. L., Tatsch, K., Bartenstein, P., Van Laere, K., and Nuclear Medicine Neuroimaging Committee, A. of. "EANM Procedure Guidelines for PET Brain Imaging Using 18F-FDG, Version 2." In: *European Journal of Nuclear Medicine and Molecular Imaging* 36 (12) (2009), p. 2103 (cit. on p. 12).

[498] Vázquez, P.-P., Feixas, M., Sbert, M., and Heidrich, W. "Viewpoint Selection Using Viewpoint Entropy." In: *Proc. of Symposium on Vision, Modeling, and Visualization*. 2001, pp. 273–280 (cit. on pp. 48, 51, 77).

[499] Viergever, M. A., Maintz, J. A., Klein, S., Murphy, K., Staring, M., and Pluim, J. P. *A Survey of Medical Image Registration – Under Review*. 2016 (cit. on pp. 35, 36).

[500] Viola, I. and Gröller, E. "Smart Visibility in Visualization." In: *Computational Aesthetics*. 2005, pp. 209–216 (cit. on pp. 33, 45).

[501] Viola, I. and Isenberg, T. "Pondering the Concept of Abstraction in (Illustrative) Visualization." In: *IEEE Transactions on Visualization and Computer Graphics* 24 (9) (2018), pp. 2573–2588 (cit. on pp. 65, 69–71, 84, 85, 98, 119, 146, 149, 167, 177, 191, 192, 200, 203).

[502] Viola, I., Kanitsar, A., and Gröller, E. "Importance-Driven Feature Enhancement in Volume Visualization." In: *IEEE Transactions on Visualization and Computer Graphics* 11 (4) (2005), pp. 408–418 (cit. on pp. 45, 46, 74).

[503] Vogl, T. J., Helmberger, T. K., Mack, M. G., and Reiser, M. F. *Percutaneous Tumor Ablation in Medical Radiology*. Springer, 2008 (cit. on pp. 101, 106–109, 149, 165).

[504] Wagenknecht, G., Kaiser, H.-J., Mottaghy, F. M., and Herzog, H. "MRI for Attenuation Correction in PET: Methods and Challenges." In: *Magnetic Resonance Materials in Physics, Biology and Medicine* 26 (1) (2013), pp. 99–113 (cit. on p. 27).

[505] Walker, C. M., Christenson, M. L. Rosado-de, Martínez-Jiménez, S., Kunin, J. R., and Wible, B. C. "Bronchial Arteries: Anatomy, Function, Hypertrophy, and Anomalies." In: *Radiographics* 35 (1) (2015), pp. 32–49 (cit. on p. 152).

[506] Wang, G., Kalra, M., Murugan, V., Xi, Y., Gjesteby, L., Getzin, M., Yang, Q., Cong, W., and Vannier, M. "Vision 20/20: Simultaneous CT-MRI–Next Chapter of Multimodality Imaging." In: *Medical Physics* 42 (10) (2015), pp. 5879–5889 (cit. on p. 28).

[507] Wang, W., Shi, Y., Yang, N., and Yuan, X. "Experimental Analysis of Drilling Process in Cortical Bone." In: *Medical engineering & Physics* 36 (2) (2014), pp. 261–266 (cit. on p. 121).

[508] Wang, X., Sofocleous, C. T., Erinjeri, J. P., Petre, E. N., Gonen, M., Do, K. G., Brown, K. T., Covey, A. M., Brody, L. A., Alago, W., Thornton, R. H., Kemeny, N. E., and Solomon, S. B. "Margin Size Is an Independent Predictor of Local Tumor Progression After Ablation of Colon Cancer Liver Metastases." In: *Cardiovascular and Interventional Radiology* 36 (1) (2013), pp. 166–175 (cit. on pp. 121, 122, 147).

[509] Ward, R. P., Pokharna, H. K., Lang, R. M., and Williams, K. A. "Resting "Solar Polar" Map Pattern and Reduced Apical Flow Reserve: Characteristics of Apical Hypertrophic Cardiomyopathy on SPECT Myocardial Perfusion Imaging." In: *Journal of Nuclear Cardiology* 10 (5) (2003), pp. 506–512 (cit. on p. 45).

[510] Watson, C. C., Townsend, D. W., and Bendriem, B. "PET/CT Systems." In: *Emission Tomography*. Elsevier, 2004, pp. 195–212 (cit. on pp. 8, 9, 23–25).

[511] Wen, Y., Kai, S., Yong-gang, Z., Guo-quan, Z., and Tian-xiang, D. "Relationship Between Lung Volume and Pulmonary Function in Patients with Adolescent Idiopathic Scoliosis: Computed Tomographic-Based 3-Dimensional Volumetric Reconstruction of Lung Parenchyma." In: *Clinical Spine Surgery* 29 (8) (2016), E396–E400 (cit. on p. 160).

[512] West, J. B. *Respiratory Physiology: The Essentials*. Lippincott Williams & Wilkins, 2012 (cit. on p. 28).

[513] Westbrook, C. *MRI at a Glance*. Oxford: Blackwell Science, 2002 (cit. on pp. 16–22).

[514] Winer-Muram, H. T., Jennings, S. G., Meyer, C. A., Liang, Y., Aisen, A. M., Tarver, R. D., and McGarry, R. C. "Effect of Varying CT Section Width on Volumetric Measurement of Lung Tumors and Application of Compensatory Equations." In: *Radiology* 229 (1) (2003), pp. 184–194 (cit. on p. 159).

[515] Wood, B. J., Locklin, J. K., Viswanathan, A., Kruecker, J., Haemmerich, D., Cebral, J., Sofer, A., Cheng, R., McCreedy, E., Cleary, K., McAuliffe, M. J., Glossop, N., and Yanof, J. "Technologies for Guidance of Radiofrequency Ablation in the Multimodality Interventional Suite of the Future." In: *Journal of Vascular and Interventional Radiology* 18 (1) (2007), pp. 9–24 (cit. on p. 121).

[516] Yamane, T., Tateishi, A., Cho, S., Manabe, S., Yamanashi, M., Dezawa, A., Yasukouchi, H., and Ishioka, K. "The Effects of Hyperthermia on the Spinal Cord." In: *Spine* 17 (11) (1992), pp. 1386–1391 (cit. on p. 113).

[517] Yang, B., Liu, Y., You, L., and Jin, X. "A Unified Smoke Control Method Based on Signed Distance Field." In: *Computers & Graphics* 37 (2013), pp. 775–786 (cit. on pp. 119, 131, 133).

[518] Yelleswarapu, V. R., Liu, F., Cong, W., and Wang, G. "Top-Level System Designs for Hybrid Low-Field MRI-CT with Potential of Pulmonary Imaging." In: *Sensing and Imaging* 15 (1) (2014), pp. 98–1–98–9 (cit. on p. 28).

[519] Yener, Ö., Türkvatan, A., Yüce, G., and Yener, A. Ü. "The Normal Anatomy and Variations of the Bronchial Arteries: Evaluation with Multidetector Computed Tomography." In: *Canadian Association of Radiologists Journal* 66 (1) (2015), pp. 44–52 (cit. on pp. 153, 163).

[520] Yu, C. C., Bajwa, N. S., Toy, J. O., Ahn, U. M., and Ahn, N. U. "Pedicle Morphometry of Upper Thoracic Vertebrae: An Anatomic Study of 503 Cadaveric Specimens." In: *Spine* 39 (20) (2014), E1201–E1209 (cit. on p. 112).

[521] Yu, C. C., Yuh, R. T., Bajwa, N. S., Toy, J. O., Ahn, U. M., and Ahn, N. U. "Lower Thoracic Pedicle Morphometry: Male, Taller, and Heavier Specimens Have Bigger Pedicles." In: *Spine* 40 (6) (2015), E323–E331 (cit. on p. 112).

[522] Zahlten, C., Jürgens, H., and Peitgen, H.-O. "Reconstruction of Branching Blood Vessel from CT Data." In: *Proc. of Eurographics Workshop of Visualization in Scientific Computing*. 1995, pp. 41–52 (cit. on pp. 68, 70).

[523] Zaidi, H. and Del Guerra, A. "An Outlook on Future Design of Hybrid PET/MRI Systems." In: *Medical Physics* 38 (10) (2011), pp. 5667–5689 (cit. on pp. 22, 25–27, 31).

[524] Zechmeister, S., Cornel, D., and Wasser, J. "3D Annotations for Geospatial Decision Support Systems." In: *Journal of WSCG* 27 (2) (2019), pp. 141–150 (cit. on p. 80).

[525] Zeeman, P. "XXXII. On the Influence of Magnetism on the Nature of the Light Emitted by a Substance." In: *The London, Edinburgh, and Dublin Philosophical Magazine and Journal of Science* 43 (262) (1897), pp. 226–239 (cit. on p. 15).

[526] Zheng, L., Correa, C., and Ma, K.-L. "Visibility Guided Multimodal Volume Visualization." In: *Proc. of IEEE International Conference on Bioinformatics and Biomedicine*. 2013, pp. 297–304 (cit. on pp. 57, 58).

[527] Zhukov, S., Iones, A., and Kronin, G. "An Ambient Light Illumination Model." In: *Proc. of Rendering Techniques*. 1998, pp. 45–55 (cit. on pp. 48, 55).

[528] Zimmer, H. D. "The Construction of Mental Maps Based on a Fragmentary View of Physical Maps." In: *Journal of Educational Psychology* 96 (3) (2004), pp. 603–610 (cit. on pp. 73, 98).

[529] Zimmer, H. D., Münzer, S., and Umla-Runge, K. "Visuo-Spatial Working Memory as a Limited Resource of Cognitive Processing." In: *Resource-Adaptive Cognitive Processes*. 2010, pp. 13–34 (cit. on pp. 72, 73).

[530] Zombori, G., Rodionov, R., Nowell, M., Zuluaga, M. A., Clarkson, M. J., Micallef, C., Diehl, B., Wehner, T., Miserochi, A, McEvoy, A. W., Duncan, J. S., and Ourselin, S. "A Computer Assisted Planning System for the Placement of SEEG Electrodes in the Treatment of Epilepsy." In: *Proc. of Information Processing in Computer-Assisted Interventions*. 2014, pp. 118–127 (cit. on pp. 114, 115, 117–119, 147).

APPENDIX – DIVISION OF WORK

JOURNAL ARTICLES

• **Merten, N.**, Adler, S., Georg, H., Hanses, M., Becker, M., Saalfeld, S., and Preim, B. "A Two-Step Risk Assessment Method for Radiofrequency Ablations of Spine Metastases." In: *Computers in Biology and Medicine* 108 (2019), pp. 174–181. [319]

This article is the extension of [320]. Adler S. and Hanses M. provided everything related to Step 2, i. e. they conducted the drilling experiments, did the math to relate bone density and drilling forces, and provided a text basis for the paper. Becker M. provided DynaCT and MR image data that was used for Step 1 and gave feedback from the clinical perspective. Moreover, he provided the case descriptions for Case 1 and Case 2. Hille G. segmented and registered structures of interest in the provided image data. Saalfeld S. and Preim B. repeatedly provided comments and feedback on the paper structure. I designed and implemented Step 1, conducted the evaluations with our clinical colleagues, and wrote the paper. The interviewees were Beuing O. and Becker M. (coauthor).

• **Merten, N.**, Saalfeld, S., and Preim, B. "Floor Map Visualizations of Medical Volume Data." In: *Journal of WSCG* 27 (1) (2019), pp. 49–58. [326]

Saalfeld S. and Preim B. repeatedly provided comments and feedback on the paper structure and results. I implemented the method and wrote the paper. The interviewees were D'Hanis W., Schumann S. & Nardi L.

PEER-REVIEWED CONFERENCE PAPERS (PROCEEDINGS)

• **Merten, N.**, Genseke, P., Preim, B., Kreißl, M. C., and Saalfeld, S. "Towards Automated Reporting and Visualization of Lymph Node Metastases of Lung Cancer." In: *Proc. of Bildverarbeitung für die Medizin*. 2019, pp. 185–190. [322]

Saalfeld S. and Preim B. provided comments and feedback on the results. Genseke P. and Kreißl M. C. provided feedback from the clinical perspective. I implemented the method and wrote the paper.

• **Merten, N.**, Genseke, P., Preim, B., Kreißl, M. C., and Saalfeld, S. "Maps, Colors, and SUVs for Standardized Clinical Reports." In: *Proc. of German Society of Computer- and Robot-Assisted Surgery*. 2019, pp. 292–297. [321]

Saalfeld S. and Preim B. provided comments and feedback on the results. Genseke P. and Kreißl M. C. provided feedback from the clinical perspective. I implemented the method and wrote the paper.

• **Merten, N.**, Lawonn, K., Genseke, P., Großer, O. S., and Preim, B. "Lung Vessel Enhancement in Low-Dose CT Scans – The LANCELOT Method." In: *Proc. of Bildverarbeitung für die Medizin*. 2018, pp. 347–352. [324]

Lawonn K. provided two code bases that could be applied to Portable Network Graphics (PNG) images. Furthermore, he provided feedback on the paper structure and results. Genseke P. and Großer O. S. provided feedback from the clinical perspective. Preim B. repeatedly provided comments and feedback on the paper structure and results. I had the original idea to enhance blood vessels in low-dose CT images, which was an extension of [323]. Furthermore, I adapted the aforementioned 2nd code base to be applicable to DICOM files, conducted the evaluation and wrote the paper. The interviewees were Lübeck C. and Genseke P. (coauthor).

• **Merten, N.**, Adler, S., Hanses, M., Saalfeld, S., Becker, M., and Preim, B. "Two-Step Trajectory Visualization for Robot-Assisted Spine Radiofrequency Ablations." In: *Proc. of Bildverarbeitung für die Medizin*. 2018, pp. 55–60. [320]

Adler S. and Hanses M. provided everything related to Step 2. Becker M. provided feedback from the clinical perspective. Saalfeld S. and Preim B. repeatedly provided comments and feedback on the results. I designed Step 1 and I wrote the paper. The paper was invited to a special issue of the *International Journal of Computer Assisted Radiology and Surgery* (IJCARS). Finally, it was published in *Computers in Biology and Medicine* (CBM) [319]. The interviewee was Becker M. (coauthor).

• **Merten, N.**, Saalfeld, S., Hanses, M., Becker, M., Adler, S., and Preim, B. "A Software Prototype for Treatment Planning and Intervention Support of Robot-Assisted Radiofrequency Ablations of Vertebral Metastases." In: *Proc. of German Society of Computer- and Robot-Assisted Surgery*. 2017, pp. 89–94. [325]

Adler S. and Hanses M. provided technical feedback related to robotics and computer-assistance for RFAs. Becker M. provided feedback from the clinical perspective. Saalfeld S. and Preim B. provided comments and feedback on the results. I implemented the software prototype and wrote the paper. The interviewees were Adler S., Hanses M. and Becker M. (all coauthors).

• Hille, G., **Merten, N.**, Serowy, S., Glaßer, S., Tönnies, K., and Preim, B. "Assessing the Benefits of Interactive Patient-Specific Visualisations for Patient Information." In: *Proc. of Bildverarbeitung für die Medizin*. 2017, pp. 224–229. [193]

Hille G. and I wrote the paper, implemented the prototype, and conducted the interviews. He took over most of the coordination, and thus, he became the first author. Serowy S. provided the used CT and MRI data. Glaßer S., Tönnies K., and Preim B. provided comments and feedback on the results.

• **Merten, N.**, Glaßer, S., Lassen-Schmidt, B., Großer, O. S., Ricke, J., Amthauer, H., and Preim, B. "Illustrative PET/CT Visualisation of SIRT-Treated Lung Metasteses." In: *Proc. of Eurographics Workshop on Visual Computing in Biology and Medicine*. 2016, pp. 99–104. [323]

Lassen-Schmidt B. provided a *MeVisPULMO 3D* prototype to segment lung lobes from CT images [263, 269]. Furthermore, she provided hints on how to structure the paper. Großer O. S. , Ricke J. and Amthauer H. provided feedback from the clinical perspective. Großer O. S. recruited clinical colleagues who evaluated our method. Glaßer S. and Preim B. repeatedly provided comments and feedback on the paper structure and results. I implemented the method and wrote the paper. The interviewees were Apostolova I., Genseke P., Großer O. (coauthor), Kupitz D., Wetz C., Behrendt B., Glaßer S. (coauthor), Köhler B. and Saalfeld P.

• Glaßer, S., Saalfeld, P., Berg, P., **Merten, N.**, and Preim, B. "How to Evaluate Medical Visualizations on the Example of 3D Aneurysm Surfaces." In: *Proc. of Eurographics Workshop on Visual Computing in Biology and Medicine*. 2016, pp. 153–162. [151]

I recruited a part of the evaluatees, conducted the described experiments with them, and provided commends and feedback on the paper.

COLOPHON

This document was typeset using the typographical look-and-feel `classicthesis` developed by André Miede. The style was inspired by Robert Bringhurst's seminal book on typography "*The Elements of Typographic Style*". `classicthesis` is available for both LaTeX and LyX:

http://code.google.com/p/classicthesis/